Titre: Title:	Performance Increase and Noise Reduction in Axial Compressor Cascades with Plasma Actuation
Auteur: Author:	Eray Akçayöz
Date:	2012
Type:	Mémoire ou thèse / Dissertation or Thesis
Référence: Citation:	Akçayöz, E. (2012). Performance Increase and Noise Reduction in Axial Compressor Cascades with Plasma Actuation [Thèse de doctorat, École Polytechnique de Montréal]. PolyPublie. https://publications.polymtl.ca/1033/

UNIVERSITÉ DE MONTRÉAL

PERFORMANCE INCREASE AND NOISE REDUCTION IN AXIAL COMPRESSOR CASCADES WITH PLASMA ACTUATION

ERAY AKÇAYÖZ
DÉPARTEMENT DE GÉNIE MÉCANIQUE
ÉCOLE POLYTECHNIQUE DE MONTRÉAL

THÈSE PRÉSENTÉE EN VUE DE L'OBTENTION
DU DIPLÔME DE PHILOSOPHIÆ DOCTOR
(GÉNIE MÉCANIQUE)
DÉCEMBRE 2012

UNIVERSITÉ DE MONTRÉAL

ÉCOLE POLYTECHNIQUE DE MONTRÉAL

Cette thèse intitulée :

PERFORMANCE INCREASE AND NOISE REDUCTION IN AXIAL COMPRESSOR CASCADES WITH PLASMA ACTUATION

présentée par : AKÇAYÖZ Eray
en vue de l'obtention du diplôme de : Philosophiæ Doctor
a été dûment acceptée par le jury d'examen constitué de :

M. TRÉPANIER Jean-Yves, Ph.D., président
M. VO Huu Duc, Ph.D., membre et directeur de recherche
M. BENNER Michael W., Ph.D., membre et codirecteur de recherche
M. LAURENDEAU Éric, Ph.D., membre
M. KNEZEVICI Daniel C., Ph.D., membre

Dedication

To my family...

Acknowledgments

This manuscript is the final product of my research project that numerous people have supported me in many ways during this long run. I would like to take this opportunity to thank at least some of them.

First, my utmost gratitude to my supervisor, Assoc. Prof. Huu Duc Vo, for his guidance, valuable comments and at the same time encouraging me to work individually to become a self-sufficient researcher. He challenged me all the time that provided me an inspiration and motivation to not only finish my studies but also submit a nice piece of work. On a personal level, I am also extremely grateful for his friendship. I would also like to express my gratitude to my co-supervisor, Dr. Micheal W. Benner, for his valuable comments and suggestions. I would also like to thank the jury members, especially Asst. Prof. Éric Laurendeau, that took the time to read this manuscript and give their valuable comments that helped to improve the quality of this thesis.

Dr. Ali Mahallati deserves a special thanks as my supervisor at NRC. The experimental part of this work became true through his unlimited support, guidance and wisdom. His perpetual energy and the countless number of nights spent in the laboratory produced the boundary layer suction flow control work and more. His way of proving a concept using the most basic method available lead us to design, manufacture and optimize endwall suction flow control on plywood in a very short time. I am also grateful to Dr. George Zhang for his insights in discussions. Mr. Nanthan Ramachandran supplied me great help in drawing the required parts. I would like to thank to Dr. Yanfeng Zhang who has shared his experience about the wind tunnel. The great help of Dr. Xiaofei Xu in plasma actuation setup is also greatly appreciated.

During the course of this work, technicians, Mr. Derek Winfield and Mr. Dave Carey made it possible to manufacture many parts precisely in the shortest time possible. I would like especially to thank Mr. Paul Hunt for his unlimited support during the manufacturing and installation of the endwall bleed arrangement. Thanks to making sacrifice and working overtime with me, the endwall bleed setup was completed just in time.

My friends, Shubhankar Ghosh and Javad Hosseini, deserve thanks to provide a way to escape from my studies by having chats on daily life.

I would like to thank my mother, my father and my sister for supporting me to be as ambitious as I wanted throughout all my studies. My wife, Engin, deserves the highest thanks since her smile turned every difficult moment to a nice memory. Her support and patience has been my foundation throughout the course of this research.

Last but not the least, project financial budged, the test equipments and test facility are provided by the National Research Council of Canada, is greatly acknowledged.

Résumé

Le compresseur axial est la composante qui contribue le plus à la longueur et au poids d'un moteur d'avion moderne, principalement dû à la limite dans le taux de pression maximal atteignable par étage, menant à un nombre d'étages élevé. Cette limite est imposée par le décollement de la couche limite sur l'extrados de l'aube et à l'intersection de cette surface avec le moyeu, ce dernier des deux phénomènes dorénavant appelé décrochage de coin. Ces phénomènes empêchent l'augmentation de la cambrure des aubes pour donner un plus grand taux de pression par étage. De plus, une proportion signifiante du bruit généré par les turbosoufflantes modernes à haut taux de dilution provient de l'interaction entre les sillages des aubes du rotor de la soufflante avec son stator en aval. Des méthodes pratiques de contrôle de l'écoulement qui pourraient réduire le décollement de la couche limite sur l'extrados de l'aube, le décrochage de coin et le sillage des aubes mèneraient à des moteurs d'avion qui seraient plus courts, plus légers et plus silencieux. L'arrivée relativement récente des actionneurs plasma de type DBD (Dielectric Barrier Discharge) pourrait fournir une solution pratique. Ces actionneurs consistent essentiellement en deux électrodes décalés axialement et séparées par un isolant électrique. En fournissant un voltage alternatif à fréquence radio avec une amplitude de plusieurs kilovolts entre les deux électrodes, l'air au dessus de l'actionneur est accéléré via son ionisation partielle. Ces dispositifs purement électriques, simples, sans pièces mobiles, à basse puissance qui peuvent être encastrés dans une surface sont idéaux pour des applications an aérodynamique. L'objectif principal de la présente recherche est d'évaluer trois concepts de contrôle de l'écoulement avec l'actionneur plasma: le premier pour contrôler le décrochage de coin, le deuxième pour supprimer le décollement de la couche limite sur l'extrados et le dernier pour réduire le sillage des aubes.

L'approche choisie repose sur des simulations numériques de l'écoulement (CFD) et une validation expérimentale dans une cascade linéaire d'aubes à haute cambrure de compresseur à basse vitesse sur lequel un nouveau système de succion d'air au moyeu a été conçu dans le cadre de cette recherche pour réduire significativement le décrochage de coin et permettre un écoulement presque 2-D à la mi-envergure de l'aube. Un modèle d'actionneur plasma a été intégré dans un code CFD commercial. Pour chacun des trois concepts, des simulations CFD sont faites pour une évaluation détaillée de leur efficacité dans le contexte de la cascade d'aubes et pour déterminer la meilleure position de l'actionneur plasma. Par la suite, pour les deux premiers concepts, des tests sont initiés dans la cascade d'aube pour démonter le concept expérimentalement et pour valider l'outil de simulation via une comparaison avec des simulations correspondantes. L'outil CFD ainsi validé est ensuite utilisé pour des simulations à hautes vitesses avec des forces d'actionnement au-delà des valeurs présentement atteignables pour obtenir une règle préliminaire de la variation de la force

d'actionnement avec le nombre de Reynolds afin de pouvoir prédire l'ordre de grandeur des requis d'actionnement pour opérer à des conditions réelles.

Pour le premier concept, les simulations CFD capturent assez bien les caractéristiques générales de l'écoulement et les tendances associées au décrochage de coin et l'effet de la succion d'air au moyeu et des actionneurs plasma sur ce phénomène. Les simulations montrent que la combinaison d'un actionneur plasma monté sur l'extrados avec un autre monté sur le moyeu, les deux placés proche du point de décrochage de la couche limite et pointant dans la direction de l'écoulement principal peut diminuer les pertes associés à la séparation de coin. Avec une force d'actionnement atteignable à très court terme, cet arrangement peut rivaliser en performance dans cette cascade d'aubes avec le système de succion d'air qui pourtant est plus efficace que les systèmes à bas débit de succion équivalents dans la littérature pour réduire le décrochage de coin.

Pour le deuxième concept, les simulations en version 2-D indiquent que l'actionnement plasma sur l'extrados de l'aube à haute cambrure augmente le rapport de pression statique et la puissance du rotor équivalent par la réduction de la déviation de l'écoulement au bord de fuite, du blocage aérodynamique et la perte de pression totale. La position optimale serait juste en amont du point de décollement de la couche limite. L'étude paramétrique montre que l'efficacité de l'actionnement augmente avec la force de l'actionneur mais que cette augmentation s'amoindrit au fur et mesure que la force d'actionnement augmente. L'actionnement en mode pulsatif est moins efficace qu'en mode continu pour la même force d'actionnement mais plus efficace à puissance d'actionnement équivalente. La fréquence pulsative et le cycle actif n'affecte pas significativement l'augmentation de pression et de puissance du rotor équivalent bien qu'une fréquence pulsative autour de la fréquence fondamentale de la couche limite nominale et un bas cycle actif donneraient une meilleure performance. Malgré que la légère protubérance de l'actionneur sur l'extrados de l'aube en cascade ait un peu changé l'écoulement nominal sur l'aube, la comparaison des distributions de pression mesurée et simulée sur l'extrados montre les mêmes tendances générales. Pour les deux premiers concepts, les résultats de simulations CFD à hautes vitesses indiquent que la force d'actionnement varie approximativement avec le carré du nombre de Reynolds.

Pour le concept de réduction du sillage/bruit, les simulations similaires en 2-D pour une cascade d'aube à faible cambrure indiquent que les actionneurs plasma sur l'intrados et l'extrados devraient être placés le plus proche possible du bord de fuite pour maximiser la réduction du sillage en terme de déficit de quantité de mouvement. Cette réduction augmenterait avec la force d'actionnement. Le retardement de la transition de la couche limite par l'actionnement plasma fait en sorte qu'un emplacement de l'actionneur trop en amont ou une force d'actionnement insuffisante pourrait empirer le sillage. Ce cas surviendrait si la couche limite reste laminaire et décolle près du bord de fuite, au lieu de subir une transition plus tôt suivi d'un ré-attachement turbulent comme dans le cas nominal. Dans tous les cas, l'actionnement en mode continu augmente un

peu la déviation de l'écoulement au bord de fuite et par conséquent diminue la puissance du rotor équivalent. L'actionnement en mode pulsatif est moins performant qu'en mode continu pour la même force d'actionnement, mais plus performant à puissance d'actionnement équivalente. Bien que la variation de la fréquence pulsative ait un effet limité, une fréquence pulsative correspondant à un nombre de Strouhal autour de 1 serait optimale. Au niveau du cycle actif, l'efficacité de l'actionnement plafonne autour d'un cycle actif de 0.7. La force d'actionnement de ce concept varie presque linéairement avec le nombre de Reynolds.

Les résultats ci-haut indiquent que les trois concepts d'actionnement plasma sous étude peuvent être efficaces pour augmenter la performance des compresseurs et diminuer le bruit des soufflantes dans des conditions d'opérations réelles avec l'avènement d'actionneurs plasma avec une force d'actionnement améliorée dans le futur.

Abstract

The axial compressor is the component that contributes the most to the length and weight of modern aircraft engines, mainly due to the limited achievable pressure rise per stage leading to high stage count. This limit is set by blade boundary layer and corner separation considerations which inhibit higher flow turning designs that could deliver higher pressure rise per stage. In addition, a significant portion of the overall noise generated by modern high bypass ratio turbofan engines is associated with the fan due to the rotor blade wakes and their interaction with the downstream stator. Practical flow control methods that can reduce boundary layer and corner separation and blade wakes momentum deficiency would allow for shorter, lighter and quieter aircraft engines. The recent advent of dielectric barrier discharge (DBD) plasma actuators could provide a practical solution. DBD actuators are essentially axially offset electrodes separated by a layer of dielectric across which a radio-frequency AC signal of a few kilovolts is applied leading to partial air ionization and flow acceleration. These purely electrical solid-state devices are simple, low-power and can be flush mounted, making them ideal for aerodynamic flow control applications. The main objective of this research is to assess three flow control concepts using plasma actuators: the first for controlling corner separation, the second for suppressing blade boundary layer separation and the last for blade wake reduction.

The chosen approach is based on CFD simulations and experimental validation on a low-speed linear high flow turning compressor blade cascade for which a new endwall suction technique has been designed within this research to reduce corner separation and provide near 2-D operation for the blade at mid-span. A plasma actuation model is implemented in a commercial flow solver. For each concept, simulations are carried out for a detailed assessment of the effectiveness of the actuation in the context of the compressor cascade test rig and to recommend the best actuator location. Subsequently, for the first two concepts, experiments are carried out in the cascade rig to experimentally demonstrate the concept and validate the CFD tool. Finally, the validated CFD tool is used for simulations at higher flow speeds and at actuator strengths much higher than presently achievable to obtain a preliminary scaling law that would allow a rough estimation of the actuation requirements at realistic operating conditions.

For corner separation, the CFD simulations capture reasonably well the experimentally measured flow features and trends associated with corner separation and the effect of both endwall suction and plasma actuation on this phenomenon. Simulations with this CFD setup show that a combination of plasma actuators on the suction surface and endwall located close to the separation point can reduce losses associated with corner separation. With high but near-term reachable actuator strength, the performance of this concept can rival the performance at the low-speed cascade

conditions of the endwall suction scheme, which itself is more effective in reducing endwall corner separation than equivalent low suction mass flow schemes in the research literature.

For the blade boundary layer separation control concept, CFD simulations with a 2-D version of the previous setup show that suction side plasma actuation increases pressure rise and equivalent power of the high camber blade design through a reduction in trailing edge flow deviation, aerodynamic blockage and total pressure loss, with the optimum actuator location being just upstream of the separation point. The parametric study also indicates an increase in effectiveness with actuator strength but which levels off at higher actuator strengths. Pulsed actuation is less effective than continuous actuation for the same actuator strength but better for the same input power. Pulsing frequency and duty cycle do not have a large impact on pressure rise and equivalent rotor power increase but simulations do point to better performance with pulsing frequency near the fundamental flow oscillation frequency in the boundary layer and lower duty cycles. While the actuator protrusion on the experimental cascade blade slightly changed the nominal flow pattern on the test blade, comparison of experimental suction surface pressure distribution with corresponding CFD simulations show the same general trends. For both concepts above, simulations at higher speeds indicate that the required actuator strength scales approximately with the square of the Reynolds number.

For the blade wake/noise attenuation concept, similar 2-D CFD simulations on a lightly loaded (lower flow turning) blade cascade indicate that placing plasma actuators on the pressure side and suction side closer to the trailing edge would best reduce wake momentum thickness. This reduction is further improved with increasing actuator strength. Since plasma actuation delays boundary layer transition, an actuator position too far from the trailing edge or an insufficient actuator strength could be detrimental to wake momentum thickness if the boundary layer remains laminar and separates at the trailing edge instead of exhibiting an earlier laminar separation followed by a turbulent reattachment prior to reaching the trailing edge as in the nominal case. In all cases, continuous plasma actuation increases deviation slightly and thus reduces equivalent rotor power. Pulsed actuation is less effective than continuous actuation at the same actuator strength but is superior for the same input power. Although the effect of pulsing frequency is small, an optimum frequency occurs at a Strouhal number around 1. In terms of duty cycle, the effectiveness of pulsed actuation reaches a ceiling above a duty cycle of 0.7. Scaling simulations indicates that the plasma actuator strength requirement for this concept increases about linearly with the Reynolds number.

The above results indicate that the three plasma actuation concepts studied can be effective for compressor performance increase and fan noise reduction at real operating conditions should plasma actuators with improved actuator strength and robustness come along in the near future.

Table of Contents

List of Tables

List of Figures

List of Appendices

Nomenclature

A	Area
c	Airfoil chord length
c_x	Airfoil axial chord length
C_p	Pressure coefficient
D	Duty cycle
DF	Diffusion Factor
f_{act}	Pulsed plasma actuation frequency
F_{act}	Plasma actuator strength
h	Blade span
l, L	Length
M	Mach number
P	Static pressure
P_0	Total pressure
PS	Pressure Side/Surface
q	Dynamic head
Re	Reynolds number
s	Blade pitch
St	Strouhal number, $St = fL_{sep}/V_\infty$
TKE	Turbulent Kinetic Energy
Tu	Turbulence intensity
u, v, w	Velocity components in axial, pitchwise and spanwise directions, respectively
V	Velocity
x, y, z	Cartesian coordinates
y^+	Dimensionless boundary layer distance
$\dot{W}$	Power
α	Absolute frame flow angle
β	Relative frame flow angle
δ	Boundary layer thickness
δ^*	Boundary layer displacement thickness
η_p	Plasma actuation efficiency
θ	Boundary layer momentum thickness
λ	Stagger angle

μ	Dynamic viscosity
ν	Kinematic viscosity
ψ	Pressure rise coefficient
ρ	Density
σ	Blade solidity
ϕ	Flow coefficient
ω	Vorticity
ω_0	Overall total pressure loss coefficient

Subscripts

1,2	Inlet and outlet plane
act	Plasma actuator property
amb	Ambient
CL	Centerline (mid-span) value
e	Boundary layer edge value
sep	Separation bubble property
x, y, z, s	Components in axial, pitchwise, spanwise and streamwise directions, respectively
∞	Freestream value

Acronyms

2-D	Two-Dimensional
3-D	Three-Dimensional
AVDR	Axial Velocity Density Ratio
BL	Boundary Layer
BPF	Blade Passing Frequency
CFD	Computational Fluid Dynamics
DBD	Dielectric Barrier Discharge
PS	Pressure Side/Surface
RANS	Reynolds-Averaged Navier-Stokes
RMS	Root-Mean-Square
SS	Suction Side/Surface
SST	Shear Stress Transport

Introduction

Axial compressors and fans are major components of aircraft gas turbine engines, the former providing high-pressure air to the combustor to sustain the engine cycle and the latter mildly pressurized air to be expanded in a nozzle to provide most of the thrust of modern subsonic aircraft. The Pratt & Whitney PW4000 112-inch fan engine, shown in Figure 0.1, consists of six-stage low-pressure and eleven-stage high-pressure compressors to generate an overall pressure ratio of 42.8. Gas turbine engine compressors are using highly-loaded blades to achieve the maximum pressure rise per stage. The current trend in axial compressor design is to increase the maximum pressure rise per stage to achieve a similar overall pressure ratio using less number of stages. Increasing the pressure rise per stages leads to a reduction in number of stages and thus, a reduction in engine weight, cost and maintenance.

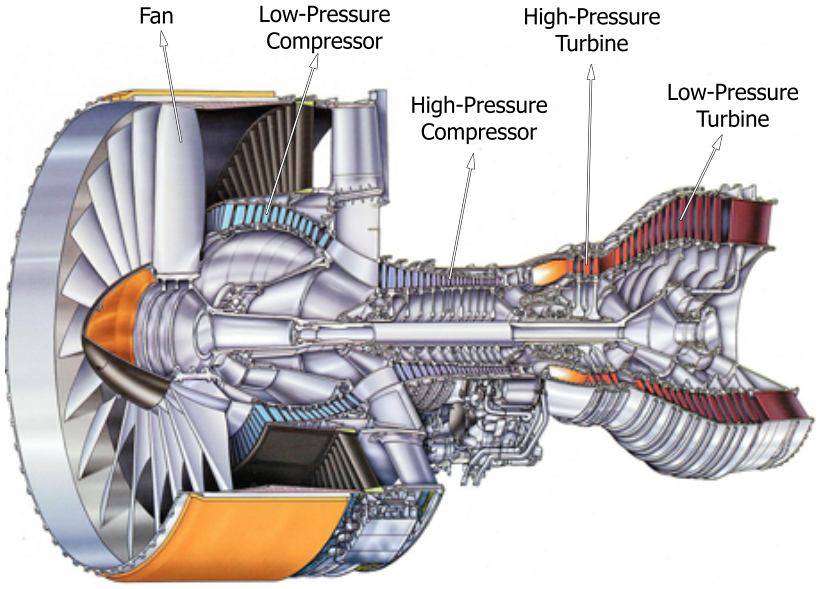

Figure 0.1: Cut-away of the Pratt & Whitney PW4000 112-inch turbofan engine

In addition to engine performance, compressor/fan noise is becoming a major issue for modern commercial aircraft. Figure 0.2 compares the noise levels of various engine components at take-off and landing for a current aircraft engine in terms of the level associated with a future "silent" aircraft. One can observe that the fan inlet noise (associated with tonal noise) represents a major source of noise for modern turbofan engines. With more restrictive aircraft noise regulations, reduction in fan noise has become an important area of research in the past decade. The importance of fan noise suppression is likely to increase for commercial airplanes as the industry moves toward even larger engine by-pass ratio (i.e. larger fan size) to increase propulsive efficiency.

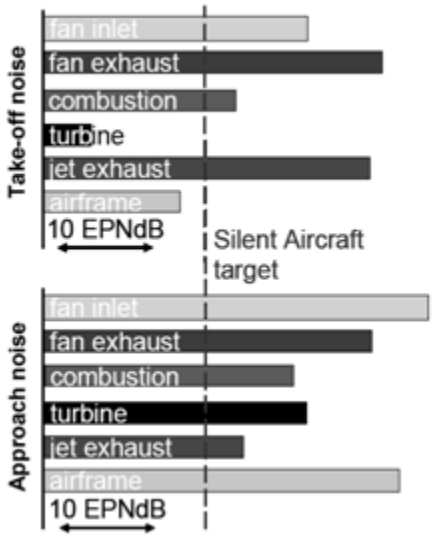

Figure 0.2: Noise levels for engine components (Hall and Crichton, 2007)

0.1 Compressor Performance Limits

The boundary layer development on blade surfaces greatly affects the axial compressor performance. To illustrate this point, Figure 0.3 depicts a constant radius cut of an axial compressor or axial fan stage, composed of a rotor and a stator, simplified with axial and constant inlet and exit velocities.

The vectors in dashed lines depict the flow in the rotating frame of reference of the rotor while the vectors in solid lines depict the equivalent flow in the static frame of reference of the stator, with the two frames being related to each other by the local rotor rotational (circumferential) velocity U. As shown in Figure 0.3, the rotor plays two roles. First, by deflecting the flow in the relative frame of reference, it increases the normal flow area ($A_2^{'} > A_1^{'}$) and thus acts as a diffuser to increase static pressure. At the same time, this flow deflection adds circumferential momentum to the flow in the static frame of reference, thus increasing its kinetic energy ($V_2 > V_1$). The stator then converts the imparted kinetic energy into pressure rise by turning the flow in the absolute frame ($A_3 > A_2$) in the same way as the rotor acted as a diffuser.

To achieve higher pressure ratio per stage of compression, modern gas turbine engines are designed with highly-loaded compressor blade profiles, where each blade has to achieve more flow turning. In terms of compressor performance, it is obvious from Figure 0.3 that the more flow turning in the rotor and stator blade passages, the higher the imparted kinetic energy and static pressure rise across each blade row. In practice, the growth of boundary layers on the blade surfaces and endwalls (hub and casing), especially in the presence of adverse pressure gradient, acts as an aerodynamic blockage. This reduces the effective area increase across the blade rows, thus reducing pressure rise. In addition, the loss in dynamic head of the fluid in the boundary layers

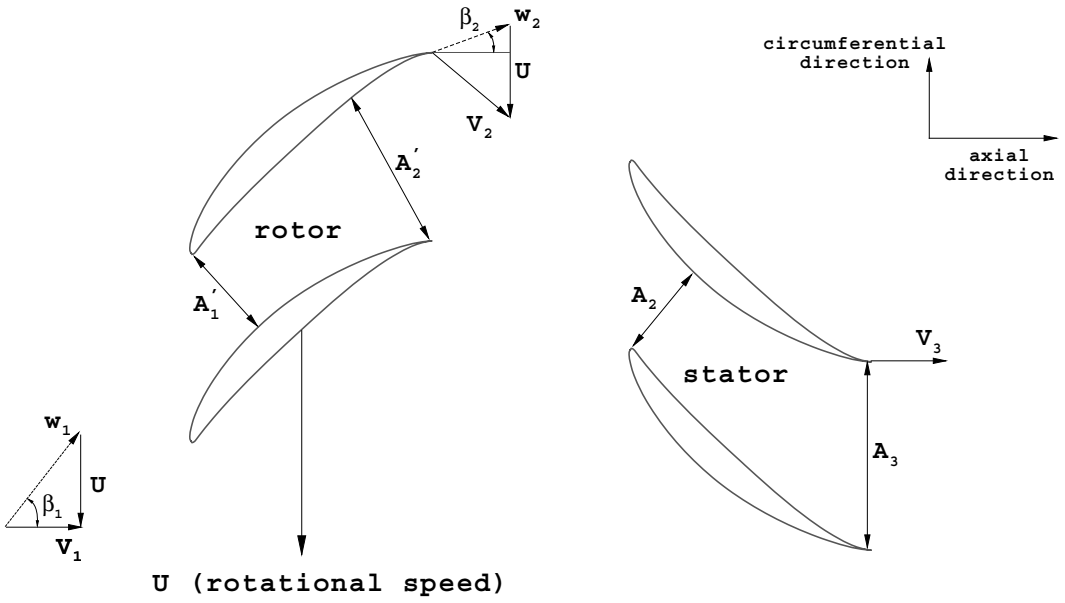

Figure 0.3: Axial compressor/fan stage representation

also reduces pressure rise and adiabatic efficiency of the stage. As the blade camber increases to enhance flow turning, the resulting increase in pressure gradient causes blockage and dynamic head loss to increase. Therefore, there is a maximum blade camber value at which the increased losses negate the effect of additional flow turning on pressure rise. If the camber is increased to the point where the boundary layer separates and fails to reattach as shown in Figure 0.4, the extra input power does not turn into pressure rise but rather into additional static temperature rise from viscous and mixing losses.

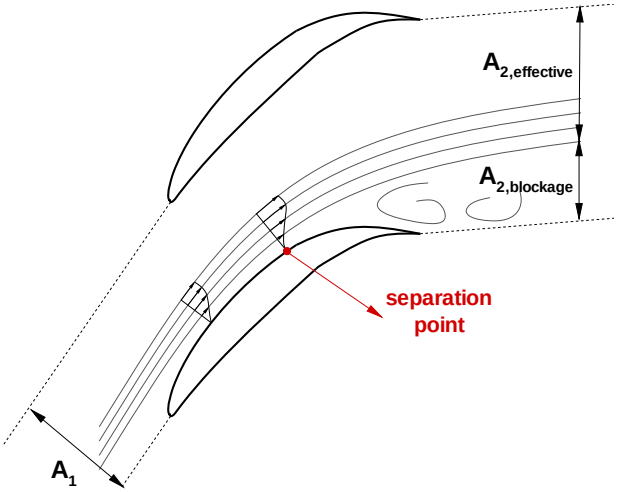

Figure 0.4: Illustration of boundary layer flow separation over a high flow turning blade

An additional source of blockage and loss, related to the endwall boundary layer, is endwall corner separation. As illustrated in Figure 0.5, while the low-velocity fluid in the endwall boundary

layer and the core flow experience roughly the same cross-passage pressure force, the former is subjected to a lower centrifugal force compared to the latter. Therefore, the endwall boundary layer fluid moves towards the blade suction side. Thus, the streamline radius of curvature of the endwall boundary layer fluid becomes smaller as shown in the figure. This results in an accumulation of low-momentum fluid at the junction of the endwall and blade suction side which in turn increases the flow blockage. The accumulation of the low-momentum endwall fluid causes large blockage and losses which becomes more severe as the flow turning is increased. The low-momentum fluid is highly susceptible to flow reversal (separation) under adverse pressure gradient, which would result in severe blockage and losses. Thus, boundary layers impose a design limit on how much pressure rise per stage can be achieved through increased flow turning.

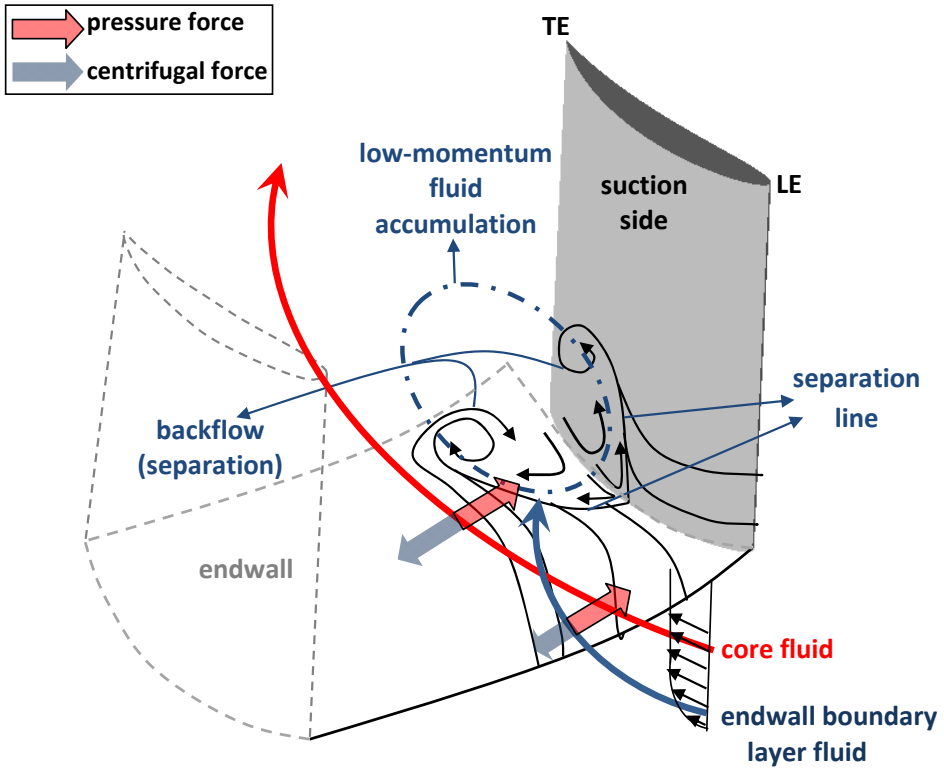

Figure 0.5: Formation of endwall corner separation

Other factors with negative impact on pressure rise include the deviation of the exiting flow from the blade trailing edge metal angle (thus aerodynamic under-turning). Although beyond the scope of the present work, the blockage and losses associated with the tip clearance flow (leakage flow across the clearance between the rotor tip and the casing) has a negative effect on pressure rise. While stage pressure ratio can also be increased through increased rotational speed and/or number of blades per row (reduced inter-blade distance improves flow turning), the associated structural and weight penalties limit the practicality of these options.

The above factors limit the achievable pressure ratio per compressor stage, thus imposing a

multiple number of stages, making the compressor a substantial contributor to the weight and length of an aircraft engine. Therefore, there is a strong motivation to decrease number of stages by significantly increasing stage pressure ratio. A promising way to achieve this is through flow control to modify the behavior of the boundary layers given their large effects on compressor performance while at the same time being easily influenced by aerodynamic inputs of limited strength and power.

0.2 Compressor and Fan Noise

Another impact of boundary layers in compressors (also in fans) is noise. At the blades' trailing edge, the boundary layers on the suction and pressure sides merge to form the blade wake, as illustrated in Figure 0.6. As the wakes from the rotor blades hit the downstream stator blades intermittently, blade-interaction noise is generated. Vibrations are also generated on the stator blades that may lead to fatigue problems. The same mechanism occurs for stator wakes hitting the adjacent rotor of a downstream stage. The noise generated through rotor-stator interaction is referred as tonal noise and is an important source of compressor/fan noise.

One promising approach is to reduce the velocity deficiency in the blade wake by the time it reaches the downstream blade row in order to alleviate the noise and vibrations generated. This can be done by controlling the boundary layers at the origin of the blade wake or the wake directly.

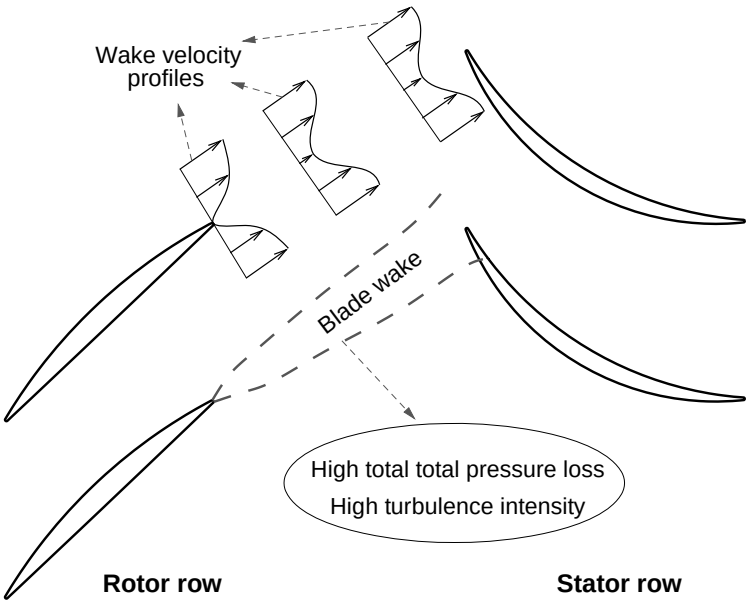

Figure 0.6: The schematic representation of rotor-stator blade interaction

0.3 Proposed Concepts

The present research aims to improve compressor/fan stage pressure ratio and efficiency as well as reduce tonal noise from rotor-stator interaction. As discussed in the next chapter, while many techniques have been studied to achieve this, some of which apply flow control to the boundary layers based on the flow physics discussed above, they all possess some practical limitations that hinder their application in real engines. The electro-fluidic plasma actuation technology has been recently developed that promises to overcome many of the practical shortcomings of traditional actuation technology for implementation on aerodynamic devices. This project aims to assess and demonstrate the potential of this technology to improve compressor/fan performance and reduce noise generation.

Plasma actuators allow conversion of electricity directly into flow momentum via partial air ionization. The most important and common type of plasma actuator, known as the Dielectric Barrier Discharge (DBD), is illustrated in Figure 7(a). The DBD plasma actuator basically consists of two axially offset electrodes, one exposed to the air and the other hidden beneath a dielectric material. When a high amplitude (1-50kV) and high frequency (1-10kHz) AC voltage is applied between the electrodes, the air above the covered electrode is partially ionized. The ionized particles, known as plasma, are accelerated under the effect of the electric field gradient and collide with neutral air particles. This results in a momentum addition to the air, which under quiescent conditions creates a thin jet parallel to the surface. The induced body force can be used for flow control. Since the air particles are accelerated using electrical energy, the force applied by the plasma actuation is referred as electro-hydrodynamic (EHD) force (Roth, 2003).

As with synthetic jets, the plasma actuators are zero-net mass flux (ZNMF) devices, i.e. they induce certain momentum to the fluid, but they do not add any mass. This effect is equivalent to that of a spatial body force distribution whose integrated value in axial direction is usually referred to as plasma actuator strength and given in mN/m (length of actuator taken in the direction perpendicular to the paper in Figure 7(a)). The position of the plasma actuator in this work refers to the location of the downstream edge of the exposed electrode as shown in Figure 7(a). Figure 7(b) shows the light emission from the plasma which is only visible in a dark environment.

Plasma actuators are low-powered, simple, light, small and devoid of movable parts, giving them high bandwidth and making them potentially more robust and cheap to manufacture, integrate and operate than other fluidic actuators. They can also be operated in continuous and pulsed (on-off) modes. Last but not least, the fact that the exposed electrode is very thin and can even be made flush with the surface insures minimal or zero perturbation to the flow when not in use, making plasma actuators suitable for aerodynamic applications.

The proposed plasma actuation concepts for suppressing endwall corner separation, increasing

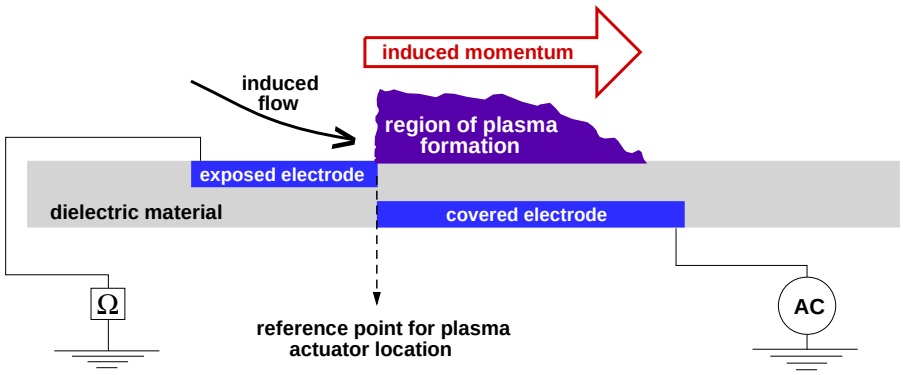

(a) The schematic representation of a plasma actuator (side view)

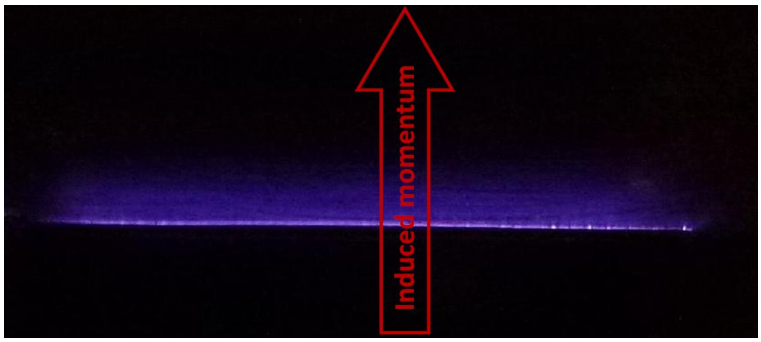

(b) Plasma formation captured by a camera in a dark environment (top view)

Figure 0.7: Plasma actuator

flow turning capability and reducing blade interaction noise are shown in Figure 0.8, Figure 0.9 and Figure 0.10, respectively. In Figure 0.8, plasma actuators are placed on the endwall and blade suction surface to add streamwise momentum to the boundary layer fluid to prevent endwall corner separation. For boundary layer flow separation control, a spanwise plasma actuator is placed on the blade suction side to add streamwise momentum to the boundary layer as shown in Figure 0.9. This setup should increase flow turning capability for higher pressure rise capability. Finally, the plasma actuation noise reduction concept illustrated in Figure 0.10 involves placing plasma actuators near the blade trailing edge to add streamwise momentum to reduce the momentum deficiency in the wake. Moreover, it should be emphasized that pulsed actuation can also be applied to all three concepts to reduce the amount of power input for plasma actuation. In this mode, the actuator pulsing frequency is chosen for resonant excitation of turbulent flow structures in the boundary layer or wake shear layer. The excited vortical flow structures will increase momentum transfer through enhanced mixing from the high-velocity fluid near the core flow to the low-velocity fluid near the wall or wake center. Thus, minimizing the amount of direct momentum input required from the actuator.

Lemire and Vo (2008) and Lemire *et al*. (2009) carried out a preliminary assessment of the boundary layer flow separation control and noise reduction plasma actuation flow control con-

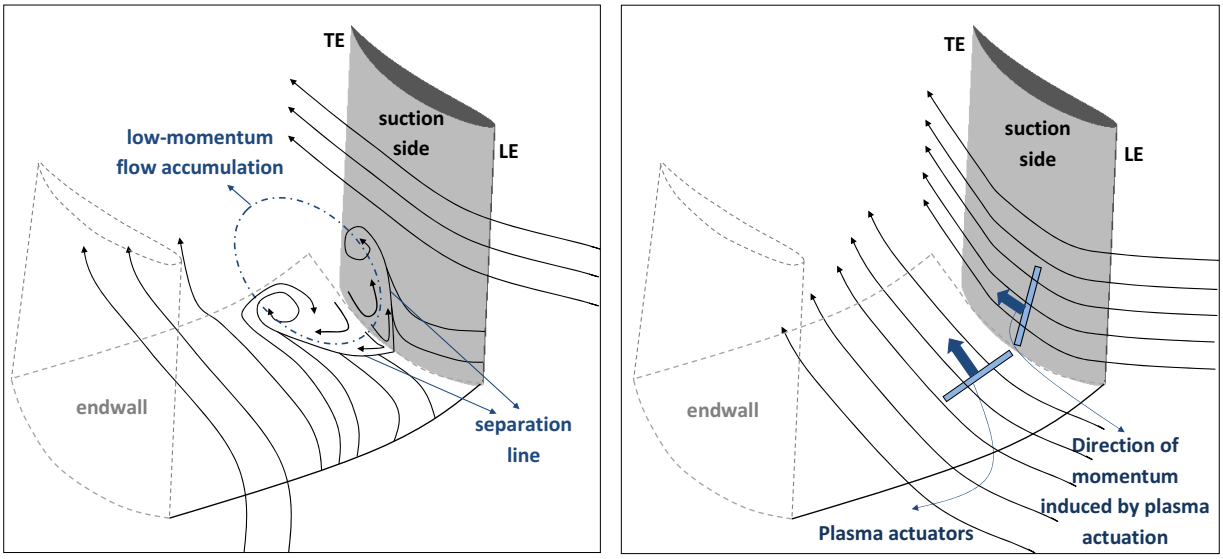

(a) Without actuation (b) With actuation

Figure 0.8: Plasma actuation concept for corner separation control

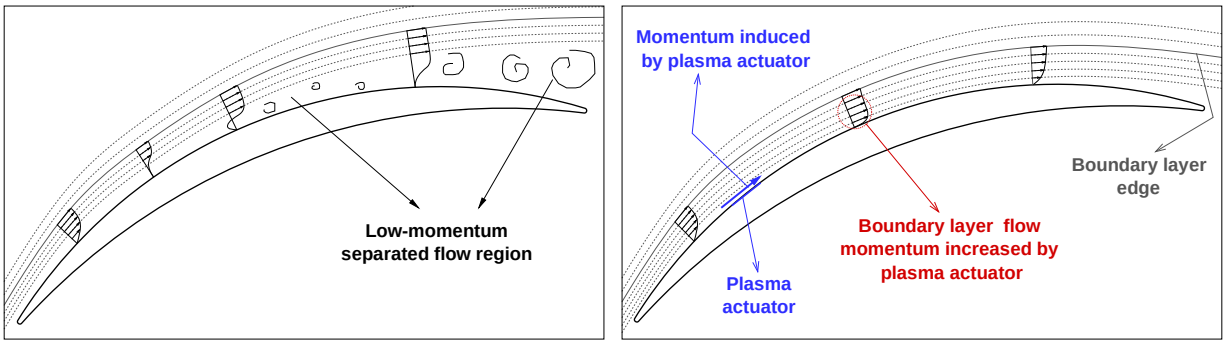

(a) Without actuation (b) With actuation

Figure 0.9: Plasma actuation concept for boundary layer flow separation control

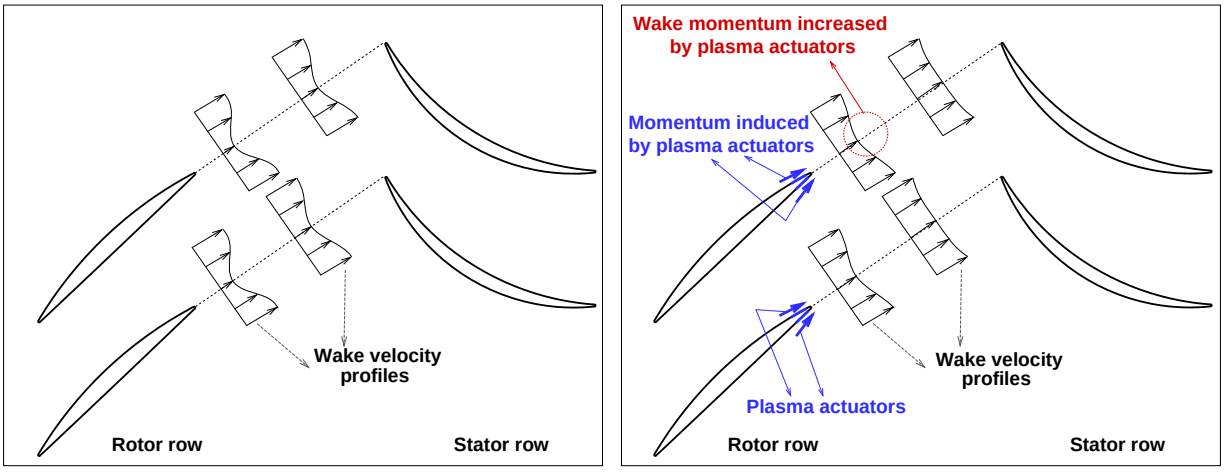

(a) Without actuation (b) With actuation

Figure 0.10: Plasma actuation concept for wake/noise suppression

cepts on rotating compressor rotor geometries. These studies were purely computational using a basic CFD code with a very simple mixing-length turbulence model and the results were not validated experimentally. The simulations were performed at realistic (high) compressor speeds and the strength limits of the plasma actuators were not taken into consideration, partially due to the very low strength of available plasma actuators at that time. Therefore, the calculated optimum plasma actuator strengths are significantly above even presently achievable values. Moreover, pulsed plasma actuation simulations were inconclusive due to possibly inadequate selection of actuation frequencies and/or limitations of the CFD code in capturing vortical turbulent structures. Last but not least, the endwall corner separation was not considered in the performance enhancement study. Nevertheless, the initial work demonstrated that the plasma actuation have enough promising results to further the investigation.

The present research is a continuation of the preliminary work by Lemire and Vo (2008) and Lemire *et al*. (2009) with the addition of endwall corner separation. To overcome the limitations encountered in these preliminary studies, this research consists of an in-depth numerical assessment and optimization of the concepts using a validated commercial CFD code. The studies were carried out at low-speeds, taking into account the limits of existing DBD plasma actuators, to allow detailed experimental validation of the computational tool and demonstration of plasma actuation flow control concepts in a cascade wind tunnel. For the pulsed actuation, the optimum pulsing frequency was determined based on the frequency of the oscillations in the unsteady solution of the flow field, vortex shedding frequency and also theoretically calculated values corresponding to frequency of flow structures within the boundary layer. The plasma actuation flow control concepts were assessed at higher speeds to determine the plasma actuator strength requirements for more realistic flight conditions. Therefore, this study was the first to carry out an in-depth numerical investigation of the three proposed concepts, coupled with detailed measurements for the endwall corner separation, boundary layer flow separation control concepts.Moreover, this research was the first to assess plasma actuator strength scaling with speed and Reynolds number for these three flow control concepts.

0.4 Research Objectives

The objectives of the present research are:

- To carry out a sophisticated computational assessment and parametric study of the actuation concepts for a linear cascade geometry taking into consideration the limitations of existing plasma actuators.
- To perform an experimental validation and demonstrate endwall corner separation suppression and flow turning enhancement concepts using plasma actuation.

- To use the validated computational tool to determine how plasma actuation requirements scale at higher speeds.

0.5 Thesis Outline

The remainder of the current thesis is structured in the following manner: Chapter 1 presents a review of flow control methods in the research literature used to enhance compressor performance and reduce noise, as well as on plasma actuation. The proposed research methodologies for the computational and experimental setup are shown in Chapter 2, followed in Chapter 3 by the computational and experimental results for plasma actuation and endwall suction flow control methods for endwall corner separation. The plasma actuation flow control results for the boundary layer flow separation and noise reduction are detailed in Chapters 4 and 5, respectively. Finally, the conclusions from the current work and recommendations for future studies are presented in Chapter 5.3.

Chapter 1

Literature Review

This chapter provides an overview of the previous flow control studies for corner separation, blade boundary layer flow separation and noise reduction concepts. Among the flow control methods, a special importance was given to the plasma actuation flow control studies for compressor blades. In addition to plasma actuation, the endwall boundary layer suction flow control studies were particularly considered.

The chapter begins the description of flow physics and flow control methods associated with boundary layer flow separation in Section 1.1. Following this, a literature review of the research on endwall corner separation control and noise reduction is presented in Sections 1.2 and 1.3. Finally, Section 1.4 discusses the plasma actuation flow control method including the plasma actuation physics, widely-used methods for plasma actuator optimization and a review of plasma actuation applications focused on gas turbine engines.

Throughout the relevant literature on compressor aerodynamics, pressure rise coefficient, diffusion factor and total pressure loss are amongst the main performance parameters. The pressure rise coefficient represents the static pressure rise across a compressor stage. The diffusion factor is a measure of flow turning by the blade passage. The higher the diffusion factor, the higher the pressure rise. For a compressor blade, a typical diffusion factor is 0.45, whereas a value greater than 0.6 is usually associated with significant boundary layer flow separation (Cumpsty, 1989). On the other hand, total pressure loss is a measure of loss in dynamic head due to viscous shear and mixing. For low-speed compressor blades, this loss is often associated with the boundary layers (and tip clearance flow) that causes a reduction in pressure rise.

1.1 Two-Dimensional Boundary Layer Flow Separation

Although the concept of the boundary layer was initially proposed by Prandtl (1904), the research on boundary layer flows is still ongoing, particularly in the areas of boundary layer flow separation and boundary layer transition which affect the performance of aerodynamic bodies significantly.

Turbomachinery blades may have extensive regions of laminar flow (Walker, 1968). Although the flow in gas turbine engines are associated with high freestream turbulence levels due to presence

of high level of disturbances coming from the wakes of the upstream blades, the portion of laminar flow region can be substantial for small engines operating at low Reynolds numbers.

The current study was performed at a fairly low Reynolds number. Therefore, a significant portion of the boundary layer flow was laminar. The laminar boundary layer experienced a boundary layer separation as depicted in Figure 1.1. The presence of adverse pressure gradient and surface curvature in compressor flows give rise to flow separation. The laminar boundary layer separates from the suction surface where an inflection point is observed in the velocity profile. This location usually corresponds to immediately downstream of suction peak where the flow starts to decelerate. The separated boundary layer becomes more prone to the boundary layer transition. As a result of intense mixing, a turbulent boundary layer generates larger skin friction. The separated laminar flow usually experiences a turbulent reattachment as depicted in Figure 1.1.

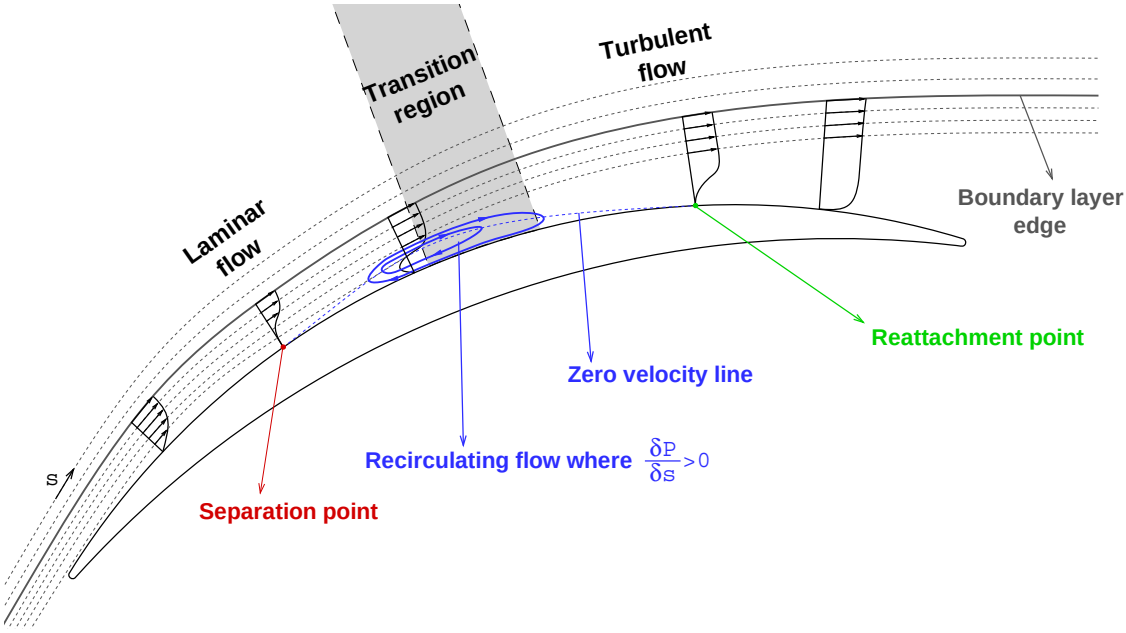

Figure 1.1: Schematic representation of the two-dimensional boundary layer flow separation for a low-Reynolds number compressor blade

In general, there are three mechanisms by which transition from laminar to turbulent flow can occur. These are natural, by-pass and separation-induced transition mechanisms. The by-pass and separation-induced transition are the most common mechanisms observed in turbomachinery applications (Mayle, 1991). The natural transition is the most ordered and slow transition mechanism and has minor importance in turbomachinery applications (Sveningsson, 2006). In this case, a laminar boundary layer becomes unstable beyond a critical Reynolds number and forms the Tollmien-Schlichting (T-S) waves (Mayle, 1991). The T-S waves, also referred as primary instabilities, tend to cause a fully turbulent flow as they are convected downstream (Schlichting and Gersten, 2000). The T-S waves start to grow until they reach an amplitude sufficiently large to trigger instabilities,

so called secondary instabilities. The secondary instabilities grow rapidly into three-dimensional structures which later break-up and form turbulent spots. Finally, these spots grow and form a fully turbulent boundary layer. In by-pass transition, a laminar boundary layer is subjected to high freestream turbulence levels ($FSTI > 1\%$), the first four stages of the natural transition are by-passed and the turbulent spots are directly formed within the boundary layer (Mayle, 1991). The separation induced transition has major importance for the present research. Separation-induced transition may be observed when a laminar boundary layer separates. The shear layer of the separated flow is highly unstable which may break down to form turbulent spots with three-dimensional instabilities. These instabilities then turn into fully turbulent flow. The enhanced mixing caused by turbulent flow tends to reattach the turbulent boundary layer. This reattachment forms a laminar separation/turbulent-reattachment bubble on the surface.

While boundary layer separation gives rise to total pressure loss in compressors, laminar-turbulent transition may be used to avoid or suppress the flow separation. A laminar boundary layer can only support very small adverse pressure gradient without separation (Schlichting and Gersten, 2000). A turbulent boundary layer on the other hand can support larger adverse pressure gradients without encountering flow separation due to mixing of high momentum fluid in the outer part of the boundary layer with the low-momentum near surface-fluid. Considering these features, flow control studies usually focus on the boundary layer to enhance the aerodynamic performance.

The initial studies to improve performance of compressor blades go back to 1950's (Sinnette and Costello, 1951). In the literature, two types of flow control techniques, passive and active, have been used. The former does not involve any energy addition to the system, while the latter requires some form of energy input. The passive flow control techniques include vortex generators, geometric shaping and use of grooves and riblets. These techniques have the disadvantage of increasing total pressure loss.

The active flow control techniques to control boundary layer flow separation are predominant. Among these techniques, boundary layer suction is a very effective way of controlling boundary layer flow separation. In this method, the low-momentum fluid inside the boundary layer is removed through openings on the wall. The boundary layer flow separation can be avoided with sufficiently strong suction if all low-momentum fluid is replaced by the high momentum core flow (Schlichting and Gersten, 2000).

In the computational study carried out by Merchant *et al*. (2000), the boundary layer suction was applied through slits located on suction side of rotor and stator blades as well as holes located on the endwalls in a compressor stage, as illustrated in Figure 1.2. The boundary layer suction was increased the stage pressure ratio from 2.3 to 3.39 using 7% of stage inlet mass flow as bleed air. However, the drawbacks of this method include the engine performance penalty from bleeding air as well as the need to incorporate air channelling and piping systems. Moreover, the risk of clogged

bleed slots and holes in real engine working environment with dust/particles taken by the air intake would require expensive preventive maintenance.

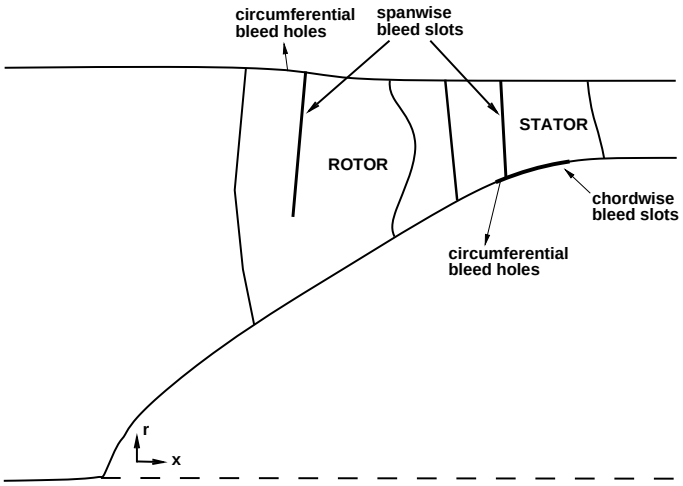

Figure 1.2: Schematic of the bleed configuration, reproduced from Merchant *et al*. (2000)

More recently, Guo *et al*. (2010a) experimentally investigated boundary layer suction effect on a compressor cascade performance through full-span slots at 25%, 35%, 48% and 60% chord locations with three different suction flow rates 0.5%, 1.0% and 1.5% at Mach number of 0.23. Since slots were sucking away the fluid from all span, they were able to reduce both 2-D blade boundary layer separation losses as well as endwall corner region losses. The total pressure loss was reduced by 16.5% using the slot at 60% chord with a suction mass flow rate of 1.5%. At 60% chord, the flow has already separated and low-momentum fluid boundary layer could be sucked away.

Another prominent active flow control technique is blowing, which consists of adding momentum to the boundary layer through air injection via surface holes or slots. An experimental study with air blowing was recently conducted by Hecklau *et al*. (2010) on a highly loaded compressor cascade with a 60° flow turning at $Re_c = 8.4 \times 10^5$. The boundary layer flow separation in the rear part of the blade was suppressed with a blowing system consisting of 3 actuators (each covering 17% span) located at 70% chord, as shown in Figure 1.3. The mid-span pressure rise coefficient was increased by approximately 5.5% and 7.8% of the inlet dynamic pressure using steady and pulsed blowing with a blowing mass flow ratio of 0.34%, respectively.

A synthetic jet is another active flow control device used for suppressing boundary layer flow separation for high performance compressor design. A synthetic jet actuator consists of a cavity with a diaphragm on one end and an orifice on the other. During the suction part of the cycle, fluid is inhaled from all sides around the opening, whereas during the injection part, the fluid leaves in the direction of the orifice, thus forming a jet and adding directional momentum to the flow without net mass addition.

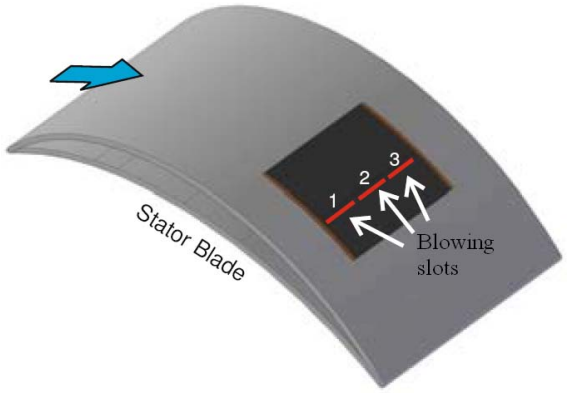

Figure 1.3: Blowing slots integrated into the stator blade (Hecklau *et al*., 2010)

Zheng *et al*. (2006) carried out an experimental study at $Re_c = 6 \times 10^5$ using synthetic jet vortex generators to control boundary layer flow separation in an axial compressor cascade rotor blade with a 43° camber angle. Small holes were drilled on the blade suction side at various chord lengths as shown in Figure 1.4(a). The effect of hole pitch angle (shown with γ in the figure) with respect to the local surface was investigated. Among the pitch angles 35°, 50° and 90° tested, the smallest pitch angle (35°) closest to the mainstream flow direction was most effective where the peak value of the wake total pressure recovery coefficient ($\sigma = P_{02}/P_{01}$) was increased from 0.952 to 0.957 as presented in Figure 1.4(b).

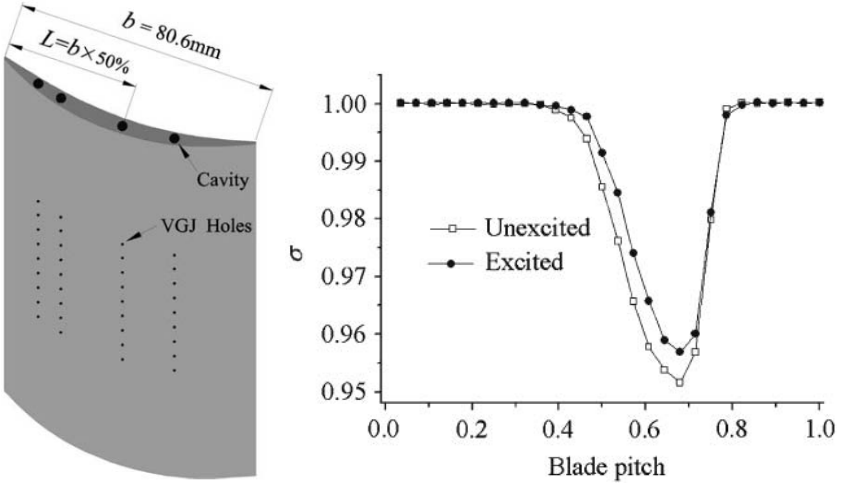

(a) Illustration of blade suction side holes

(b) Wake total pressure recover coefficient

Figure 1.4: Synthetic jet vortex generation boundary layer flow control (Zheng *et al*., 2006)

Contrary to conventional blowing and suction methods, the synthetic jet actuators do not require any piping. Moreover, the advent of micro-fabrication has made these actuators very small and light, thus easy to integrate and possessing high bandwidth. However, the small size of the orifice associated with these small actuators make them susceptible to fouling in real engine operating environments.

1.2 Endwall Corner Separation

While the secondary flows in compressor blade passages have been studied since 1950's (Herzig *et al*., 1953; Horlock *et al*., 1966), researchers still intend to understand the flow physics of secondary flows. The hub corner separation is a more severe problem in stator blades compared to the rotor blades. Experimental studies performed on rotor blades (Dring *et al*., 1982; Murthy and Lakshminarayana, 1987; Dong *et al*., 1987) have shown that the centrifugal force on the flow in the rotor passage increases the momentum of the hub boundary layer flow and diminishes the risk of hub corner separation (Schulz *et al*., 1990). In addition, stator blades usually have higher camber angle which make them more susceptible to hub corner separation.

As one of the early studies on the corner stall, Joslyn and Dring (1985) investigated the effect of corner stall on the performance of a stator blade of a large scale, two-stage axial compressor. The experimental data was acquired at three flow coefficients (the ratio of axial velocity to the blade speed) representing high flow, design flow and near stall conditions. Both total pressure measurements and surface oil flow visualizations showed the presence of hub corner stall which grows significantly as the flow coefficient decreases. This result was explained by higher diffusion of the streaklines with reduced flow coefficient. The blockage due to hub corner stall was found to be the major source of total pressure loss. An experimental study performed by Thiam *et al*. (2008) also showed that the corner separation grows in size as the flow coefficient decreases.

The basic understanding of the extent and nature of the hub corner stall is further enhanced by the experimental study of Schulz and Gallus (1988), which investigated the effect of increased loading on the stator hub corner stall in an annular compressor cascade. It has been observed that the hub boundary layer flow is turned by the cross passage pressure gradient and this effect becomes more dominant at high incidence. Later, Schulz *et al*. (1990) repeated the experiments on the same stator geometry in the presence of upstream wakes generated by a moving row of cylinders to determine effect of rotor-stator interference on the flow separation behavior. The hub corner stall observed in the previous experiment was further investigated to give an additional insight into the structure of the flow. They showed the presence of two vortices by using endwall and blade flow visualization for the case without upstream wakes. According to their observation, one vortex forms on the suction surface and other vortex forms on the hub endwall; both vortices were normal to the surface. As shown in Figure 1.5, they proposed a topology for the corner stall in which these vortices are shown as a part of ring vortex. This experimental study further showed that an increase of freestream turbulence levels through the introduction of the upstream wakes enhances the formation of vortical structures in the separated shear layer and re-energizes the low-momentum fluid near the wall. As a result, flow visualizations indicated a reduction in the hub corner stall, although the structure of the hub corner stall was conserved.

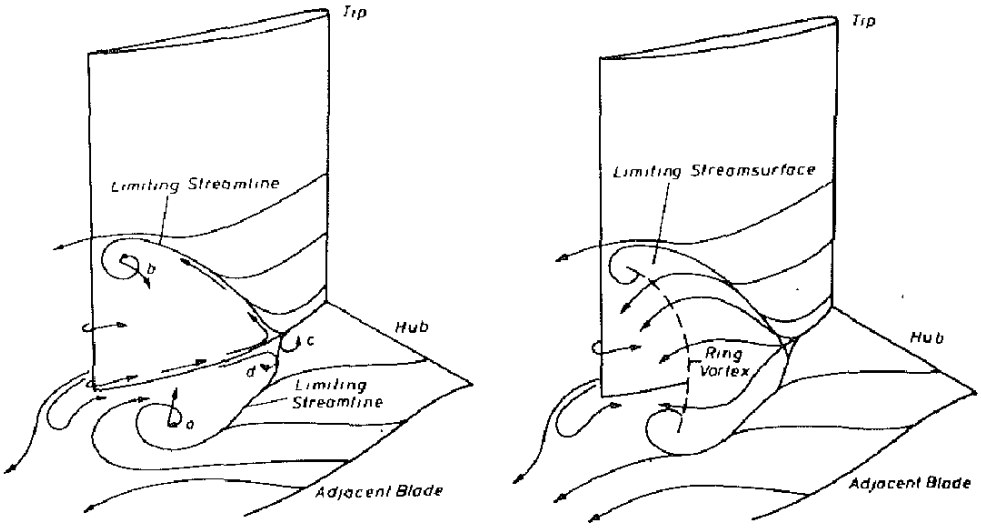

Figure 1.5: Topology of corner stall proposed by Schulz *et al.* (1990)

A better understanding of the endwall corner separation can be gained by understanding the formation of secondary flows in a compressor passage. The formation of passage vortex and horseshoe vortex in a compressor cascade passage is explained by Kang and Hirsch (1991). As schematically illustrated in Figure 1.6, the horseshoe vortex (also referred to as the wing-body junction vortex) forms as the endwall boundary layer impinges on the leading edge of the blade and separates from the surface due to adverse pressure gradient. The separated boundary layer wraps around the blade surface. The passage vortex, depicted in Figure 1.6, caused by the movement of endwall boundary layer fluid from pressure side of the blade towards the suction side of the adjacent blade.

Thiart (1991) aimed to obtain a numerical procedure for the calculation of corner stall in axial compressor stators based on the experimental work done by Schulz and Gallus (1988); Schulz *et al.* (1990). The detailed comparison between the experiments and numerical simulations revealed that the three-dimensional flow near the endwall, including corner stall, vortex motion and radial mixing, can be captured with CFD.

The topological structure of corner stall has not been uniquely explained yet. Hah and Loellbach (1999) also proposed a topology for the corner stall. He used numerical results based on the RANS solutions to understand the compressor hub corner stall in a subsonic annular compressor stator. Similar to Schulz *et al.* (1990), he observed two counter rotating vortices in the hub corner stall region, one was located at 80% axial chord and the other was located closer to the trailing edge as shown in Figure 1.7(a). The proposed topology of corner stall is shown in Figure 1.7(b). They have mentioned that the vortices observed in the corner stall region are actually two legs of a single vortex. The interaction of these vortices creates a reversed flow region and a limiting streamline on the suction surface.

Lei *et al.* (2008) defines three processes to indicate the hub corner stall. These are adverse

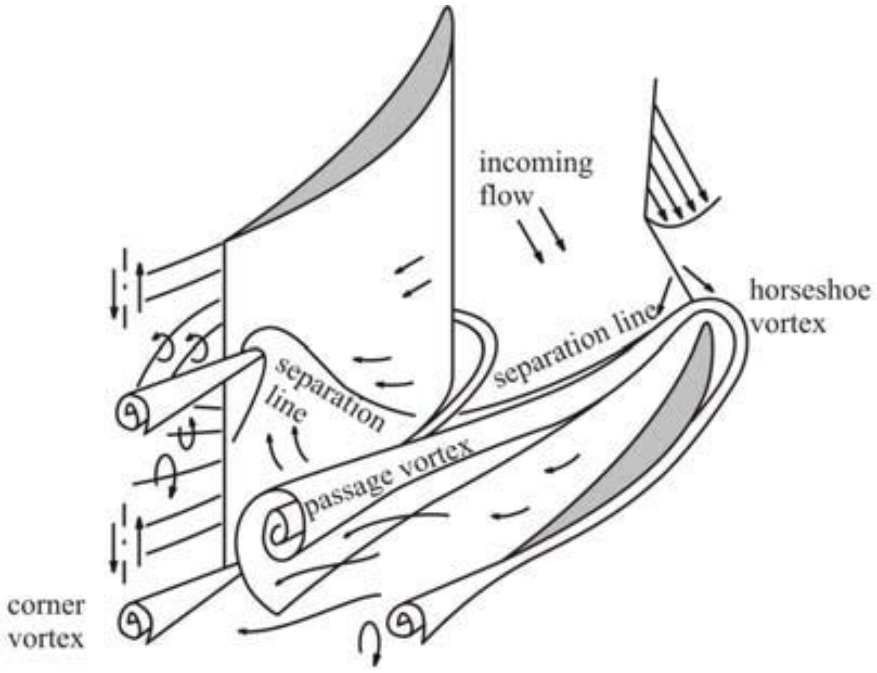

Figure 1.6: Horseshoe vortex and passage vortex in a compressor cascade (Kang and Hirsch, 1991)

pressure gradient in the blade passage, the cross-flow from pressure surface to suction surface (due to overturning of the passage flow) and the incoming endwall boundary layer flow. Moreover, they have defined a critical value for the diffusion parameter as $D = 0.4 \pm 0.05$ for the onset of the hub corner stall based on the numerical flow simulations. Their study have shown that the blade does not experience a hub corner stall for the values of $D < 0.4$, although there may be a presence of suction surface separation. They have also computationally shown that streamwise flow injection with 0.8% inlet mass flow over the blade suction surface had limited effect on reducing the extent of corner stall, although it energizes the boundary layer and reduces the wake size. However, the streamwise flow injection together with the spanwise flow injection (towards the hub) with the same inlet mass flow reduced the extent of the hub corner stall significantly.

The endwall corner separation can be very detrimental to flow two-dimensionality. As blade aspect ratio decreases, the proportion of low-momentum fluid thickness from corner separation with respect to blade span increases. Finally, the presence of adverse pressure gradient in compressor cascades increases the severity of the corner separation. Figure 1.8(a) depicts the low-momentum fluid accumulated due to corner stall at the corners of the blade trailing edge. The low-momentum fluid accumulation increases the flow blockage which in turn reduces effective flow area and increases the centerline flow velocity. The reduction in the cascade flow two-dimensionality is highly undesirable for linear cascade flow experiments. The flow two-dimensionality can be improved by using porous endwalls and/or endwall slots (Webber, 1993; Song, 2003). Figure 1.8(b) depicts how endwall bleed reduces the size of the boundary layer and streamlines become more two-

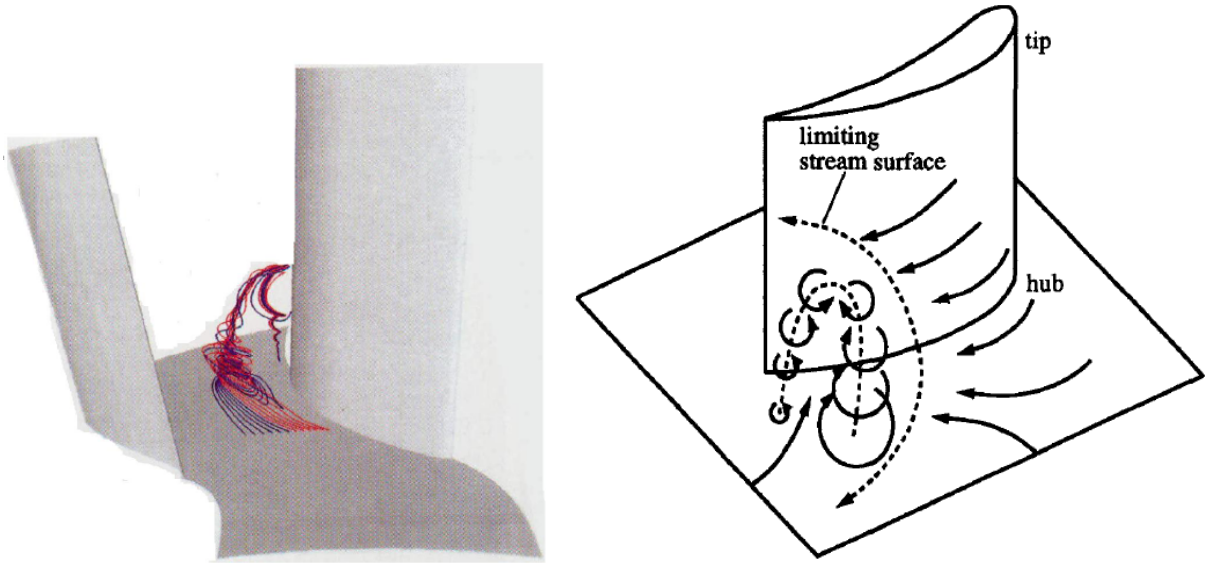

(a) Predicted structure of corner stall vortex (b) Proposed topology of corner stall

Figure 1.7: Corner stall structure proposed by Hah and Loellbach (1999)

dimensional. A way to determine the degree of flow two-dimensionality is to use *Axial Velocity Density Ratio* (AVDR), that is the ratio of outlet to inlet axial mass flow rates (Rodger *et al*., 1992).

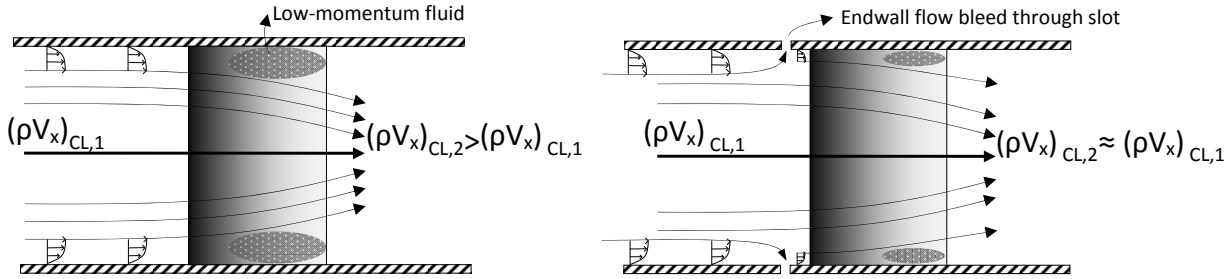

(a) Three-dimensional flow (AVDR>1) (b) Quasi two-dimensional flow (AVDR≈1)

Figure 1.8: The endwall boundary layer flow effect on cascade flow

Endwall corner separation control have been studied and achieved through both passive and active flow control techniques. Vortex generators are a well known passive flow control technique traditionally used to prevent or delay boundary separation on aircraft wings. Vortex generators are basically small perpendicular protruding aerodynamic surfaces that generate small streamwise tip vortices from their open extremities to enhance mixing between the low-momentum fluid in the boundary layer and high momentum fluid in the outer layers. In the turbomachinery context, Hergt *et al*. (2006) performed experiments with two vortex generators attached on the suction surface of a compressor vane to reduce the extent of endwall corner separation at high speeds, as shown in Figure 1.9. While vortex generators can be successful in controlling boundary layer flow separation, they also increase total pressure loss through mixing (by 2% to 8% in this study).

Endwall contouring is another passive flow control technique applied to reduce corner sep-

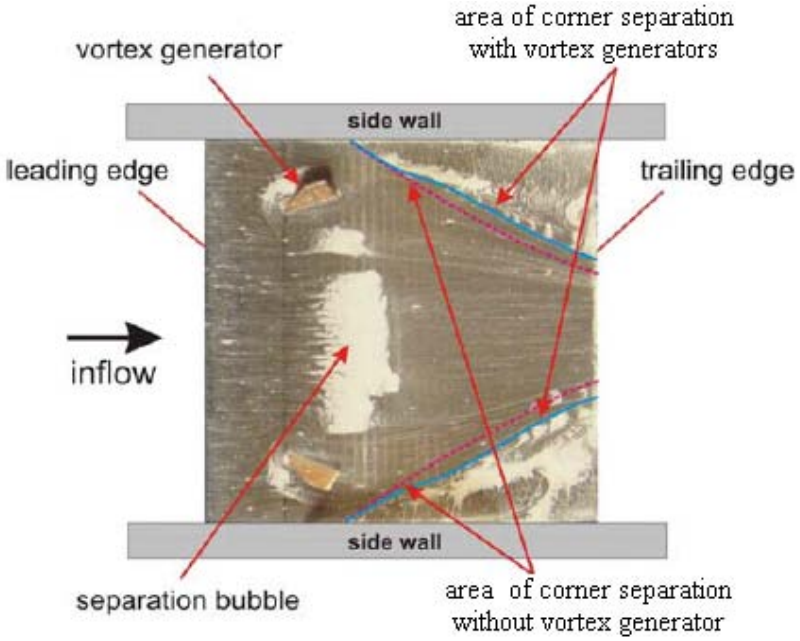

Figure 1.9: Flow visualization on suction side of the vane at Mach=0.66 (Hergt *et al*., 2006)

aration. In this method, the planar endwall profile is modified in such a way to alleviate low-momentum flow accumulation at the blade corner of the suction surface and the endwalls. Hergt *et al*. (2009) studied the effect of the endwall grooving on loss behavior and cascade performance. By forcing some portion of the endwall boundary layer fluid to follow the endwall groove, Figure 1.10 shows (through oil visualizations) that the migration of endwall boundary layer fluid to the blade suction side is reduced, resulting in a reduced corner separation compared to the reference design. In addition, the total passage loss was decreased by up to 30%, the relative inlet flow angle at which the blade stalled was increased (i.e. maximum flow turning was increased), leading to an increase in static pressure ratio.

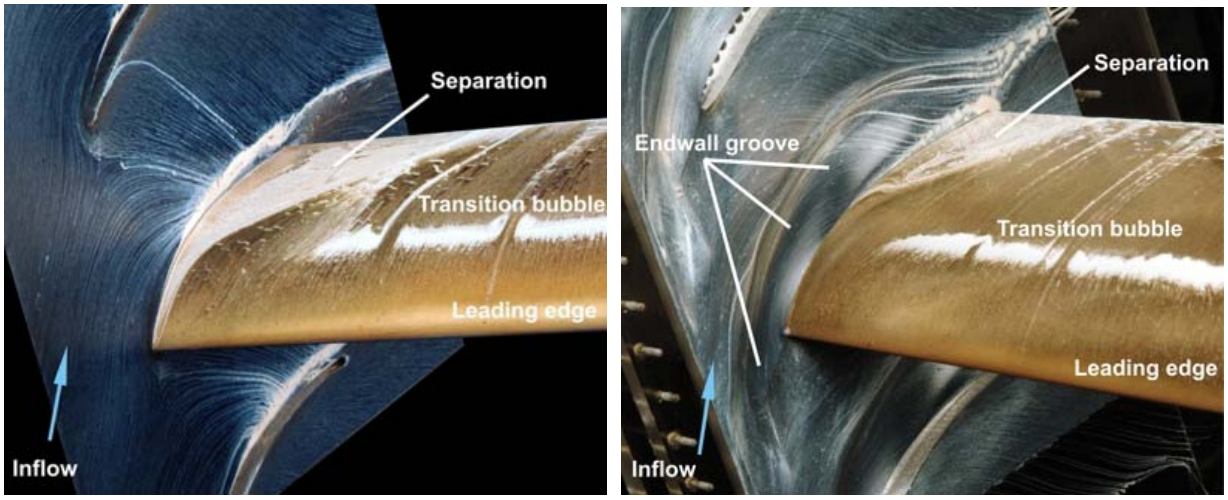

(a) Datum cascade (b) Endwall grooved cascade

Figure 1.10: Oil flow visualizations on the endwall and blade suction surface (Hergt *et al*., 2009)

Endwall contouring was also studied numerically by Lu *et al*. (2009) on a subsonic axial-flow compressor stator blade row to suppress corner separation. The blade endwalls were profiled in both axial and azimuthal directions. The static pressure ratio was increased by less than 1% and efficiency was improved about 1.2% $\sim$ 1.6% with the endwall contouring. However, the endwall contouring can only make partial improvement in the endwall boundary layer flow. Moreover, the effectiveness of the method is very sensitive to the inlet flow angle and velocity.

Active flow control technologies are relatively new technologies for controlling corner flow in turbomachines. The boundary layer suction is one of the intuitive approaches which was initially used by Prandtl (1927) to control the boundary layer flow separation on a circular cylinder.

One of the earliest attempts to control corner separation in compressor cascades using the boundary layer suction was made by Peacock (1971). The compressor cascade, having a low camber angle (30°) and a blade aspect ratio of 2.75, had a small corner separation region. The experiments performed at $Re = 2 \times 10^5$ showed that corner separation was suppressed partially by ingesting 1.3% of the half channel flow with a suction slot (2.1% chord in width) located on the endwall close to the blade suction surface covering the entire chord. The parametric study performed for the slot length and width suffered from inadequate estimates of the corner separation size via trailing edge measurements.

Zierke and Deutsch (1989) used endwall suction in combination with tailboards for testing the same compressor cascade (DCA-1) used in the present study. The flow two-dimensionality and periodicity were controlled by using a 5-hp blower operated at full power for the top and bottom channel suction. Moreover, a second blower with a 10-hp power has been operated at full power for the side wall suction. The distribution of the side flow was controlled by a complex baffling system. The average AVR was measured as 1.0 with an error of ±3% (Deutsch and Zierke, 1987).

Song (2003) used slotted endwalls to control the axial velocity density ratio (AVDR) of the cascade flow in a transonic compressor cascade. They have used endwall slots starting from 63% chord extending up to the trailing edge as shown in Figure 1.11 for cascade geometries having a flow turning angle of 55° and an aspect ratio of 1.77. They were able to reduce AVDR from 1.07 to around unity. Although endwall bleed mass flow rate has not been mentioned, Figure 1.11 reveals that significant amount of inlet mass flow has been used to control AVDR. It is interesting to state that the total pressure loss coefficient was observed to increase as the AVDR became closer to unity. This result was attributed to the increase of losses due to formation of stronger passage shock and resultant increase of the suction surface boundary layer separation size when the AVDR becomes closer to unity.

As a practical application of the boundary layer suction, the study performed by Gbadebo *et al*. (2008) aimed to eliminate corner stall for a compressor blade with a lower camber angle of 42° at $Re = 2.3 \times 10^5$. The computationally predicted limiting streamlines on the endwall and suction

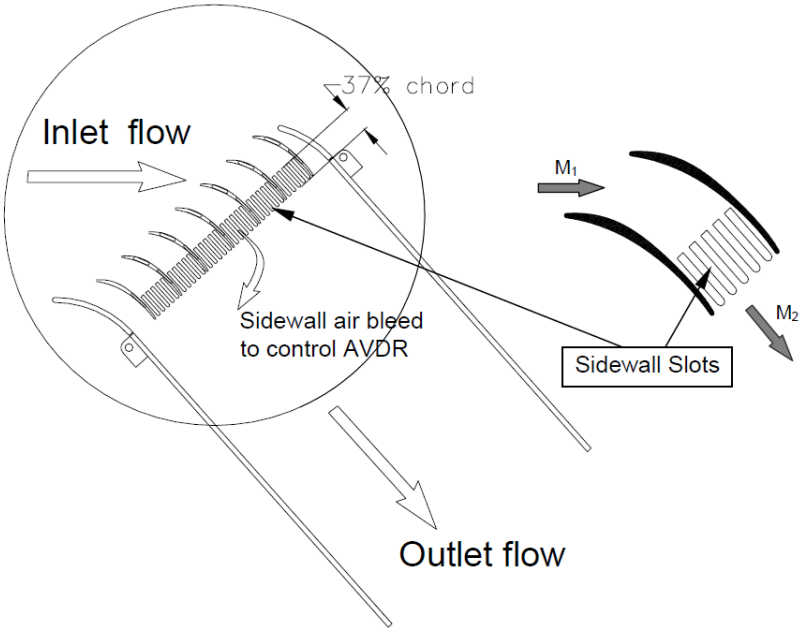

Figure 1.11: Sidewall slots (Song, 2003)

surface are shown in Figure 1.12 for the four slot configurations, two with the slot on the suction surface and two with the slot on the endwall. Endwall and suction surface slots had widths of 2% and 3% of the chord, respectively. For the endwall suction, two slots located 2% chord away from the suction surface are used, one is extending from 55% to 90% (referred as EWA) axial chord and other is extending from 16% to 90% axial chord (referred as EWB). They have observed that the EWA slot did not work well because it is located at the downstream of the dividing streamline. The EWB slot was able to remove the entire 3-D corner stall region using 0.7% of the inlet mass flow and the overall mass-averaged total pressure loss was reduced by 22%. The numerically optimized slot location was used in experimental investigations where the slot configuration was replaced by a series of holes with 2% chord diameter. The suction surface tuft flow visualization was consistent with the computationally predicted limiting streamlines.

Guo *et al*. (2010b) carried out an experimental study to investigate the effect of suction on the endwall of a compressor cascade with a 60° blade camber at a Reynolds number of 5.1×10^5. Two endwall slots located 3mm away from the suction surface as shown in Figure 1.13. The first endwall slot (EW1) was located at mid-chord and the second slot (EW2) was located towards to the trailing edge. The mid-chord endwall slot (EW1) was observed to be more effective. They were able to reduce total pressure loss by 17% using the blade suction side slot at 60% together with the mid-chord endwall slot with a suction mass flow rate of 1.5%.

An interesting experimental study of air suction was carried out by Bloxham and Bons (2010). The effect of endwall inlet boundary layer thickness on the secondary flows was investigated for a linear turbine cascade. The endwall boundary layer was partially removed using a suction slot lo-

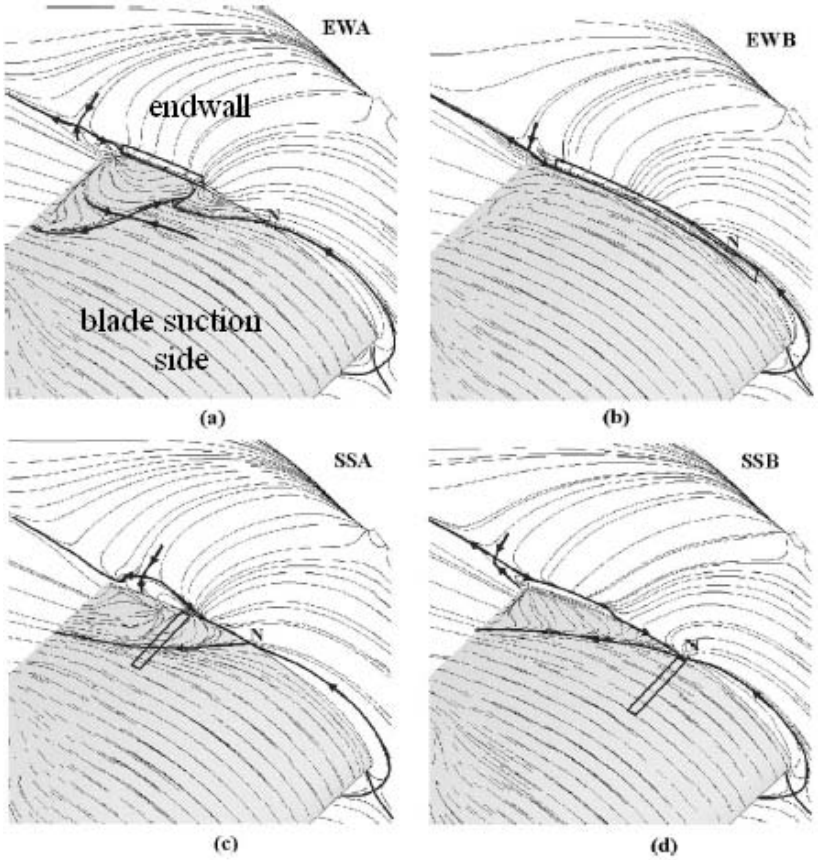

Figure 1.12: Slot locations and predicted limiting streamlines (Gbadebo *et al*., 2008)

cated just upstream of the leading edge of a turbine blade at $Re_{Cx} = 5\times10^4$ as shown in Figure 1.14. They have obtained a 7% reduction in the wake total pressure loss using 11% of the inlet endwall boundary layer fluid.

More recently, Gmelin *et al*. (2011) carried out a study to investigate endwall suction on a high-speed compressor cascade both experimentally and computationally. The experiments were performed at $Re = 5.6 \times 10^5$ based on chord for a blade with 42° turning angle. The endwall flow suction was realized with a 3.5 kW blower. They have used the findings of Gbadebo *et al*. (2008) and located the first endwall slot at 2% chord away from the suction surface. A second slot was located at 5% chord away from the blade. As suggested by Gbadebo *et al*. (2008), the experiments have shown that the slot located 2% chord away from the suction surface performed better in reducing the total pressure loss. This result shows that the endwall suction slot should be close enough to the suction surface to draw most of the corner flow. This study has proved that the corner separation can be controlled effectively by ingesting air using endwall slots located very close to the suction surface.

Finally, experimental and computational work carried out by Pönick *et al*. (2011) also focused on performance increase with endwall bleed air removal. The performance evaluation of the study

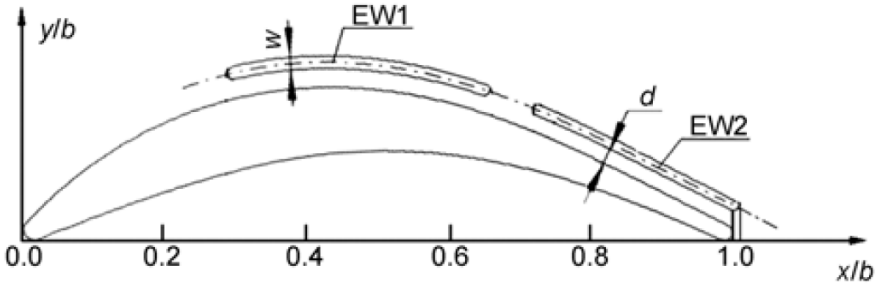

Figure 1.13: Slot locations on the endwall (Guo *et al*., 2010b)

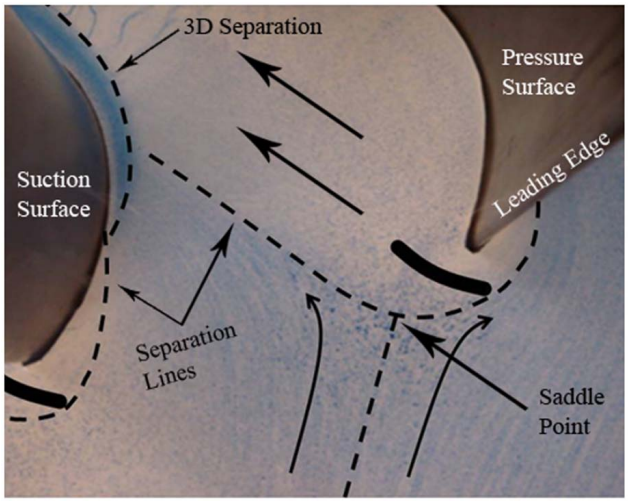

Figure 1.14: Inlet endwall oil-flow visualization for the turbine passage (Bloxham and Bons, 2010)

was referenced to the numerical study performed by Gümmer *et al*. (2008) discussed previously. The studies were performed on a low-speed compressor stator blade with a relatively low turning angle (30°). Figure 1.15 illustrates the reference bleed configuration where significantly large cavity was introduced to the casing endwall to bleed the air. Although the reference cavity configuration was improved to avoid the negative bleed (flow in to the passage), a small amount of negative bleed was still observed. The improved configuration was observed to improve non-uniform flow present at the inlet plane of the cavity for the reference configuration. The half-span passage loss coefficient was reduced by more than 50% compared to the planar endwall case.

Although the bleed flow is a source of loss for the engine performance, this method is still beneficial as long as the performance gain obtained through the method overcomes the performance penalty from bleed air.

1.3 Rotor/Stator Interaction Noise

There are two sources of wake interaction noise. The first source is the broadband noise, which is associated with the interaction of non-periodic unsteadiness inside the blade wake with the blade

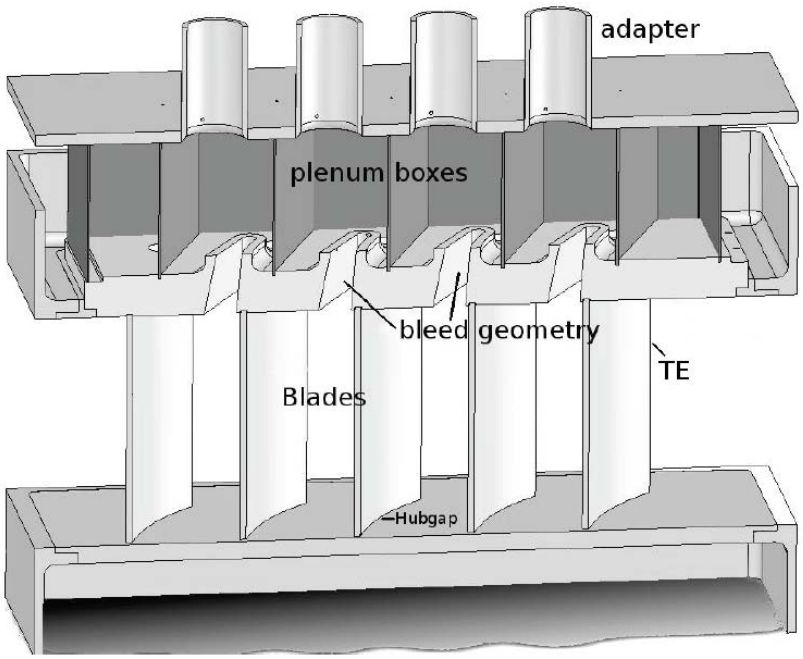

Figure 1.15: Cross sectional view of the reference cavity configuration (Pönick *et al*., 2011)

located downstream (Ganz *et al*., 1998). These fluctuations are mainly caused by inflow turbulence, vortex shedding, blade to blade differences and wake turbulence (Brookfield and Waitz, 2000; Huff, 2007). The second source is tonal noise, which comes from the interaction of the rotor blade wake with the downstream stator blade or of the stator blade wake with the downstream rotor blade. Therefore, the tonal noise is strongly related to the blade passing frequency (BPF). Although these two sources have different mechanisms, many studies have shown that reducing the tonal noise also reduces the broadband noise (Brookfield and Waitz, 2000; Huff, 2007; Carolus *et al*., 2007; Woodward *et al*., 2001).

Passive and active flow control techniques have been used to achieve rotor-stator noise reduction in compressors and fans. Passive noise control techniques include the work by Tyler and Sofrin (1962) which was focused on selecting rotor/stator blade counts to create destructive interferences between acoustic waves to suppress noise. While this technique could work, the potentially high blade count to reduce noise at all harmonics of the blade passing frequencies could make it impractical due to cost and weight considerations.

Another potential passive flow control technique is to increase the axial spacing between adjacent blade rows to allow the wakes to mix out before reaching the downstream blade row (Tyler and Sofrin, 1962; Woodward *et al*., 2001). However, this approach adds length and weight to the engine. Woodward *et al*. (2001) have also used swept and leaned stator vanes to reduce the effect rotor wake on the downstream stator vanes. They observed not only a significant reduction in the tonal noise levels but also a less pronounced reduction in the broadband noise. However, the

swept and leaned stator blade showed higher aerodynamic losses in addition to drawbacks related to structure and manufacturing.

Active noise control techniques for noise reduction aim to overcome these drawbacks. They generally rely on two basic techniques. The first is the use of acoustic resonance, which consist of canceling the acoustic field generated within compressor by another field with the same magnitude, but of opposite phase (Envia, 2001). The concept of noise cancellation has been studied numerically by Dyson *et al*. (2004) using time-accurate inviscid simulations. The main drawbacks of this method are the reliance on accurate measurement of acoustic modes and production of noise at the same tone and amplitude as the noise source. Any defect on either of these parameters reduces the method's effectiveness (Envia, 2001).

The second category of active noise control techniques is based on reducing the wake size and momentum deficiency which gives more promising results than the acoustic resonance in terms of noise reduction. Trailing edge blowing has been used by several authors (Brookfield and Waitz, 2000; Halasz *et al*., 2005; Fite *et al*., 2006; Woodward *et al*., 2007) to reduce blade wake momentum deficit and thus compressor/fan noise. Wake filling reduces the magnitude of variations in the mean velocity profile which causes a reduction in the tonal noise. Additionally, the wake filling also reduces the wake shear which in turn reduces the wake turbulence and therefore the broadband noise. Computational predictions have shown that filling the fan wake using trailing edge blowing reduces both wake defect and turbulent intensity which reduce the tonal noise and broadband noise, respectively (Huff, 2007). Minton (2005) have used particle image velocimetry (PIV) measurements to investigate the mechanism of wake management with the air injection near the blade trailing edge. His measurements illustrate that air injection near the blade trailing edge induces vortical structures which accelerate mixing of the wake with the outer flow to reduce the wake momentum deficiency. According to the work conducted by Ho and Huerre (1984) on shear layers (such as wakes), pulsed actuation at a resonant excitation frequency can produce the same effect with lower energy input.

Brookfield and Waitz (2000) applied trailing edge blowing experimentally on a scaled transonic fan stage using passages inside the fan blade. With a mass flow rate of less than 2% of the fan inlet mass flow, the authors reported that the amplitude of wake harmonics can be reduced by 85% for the first and second harmonics of BPF, giving a 10dB reduction in the radiated tonal noise. In another experimental study, Woodward *et al*. (2007) investigated trailing edge blowing on a model fan rotor. The sound power level spectra was measured at various fan speeds. It was observed that the noise has been reduced as much as 3 dB when full-span blowing was applied with 2% of the inlet mass flow.

However, trailing edge blowing induces an aerodynamic penalty due to loss introduced by injected mass flow. As an experimental effort to reduce trailing edge mass injection, Halasz (2005)

applied the trailing edge blowing only on some of the fan blades. The partial blowing configuration achieved a significant noise reduction while the amount of injected air was halved. Figure 1.16 shows the air being injected in alternating fan blades reducing the amplitude of original tones while distributing the noise on half BPF harmonics. It was found that conventional trailing edge blowing provided a sound reduction of 7.7 dB using 1.5% of the fan mass flow, whereas 3.0 dB sound reduction was obtained using 0.9% of rig mass flow in partial trailing edge blowing.

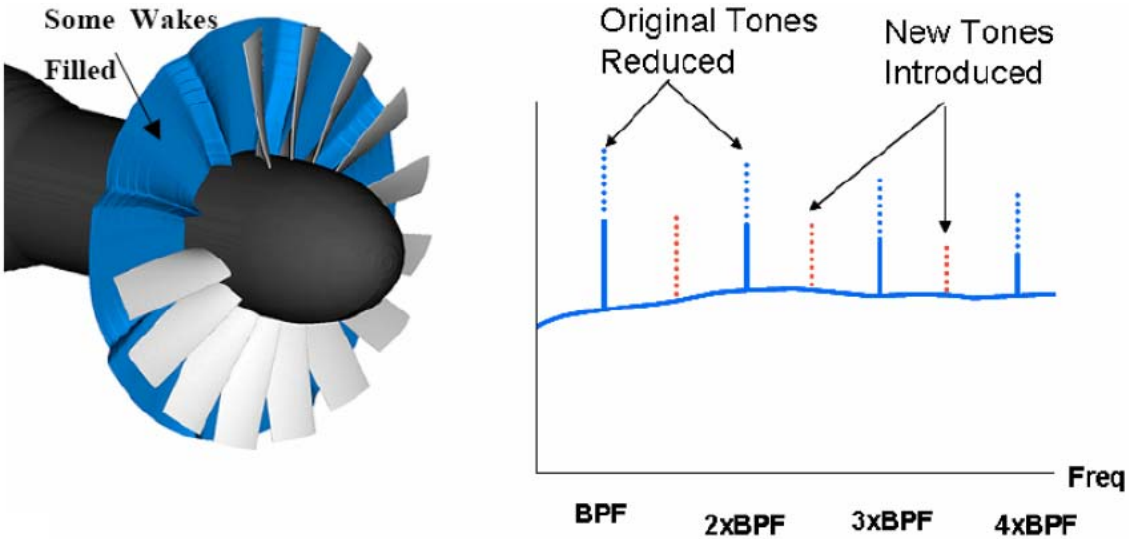

Figure 1.16: Schematic of partial blowing concept (Halasz, 2005)

Although effective, trailing edge blowing can incur a large penalty in engine efficiency. This is especially true for modern high-bypass ratio aero-engines where the air bled from the large fan can represent a significant portion of the engine core mass flow, from which the high-pressure air is drawn. Moreover, this technique creates cost and/or weight penalties from air recirculation and piping systems and manufacturing challenges associated with the need for air passages inside the rotating fan blades.

1.4 Plasma Actuators

There has been a significant increase in plasma actuation flow control studies in the past 15 years. Although plasma actuator applications are still limited to low-speed flows due to low actuation strength, extensive research on plasma actuators promise increases in their strength to levels high enough for effective flow control of high-speed flows.

While the plasma actuation physics and plasma actuator optimization are beyond the scope of the current research, a basic review is carried out to justify the selected plasma actuator configurations used in the current research. This review is followed by a discussion on plasma actuator applications studied in the past few years.

1.4.1 Plasma Actuation Physics

The formation process of a plasma in a SDBD actuator has been studied by Corke *et al*. (2010). This process consists of two parts in the AC input cycle. In the first part, the electrons move from the exposed electrode towards the dielectric material surface over the covered electrode. The accumulated electrons on the dielectric material then moves back towards to the exposed electrode during the second part of the cycle. The periodic motion of the electrode between the exposed electrode and dielectric material is referred to as micro-charge rearrangement. The time scale for the micro-charge rearrangement is on the order of $10^{-9} - 10^{-8}$ seconds whereas the timescale for the plasma induced velocity generation is several orders of magnitude larger on the order of 10^{-2} seconds (Orlov and Corke, 2005; Orlov, 2006; Corke *et al*., 2010). Another time scale on the order of $10^{-3} - 10^{-4}$ seconds (for an AC cycle on the order of kHz), that appears between these two time scales, is related with the plasma actuator formation i.e. with the period of AC cycle.

The large difference between the time scales allows model developers to assume that actuation process is virtually steady from the point of view of the flow which is the main theory behind the numerical modeling of plasma actuators. Another problem for plasma actuation model development is the presence of two parts in the AC input cycle as discussed above. Although there are two discharges (forward and back) in positive and negative halves of the AC cycle, the reversed electric field still induces a body force on air in same direction with a lower magnitude, called as "PUSH-push". Corke *et al*. (2009) stated that the body force induced by the plasma actuator is always oriented in the direction from the exposed electrode towards the covered electrode throughout the ac cycle. This was also proved by the measurements of Forte *et al*. (2007); Font *et al*. (2010). These experiments showed that induced velocity is larger in one half of the cycle compared to the other, but always in the same direction and adds momentum to the flow in the same direction.

In many studies, the plasma induced body force (or actuator strength) has been related to the intensity of the light emission from the plasma formation. The light emission was observed to be the maximum at the junction of the electrodes and decreases exponentially at locations away from the axial junction point (Enloe *et al*., 2004; Orlov, 2006). Therefore, the plasma induced body force is the highest at the junction of the electrodes.

1.4.2 Plasma Actuator Optimization

The strength of plasma actuators depend on several factors including input voltage, input frequency, signal waveform, electrode material and geometry, dielectric material and thickness, electrode configuration, type of gas surrounding the plasma actuator, ambient pressure, temperature and humidity (Santhanakrishnan and Jacob, 2007). Thus, its optimization depends on many parameters. This section reviews some of the techniques that have been considered to set up plasma

actuator configurations for the current study.

As stated before, the plasma actuation flow control has many practical advantages over other passive and active flow control techniques. The most important shortcoming of the plasma actuators seems to be the low plasma actuator strength levels which make them at present only applicable to the low-speed applications. In an effort to increase the plasma actuator strength, Thomas *et al*. (2009) investigated the dielectric material effect. Figure 1.17 shows measured thrust (given in gram/span, 1 g/m=9.81 mN/m) versus applied voltage for various dielectric materials. It is seen that the maximum plasma actuation strength was increased up to approximately 250 mN/m (25 gram/m) using Teflon instead of Kapton as the dielectric material. This study is very promising in terms of plasma actuator strength enhancement since the plasma actuator strength was increased by an order of magnitude.

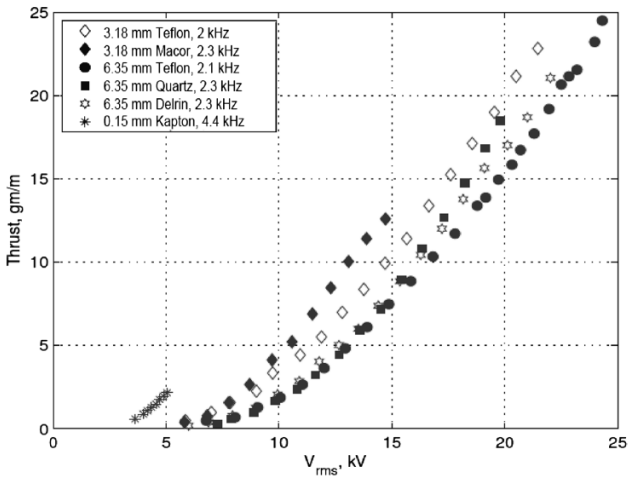

Figure 1.17: Dielectric material effect on plasma actuation strength (Thomas *et al*., 2009)

The dielectric material thickness also plays an important role on the level of plasma actuation strength. For a given voltage, a higher induced velocity can be obtained with a thinner dielectric material (Forte *et al*., 2007). However, thinner material can not withstand high voltages. Therefore, thicker materials induce a higher velocity in the expense of a larger power consumption since a thicker material requires larger AC voltage amplitude to get the same electric field strength.

There has been an effort to increase plasma actuator strength by varying the shape and size of the exposed electrode. Hoskinson and Hershkowitz (2010) have compared exposed electrodes with circular and rectangular cross sections as shown in Figure 1.18. In Figure 1.18(c), the force efficiency (defined as force/power) variations with exposed electrode thickness are shown for the circular and rectangular exposed electrodes. The forces generated by the cylindrical exposed electrodes stated to increase exponentially as the diameter is reduced. They demonstrated that a cylindrical exposed plasma actuator can induce a plasma force 2 to 5 times larger than a rectangular exposed electrode of the same thickness. They have also mentioned that the cylindrical electrode requires

a lower electrical power which was attributed to the filament-free plasma (plasma formation without having filament) generated by the cylindrical exposed electrode. In the filamentary mode, the voltage in the plasma is too high and the plasma generates electrical arcs. Enloe *et al.* (2004) have experimentally shown that there is a linear increase in actuator strength as the diameter of the exposed electrode decreases (electrode size was reduced to 0.1 mm). Hoskinson *et al.* (2008) further decreased the exposed electrode diameters. This study revealed that actuator strength increases exponentially with decreasing exposed electrode diameter rather than linearly. A similar observation was made by Corke *et al.* (2009) for the straight edge exposed electrodes. They have observed that the sharpness of the exposed electrode edge close to the covered electrode strongly affects the actuator strength. As the exposed electrode edge gets sharper, the electric field concentrated on the exposed electrode edge gets stronger which in turn increases the actuator strength.

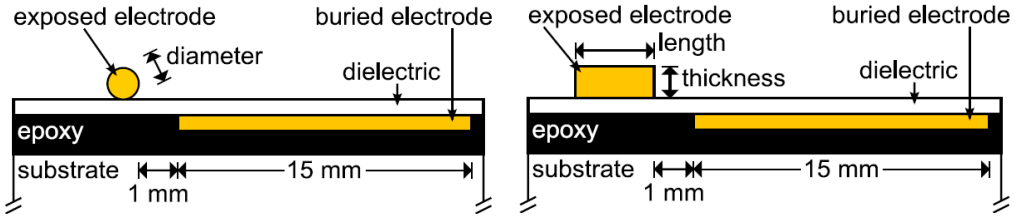

(a) A cylindrical exposed electrode (b) A rectangular exposed electrode

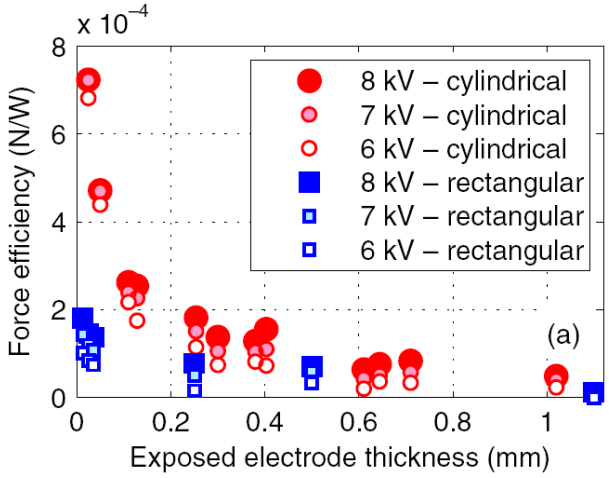

(c) Force efficiencies of actuators

Figure 1.18: Exposed electrode thickness effect Hoskinson and Hershkowitz (2010)

Studies also focused on increasing effective length (exposed electrode length within the plasma region) of the exposed electrode by changing the shape of the edges. Thomas *et al.* (2009) studied the effect of the exposed electrode geometry using straight and sawtooth edges. Measurements showed that sawtooth edged exposed electrode resulted in an actuator strength improvement around 50-60% within the 40-50 kV peak to peak (kV_{pp}) AC voltage range. PIV measurements made by Liu *et al.* (2011) on the boundary layer flows using sawtooth and sine-wave shaped electrodes have proven that these actuators induce a flow both in streamwise and spanwise directions as opposed to

the rectangular strip electrodes which adds momentum only in the streamwise direction. The flow induced in streamwise and spanwise directions causes vortex formation in the flow field, which can be used to increase the flow mixing to control the flow separation. Moreover, the flow velocity (and actuation strength) induced by the sine-wave and sawtooth edge electrodes were larger than straight edge electrodes.

The parametric study performed by Thomas *et al*. (2009) for the covered electrode width showed that increasing its width up to a certain value (50.8 mm) increases the actuation strength, but further increase does not cause any improvement. A similar experiment was also performed by Forte *et al*. (2007) where they were able to increase the induced velocity by increasing the covered electrode size. Their measurements revealed that the induced velocity reaches a plateau at a covered electrode size of 22 mm.

For the AC voltage and frequency, the actuator strength (given in gram) was observed to increase with both voltage and frequency up to a certain value (Corke *et al*., 2010). However, the actuator has a lower saturation voltage (voltage at which actuator strength does not increase with the voltage anymore) at lower frequency as presented in Figure 1.19.

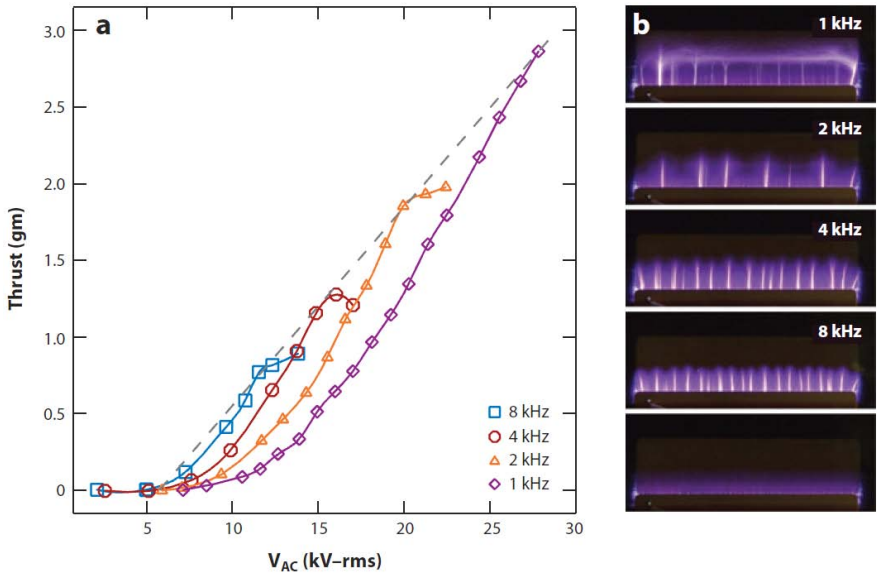

Figure 1.19: AC voltage effect on plasma actuator strength (Corke *et al*., 2010)

Thomas *et al*. (2009) also studied the effect of AC frequency input for various materials with different dielectric constants, ϵ. They have observed that the optimum AC frequency decreases as the ϵ increases. This result was explained by the increased capacitance of the material, which is proportional to ϵ/h, where h is the dielectric material thickness. So, for the same dielectric thickness, dielectric materials with higher capacitance works more efficiently at lower AC frequency.

There are two cycles in the formation of plasma where one phase induces larger thrust ("PUSH" phase) and the other phase induces smaller thrust both being in the same direction. Researchers

have used various waveforms to maximize "PUSH" phase and minimize the "push" phase to obtain higher actuation strength. Post (2004) have tested various waveforms for the AC voltage. The positive sawtooth waveform was found to be optimum in terms of higher actuation strength which essentially maximizes the "PUSH" phase while minimizing the "push" phase (Corke *et al*., 2010). This waveform introduces higher rate of voltage change in time, which increases the formation of plasma. This finding was also supported by the experimental study of Enloe *et al*. (2006). The triangle wave, sine wave and finally square wave follow the sawtooth wave (Corke *et al*., 2009) in terms of plasma actuation strength effectiveness.

Versailles *et al*. (2010) experimentally investigated the effect of pressure and temperature on plasma actuator strength. They observed that the actuator strength increases by increasing the particle's mean free path (the average distance traveled by a moving particle between successive impacts). Therefore, the actuator strength was shown to decrease in a non-linear fashion with increasing pressure (100 to 690 kPa) at room temperature, and to increase linearly with temperature (30 to 200 $^{\circ}C$) at atmospheric pressure. For turbomachinery flows operating at high pressure and high temperature, these two factors may compensate each other.

1.4.3 Plasma Actuator Applications

Active flow control concepts using plasma actuators have been extensively investigated in external flows as well as turbomachinery flows. While most of the studies aim to reduce/eliminate 2-D boundary layer flow separation, there are only a few studies addressing endwall corner separation. Endwall flow control applications have so far been mostly limited to tip clearance flow control. Noise reduction studies have usually focused on the demonstration of plasma actuation flow control concept over circular cylinders.

Boundary Layer Flow Separation Control with Plasma Actuators

Boundary layer flow separation was among the first applications investigated for plasma actuators. Post and Corke (2003) experimentally investigated leading edge separation control using a plasma actuator covering 15%chord of the $NACA66_3 - 018$ airfoil starting from the leading edge. They were able to increase the lift-to-drag ratio from 14 to 60 using a plasma power of approximately 78 W/m at Re=7.5×10^4.

List *et al*. (2003) applied plasma actuation on a turbine blade in a linear cascade experimentally to control laminar separation. At a Reynolds numbers of 3×10^4, the separation bubble was eliminated and the profile loss coefficient was reduced by 14%. The reduction in the exit flow angle, 0.1°, was smaller than the experimental uncertainty which was estimated to be ±0.7°. At a Reynolds number of 7.4×10^4, the reduction in the loss coefficient was not measurable.

Huang (2005) also used steady and unsteady plasma actuation for experimental laminar separation flow control on a cascade of PakB low-pressure turbine blades. Pulsed plasma actuation was found to be more effective than steady plasma actuation, reducing the total pressure loss coefficient from 0.28 to 0.16 (by 43%) and from 0.11 to 0.09 (by 18%) at Re_c=2.5×10^4 and Re_c=5×10^4, respectively. The plasma actuation duty cycle was observed to be ineffective in a range of 10% and 50%.

Schatzman and Thomas (2008) used spanwise and streamwise plasma actuators in an experimental study of turbulent boundary layer flow separation control over a convex ramp. The unsteady spanwise actuation was observed to induce a thicker flow normal to the wall. This study has shown that the spanwise plasma actuators generate spanwise vortices and add momentum to the streamwise flow, whereas the streamwise plasma actuators generate counter rotating streamwise vorticity and increase the mixing of low and high momentum fluid in boundary layer which delays/prevents the flow separation. The experiments were conducted over a convex ramp showed that both actuator configurations reattached the turbulent, separated boundary layer flow.

Williamson (2008) carried out an experimental study on an axial compressor rotor blade at Reynolds numbers of 1.7×10^5 and 2.6×10^5. The plasma actuation was applied on a single blade in the annular compressor cascade. The study focused on increasing the compressor efficiency by adding/removing momentum to/from the boundary layer. A plasma actuator was mounted at 25% chord in counter and co-flow directions. Measurements have shown that the effect of plasma actuation is highly dependent on the Reynolds number. At Re=1.7×10^5, steady actuation in co-flow arrangement observed to decrease the drag coefficient by 12%. However, steady actuation in counter flow arrangement had a deleterious effect by increasing the drag coefficient by 9%. Pulsed actuation at 50 Hz increased the drag coefficient by 10% in co-flow direction and decreased the drag coefficient by 4% in counter flow direction. At Re=2.6×10^5, steady actuation in co-flow arrangement increased the drag coefficient by 13% but, steady actuation in counter flow direction had no effect. Finally, pulsed actuation at 50 Hz in co-flow and counter flow directions caused 18% and 13% reduction in the drag coefficient, respectively.

Numerous studies (Huang, 2005; Little and Samimy, 2010; Corke *et al*., 2011) have stated that the optimum plasma actuation pulsing frequency for the boundary layer flow separation control corresponds to a Strouhal number ($St = fL_{sep}/V_\infty$ where L_{sep} is the streamwise extent of the separated flow region) near unity. The optimum plasma actuator location was observed to be just upstream of the separation point.

Lemire *et al*. (2009) carried out a computational study of plasma actuation to reduce and suppress boundary layer flow separation on a compressor rotor blade row at a (circumferential) tip Mach number of 0.5. Their results for continuous actuation show that the increase in pressure ratio and efficiency varies almost linearly with actuator strength, and that the exact actuator location

does not affect the performance increase as much as it does the actuation power. Their study also indicated that an actuator strength at least one order of magnitude above what can be achieved so far would be needed to suppress blade boundary layer flow separation at anything close to realistic compressor speed. As mentioned in Chapter , the results for pulsed actuation were inconclusive. It was claimed that this could be due to pulsing frequency selection and CFD code limitations.

Endwall Flow Control with Plasma Actuators

Only two studies were found addressing the corner separation control in axial compressors using plasma actuation. Li *et al*. (2010a) carried out an experimental study on a low-speed compressor cascade with a flow turning of 30° at Re=2.23×10^5 in an attempt to control the corner separation with plasma actuation. The plasma flow control was applied from the suction surface using actuators located at 5%, 25%, 50% and 75% x/c. Total pressure recovery coefficient ($\sigma = P_{02}/P_{01}$) and total pressure loss coefficient ($\omega = (P_{01} - P_{02})/(P_{01} - P_1)$) were used to assess the effectiveness of the plasma actuation. The steady plasma actuator located at 25% x/c was stated to be the most effective, where 10.3% reduction in total pressure loss coefficient was observed at 70% span compared to the baseline. Their parametric study for the excitation frequency showed that plasma actuation effectiveness increases with frequency reaching a plateau at 400 Hz (corresponding to a Strouhal number of 0.4 based on the chord length and freestream velocity). The control effectiveness stays the same beyond this frequency. Pulsed actuation was observed to be more effective than continuous actuation where a 28% reduction was achieved in total pressure loss coefficient when 60% duty cycle was used. The control effectiveness was observed to be increasing with duty cycle up to 60% and levels off beyond this value.

Following the above study, a second attempt has been made by the same research group to control the corner separation (Wu *et al*., 2012). Three plasma actuator configurations shown in Figure 1.20 were tested at Re=3.3×10^5 (M=0.15). The first configuration had suction side streamwise plasma actuation at 8% and 30% of axial chord. The second configuration was endwall pitchwise plasma actuation (in counter-flow direction) from 15% and 85% pitch. The third configuration was a combination of the first and second configurations. Experimental measurements revealed that the plasma actuation from the suction surface had almost no effect on the corner separation. Pithcwise plasma actuation was observed to be more effective which inhibits the crossflow coming from pressure surface. At 70% span, the pitchwise-averaged total pressure loss coefficient was reduced by 2.7, 7.2 and 11.6% with the first, second and third plasma actuator combinations with respect to the baseline, respectively.

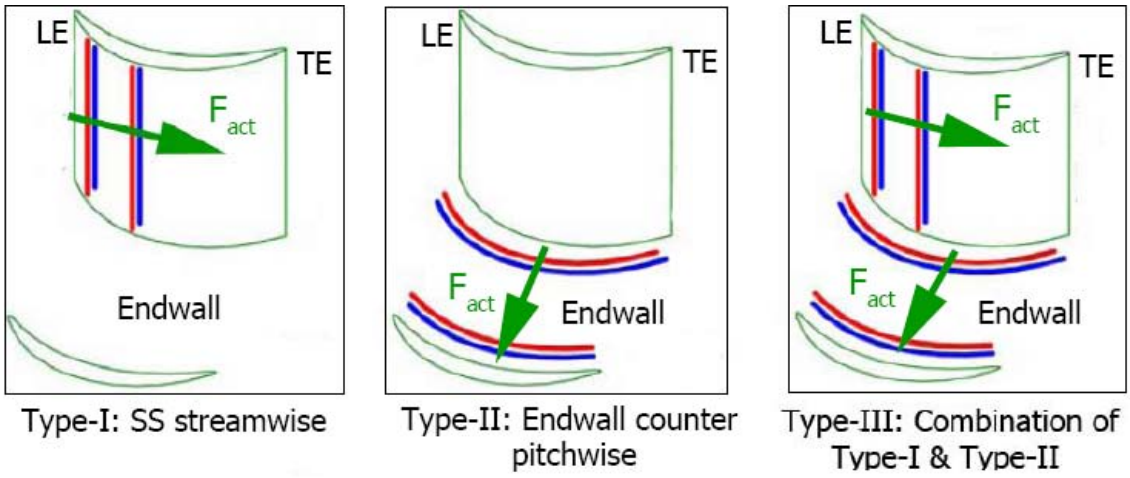

Figure 1.20: Schematic of plasma actuator configurations (Modified from Wu *et al*. (2012))

Wake Control with Plasma Actuators

In an experimental effort to reduce broadband noise generated by a bluff body, Li *et al*. (2010b) applied plasma actuation on a circular cylinder and an oblique strut. The broadband noise has been significantly reduced at freestream speeds up to 30 m/s. Above this speed, a higher plasma actuation strength was required.

Thomas *et al*. (2008) have tested plasma actuation on a cylinder to assess a concept of reducing landing gear noise for commercial aircrafts at a low Reynolds number, $Re_D = 3.3 \times 10^4$. The PIV images of the cylinder near wake region in Figure 1.21 reveal that the separated flow region and vortex shedding, being two sources of the noise, were significantly reduced with the continuous and pulsed plasma actuation where the difference between continuous and pulsed actuation was mentioned to be small. Microphone measurements showed that the noise levels were reduced by 13.3dB by steady and unsteady actuation.

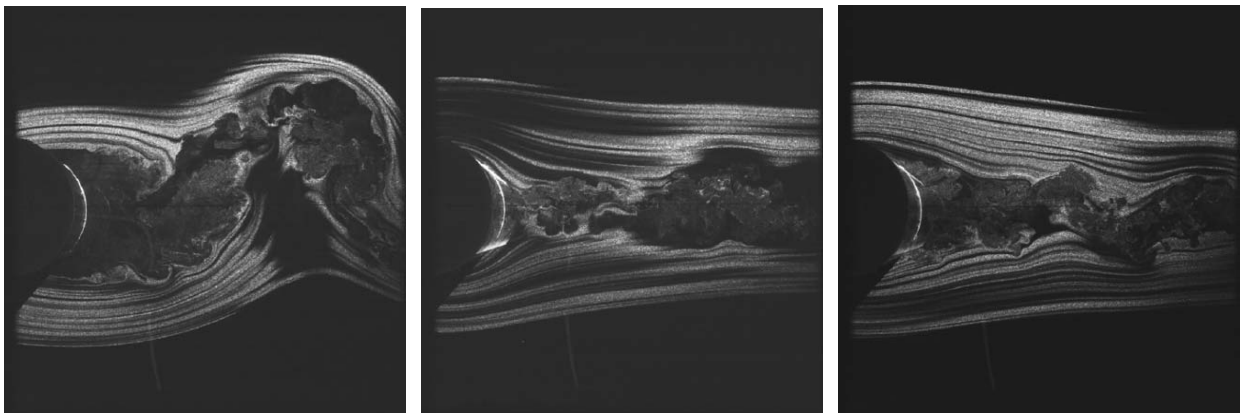

(a) No actuation (b) Continuous actuation (c) Pulsed actuation

Figure 1.21: PIV flow visualization images at $Re_D = 3.3 \times 10^4$ (Thomas *et al*., 2008)

Kozlov and Thomas (2011a) carried out a similar study on circular cylinders for landing gear noise reduction. They have compared spanwise and streamwise located plasma actuators. The flow visualization performed for $Re_D = 1.7 \times 10^4$ revealed that the von Kármán vortex shedding (repeating pattern of swirling vortices) was effectively suppressed by both actuator configurations as shown in Figure 1.22. The noise levels are reduced by 11.2 dB and 14.2 dB using spanwise and streamwise actuator configurations, respectively.

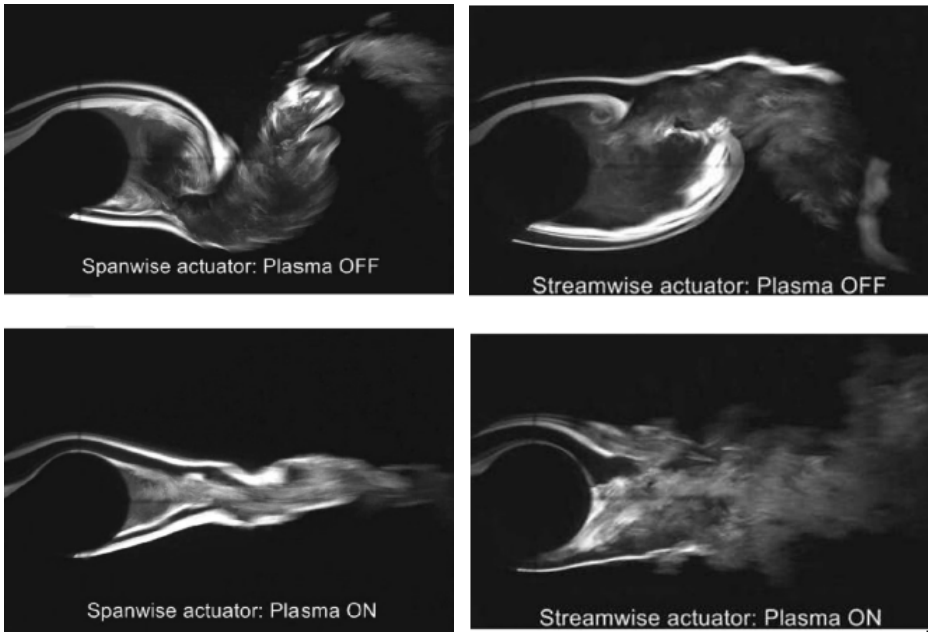

(a) Spanwise oriented actuators (b) Streamwise oriented actuators

Figure 1.22: Near-wake flow visualization (Kozlov and Thomas, 2011a)

Kozlov and Thomas (2011b) further investigated the control of vortex shedding on circular cylinders in a tandem configuration in an effort to reduce interaction between the upstream cylinder's wake and the downstream cylinder over a range of $2.2 \times 10^4 \leq Re_D \leq 1.72 \times 10^5$. Similar to the previous study, spanwise plasma actuators were used on the bottom and top of the cylinder. Figure 1.23 shows that the plasma actuation was effective in suppressing the von Kármán vortex shedding generated by the upstream cylinder which was also observed to reduce the downstream blade wake.

In a computational study for axial compressor and fan noise suppression with plasma actuation, Lemire and Vo (2008) positioned plasma actuators on either side of a compressor rotor blade with a (circumferential) tip Mach number of 0.2 to control the wake. The plasma actuation noise control effectiveness was determined by considering the first harmonics of the relative streamwise velocity profile over one pitch. A significant wake reduction was achieved by applying the continuous plasma actuation. Figure 1.24 shows the amplitudes of first five BPF harmonics for various continuous plasma actuation cases, where a 50% reduction in the magnitude of the first harmonic and

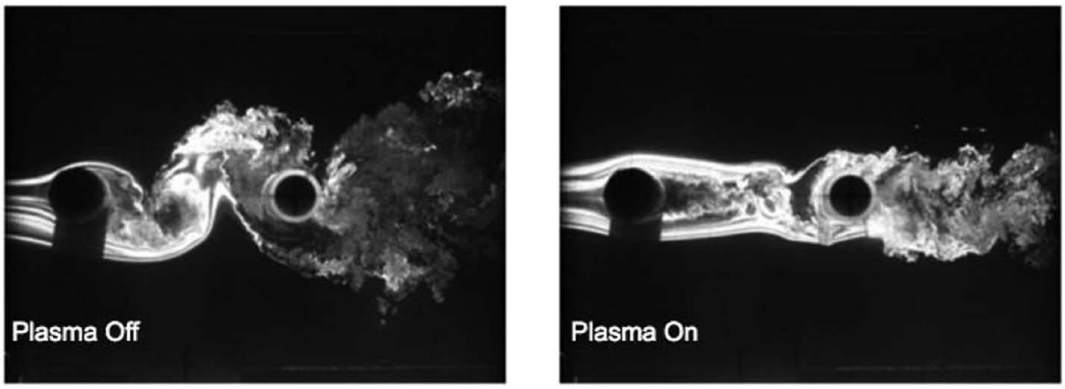

Figure 1.23: Wake flow visualization at $Re_D = 2.2 \times 10^4$ (Kozlov and Thomas, 2011b)

a 60% reduction in the magnitude of the second and the third harmonics were achieved with 1.2 N/m actuator strength. As with Lemire *et al*. (2009), the required plasma actuator strength for this moderate compressor speed was excessively high and the pulsed actuation study was inconclusive.

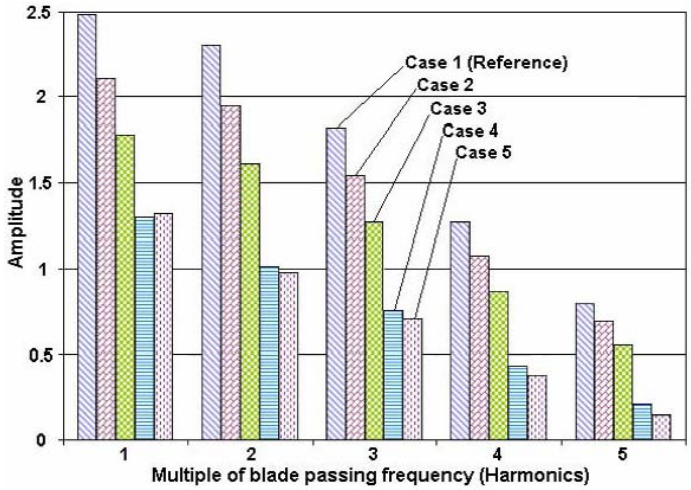

Figure 1.24: Harmonic amplitude for continuous actuation cases (Lemire and Vo, 2008)

Chapter 2

Methodology

An approach combining both numerical simulation and experiments is chosen for this study. The numerical simulations were carried out to determine the optimum plasma actuation parameters for endwall corner separation control, boundary layer separation control and noise reduction concepts. Once an optimum plasma actuator configuration is determined for each concept, the endwall corner separation control and boundary layer separation control concepts with plasma actuation were tested experimentally to validate the computational approach. The validated computational approach is then used to assess plasma actuation flow control at more realistic speeds without constraining the plasma actuator strength within the limits of real plasma actuators. As a reference approach to corner separation control with plasma actuation, endwall boundary layer suction was studied both computationally and experimentally to control endwall corner separation.

The methodology of this research project is divided into two phases. The computational studies form the first phase and the second phase includes the experimental studies. The computational study starts with the computational tool setup, followed by the simulation and analysis of each concept for assessing the plasma actuation parameters for the experimental evaluation. The computational study also includes computational analysis for assessing the endwall corner separation control with endwall boundary layer suction. The experimental study consist of setting the experimental rig and measurements methods, including design and integration of the plasma actuator, and carrying out specific tests for validation of CFD predictions.

2.1 Computational Tool Setup

The flow field for low-speed turbomachinery blades is very complex due to laminar flow separation caused by unfavourable pressure gradient, the presence of flow transition, flow reattachment due to turbulence and secondary flows and other endwall effects, which make accurate flow simulations challenging. Prediction of transition is among the more difficult aspect, and is needed to predict the performance of low-speed gas turbine engines accurately. In the present study, the computations were performed at a low Reynolds number range ($1.5\times10^5<Re_c<3.5\times10^5$). Therefore, the boundary layer over the cascade airfoil was primarily laminar with a laminar flow separation further downstream. The separated flow experiences a laminar to turbulent flow transition and in turn

reattaches to the surface. Therefore, precise prediction of transition onset and length was crucial.

In this study, 2-D and 3-D flow fields over the compressor cascade airfoils were solved using ANSYS-CFX version 13. ANSYS-CFX is a commercial Reynolds-Averaged Navier-Stokes (RANS) flow solver often used to simulate turbomachinery flows. It incorporates a finite volume, node-centered, pressure-based, implicit flow solver. A second-order accurate advection scheme was used in the flow solutions. ANSYS CFX works with structured and unstructured hybrid grids consisting of tetrahedral, hexahedral, prism, and pyramid elements.

For turbulence closure, the Shear Stress Transport (SST) turbulence model was used in simulations. The turbomachinery flows with boundary layer flow separation and adverse pressure gradient can be simulated accurately using SST model (Inc., 2006; Huang and Lexington, 1997; ANSYS, 2009). The SST model of Menter, combines the $k-\epsilon$ and and $k-\omega$ models. This model can accurately capture free shear flows (wakes and vortex shedding) as well as wall flows (boundary layer) (ANSYS, 2009).

The two-equation, $\gamma - Re_\theta$ transition model was used in the transition calculations. This model is based on the two transport equations for intermittency γ and transition onset momentum thickness Reynolds number $\widetilde{Re}_{\theta t}$ (ANSYS, 2009). This transition model has been extensively validated together with the SST turbulence model for turbulence closure for a wide range of transitional flows including a highly loaded Zierke & Deutsch compressor cascade (Langtry *et al*., 2006).

The computations were performed using both steady and unsteady flow solutions. For the steady flow solutions, the computations were carried out until a constant value was reached for local flow variables as well as integrated parameters. For the unsteady flow solutions, the level of convergence, was based on the comparison of two consecutive periodic signal intervals, determined using the method defined by Clark and Grover (2007) as discussed in further detail in Appendix A.1.

2.1.1 Compressor Cascade Airfoils

Active flow control assessment was applied on two double circular arc compressor airfoil profiles, namely DCA-1 and DCA-2, intended for use in the linear cascade rig at the NRC Gas Turbine Laboratory. Figure 2.1 depicts the DCA-1 and DCA-2 airfoil geometries and pertinent properties. The DCA-1 airfoil is a high flow turning, double circular arc (DCA) compressor cascade blade, which is very similar to that of Zierke and Deutsch (1989). This blade was used for the corner separation and blade boundary layer separation studies. Two notable features of this airfoil were its high flow turning of approximately 52° and diffusion factor of 0.54. This blade had a significantly high diffusion factor, compared to a typical diffusion factor of 0.45 (Cumpsty, 1989). In this design, the flow experienced suction surface laminar boundary layer separation, separated flow transition

and turbulent flow reattachment, and, strong endwall corner stall. This blade design was used in the past in many computational studies (Chen *et al.*, 1998; Malan *et al.*, 2009; Langtry *et al.*, 2006) mainly to investigate the accuracy of the flow solver in predicting the transition from laminar to turbulent flow. The DCA-2 airfoil is a low flow turning (approximately 10°) and low diffusion factor (0.23) DCA compressor airfoil used for the wake/noise attenuation study. It was designed using an in-house blade generation program to have a very small flow turning to avoid significant flow separation. The DCA-2 airfoil has a larger chord length compared to DCA-1 airfoil in an effort to have enough blade thickness close to the blade trailing edge for plasma actuator implementation both from suction and pressure sides.

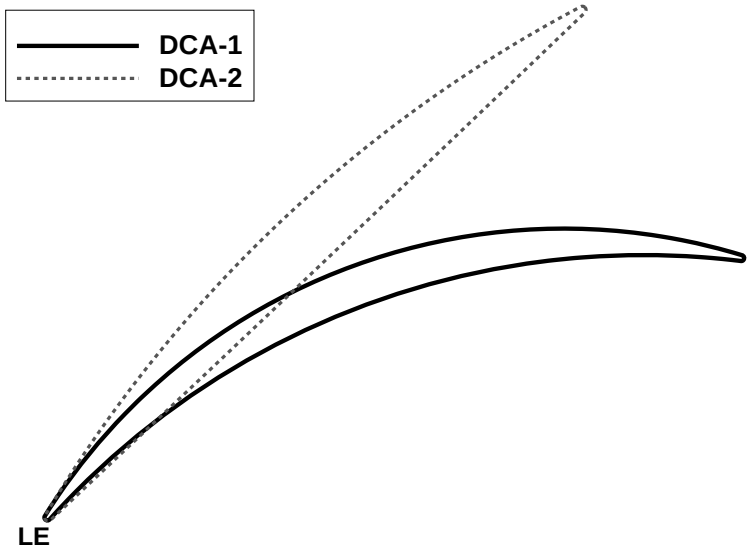

Parameters	DCA-1	DCA-2
Chord, c [mm]	114.9	250
Axial chord, c_x [mm]	107.6	181.3
Span, h [mm]	200	200
Pitch, s [mm]	53.4	154.7
Solidity, $\sigma = c/s$	2.15	1.62
Aspect ratio, h/c	1.74	0.8
t_{max}/c	0.055	0.08
L.E. diameter, d_{LE} [mm]	1	2.5
T.E. diameter, d_{TE} [mm]	1	2.5
Stagger angle, λ [°]	20.5	43.5
Inlet metal angle, β_1 [°]	53	53
Outlet metal angle, β_2 [°]	-12	39

Figure 2.1: Airfoil geometries and pertinent properties

2.1.2 Computational Mesh

The computations were performed using both structured and unstructured meshes. Structured, two-dimensional and multi-block meshes were employed for the boundary layer separation and wake/noise reduction plasma flow control computations. For the plasma endwall flow control cases, structured, three-dimensional meshes were employed. For the endwall boundary layer suction studies, an unstructured, three-dimensional mesh was used (see Appendix A.2 for details).

The structured meshes for DCA-1 and DCA-2 airfoils were generated in Gambit, a commercial, structured and unstructured mesh generator. The structured meshes consist of an O-grid around the airfoil, with the remainder of the mesh generated using a multi-block H-grid. Mesh expansion ratio of the O-grid mesh normal to the wall was kept less than 1.1. Three-dimensional meshes consisting of hexahedral mesh elements were generated by sweeping the two-dimensional mesh in the spanwise direction. To determine the optimum mesh density, mesh convergence studies were performed for each airfoil geometry. The details of the mesh convergence studies are further discussed in Appendix A.2.

2.1.3 Boundary Conditions

To define the physical problem uniquely, the boundary conditions shown in Figure 2.2 were used in two-dimensional flow simulations. At the blade surfaces, no slip boundary condition was implemented to simulate viscous walls. For the inlet boundary; relative total pressure, flow direction and turbulence intensity were prescribed. For the outlet boundary; relative static pressure was defined. The periodic boundaries were used to simulate periodicity in a cascade environment.

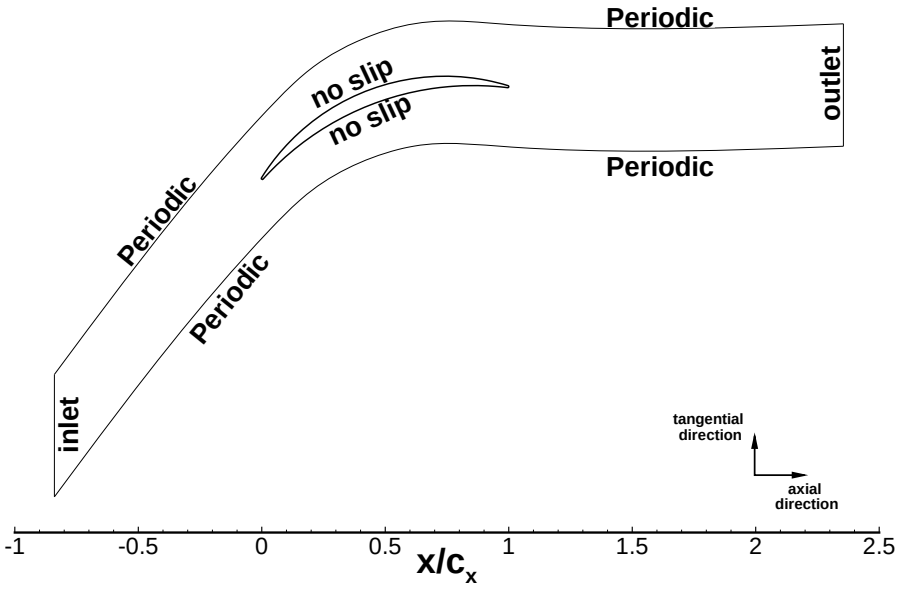

Figure 2.2: Boundary conditions used in the flow simulations

In three-dimensional flow simulations, a half span model was used to reduce the computational cost. Therefore, mid-span boundary was defined as a symmetry plane and the endwall boundary was defined as a no-slip wall. A spanwise total pressure profile was obtained for endwall boundary from experimental measurements (see Section 3.1.1). Thereafter, a flat plate flow simulation was performed to obtain boundary layer profile data for turbulence intensity. In the simulation, the turbulence intensity at the inlet of the flat plate was adjusted such that the turbulence intensity at the plane of interest (location where the boundary layer thickness matches with the measured boundary layer thickness) is equal to the experimentally measured turbulence intensity (Tu=0.3%). Therefore, the computations represented the experimental conditions as accurately as possible by implementing a computational boundary layer profile at the inlet plane where boundary layer profiles for total pressure, velocity magnitude and turbulence intensity were prescribed. Figure 2.3(a) shows the comparison of the measured and simulated boundary layer profiles in terms of non-dimensional velocity. The computationally obtained inlet boundary layer profile is presented in Figure 2.3(b). The computationally obtained turbulence intensity was 0.3% outside of the boundary layer as measured experimentally.

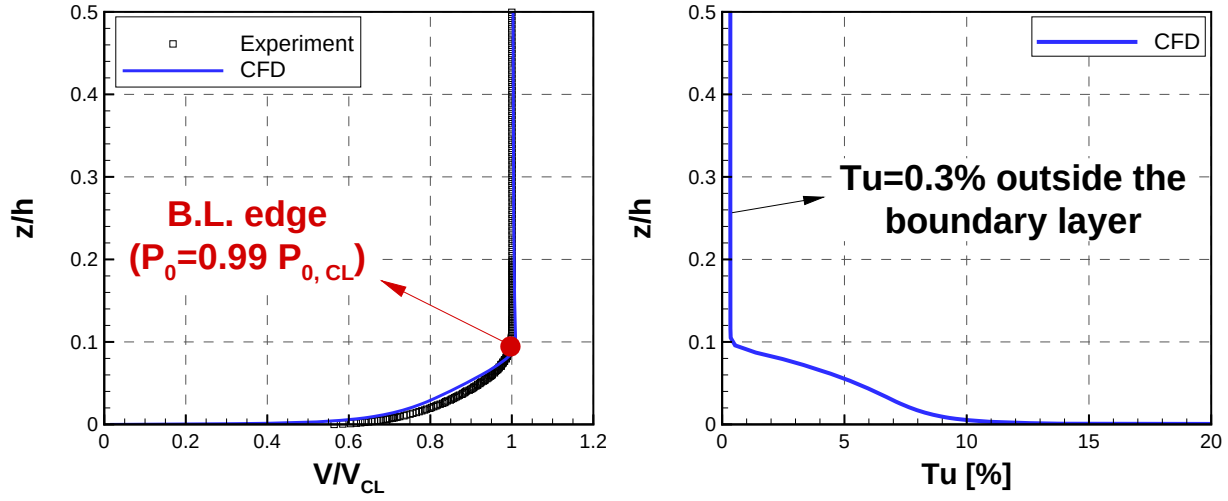

(a) Experimental and computational velocity profiles (b) Computational turbulence intensity profile

Figure 2.3: Experimental and computational boundary layer profiles

For the endwall suction flow control simulations, the boundary type for suction slot/holes (see Figure A.7 in Appendix A.2.3) were defined as the opening in which the corresponding static pressure and flow direction were set on each suction surface. The static pressure of the suction surfaces were set equal to each other and adjusted such that the bleed mass flow rate is equal to the experimentally measured bleed mass flow rate.

2.1.4 Plasma Actuator Modeling

The plasma actuation models are generally based on the two approaches, namely micro-scale and macro-scale approaches. In micro-scale modeling, the plasma actuation is modeled by solving the chemical reactions around the electrons and the motion of the inert and charged particles. These models include those by Roy *et al*. (2006); Jayaraman *et al*. (2006). These models require solution of 20-30 reaction equations which have different reaction times (Orlov, 2006). This approach requires the solution of equations in very small time scales making it computationally expensive. These models can be used to understand the physics behind the plasma actuation; however, they are still far from being practical to implement into flow solvers due to computational limitations.

In macro-scale models, the effect of a DBD actuator is modeled as a spatial body force distribution. The latest models in this category include those by Suzen *et al*. (2005); Orlov *et al*. (2007). The model by Suzen *et al*. (2005) solves for the electric potential field and charge distribution around the actuator, taking into account the exact actuator geometry and the nature of the fluid and dielectric material. However, this model does not capture time variation in body force. Orlov *et al*. (2007) developed a promising model that uses a network of electrical elements to model the glow discharge plasma region over the encapsulated electrode in an effort to capture the time variation of plasma formation process (and thus the body force). However, their model did not produce a reasonable spatial body force distribution.

For CFD flow control simulations, a time-averaged (over an AC input cycle) body force is an adequate modeling approach. According to Orlov *et al*. (2007), the time-scales associated with the ionization process and AC input cycle are six and two orders of magnitude, respectively, faster than the flow response time, and are thus virtually instantaneous from the point of view of the flow. In addition, as commonly done in other plasma flow control studies (Gaitonde *et al*., 2006a; Vo, 2007), the spatial body force distribution was assumed to be independent of the actuator strength and the spatial body force vectors can be scaled to give the desired actuator strength.

Lemire and Vo (2008) integrated the best features of models proposed by Suzen *et al*. (2005) and Orlov *et al*. (2007) into a hybrid model whose spatial body force distribution was found to best match the time-averaged body force distribution obtained by the micro-scale models. In the hybrid model, two equations were solved at each time step in the AC input cycle for the spatial distribution of the electric potential (ϕ) and charge density (ρ_c). The electrodes and the dielectric material were added as boundary conditions to the solutions. After the spatial distribution of ϕ and ρ_c was obtained, the body force per unit actuator length (actuation strength) in [mN/m] was calculated with the following equation:

$$\overrightarrow{F} = \rho_c \overrightarrow{E} A = \rho_c(-\nabla\phi)A \tag{2.1}$$

where A is the area of the mesh.

The spatial body force distribution obtained with the hybrid model is shown in Figure 2.4(b). The main characteristics of this force distribution are in good agreement with small scale models (Gaitonde *et al.*, 2006a; Roy *et al.*, 2006). At the junction of the two electrodes, the force is directed in axial direction. The body force gets smaller through the end of the covered electrode (in the positive x-direction) and finally a resultant force in the y-direction that is directed toward the surface over the covered electrode. Recently, Palmeiro and Lavoie (2011) compared a number of plasma actuation models in the literature. It was stated that the hybrid model of Lemire and Vo (2008) is the only model predicting the trends in body force and induced velocity appropriately for different geometries. Furthermore, it was the only model predicting velocity magnitudes comparable to the experiments on two out of the three configurations. In summary, this model stated to be exhibiting the most accurate behavior among the models evaluated.

In the present study, the hybrid model of Lemire and Vo (2008) was used. The model was written in a Matlab code to produce a time-averaged spatial body force on a very fine cartesian mesh as shown in Figure 2.4(a). The procedure to obtain plasma body force on CFD mesh is shown in Figure 2.5. Initially, the spatial body force distribution associated with the plasma actuator is calculated for a fine cartesian plasma actuator mesh. This distribution is then mapped onto the coarse structured CFD mesh using the algorithm written by Lemire and Vo (2008). The area of each cell in the plasma actuator mesh was conserved by the mapping process to preserve the associated body force. The transferred, body force vectors on the blade mesh is shown in Figure 2.5. The resultant induced body force distribution on CFD mesh was then introduced into the flow solver using a CFX Expression Language (CEL) function.

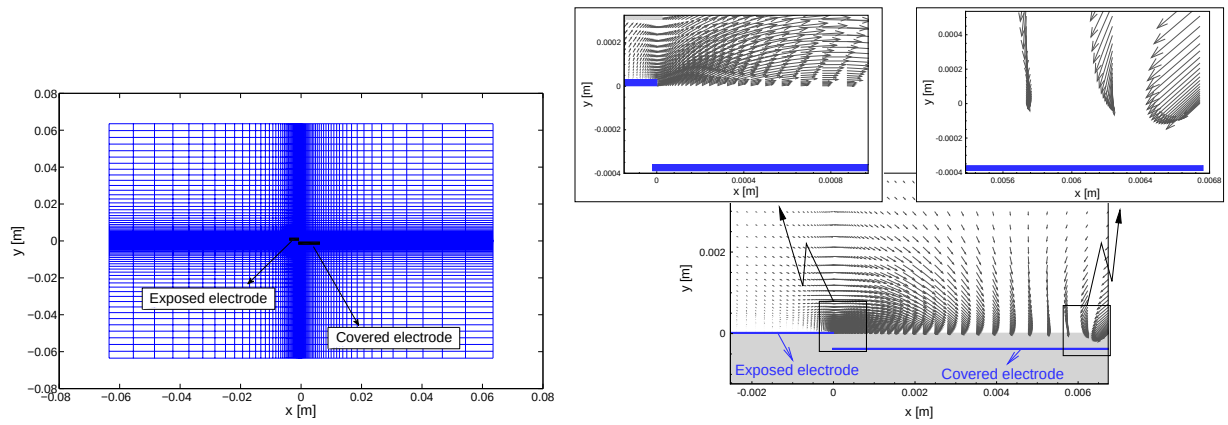

(a) Plasma actuator mesh (b) Time-averaged distribution of the body force

Figure 2.4: Plasma actuator mesh and spatial body force

The plasma actuation can be applied in continuous and pulsed modes. The pulsed plasma actuation was numerically modeled using a pulsing (on/off) frequency (f_{act}) and duty cycle (D). Duty cycle, D, is defined as the ratio of time that the plasma actuator is active (τ) to the pulsing

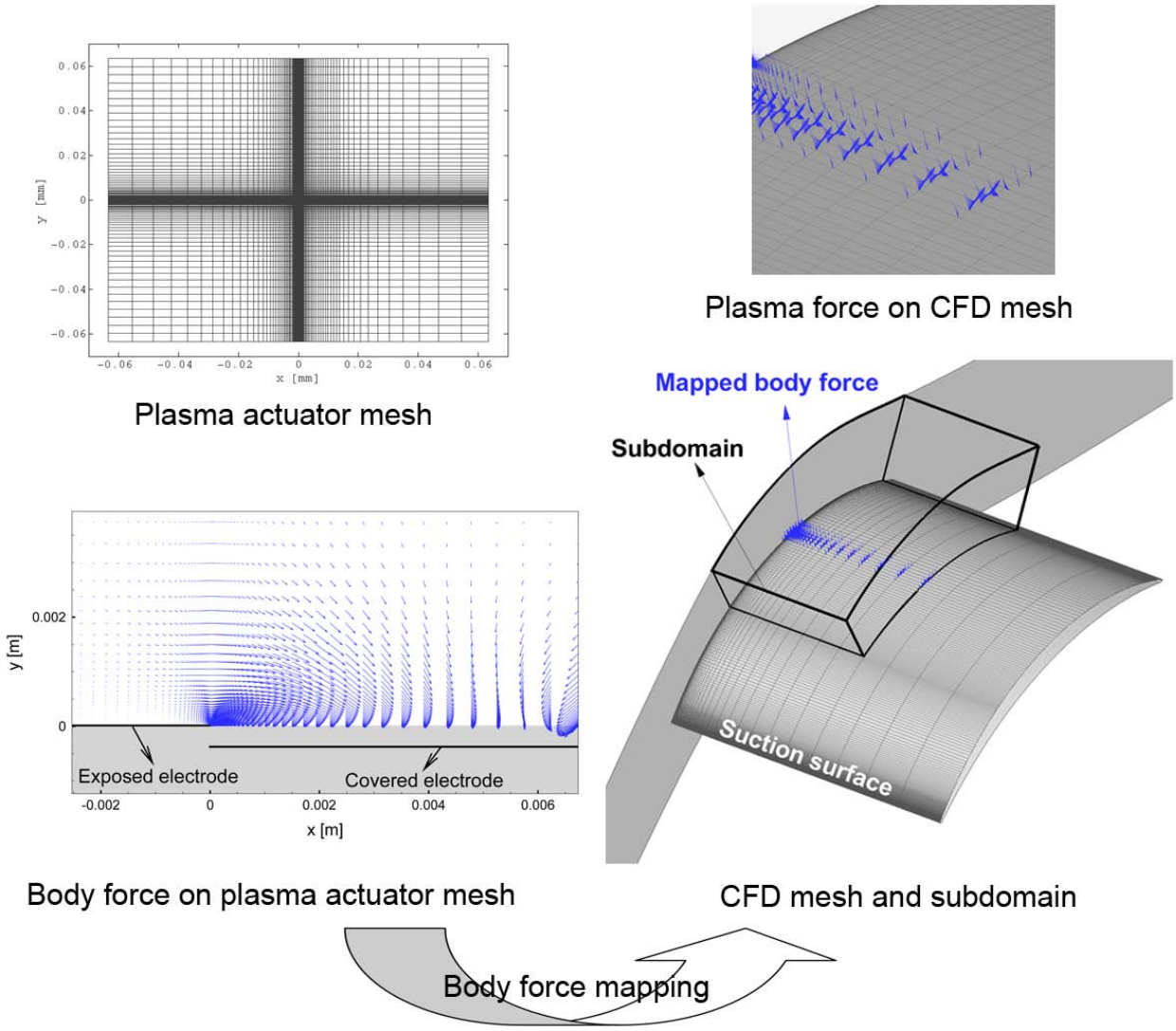

Figure 2.5: Mapping of the spatial body force

period (T). Figure 2.6 shows the numerical implementation of the pulsed plasma actuation. In this figure, the upper plot illustrates the time variation of AC voltage applied on a real plasma actuator. The computationally modeled, pulsed, time-averaged body force variation over time is shown in the lower plot. This approach has been applied in most of the numerical plasma actuation flow control studies such as those by Gaitonde *et al*. (2006b); Vo (2007); Lemire and Vo (2008); Lemire *et al*. (2009). The Strouhal number, based on the separation length and inlet flow velocity, is used to normalize the pulsing frequency.

The body force induced by the plasma actuation is used to give momentum to the air particles on the surface. However, a certain amount of the induced body force is used to overcome the wall shear stress, τ_w. As a results, the remaining portion of the induced body force can be used

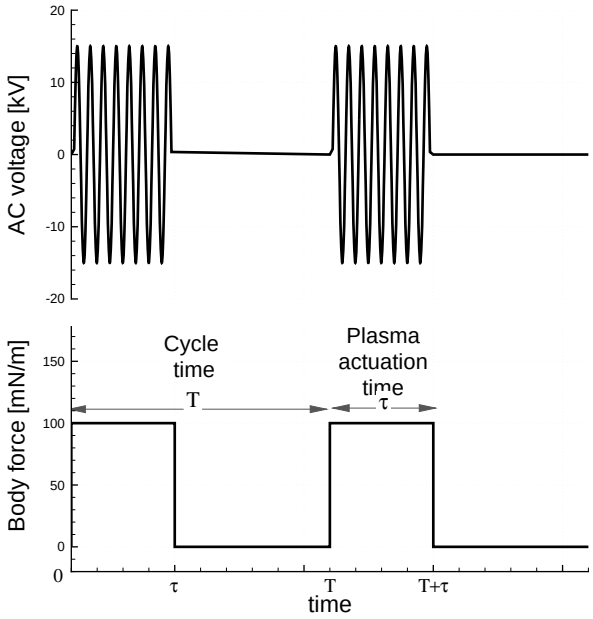

Figure 2.6: Plasma actuator modeling for pulsed actuation

effectively to accelerate the fluid above the surface. In an effort to estimate the magnitude of the shear force relative to the plasma induced force, a plasma actuator was located on the DCA-1 airfoil. The plasma actuation was applied at various plasma strengths at quiescent air ($V_\infty = 0$). The simulation results presented in Appendix A.3 reveal that the wall shear force represents about 22%-25% of the plasma actuator strength.

2.2 Computational Assessment of Flow Control

The computational analysis were carried out to assess plasma actuation flow control for endwall corner separation, blade boundary layer separation and wake/noise suppression. Additional computations were performed to control the corner separation using endwall boundary layer suction.

Unsteady flow solutions were performed for boundary layer separation control and blade wake control computations. The unsteady flow solutions without plasma actuation were initialized with a steady-state flow solution. The unsteady flow solutions were then used as initial condition for the unsteady flow solution with plasma actuation. A time-averaged flow field was obtained after averaging unsteady results over several oscillating time periods following the flow convergence.

2.2.1 Corner Separation Control

To assess plasma actuation flow control for the endwall corner separation on DCA-1 airfoil, computations were performed using the plasma actuator configurations shown in Figure 2.7 at a

Reynolds number of 1.5×10^5. It can be seen that three plasma actuators, two of them on the endwall (at 0.5 chord and 0.75 chord) and one of them on the suction surface (at 0.5 chord), were used. As illustrated, the plasma actuators at 0.5 chord ($F_{act,1}$ & $F_{act,3}$) reside at the upstream of the endwall corner separation and the plasma actuator at 0.75 chord ($F_{act,2}$) resides inside the endwall corner separation region. The endwall plasma actuators ($F_{act,1}$ & $F_{act,2}$) cover approximately half pitch starting from the blade suction surface. The suction surface plasma actuator ($F_{act,3}$) covers approximately 0.3 span starting from the endwall. All plasma actuators were arranged such that the induced plasma actuator force acts in streamwise direction. Table 2.1 shows the configurations studied for the endwall corner separation. In all cases, the plasma actuation was applied in continuous mode.

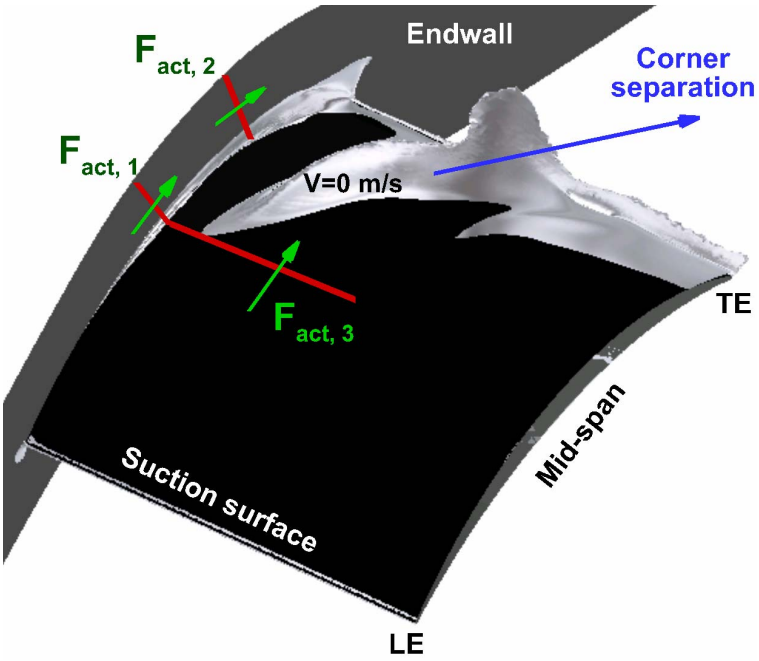

Figure 2.7: Plasma actuator locations for corner separation control

Table 2.1: Configurations studied in plasma actuation endwall corner separation control

Configuration #	Plasma actuator(s)
1	$F_{act,1}$
2	$F_{act,2}$
3	$F_{act,3}$
4	$F_{act,1}$ & $F_{act,3}$

As a reference endwall corner separation control method, the endwall boundary layer suction was studied computationally at a Reynolds number of 1.5×10^5. Three boundary layer bleed mechanisms, namely suction surface holes (SSH), passage holes (PH) and inlet bleed (IB), were used.

As shown in Figure 2.8, these bleed mechanisms were used in various configurations to assess the highest flow control capability in suppressing the endwall corner separation. As listed in Table 2.2, EC-1 configuration corresponds to endwall boundary layer suction flow control using SSH only. In EC-2 configuration, PH are also used. Finally, EC-3 configuration corresponds to the endwall boundary layer suction case with all three suction surfaces (SSH, PH and IB) are open as shown schematically in Figure 2.8(d). The endwall boundary layer suction computations were carried out using various suction slots and holes. The discharge mass flow rate was adjusted to obtain the maximum flow control effectiveness with the minimum discharge flow rate.

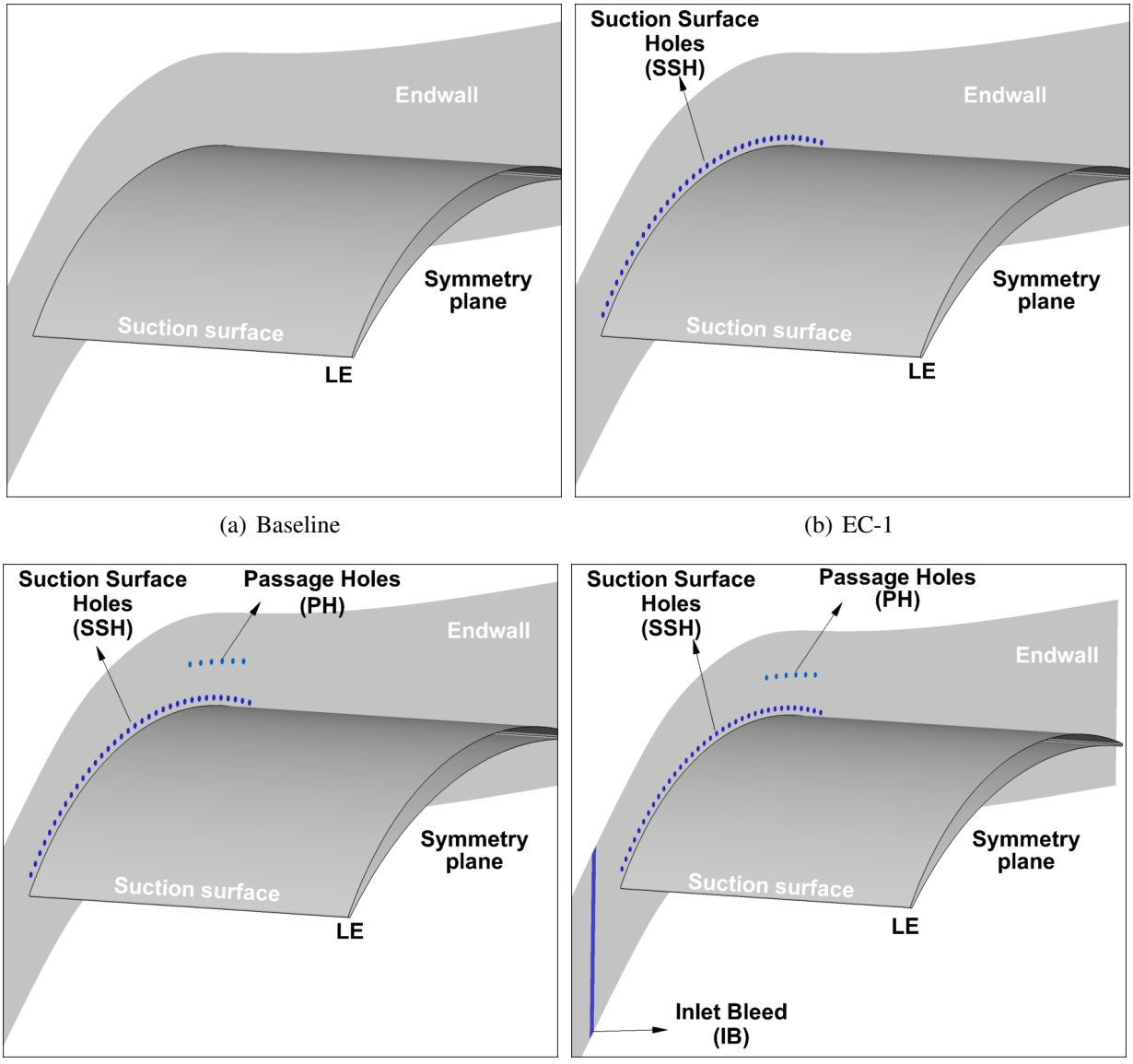

(a) Baseline (b) EC-1

(c) EC-2 (d) EC-3

Figure 2.8: Endwall boundary layer suction flow control configurations

Table 2.2: Cases studied in endwall boundary layer suction flow control

Case	IB	SSH	PH
EC-1	Closed	Open	Closed
EC-2	Closed	Open	Open
EC-3	Open	Open	Open

2.2.2 Boundary Layer Separation Control

For the blade boundary layer flow separation control, an assessment and evaluation of plasma actuation parameters were carried out on DCA-1 blade at a Reynolds number of 1.5×10^5. CFD simulations were performed in 2-D to eliminate the three-dimensional effects of the endwalls. An incidence angle of -1° was used in the simulations. A parametric study was carried for the plasma actuator location, actuation strength, pulsing frequency, duty cycle and actuation mode to determine the plasma actuation effectiveness in controlling the boundary layer flow separation to achieve the maximum pressure rise coefficient. The comparisons were made for the surface pressure, skin friction and boundary layer momentum thickness distributions. The deviation angle, overall total pressure loss coefficient and trailing edge displacement thickness were used to explain plasma actuation effectiveness based on the cascade performance. Contours of the symmetry plane turbulent kinetic energy, vorticity and axial pressure gradient were used to explain flow physics. The plasma actuation power consumption was also considered to determine the plasma actuation efficiency.

Table A.6 in Appendix A.4 shows the cases studied for the parametric study of plasma actuation parameters. As schematically shown in Figure 2.9, the plasma actuation was applied at four locations on the blade suction surface. Plasma actuators 1 and 2, located at 0.15 chord and 0.22 chord, were at the upstream of the separation point. Plasma actuators 3 and 4, residing inside the laminar separation bubble, were located at 0.3 chord and 0.35 chord. The plasma actuation strength was investigated for plasma actuator strengths varying between 50 mN/m and 400 mN/m. The pulsing frequency effect was investigated for 3 frequencies, 388 Hz, 530 Hz and 776 Hz. Then to capture the pulsing frequency in a wider range, the frequency range was extended from 50 Hz to 1000 Hz. The effect of duty cycle was assessed at 5 duty cycle values: 0.1, 0.3, 0.5, 0.7 and 0.9. Finally, the continuous and pulsed actuation results were compared at the same plasma power (Cases 9 and 15 in Table A.6).

2.2.3 Wake/Noise Suppression

For the final concept, an assessment and evaluation of plasma actuation parameters were performed on DCA-2 airfoil for wake/noise attenuation at a Reynolds number of 3.5×10^5. The in-

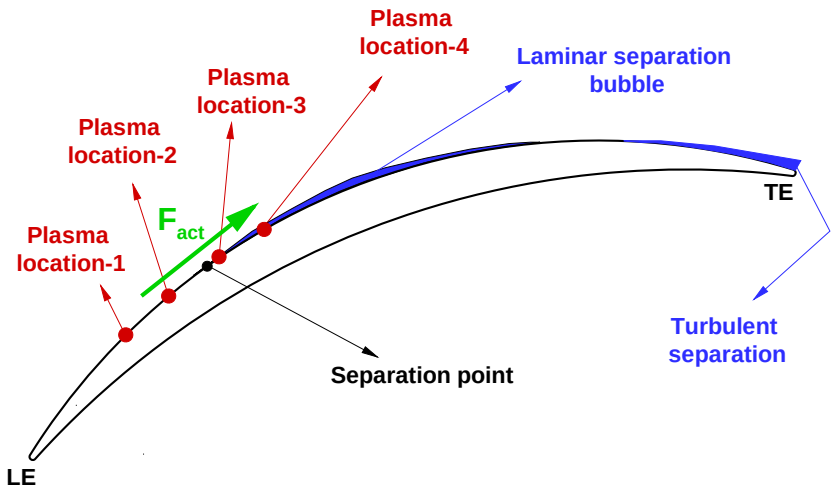

Figure 2.9: Plasma actuator locations for blade boundary layer separation control

cidence angle was set to -1°. Two-dimensional flow simulations were carried out for actuator location, actuation strength, pulsing frequency, duty cycle and actuation mode. Table A.7 in Appendix A.4 lists the plasma actuation parameters used for each case. The plasma actuator location effect was studied using 5 plasma actuator locations (0.65, 0.70, 0.75, 0.80 and 0.85 chord) where the plasma actuators were located on each side of the blade for each case as shown in Figure 2.10. Then, the plasma actuation strength was varied between 50 mN/m and 200 mN/m. The pulsing frequency was investigated over a wide frequency range between 50 Hz and 650 Hz. Duty cycle effect was assessed using values of 0.1, 0.3, 0.5, 0.7 and 0.9. Finally, plasma actuation mode effect was investigated for the same plasma power.

The effectiveness of the plasma actuation was determined based on the wake momentum thickness at 0.2 chord downstream of the blade trailing edge. Total pressure loss coefficient at 0.2 chord downstream of blade trailing edge and time-averaged velocity profiles on the blade surface were used to evaluate the effectiveness of the plasma actuation. Moreover, the contours of TKE and axial pressure gradient were used to explain flow field. The plasma actuation power calculations were performed to evaluate plasma actuation cases from a power point of view.

2.3 Experimental Setup and Measurement Methods

The experimental part of this research project was conducted in a low-speed, linear cascade wind-tunnel at the Gas Turbine Laboratory at National Research Council of Canada. The wind tunnel, test section and cascades are described in Section 2.3.1 and Section 2.3.2, followed by that of endwall bleed arrangement, data acquisition, instrumentation and uncertainties. The pressure measurements were complemented by flow visualizations which is explained in Section 2.3.7.

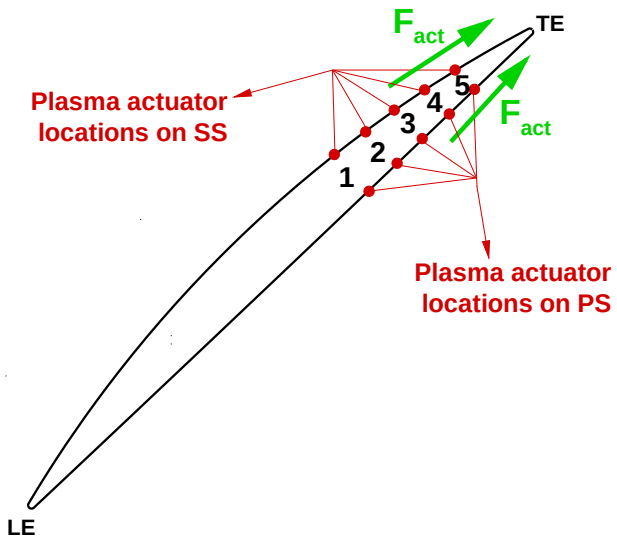

Figure 2.10: Plasma actuator locations for wake/noise attenuation

2.3.1 Low-Speed Cascade Wind Tunnel

The low-speed, open-circuit, blower type cascade wind tunnel is shown in Figure 2.11. The centrifugal blower is driven by a 40 HP AC motor. The air is drawn into the blower through a bell-mouth. A honeycomb section at the diffuser inlet was used to remove any swirl induced by the blower. The diffuser has six evenly-spaced screens used to reduce the turbulence and establish flow uniformity. The flow uniformity was further improved and the turbulent length scale was decreased through seven evenly-spaced screens placed in the settling chamber. The uniform and nearly-stagnant flow from the settling chamber was contracted and accelerated through a rectangular, 14:1 area ratio contraction section.

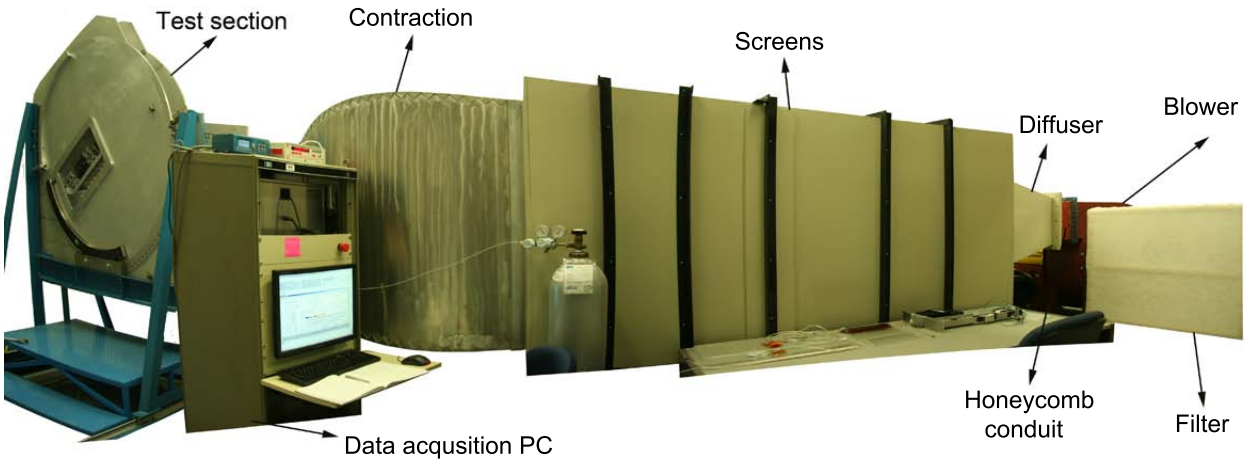

Figure 2.11: NRC low-speed wind tunnel

2.3.2 Test Section and Compressor Cascade

The experimental investigations were carried out in the linear cascade test section shown in Figure 2.12. The rectangular test section inlet has a cross section of 67.7×20 cm. The cascade inlet flow uniformity and outlet flow periodicity were achieved by adjusting tail boards, side flaps, floating wall and boundary layer slots of the test section. The freestream turbulence intensity (FSTI) upstream of the cascade was measured at about 0.3% (Zhang, 2011). Plexiglass/lexan mounting plates on the endwalls allowed for flow visualization and, more importantly, ensured that the test section was electrically insulated for the plasma actuation experiments.

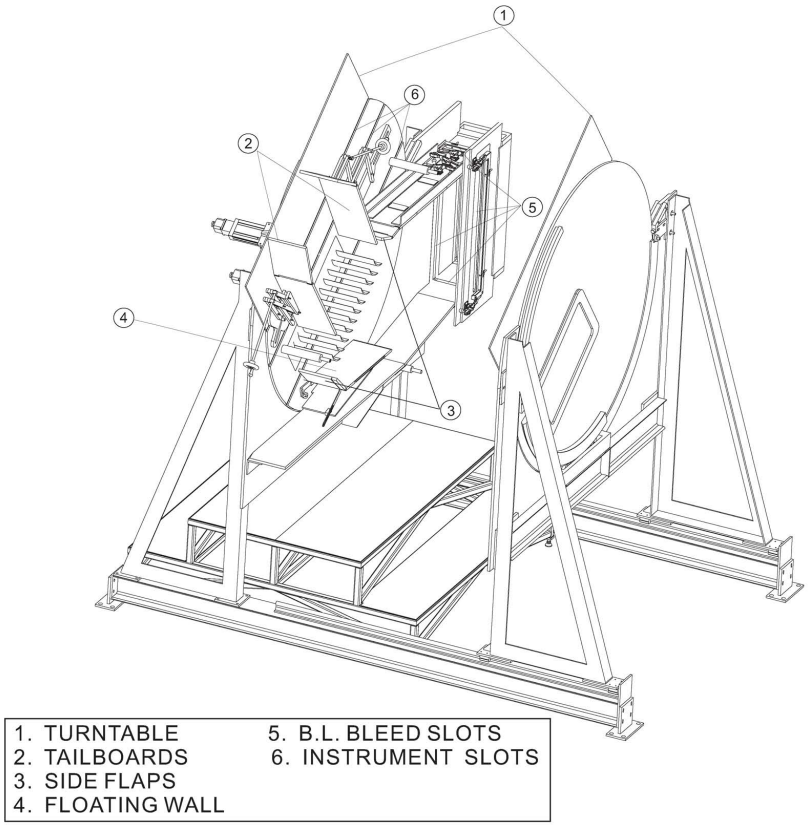

Figure 2.12: Schematic of variable incidence test section

The high flow turning DCA-1 airfoil was used in the experiments. The cascade consisted of 11 DCA-1 blades. Figure 2.13 depicts the DCA-1 cascade and relevant notations. The table in this figure summarizes the cascade key geometric and aerodynamic parameters.

Cascade Flow Quality

Establishing a uniform inlet flow and a periodic outlet flow is essential for cascade testing to ensure the quality of the results. Inlet flow uniformity implies that the inlet flow velocity and

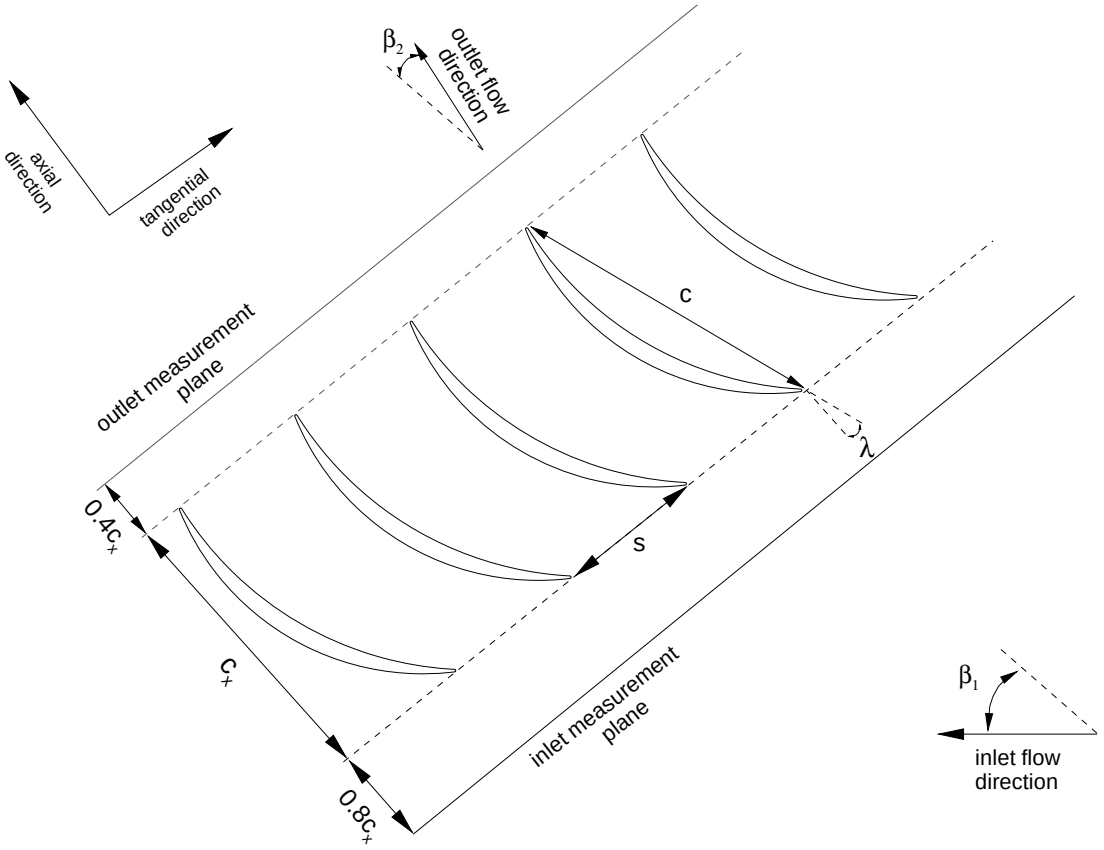

Parameters	DCA-1 cascade
Chord, c [mm]	114.9
Axial chord, c_x [mm]	107.6
Span, h [mm]	200
Pitch, s [mm]	53.4
Solidity, $\sigma = c/s$	2.15
Aspect ratio, h/c	1.74
Inlet metal angle, β_1 [°]	53
Outlet metal angle, β_2 [°]	-12
Stagger angle, λ [°]	20.5
t_{max}/c	0.055
L.E. diameter, d_{LE} [mm]	1
T.E. diameter, d_{TE} [mm]	1

Figure 2.13: DCA-1 cascade geometry and parameters

angle does not change in pitchwise direction over a certain number of passages. The outlet flow periodicity implies a periodic flow in terms of flow velocity, flow angle and total pressure losses at the outlet plane as its name suggests. Inlet uniformity and outlet periodicity is usually achieved through the use of control surfaces inside the test section as previously shown in Figure 2.12. However, this study involved some modifications on the test section which required addition of an extra control surface to achieve cascade flow quality (see Appendix B.1.1).

As shown in Figure 2.14, a good inlet flow uniformity and outlet flow periodicity was established for the baseline as well as for the endwall suction flow control cases after making the modifications in the test section. The details of the cascade flow quality are discussed in Appendix B.1.2.

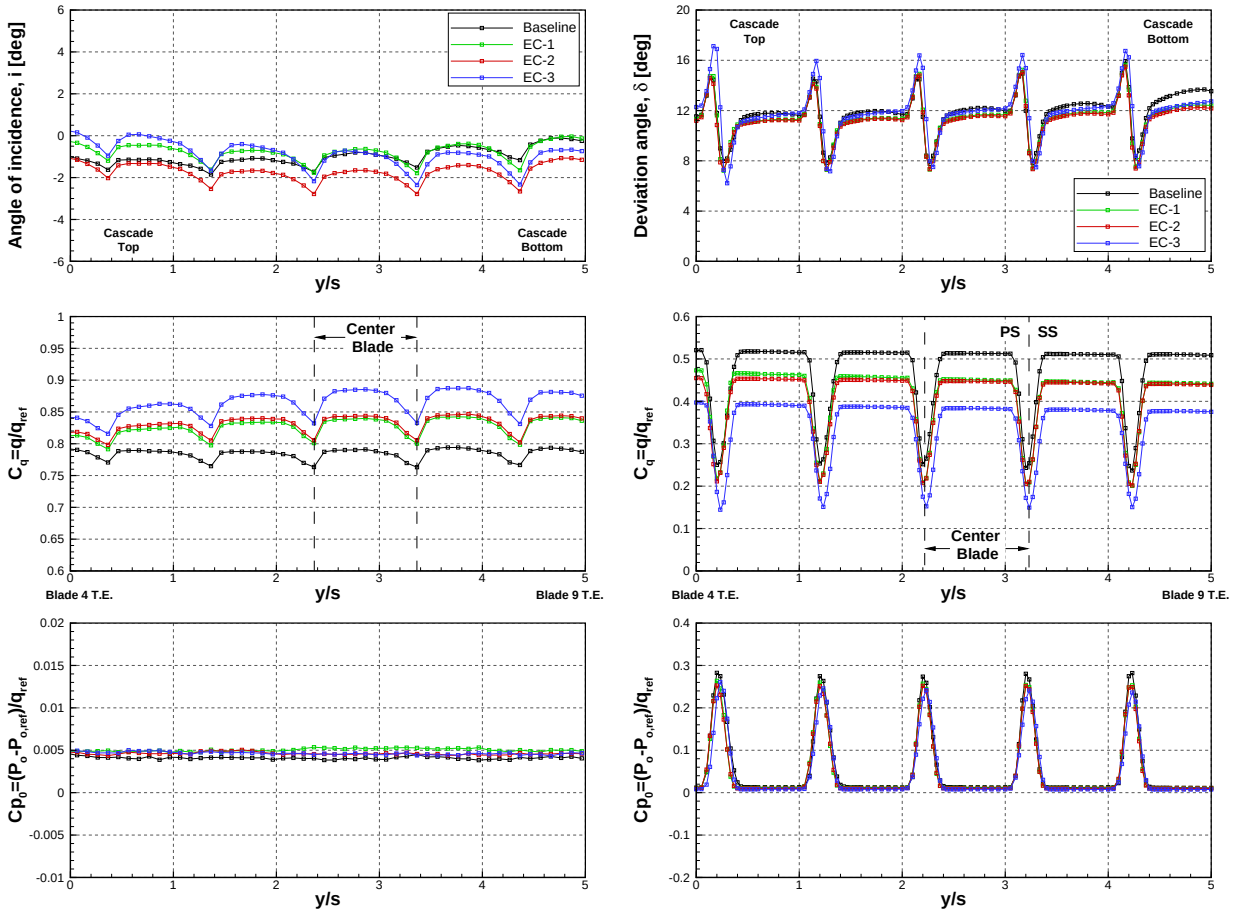

(a) Inlet flow uniformity (b) Outlet flow periodicity

Figure 2.14: Inlet flow uniformity and outlet flow periodicity

2.3.3 Endwall Bleed Arrangement

In this study, endwall boundary layer flow bleed/suction was used to increase flow two-dimensionality and reduce endwall corner separation. As discussed in the literature review in Chapter 1, the flow two-dimensionality is usually achieved using complex systems for the suction of

the endwall boundary layer flow. This increases the cost of the experiments but also adds too much complexity to the cascade flow measurements. As opposed to the complex endwall boundary layer suction method (requiring 10-hp power) followed by Deutsch and Zierke (1987) for the same cascade airfoil, a practical endwall boundary layer suction method was investigated to achieve a two-dimensional flow with the least amount of complexity and minimum bleed mass flow. The design strategy for endwall bleed arrangement was based on the findings observed in the endwall boundary layer suction studies presented in Chapter 1. The studies by Gbadebo *et al*. (2008) and Gmelin *et al*. (2011) suggest that the endwall slot should be close to the blade suction surface where slots located 2% chord away have shown to be successful. Moreover, Gbadebo *et al*. (2008) have proven that the suction slot should start upstream of the dividing streamline on the suction surface. The results presented in Pönick *et al*. (2011) suggest that the bleed slot or cavity inlet surface on the endwall should not be large to avoid negative bleed and highly three-dimensional flow.

Based on the preceding arguments, three separate boundary layer bleed mechanisms (schematically shown in Figure 2.8) were located on each side of the endwalls to improve the flow two-dimensionality, hence eliminating the endwall corner separation. As shown in Figure 2.15(a), the first suction surface is a 5.5% chord wide slot located 11% chord upstream of the leading edge. This slot is called as inlet boundary layer bleed slot and will be referred as IB from now on. Using that slot, the inlet endwall boundary layer thickness was reduced by replacing the low-momentum fluid with the high-momentum core flow. The slot size can be varied using a metal adjusting plate attached to it. In the experiments, the IB slot width was set to 2.2% chord approximately. The second control mechanism, as presented in Figure 2.15(b), includes 35 holes on the endwall with 1.38% chord diameter drilled at a 1.75% chord away from the blade suction surface covering the whole length of the chord, referred as the suction surface holes (SSH). These holes were used to ingest the low-momentum endwall fluid coming from pressure side and ending up at the junction of the endwall and blade suction surface. The last endwall control mechanism, referred as the passage holes (PH), was comprised of 6 holes (having the same size with SSH) located approximately 25% pitch away from the blade suction surface. These holes were used to increase the strength of the dividing streamline on the endwall in an effort to reduce the amount of cross flow moving towards to the suction surface. The method of mass flow measurements for the endwall bleed arrangement is presented in Appendix B.1.3.

2.3.4 Data Acquisition

The computerized/automated data acquisition system consisted of a PCI card, installed on a windows based personal computer, and an in-house data acquisition software, named TurboDAQ. The pressure probe data acquisition and control of traverse mechanism for pressure probe traverses

(a) Suction surface IB

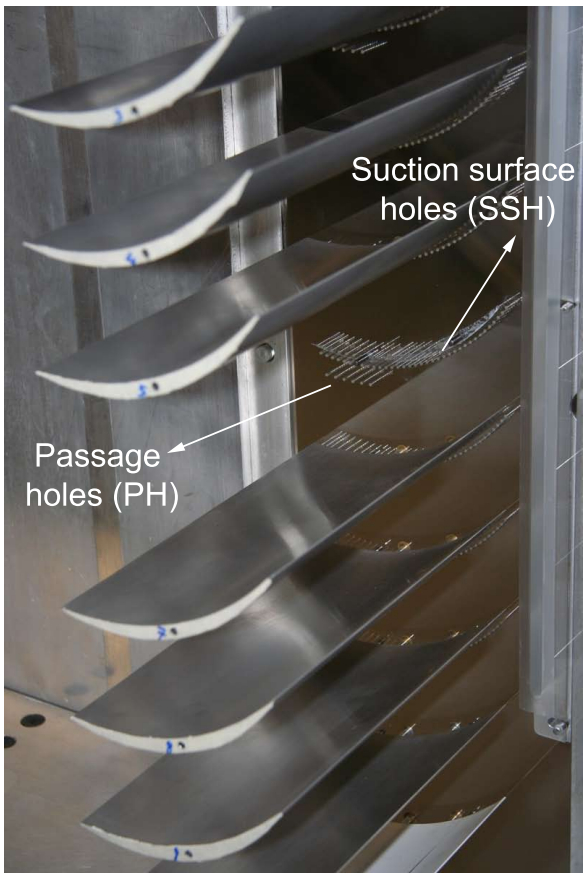

(b) Suction surfaces SSH and PH

Suction surface	Type	Number (on each endwall)	Size	Location
IB	Slot	1	width=2.2% chord	11% upstream of LE
SSH	Hole	35	ϕ=1.38% chord	1.75% chord away from SS
PH	Hole	6	ϕ=1.38% chord	25% pitch away from SS

Figure 2.15: Boundary layer suction surfaces

were accomplished through TurboDAQ.

Two pressure scanners, Model DSA3217, with a range of ±1250 Pa and ±2500 Pa were used to measure pressure from 16 independent, temperature compensated piezoresistive pressure sensors. The calibration capability of DSA3217 eliminated sensor zero drifts with a long term accuracy of $\pm 1.5Pa$ and $\pm 2.5Pa$ for low range (±1250) and high range (±2500) pressure transducers, respectively. All measurements were performed using the lower range (±1250) pressure scanner except endwall boundary layer bleed measurements where measured pressures were higher. The DSA3217 pressure scanner was calibrated using a GE Druck DPI 615 pressure calibrator prior to use (see Appendix B.2). The pressure calibrator has an accuracy of 0.025% of full scale for ranges 1 to 10000 psi.

Two static pressure taps, P_{c1} and P_{c2} at the inlet and the outlet of the contraction section, were used to determine wind tunnel operating pressure. The pressure data measured from each channel was referenced to the wind tunnel static pressure, P_{c2}. The pressure data was non-dimensionalized by the wind tunnel dynamic pressure, $P_{c1} - P_{c2}$. Before acquiring the pressure data, a running average study was performed to determine the required sampling time. Figure 2.16(a) shows total pressure contours from seven-hole pressure probe measurements. The running average study was performed for the critical locations shown in this figure. The data was acquired at a rate of 100 samples/second/transducer and averaged. Figure 2.16(b) shows the non-dimensional pressure data for the seven-hole probe channel 7. The results suggested that when the sampling number is larger than 1000 (corresponding to a data acquisition time of 10 sec), a repeatable measurement data can be obtained.

Based on the running average studies, the total sampling time at each measurement was set to 25 seconds for each channel during the three-hole and seven-hole pressure probe traverses. Although running average studies showed small deviations in the averaged data for various sampling numbers, the sampling time was reduced to 5 seconds for the plasma actuation experiments to prevent degradation and, even worse, breaking of dielectric material. During the surface static pressure measurements, the sampling time was set to 60 seconds. In all cases, the pressure data were acquired at 100 samples/second/transducer.

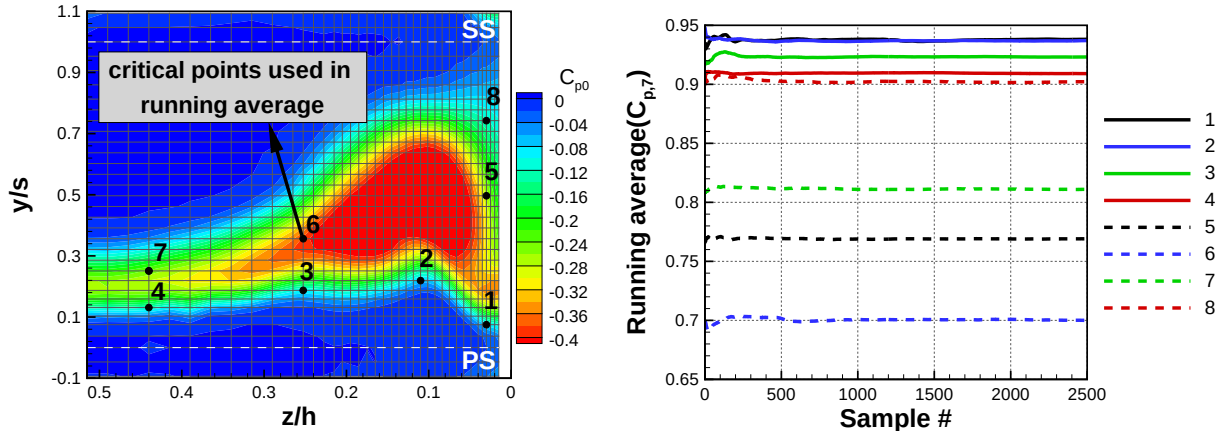

(a) Points used in the running average study

(b) Running average results

Figure 2.16: Running average results for the pressure measured by seven-hole probe channel 7

The dynamic pressure term $C_{q_{wt}}$ represents the wind tunnel calibration coefficient, calculated from normalizing the inlet mid-span dynamic pressure with the wind tunnel dynamic pressure as follows:

$$C_{q_{wt}} = \frac{q_{CL}}{P_{c1} - P_{c2}} \tag{2.2}$$

The inlet dynamic pressure $q_{CL} = P_{0_{CL}} - P_{CL}$ was measured using three-hole probe traverses

at the mid-span. The discussion of the measurement results will be presented in Appendix B.1.2. Similarly, the wind tunnel calibration coefficient for the total pressure, $C_{0_{wt}}$, is defined as:

$$C_{0_{wt}} = \frac{P_{0_{CL}} - P_{C1}}{P_{c1} - P_{c2}} \tag{2.3}$$

2.3.5 Instrumentation

Figure 2.17 presents a schematic of the test section with the instruments. The model, measurement range, purpose and accuracy of each instrument is listed under the figure. As illustrated in the figure, the inlet plane three-hole probe and outlet plane seven hole probe measurements were performed at 0.8 axial chord upstream of the blade leading edge and 0.4 axial chord downstream of the blade trailing edge, respectively. Pressure probes were calibrated in an in-house probe calibration rig (see Appendix B.3).

Barometer and Thermometer The ambient pressure and ambient temperature were recorded using a barometer and thermometer, respectively. These measurements were carried out to determine the operating Reynolds number. The Reynolds number was defined as:

$$Re = \frac{\rho V_1 c_x}{\mu} \tag{2.4}$$

where ρ and μ are the test section density and viscosity, calculated based on the tunnel static pressure and temperature. The test section inlet flow was essentially incompressible within the target velocity range. The test section inlet velocity was calculated from the tunnel contraction pressure $P_{c1} - P_{c2}$, such that:

$$V_1 = \sqrt{\frac{2C_{q_{wt}}(P_{c1} - P_{c2})}{\rho}} \tag{2.5}$$

Pitot-Tube A gooseneck pitot-tube with 0.75 mm outer diameter (approximately 4.3% of the endwall boundary layer thickness) was used to measure the endwall boundary layer thickness. As shown in Figure 2.17, the spanwise traverses were made 1.7 c_x upstream of the central blade extending from endwall to the mid-span. The velocity profiles were calculated based on the static pressure measurements performed using the static tap located on the plexiglass endwall. The same probe was also used during the endwall bleed/suction mass flow rate measurements to determine the velocity profile inside the pipe.

Pitot-Static Tubes Two pitot-static tubes, with 1.65 mm outer diameter, were used to measure flow velocity to predict the endwall bleed/suction mass flow rate (see Appendix B.1.3).

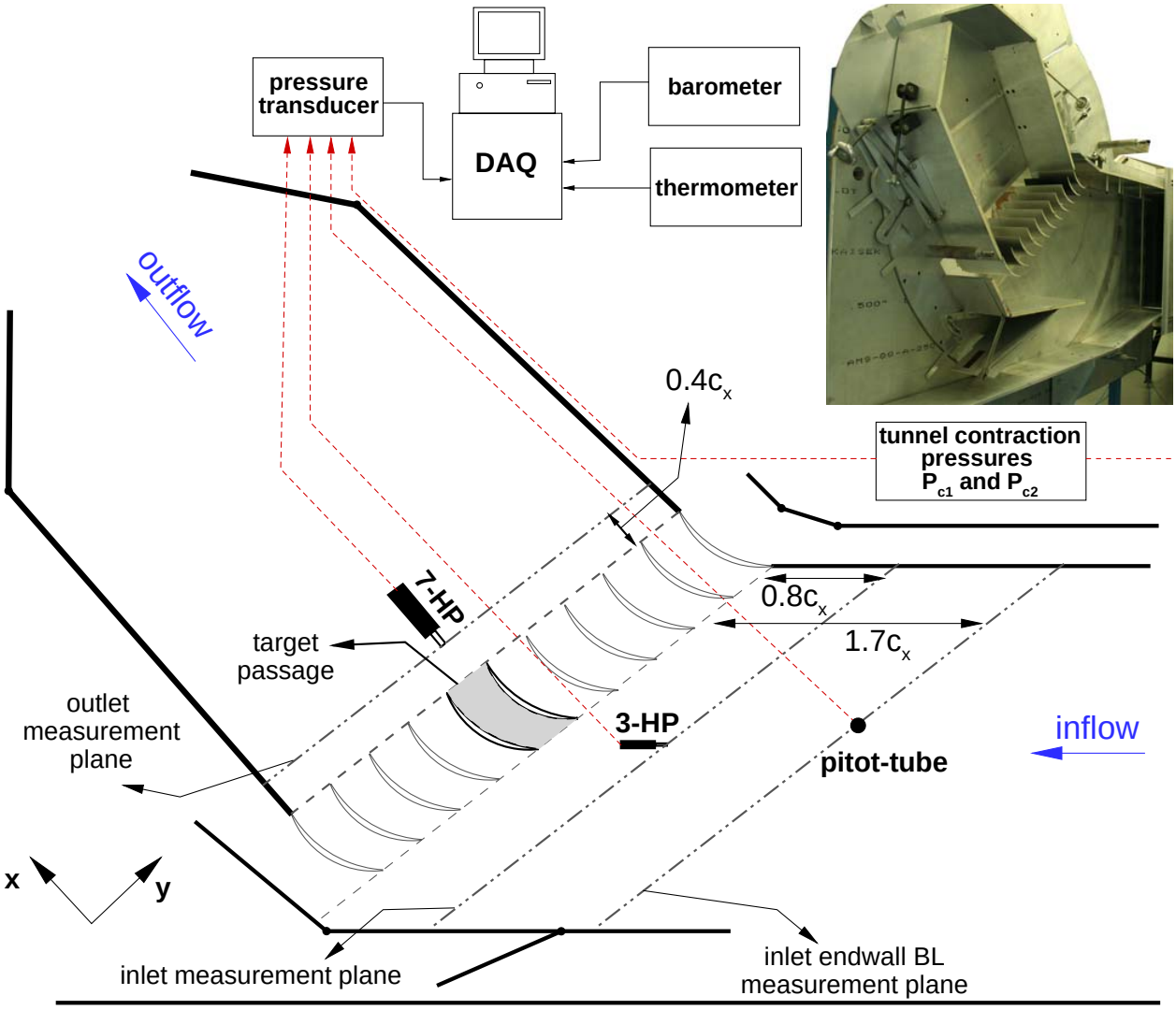

Instrument	Model	Measuring range	Target data	Accuracy
Barometer	GE Druck DPI 142	345 kPa	P_{amb}	±0.01% FS
Thermometer	Guildline Model 9540	10°C-40°C	T_{amb}	±0.03°C
Pitot-tube	-	-	δ	-
Pitot-static tube	-	-	$\dot{m}_{bleed}$	-
Three-hole probe	-	±20°	$P_1, P_{0,1}, \alpha_1$	See Table 2.3
Seven-hole probe	-	±44°	$P_2, P_{0,2}, \alpha_2, \beta_2$	See Table 2.3
Instrumented blade	-	-	C_p	See Table 2.4

Figure 2.17: Schematic of experimental setup

Three-Hole Pressure Probe A three-hole wedge probe was used to determine inlet flow uniformity at mid-span of the cascade. The geometry of the probe is shown in Figure 2.18(a). The probe consists of three stainless steel tubes soldered into each other in a two-dimensional plane. The side tubes had 45° wedge. The 2.25 mm width probe tip corresponded to 4.2% of the blade pitch. A digital protractor (Pro 360) with an accuracy of ±0.1° was used to for three-hole alignment. The probe calibration and data reduction procedures are given in Appendix B.4.1. The data reduction routine includes Reynolds number interpolation.

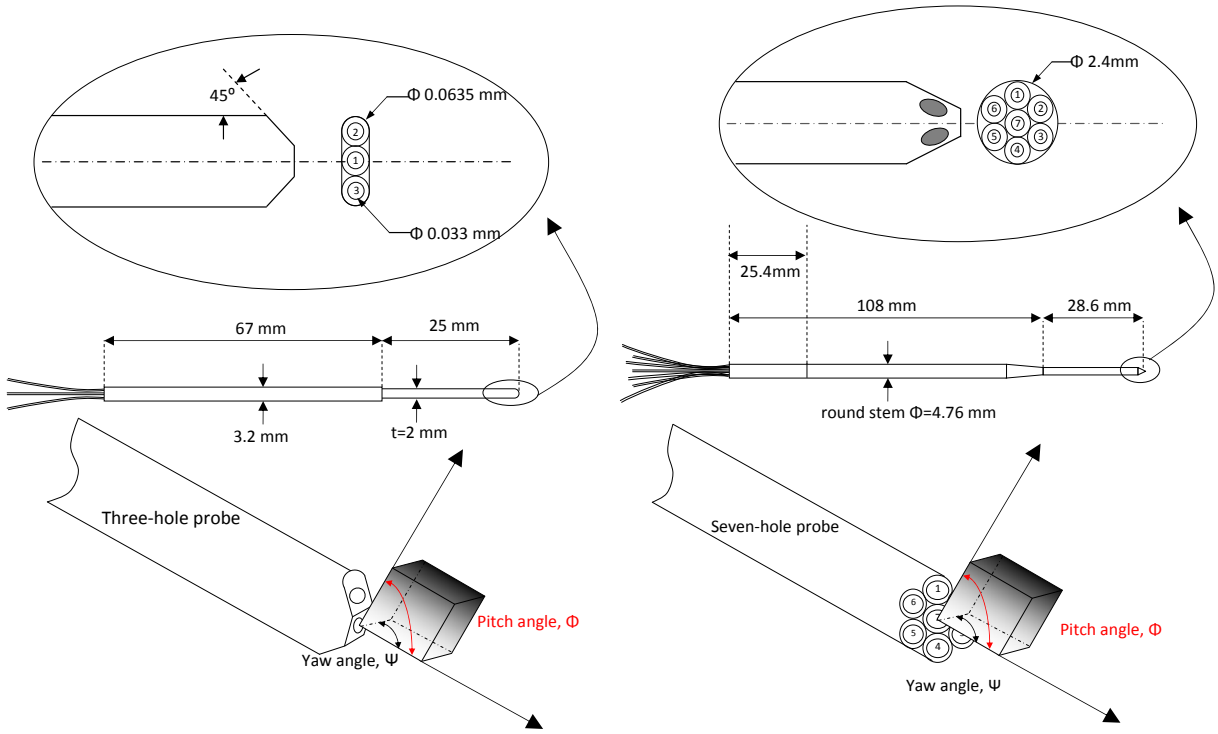

(a) Three-hole pressure probe (b) Seven-hole pressure probe

Figure 2.18: The schematics of pressure probes

Seven-Hole Pressure Probe In an effort to determine the characteristics of the three-dimensional flow field at the outlet measurement plane, a seven-hole probe with an outer diameter of 2.4 mm (corresponding to 4.5% of the blade pitch) was used in non-nulling mode. The probe geometry is shown in Figure 2.18(b). The probe is made of seven stainless steel tubes.

Measurements at the outlet plane has shown that the velocities at the downstream of the trailing edge varies significantly. To minimize the errors due to Reynolds number disparity, the probe was calibrated at various Reynolds numbers. The data reduction was performed by carrying out Reynolds number interpolation. The seven-hole probe alignment was performed using the digital protractor. The details for the probe calibration and data reduction procedures can be found in Appendix B.4.2.

Instrumented Blades Blade surface static pressure measurements were performed using two blades instrumented with arrays of static pressure taps. As shown in Figure 2.19(a), the lower and upper blades were instrumented with pressure taps on the suction and pressure surfaces, respectively. As illustrated in Figure 2.19(b), the lower instrumented blade had a pattern of 24 static taps in chordwise direction, repeated 4 times in spanwise direction. The spanwise taps were at 7.5%, 15%, 30% and 50% blade span. The upper blade was instrumented in the same manner with 10 static pressure taps in chordwise direction repeated 4 times in spanwise direction. The spanwise and chordwise locations of the pressure taps are given as a table in Appendix B.5.

The surface static pressure, P_{tap}, measurements were made with reference to P_{c2} and normalized by the wind tunnel dynamic pressure as follows:

$$C^*_{p,tap} = \frac{P_{tap} - P_{c2}}{P_{c1} - P_{c2}} \tag{2.6}$$

Then, $C^*_{p,tap}$ was corrected by referencing it to the test section inlet static pressure, P_{si}, and normalized with the inlet dynamic pressure, $P_{0i} - P_{si}$, such that:

$$C_{p,tap} = \frac{P_{tap} - P_{si}}{P_{0i} - P_{si}} = \frac{C^*_{p,tap} - C_{s_{wt}}}{C_{q_{wt}}} \tag{2.7}$$

where $C_{s_{wt}} = C_{0_{wt}} - C_{q_{wt}}$.

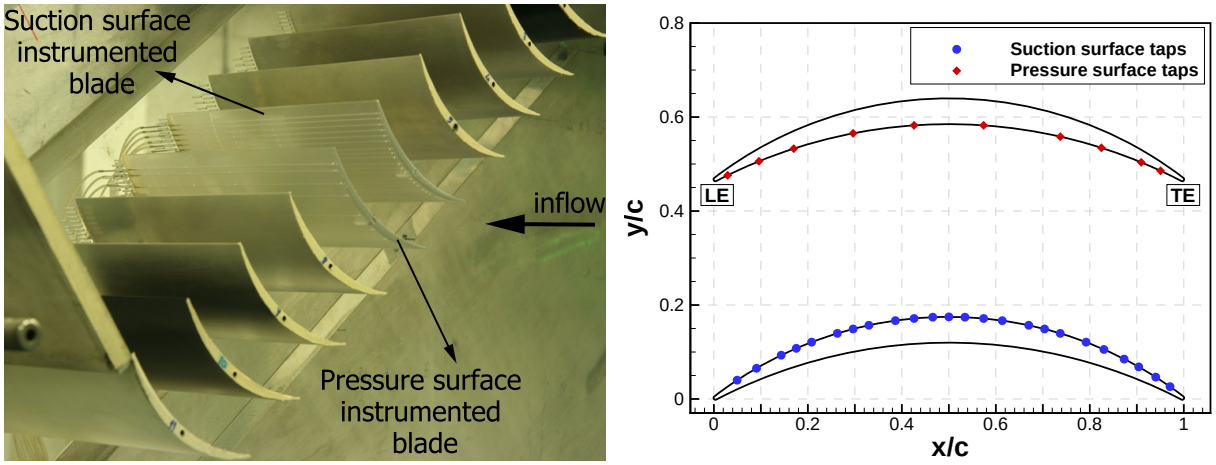

(a) Instrumented blades inside the test section

(b) Surface static pressure tap locations

Figure 2.19: Instrumented blades for surface static pressure measurements

2.3.6 Uncertainties

The experimental measurements are approximations or estimates of a quantity; therefore, they should be displayed with their uncertainty or error band. The uncertainties in an experimental measurement can arise due to bias error and a random error. Bias error (related to accuracy) refers

to deviation from the actual value of measured quantity in many separate measurements. The random error (related to precision) are encountered when making repeated measurements.

In wind tunnel measurements, single sample analysis by Moffat (1982) is the most used method for uncertainty analysis. In this method, the bias errors are ignored and introduced in the form of calibration errors. The random errors are estimated using data collected over a series of experimental measurements. The standard deviation (σ) is calculated for any measured quantity. Using a 95% confidence level, the calculated error resides in $\pm 2\sigma$.

In this experimental study, all uncertainty estimates are given at 95% confidence level. The error arising from each component is combined using the "root-sum-of-squares" (RSS) by the method defined by Kline and McClintock (1953). The uncertainty of a dependent flow quantity F is calculated using RSS of all effects on that variable as such:

$$\delta F = \pm \sqrt{\sum_{n=1}^{N} \left(\frac{\partial F}{\partial fn} \delta f_n \right)^2} \tag{2.8}$$

where F is a function of N independent flow variables, F=F(f_1,f_2,...,f_n).

The sum of errors due to pressure transducer uncertainty, measurement repeatability and calibration repeatability were combined using RSS method for three-hole pressure probe and seven-hole pressure probe. Table 2.3 presents the uncertainty results for total pressure, dynamic pressure and flow angle. The uncertainties in the measured dynamic and total pressures were estimated with respect to the reference dynamic pressure. Moreover, the uncertainties in the AVR, C_p, ω_0 and bleed mass flow rate (m_{bleed}/m_{inlet}) measurements are listed in Table 2.4.

Table 2.3: Pressure probe uncertainties

Flow field parameter	Uncertainty interval 3-HP	7-HP
Total pressure	±0.9%	±0.9%
Dynamic pressure	±1.5%	±1.3%
Flow angle	±1.0°	±1.1°

2.3.7 Flow Visualization Technique

In this study, surface oil-film flow visualization technique was applied to demonstrate the flow features over the airfoil surface and the endwalls. The oil flow visualization provides further insight into development of three-dimensional flow over the solid walls. For a steady flow, the streaklines become the same as streamlines and pathlines. Therefore, the oil flow pictures obtained from

Table 2.4: Uncertainty of calculated parameters

Parameter	Uncertainty interval
AVR	±0.02
C_p	±0.03
ω_0	±0.01
m_{bleed}/m_{inlet}	±0.2%

the experiments were compared with the streamlines obtained from the steady state computations to validate the computational results. Once the confidence was gained for the accuracy of the computational results, further understanding for the three-dimensional flow structures was obtained using the power of computational post processing tools.

The following procedure was used during the oil-film flow visualization study. Initially, the cascade airfoil was covered with a 0.0035 inches of thick matte black paper. Then, a mixture of 15W-40 motor oil and linseed oil and white titanium dioxide powder, (TiO_2) was applied on the surface. The run time was kept sufficiently long to avoid any variation in the streaklines after stopping the wind tunnel (Merzkirch, 1987). The attempts to obtain a good picture of flow pattern have shown that 1.5 to 2 hours of wind tunnel running time gives a meaningful data. After stopping the wind tunnel, the established surface oil flow streaks were photographed as quickly as possible.

2.4 Design and Integration of Plasma Actuators

In this section, the plasma generation system is briefly described in Section 2.4.1. It is followed by the plasma actuator setups used in the experiments.

2.4.1 Plasma Generation Setup

A plasma generation system consisting of a signal generator, power amplifiers, resistor module, and transformers was used in the plasma flow control experiments as shown in Figure 2.20. The signal generator forms the AC signal including sine, square, triangle and sawtooth waveforms. This signal was amplified by two power amplifiers. A resistor module connected to the power amplifiers. Then, a transformer with a 360:1 turn ratio was used to obtain high voltage ($\sim 10kV$).

The voltage applied on the plasma actuator system was measured by a voltage probe connected to the electrode. The current was measured with a current monitor. The voltage and current signals were acquired by a NI DAQ card and the data was monitored by a digital oscilloscope. The power dissipated by the plasma actuator was calculated by point-by-point integration of the instantaneous product of voltage and current over many AC cycles (20 AC cycles was found to be enough).

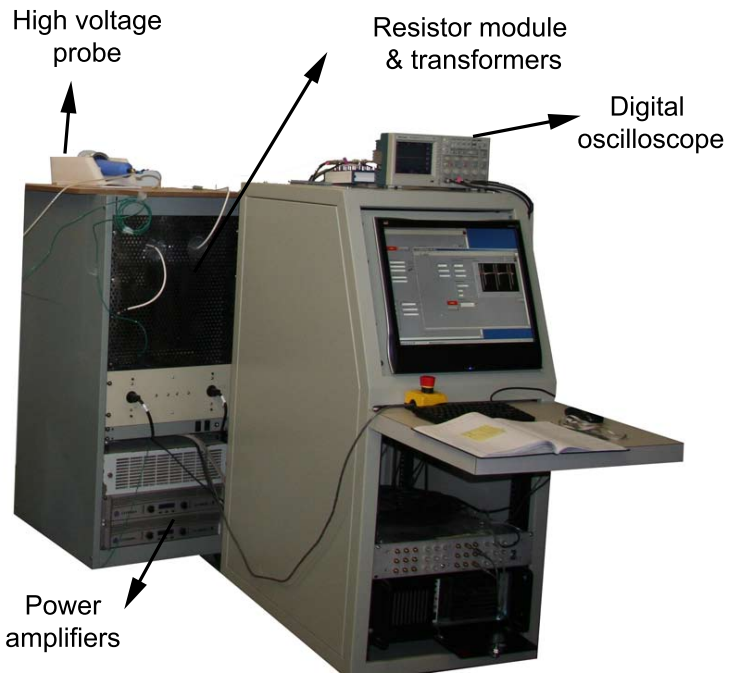

Figure 2.20: A picture of the plasma Generation System

2.4.2 Plasma Actuators

The plasma actuation flow control experiments were carried out using two plasma actuation setups located inside the compressor cascade test section to control the endwall corner separation and boundary layer separation. In all cases, the covered electrode was charged and the exposed electrode was grounded to avoid high voltage discharge to pressure probes used for downstream measurements. The metal parts (screws and pins) used to hold blades were replaced with the plastic ones to avoid any discharge. The electrical properties of the materials used as the dielectric barrier are shown in Table 2.5. As discussed in Section 1.4.2, the plasma actuation strength can be increased by an order of magnitude using Teflon (due to its lower dielectric constant) instead of Kapton as the dielectric material. However, such a small scale compressor blade could not be manufactured out of Teflon due to machining difficulties. Therefore, the blades were manufactured using rapid prototyping using a SLA material Accura ® 60. The exposed electrode was located on the suction surface and covered electrode was located on the pressure surface. Therefore, the blade used as the dielectric material. For the endwall, a slot is cut into the plexiglass endwall and a Teflon insert is located inside. As can be seen from the table, Kapton has a very large breakdown voltage compared to Accura ® 60 and Teflon. Hence, the surface of the dielectric materials were covered with a layer of 0.002 inch thick Kapton® tape to slow down the dielectric material degradation problem and protect the material against an electrical breakdown. The upstream of the exposed electrode was covered with a layer of 0.005 inch thick Kapton® tape to avoid plasma formation in

the counter-flow direction. The covered electrode was sealed under 5 layers of 0.005 inch thick Kapton® tape to prevent plasma formation on the pressure surface. The gap between the exposed and covered electrodes was approximately 2 mm based on the parametric study performed by (Roth and Dai, 2006). The electrode thickness was minimized using a 0.005 inch thick copper foil tape to increase the actuation strength Enloe *et al*. (2004); Hoskinson *et al*. (2008); Corke *et al*. (2009). A covered electrode with 1 inch width was used in an effort to increase the plasma actuation strength as suggested by (Thomas *et al*., 2009).

Table 2.5: Electrical properties of the materials

Material	Dielectric constant, ε_r	Breakdown voltage [kV/mm]
Kapton®	3.5	154
Accura ® 60	3.5	13.2
Teflon	2.1	11.2

Plasma Actuator Configuration for Endwall Corner Separation Control

For the corner stall control, two plasma actuators were used, one placed on the endwall and the other placed on the blade suction surface. As shown for the endwall plasma actuation setup in Figure 2.21, a slot is cut into the plexiglass endwall covering almost a passage area into which a Teflon insert is placed. A 0.5 inch width covered electrode remained under the Teflon dielectric. A 0.125 inch wide exposed electrode located on the Teflon covers 0.5 pitch starting from the junction of endwall and blade suction surface. For the plasma actuator mounted on the suction surface, the exposed electrode was located on the blade suction surface at 0.5 chord and the covered electrode was located on the pressure surface. The 0.125 inch wide exposed electrode on the blade suction surface covers almost the entire span and is connected to the ground cable from the other endwall. A 1 inch wide covered electrode extends from 0.05 span to 0.35 span. Therefore, the effective plasma actuator region extends from 0.05 span to 0.35 span as shown with the green line in the figure. The induced plasma actuation force is directed in the downstream direction. The thickness of the blade was approximately 0.25 inch at the plasma actuator location. Figure 2.22 shows a picture where the plasma formation can be seen both on the endwall and on the suction surface.

Plasma Actuator Setup for Boundary Layer Separation Control

Figure 2.23(a) shows the plasma actuator configuration for the boundary layer separation control. It can be seen that the plasma actuator was located on the pressure tap instrumented blade to carry out surface static pressure measurements. The electrodes did not cover the full span to avoid electrical discharge from the edges of the blade. The exposed electrode, 0.125 inch wide

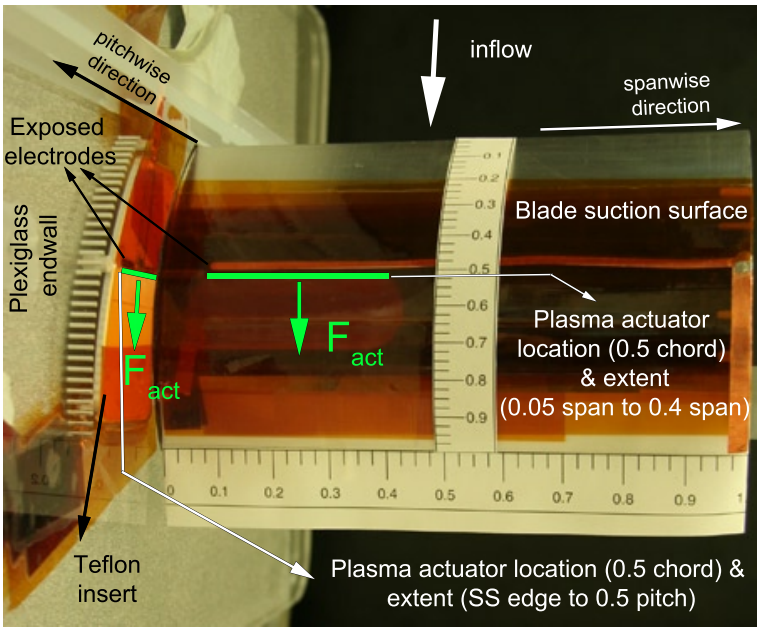

Figure 2.21: Plasma actuator configuration for corner stall control

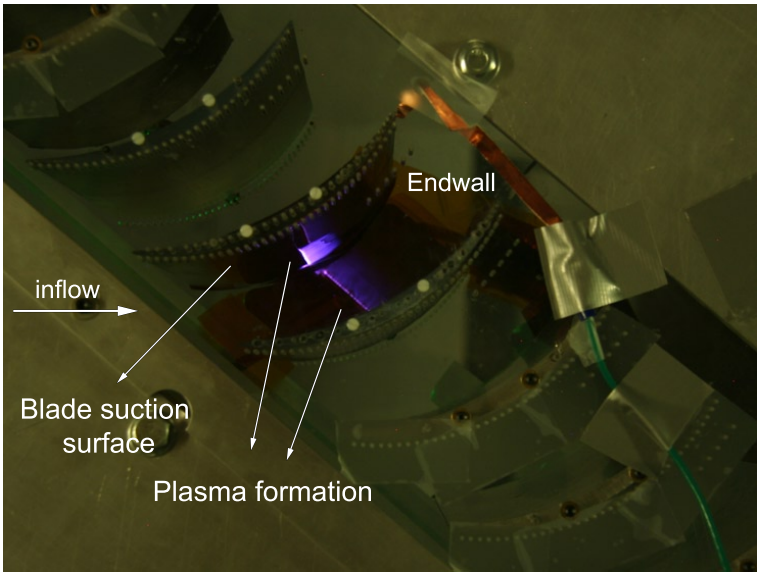

Figure 2.22: Plasma formation for corner stall control configuration

and 5.5 inch long, was mounted on the blade suction surface at 0.25 chord. The exposed electrode covers 0.65 span extending from 0.25 span to 0.90 span. The covered electrode, 1 inch wide and 4 inch long (covering from 0.25 span to 0.75 span), was mounted on the blade pressure surface. As shown with the green line in the figure, the effective plasma actuator region extends from 0.25% span to 0.8 span. The thickness of the blade was less than 0.25 inch at the plasma actuator location. As shown in Figure 2.23(b), the cables connecting the electrodes to the plasma generation system were passed through the holes drilled on the plastic endwalls. Figure 2.23(c) shows the final plasma actuation setup where a distance was maintained between the exposed electrode cable and metal needles (used for wall static pressure measurements).

Since the blade has a thickness of less than 6 mm at the plasma actuator location, a parametric study was carried out experimentally to determine the plasma actuator setup effect on the blade surface pressure distribution. As discussed in Appendix C.4, three thicknesses (0.0075 inch, 0.0105 inch and 0.0135 inch) of rectangular surface trips were located at three chordwise locations of the instrumented blade suction surface. Measurements have shown that a protrusion greater than 0.0075 inch would trip the boundary layer. Figure 2.24 depicts the plasma actuator setup located on the suction surface which has a 0.0105 inch thickness, which would trip the boundary layer and cause an early turbulent reattachment. This result suggests that the plasma actuator should be flush-mounted to the airfoil surface to eliminate or minimize the actuator setup aerodynamic effect. This may be practically possible for a real size fan blade; however, the current blade size did not allow such a flush-mount. The plasma actuator setup could not be recessed in the suction surface since blade thickness was already too small to obtain enough plasma actuation strength. In order to minimize the boundary layer tripping effect of the plasma actuator setup, two grooves (leading edge and trailing edge grooves), were introduced to the blade suction surface as schematically depicted in Figure 2.24. These grooves were used to reduce the size of the forward and backward steps, where positive and negative steps were introduced at the plasma actuator leading and trailing edges, respectively.

The leading edge groove was located just downstream of the second pressure tap (see Figure 2.24) on the suction surface approximately at 0.1 chord to make plasma actuator leading edge flush with the blade surface. The trailing edge groove, representing the plasma actuator location, was located approximately at 0.25 chord, just upstream of the sixth pressure tap. As mentioned earlier, the blade suction surface was covered with a layer of 0.002 inch thick Kapton® tape to protect the blade material. The pressure taps were re-drilled before mounting the blade inside the test section.

The plasma actuation strength was estimated for each plasma actuator setup through force measurements obtained using a scale. The details of the force measurements are given in Appendix B.6.

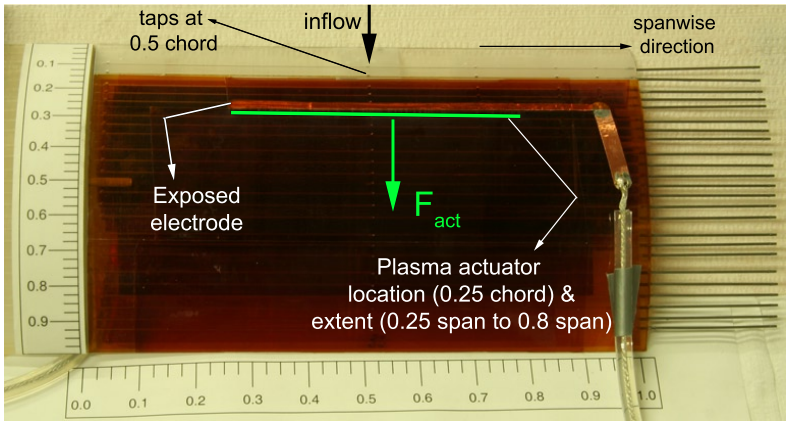

(a) Plasma actuator mounted on instrumented blade

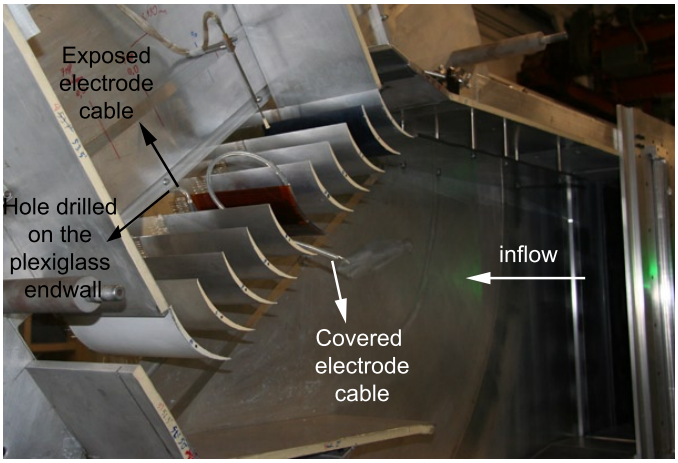

(b) Plasma actuator mounted blade inside the test section

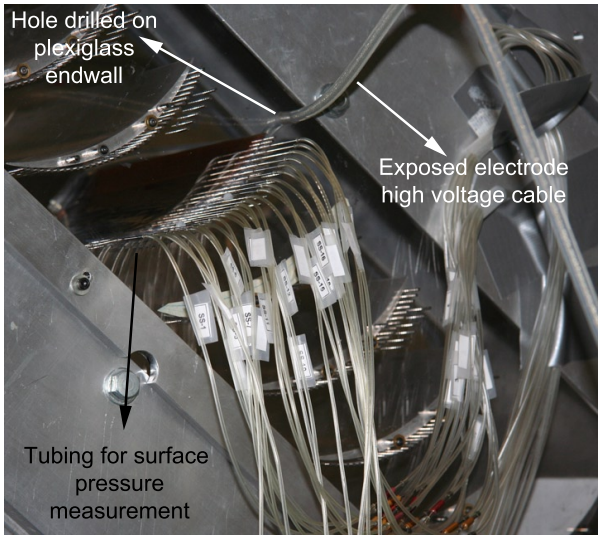

(c) Plasma actuator and blade surface pressure measurement connections

Figure 2.23: Plasma actuator configuration for boundary layer flow control

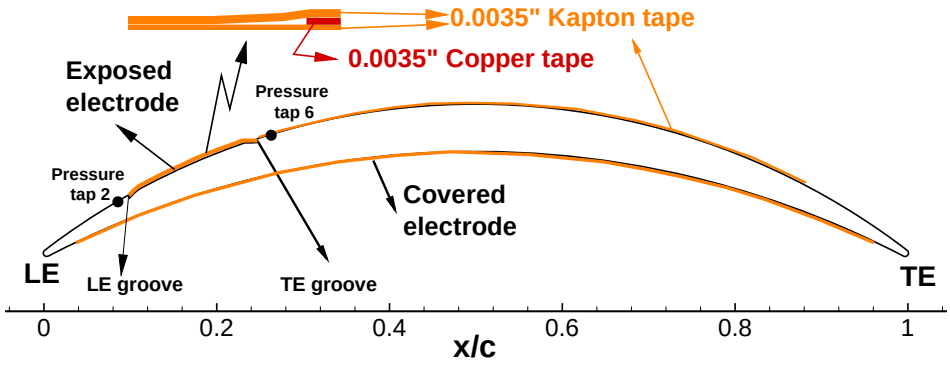

Figure 2.24: Plasma actuator mounted on suction surface instrumented blade

2.5 Experimental Validation

The experimental studies were performed at a Reynolds number of 1.5×10^5 corresponding to an inlet velocity of 20 m/s. The experiments were performed over the high-flow turning compressor cascade. The experiments were carried out in the following order:

- The initial experiments were performed to establish cascade inlet flow uniformity and outlet flow periodicity. Pitchwise traverses were performed at the cascade mid-span using three-hole probe and seven-hole probe at the inlet and outlet plane, respectively.
- Measurements were carried out on the baseline cascade (without plasma actuator) to characterize the inlet endwall boundary layer, blade suction surface boundary layer and blade downstream flow. The inlet endwall boundary layer measurements were performed using a pitot-tube. The surface static pressure measurements together with the surface oil-film flow visualizations were used to identify boundary layer flow separation, transition, reattachment and endwall corner separation on the compressor airfoil. Finally, seven-hole probe measurements were carried at the outlet measurement plane to quantify losses, flow angle, streamwise vorticity etc.
- The concept for endwall corner separation control with plasma actuation was experimentally investigated to validate the computational data. The plasma actuation effectiveness was determined based on the outlet plane seven-hole probe measurements.
- The endwall corner separation control was assessed using endwall boundary layer suction. Various suction slot and hole configurations were tested. The experiments were carried out by performing oil surface visualization, surface static pressure measurements, seven-hole probe outlet plane measurements and discharge flow rate measurements for each configuration. Moreover, the AVR was calculated for each endwall boundary layer suction configuration.
- The boundary layer separation plasma flow control was carried out experimentally. To eliminate effect of the endwalls, the EC-1 (endwall boundary layer suction used to improve flow

two-dimensionality) configuration with AVR≈1 was used as the baseline case. The experiments were carried out by performing surface static pressure measurements and mid-span seven-hole probe outlet plane measurements. The actuation strength, pulsing frequency and duty cycle were among the plasma actuation parameters investigated.

As illustrated in Figure 2.17, the seven-hole probe measurements at the downstream of the target passage were performed at a plane extending from 3 mm to 103 mm in spanwise direction (covering 0.5 span) and 63.4 mm in pitchwise direction (covering 1.2 pitch). The measurements were carried out using a non-uniform traverse mesh with 39 points in spanwise direction and 33 points in pitchwise direction resulting in 1287 measurement points. The spacing between the measurement points was 1 mm near the endwall and it was increased to 5 mm at the mid-span. For the seven-hole probe measurements with endwall plasma actuation, the number of points was reduced (without altering the measurement plane size) to avoid deterioration/burnout of the dielectric material from extended running time. The measurements were carried out using a non-uniform traverse mesh with 35 points in spanwise direction and 25 points in pitchwise direction resulting in 875 measurement points. In all cases, the datum point of seven-hole probe was kept the same.

2.6 Data Reduction Procedures

The effectiveness of the plasma actuation flow control was based on the cascade performance parameters and plasma actuation power calculations. The inlet and outlet plane calculations were performed using the numerical data obtained at 0.8 axial chord upstream of the blade leading edge and 0.4 axial chord downstream of the blade trailing edge, respectively. The planes, located over the suction and pressure surfaces as shown in Figure 2.25, were used to calculate boundary layer properties.

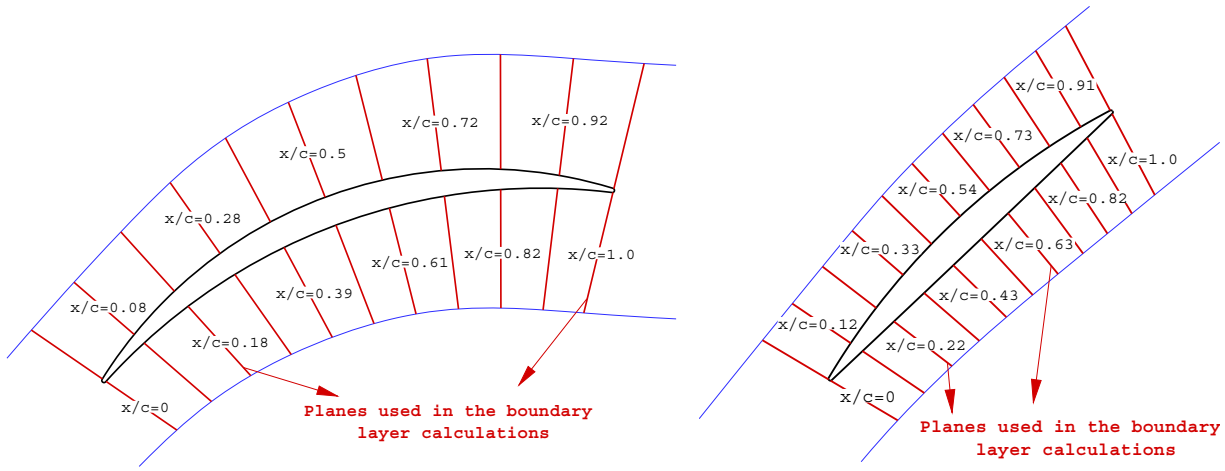

(a) DCA-1 (b) DCA-2

Figure 2.25: Planes used for the boundary layer properties' assessment

The following parameters are used to determine cascade performance and their formulation are given as follows:

- The total pressure loss coefficient is calculated as follows;

$$C_{p_0} = \frac{P_{0_{local}} - P_{0_{CL}}}{q_{CL}} \tag{2.9}$$

  where $P_{0_{local}}$ and $P_{0_{CL}}$ represent local and inlet centerline total pressures, respectively, and q_{CL} is the inlet centerline dynamic pressure.

- The overall total pressure loss coefficient, calculated by non-dimensionalizing the loss in total pressure across the blade row with inlet dynamic pressure, is given as;

$$\omega_0 = \frac{P_{01} - P_{02}}{q_1} \tag{2.10}$$

  where q_1 represents inlet dynamic pressure and P_{01} and P_{02} represent inlet and outlet total pressures, respectively. The mass flow averaging was used in the calculation of dynamic and total pressures.

- The static pressure rise coefficient was calculated as follows;

$$\psi = \frac{P_2 - P_1}{q_1} \tag{2.11}$$

  where P_1 and P_2 represent area averaged inlet and outlet static pressures.

- A factor used to determine the blade loading is the diffusion factor. For a two-dimensional geometry, the diffusion factor derived by Lieblein is as follows (Cumpsty, 1989):

$$DF = 1 - \frac{W_2}{W_1} + \frac{W_{\theta 1} - W_{\theta 2}}{2\sigma W_1} \tag{2.12}$$

- In this study, the flow was essentially incompressible; therefore, axial velocity ratio (AVR) was used instead of axial velocity density ratio (AVDR). The AVR is a ratio of the area-averaged outlet to inlet mid-span axial velocities, as given below;

$$AVR = \frac{\int_0^s (u_2)_{mid-span}\, dy}{\int_0^s (u_1)_{mid-span}\, dy} \tag{2.13}$$

  with y is the pitchwise distance, u_1 and u_2 are the axial velocities at the inlet and outlet, respectively. The flow two-dimensionality increases as AVR gets closer to a value of unity. The use of AVR is most satisfactory for high aspect ratio blades (Rodger *et al.*, 1992). For low aspect ratio blades, it is safer to carry out the two-dimensionality survey with the surface flow visualization. Therefore, the AVR predictions were supported with the surface oil-film flow visualizations to interpret the surface flow features.

In addition to cascade performance parameters, the integral boundary layer parameters, boundary-layer displacement thickness (δ^*) and boundary-layer momentum thickness (θ), were used to determine plasma actuation effect on the cascade airfoil boundary layer flow. The boundary layer edge was predicted as the location where the total pressure is equal to the 99% of the core total pressure. The formulation of integral boundary layer parameters are given below:

- The boundary-layer displacement thickness, δ^* , was calculated as follows;

$$\delta^* = \int_0^{\delta} \left(1 - \frac{V(y)}{V_e}\right) dy \tag{2.14}$$

  where V_e represents boundary layer edge velocity. The boundary layer thickness(δ) was defined as the location where $P_0(y) = 0.99P_{0,core}$.

- The boundary-layer momentum thickness, θ, was defined as;

$$\theta = \int_0^{\delta} \left|\frac{V(y)}{V_e}\right| \left(1 - \frac{V(y)}{V_e}\right) dy \tag{2.15}$$

Rotor equivalent cascade power ($\dot{W}_{eq}$), power ratio (R_p) and plasma actuation efficiency (η_p) were the parameters used to quantify the plasma actuation power and their formulation is given below:

- Assuming an axial-inlet rotor, the cascade velocities are relative velocities in the rotating frame of reference and the tangential component of the cascade inlet velocity is equal to the rotational velocity of the rotor. Details are given in Appendix A.5. Therefore, the rotor equivalent cascade power is calculated as follows:

$$\dot{W}_{req} = \dot{m} V_{\theta 1} (V_{\theta 2} - V_{\theta 1}) \tag{2.16}$$

- The plasma power was calculated to determine the efficiency of the plasma actuator. The plasma power was calculated by carrying out an integral over the plasma actuation domain V_{plasma} as such:

$$\dot{W}_{plasma} = D \left(\iiint_{V_{plasma}} (\vec{F}_{plasma} \cdot \vec{V}) \cdot dV \right) \tag{2.17}$$

  where $\vec{F}_{plasma}$ is the plasma actuator body force vector and $\vec{V}$ is the velocity. D is the pulsed actuation duty cycle varying in a range of 0 and 1. The duty cycle was taken as 1 while calculating the continuous plasma actuation power. This calculation was carried out as an area integral over the plasma actuation area for two-dimensional simulations and the

resultant plasma power was expressed as power per span in [W/m].

- The percentage of power required to drive plasma actuator with respect to the rotor equivalent power, called as power ratio, calculated from:

$$R_p = \frac{\dot{W}_{plasma}}{\dot{W}_{req}} \times 100 \tag{2.18}$$

- The plasma actuation efficiency was determined using the following formula:

$$\eta_p = \frac{\triangle\dot{W}_{req} - \dot{W}_{plasma}}{\triangle\dot{W}_{req}} \times 100 \tag{2.19}$$

where the rotor equivalent power increase, $\triangle\dot{W}_{req}$, was calculated with respect to no actuation case.

In addition to performance and power parameters, to explain flow mechanics vorticity fields are plotted. The vorticity is mathematically defined as the curl of velocity ($\vec{\nabla} \times \vec{V}$). Physically, it is a measure of local rate of rotation of a fluid element. The streamwise component of the vorticity was used to determine the rotational motion of the flow at the exit plane of the cascade. The streamwise vorticity was calculated as follows:

$$\omega_s = \vec{\omega} \cdot \vec{V} \tag{2.20}$$

In the experiments, the velocity gradients are calculated from seven-hole probe measurements. The pitchwise gradients ($\frac{\partial}{\partial y}$) and the spanwise gradients ($\frac{\partial}{\partial z}$) can be estimated from the seven hole probe measurement data. Therefore, the axial component of the vorticity was calculated as follows:

$$\omega_x = \frac{\partial w}{\partial y} - \frac{\partial v}{\partial z} \tag{2.21}$$

However, the axial gradients ($\frac{\partial}{\partial x}$) could not be calculated directly from measurements due to large axial spacing between the measurement planes. Therefore, the pitchwise and spanwise vorticity components, which include axial velocity gradients, are approximated using method proposed by Gregory-Smith *et al*. (1988) based on the incompressible Helmholtz equation given as such:

$$\vec{V} \times \vec{\omega} = \frac{1}{\rho} \nabla P_0 \tag{2.22}$$

Using this equation, the pitchwise and spanwise components of the vorticity were derived, such that:

$$\omega_y = \frac{1}{u}\left(v\,\omega_x + \frac{1}{\rho}\,\frac{\partial P_0}{\partial z}\right) \tag{2.23}$$

$$\omega_z = \frac{1}{u}\left(w\,\omega_x - \frac{1}{\rho}\,\frac{\partial P_0}{\partial y}\right) \tag{2.24}$$

The streamwise vorticity is calculated as follows:

$$\omega_s = \omega_x\, cos\,\alpha\, cos\,\beta + \omega_y\, sin\,\alpha\, cos\,\beta + \omega_z\, sin\,\beta \tag{2.25}$$

with α and β are the local angle of attack and angle of sideslip. Finally, the streamwise vorticity was normalized as follows:

$$C_{\omega_s} = \frac{\omega_s c}{V_{CL}} \tag{2.26}$$

Chapter 3

Endwall Flow Control

This chapter presents the results from computational and experimental work on the corner separation control concept. The chapter starts with the results for the baseline cascade, followed by the results for plasma actuation and endwall suction flow control methods for endwall corner separation. Finally, endwall plasma actuation results at higher speeds are presented.

3.1 Baseline Compressor Cascade

Before introducing the endwall flow control study, the experimental and computational results for the baseline configuration are discussed in this section. The measurements for the inlet flow endwall boundary layer thickness are first presented. Then, the experimental and computational results were used to determine the main features of the flow focusing primarily on corner stall. Unless otherwise stated, the computations were performed at a Reynolds number of 1.5×10^5 corresponding to an inlet velocity of 20 m/s.

3.1.1 Inlet Endwall Boundary Layer

Figure 3.1(a) shows the boundary layer velocity profile at 1.7 c_x upstream of the central blade leading edge normalized by the centerline velocity, V_{CL}. The corresponding total pressure loss coefficient is presented in Figure 3.1(b) where the total pressure loss is calculated with respect to centerline flow and normalized by the centerline dynamic pressure, q_{CL}. The flow outside the endwall boundary layer shows a good uniformity.

The inlet endwall boundary layer properties are listed in Table 3.1. The boundary layer edge was approximated as the point where the total pressure is equal to the 99% of the centerline total pressure. The shape factor is a useful parameter to determine whether a boundary layer is laminar or turbulent. The shape factor is typically 2.6 for a laminar flat-plate boundary layer flow while a shape factor of 1.3 implies a turbulent flow over a flat-plate (White, 1998). Therefore, the measured value of shape factor, H=1.26, suggests a turbulent flow at the endwall inlet. In addition, the value of displacement thickness had a special importance for the endwall boundary layer suction studies. The size of the boundary layer slot used to ingest low-momentum endwall boundary layer flow was determined based on the displacement thickness.

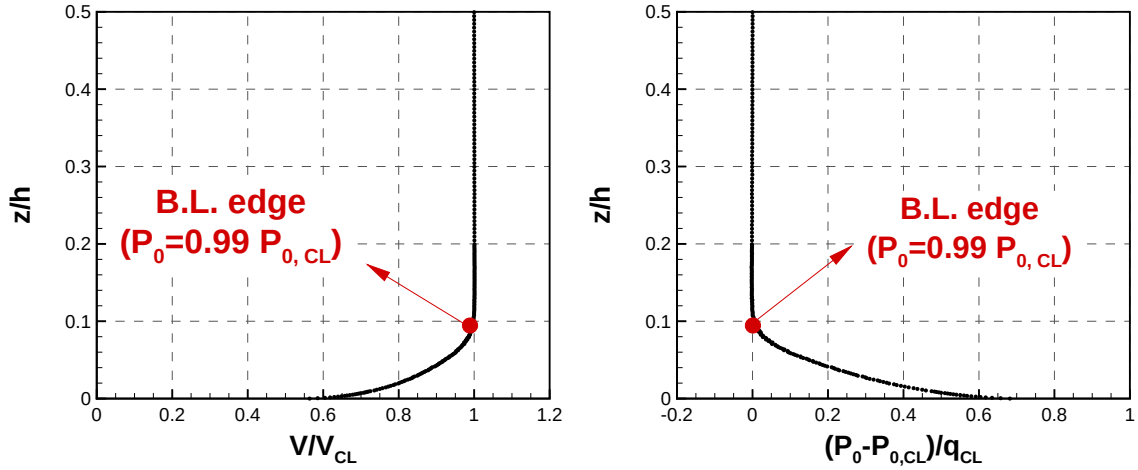

(a) Velocity profile

(b) Total pressure loss profile

Figure 3.1: Endwall boundary layer measurements

Table 3.1: Summary of inlet boundary layer properties

Parameters	Values
δ/h	0.095
δ^*/h	0.011
θ/h	0.0087
$H = \delta^*/\theta$	1.26

3.1.2 Surface Flow Visualization

Figure 3.2 shows the suction surface oil flow visualization results together with the computational results. The CFD results are presented by limiting streamlines for velocity superimposed on the streamwise skin-friction coefficient contours. It can be seen that both experimental and computational flow patterns indicate an attached laminar flow (inferred from CFD) near the blade leading edge, followed by a laminar boundary layer separation. The separated laminar boundary layer eventually becomes turbulent and the turbulent boundary layer reattaches close the mid-chord. The oil-film surface flow visualizations show a smaller laminar separation bubble which resides between the two lines where the oil is accumulated. This region is a dead-air region where the wall shear stress is very low such that the oil layer cannot be moved by boundary layer shear force. The attached turbulent boundary layer experiences a small separation near the trailing edge. The computations predict an earlier turbulent boundary layer separation compared to the experiments. The oil flow visualization shows that a lot of oil-powder mixture has accumulated at the blade mid-span near the trailing edge. The accumulated oil-powder mixture tries to move upstream starting from the blade trailing edge. However, it stagnates at the turbulent boundary layer separation line.

Both data shows that the laminar separation bubble disappears close to the endwalls. This can

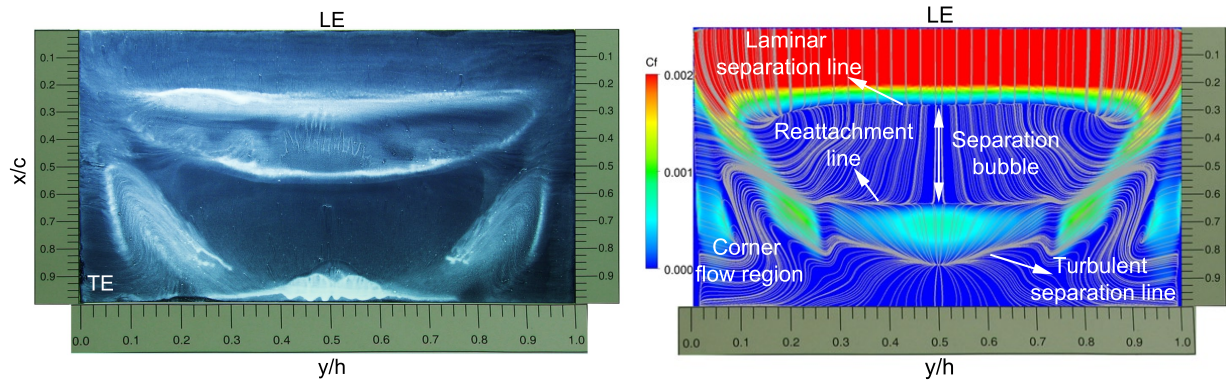

(a) Experiment (b) CFD

Figure 3.2: Baseline oil flow visualization results on the left; Predicted streamwise skin-friction coefficient plotted together with the limiting streamlines for velocity on the right

be attributed to the spanwise motion of the low-momentum suction surface boundary layer near the endwall towards the mid-span. The low-momentum spanwise flow reverses direction in the presence of high adverse pressure gradient. Therefore, the corner boundary layer flow formed by the interaction of suction surface and endwall boundary layers initially moves in spanwise direction then moves upstream. It is interesting to see that some portion of the corner flow moves in reversed direction and ends up at the laminar separation line. The rest of the corner flow merges with the upstream flow and ends up at the turbulent reattachment and turbulent separation lines. Additionally, the streamlines show that the portion of reversed endwall corner flow becomes more pronounced closer to the trailing edge. This can be due to higher adverse pressure gradient close to the trailing edge, increased boundary layer thickness and trailing edge reversed flow caused by the movement of pressure surface trailing edge flow towards to the suction surface trailing edge.

In summary, the surface flow visualizations reveal that the corner stall has a large effect on the overall suction surface flow. As opposed to the conventional depiction of corner stall shown in Section 1.2, the reversed trailing edge corner flow modifies the entire structure of the suction surface flow. The surface flow visualizations only illustrated the boundary layer flow features. The three-dimensional nature of the corner stall will be explained later in Section 3.1.5.

In terms of validation of the computational predictions, the computations are in good agreement with experiments in terms of predicting the location of laminar flow separation and capturing the corner separation flow pattern on the suction surface, even if the separation bubble size was under-predicted. A numerical assessment of the effect of freestream turbulence intensity on the suction surface boundary layer flow (Appendix C.2) showed that the laminar boundary layer separation bubble size decreases with increasing freestream turbulence intensity above the blade. This means that if the simulated freestream turbulence intensity, which is matched at 0.3% to the measured data at the computational domain inlet location, should decay more than in a physical flow, the length of the separation bubble would be over-predicted. However, as shown in Figure C.3 in Appendix C.2,

the decay in the freestream turbulence intensity in the simulation is negligible, which means that this hypothesis can not be reason behind the over-prediction of the separation bubble length.

3.1.3 Surface Pressure Coefficient Distributions

The surface pressure distribution is an important flow feature to identify the boundary layer development over the blade. Figure 3.3 shows the experimental and computational surface pressure distributions at 50%, 30%, 15% and 7.5% spanwise locations. For the mid-span pressure distribution, a laminar (inferred from CFD) boundary layer separation, characterized by the relatively flat (plateau) region in the pressure distribution, was observed on the suction surface. The rapid pressure recovery just downstream of the laminar separation suggests a turbulent reattachment. Figure 3.5 further shows that the laminar boundary layer separation took place at 0.29 chord, followed by a turbulent reattachment at 0.65 chord and a turbulent separation at 0.86 chord.

Spanwise variation of the pressure distribution shows that the separation bubble becomes less pronounced near the endwall. The laminar separation point remains relatively unchanged between 15% and 50% span. However, the reattachment point moves upstream near the endwall. Although pressure distribution at 7.5% span does not indicate any flow separation, the computational skin friction coefficient distributions presented in Figure 3.4 show a separation bubble between 0.5 chord and 0.68 chord. These interpretations were previously confirmed by the experimental and computational surface flow visualizations. As a final note, the pressure coefficient distributions predicted by CFD are in a good agreement with the experimental data in terms of showing the main flow features. In adddition to that, computational results obtained with the endwall suction mesh for pressure distribution are also in agreement with the experimental data (Appendix C.3).

3.1.4 Downstream Flow Field Measurements

In the previous sections, it has been shown that the boundary layer flow properties predicted by computations were in good agreement with the experimental data. To determine the three-dimensional features of the corner stall, experimental and computational total pressure loss coefficient contours at 0.4 c_x downstream of the blade trailing edge are compared. The experimental data did not include loss measurements between close to the endwall since the initial measurement point was constrained by seven-hole pressure probe diameter. Therefore, the seven-hole probe measurements were started 3 mm (1.5% of span or 16% of the endwall boundary layer thickness) away from the endwall.

Figure 3.6 shows experimental and computational total pressure loss coefficient contours. The high total pressure loss regions indicate the blade and corner separation wake flows. The high total pressure loss region between 5% span and 25% span is caused by the corner separation. The

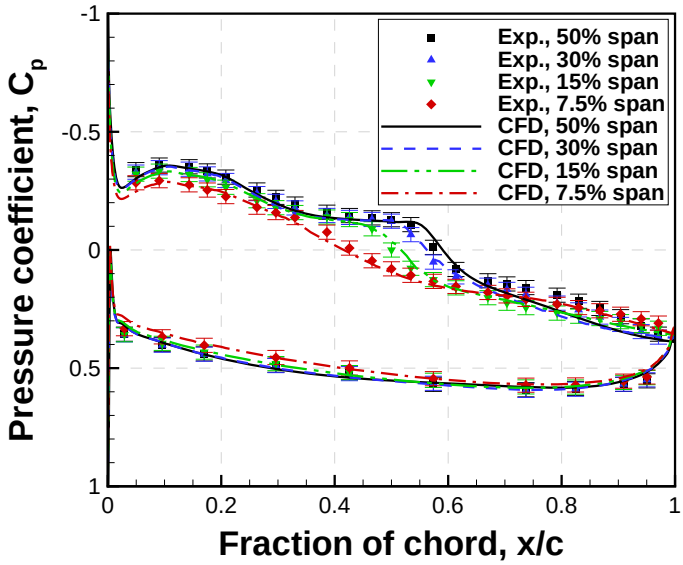

Figure 3.3: Experimental and computational pressure coefficient distributions at various spanwise locations

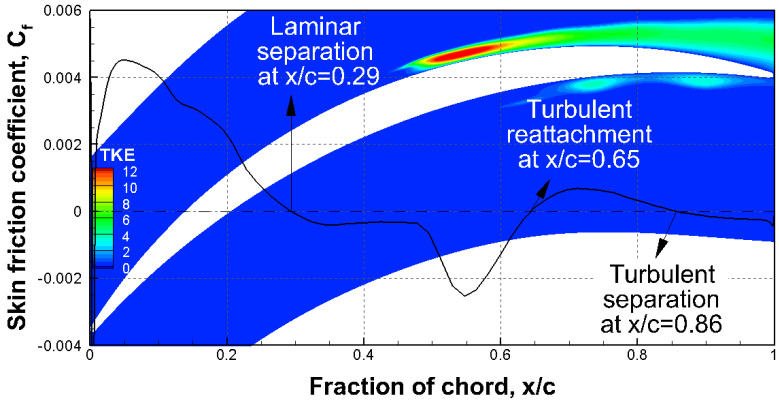

Figure 3.4: Predicted mid-span skin friction coefficient distributions plotted together with the turbulent kinetic energy contours

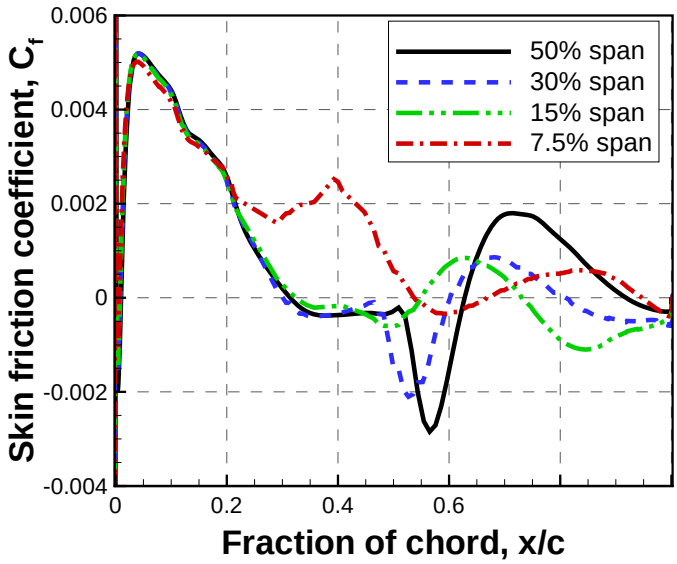

Figure 3.5: Predicted skin friction coefficient distributions at various spanwise locations

computations seem to over-predict the profile losses similar to the observation made by Gmelin *et al*. (2011).

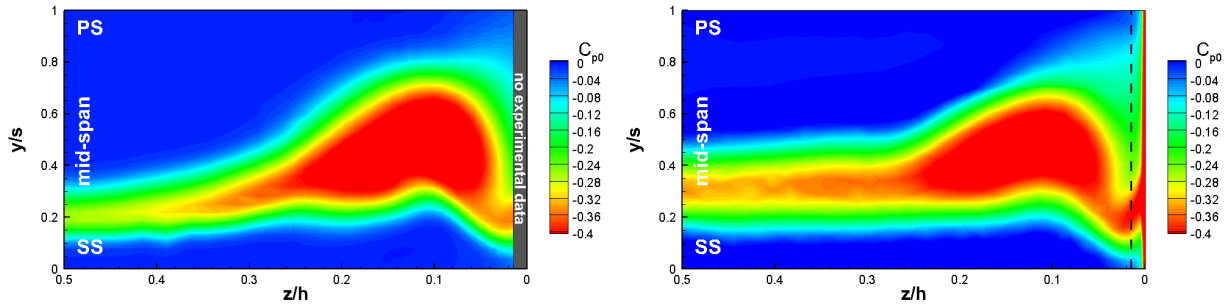

(a) Experiment (b) CFD

Figure 3.6: Contours of total pressure loss coefficient (C_{p_0}) at 0.4 c_x downstream plane for baseline

3.1.5 Endwall Corner Separation Flow Features

To summarize the experimental and computational results presented up to this point, the surface flow visualizations have shown that the suction surface boundary layer flow pattern was significantly altered by the endwall corner separation. Additionally, total pressure loss coefficient contours at 0.4 c_x downstream of the blade trailing edge have shown that the corner separation induces a high total pressure loss. In this section, additional data is presented to further reveal the corner separation flow features.

The flow features around the corner separation region are depicted in Figure 3.7. Streamline rakes, positioned at 0.75% span away from the endwall, were located at various chordwise locations

and coloured by different colours. It can be seen that the streamlines originated from the most upstream position (shown with red) lean away from the endwall under the effect of blockage caused by the corner separation. The red streamlines end up at 35% span at the trailing edge. Furthermore, the blue streamlines do not cross the blockage caused by the corner separation region, instead they turn around the corner separation blockage. The streamlines originated after 0.5 chord, coloured by orange, green and white, contribute to the blockage caused by the corner separation.

Finally, the iso-surface was generated for u=-0.01m/s to reveal the reversed flow region. It is shown that the reversed flow in the corner stall region does not only reside inside the suction surface boundary layer but also it is involved in the core flow outside the boundary layer. This is a clear evidence that corner separation is highly three dimensional as opposed to the boundary layer separation.

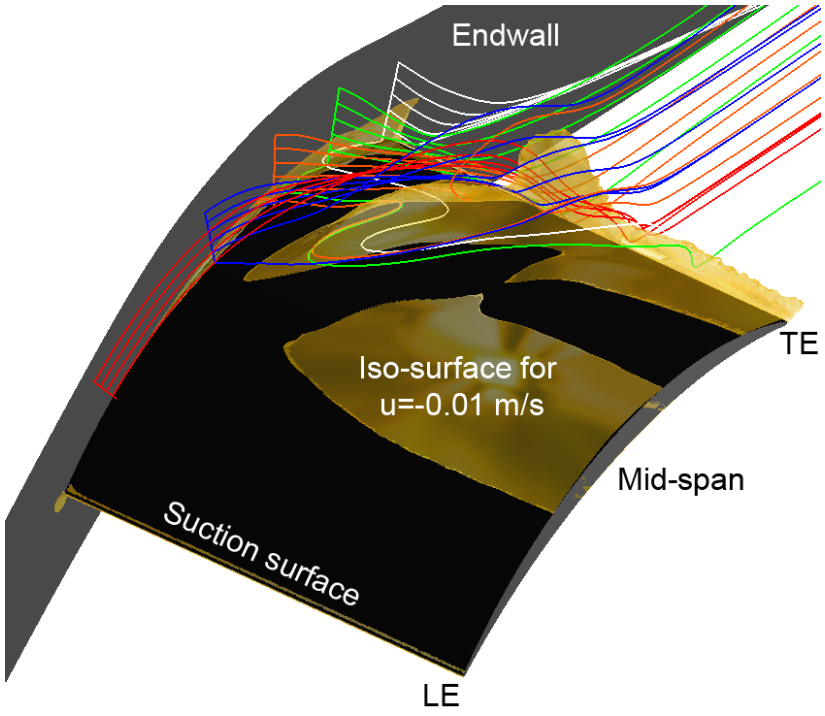

Figure 3.7: Overview of the corner stall using streamlines and velocity iso-surface for u=-0.01m/s predicted from CFD

Figure 3.8 shows the boundary layer flow features using the limiting streamlines on the endwall and suction surface. The dividing streamline shown in the figure emanates from the leading edge stagnation point and ends up on the suction surface and forms a saddle points S_1 at the junction of suction surface and endwall. The flow originating from the saddle point, which has initially zero wall shear stress (Gbadebo *et al.*, 2005), is susceptible to flow separation under the effect of adverse pressure gradient. Therefore, this point is considered to be the origin of three-dimensional separation. For this particular blade, the flow originating from the saddle point moves downstream

then reverses direction under the effect of adverse pressure gradient and ends up at the suction surface separation line. On the endwall, the boundary layer flow driven toward the suction surface by the circumferential pressure gradient separates from the endwall separation line which originates from the saddle point S_2. The separated, low-momentum endwall boundary layer fluid ends up on the suction surface where it attaches to the suction surface at the corner reattachment line.

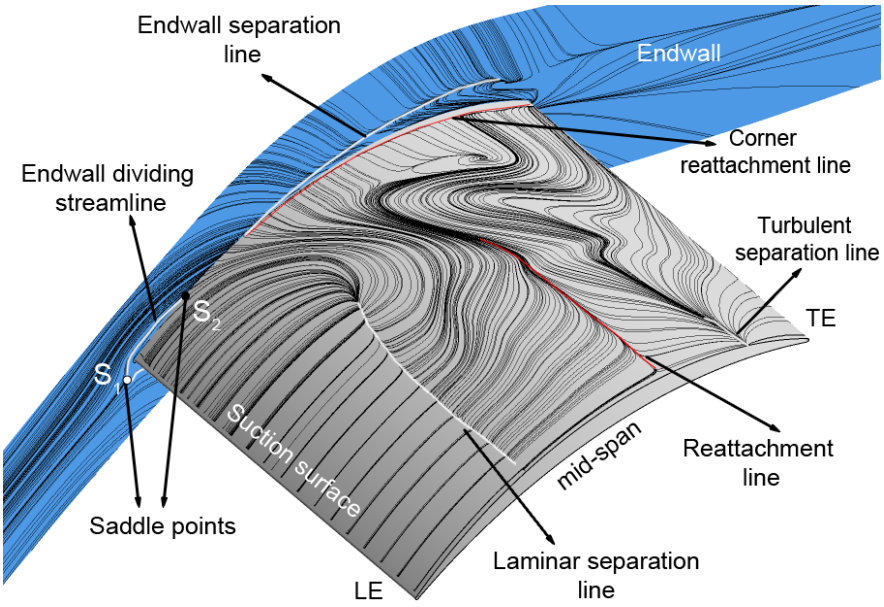

Figure 3.8: Predicted limiting streamlines for velocity on the suction surface and endwall

Figure 3.9 compares the experimental and computational streamwise vorticity coefficient distributions at 0.4 c_x downstream of the blade trailing edge. Both experimental and computational results prove the presence of two counter-rotating streamwise vortices, namely the passage vortex and horseshoe the vortex. As mentioned previously in Section 1.2, these vortices play a significantly important role in the formation of the corner stall. The passage vortex, represented with the red contour, is generated due to fluid motion from the pressure surface to the suction surface. The vortex represented with the blue contour shows the wake of the horseshoe vortex which forms as the vortex sheet associated with the endwall boundary layer wraps around the blade leading edge. As a final remark, the discrepancy between experimental and computational data can be attributed to differences between experimental and computational velocity fields. In addition to that, the method (discussed in Section 2.6) used to approximate tangential and spanwise components of the vorticity in the experimental data may induce some error near the vorticity core where the velocity gradients are large and viscous forces are important (Yaras and Sjolander, 1990).

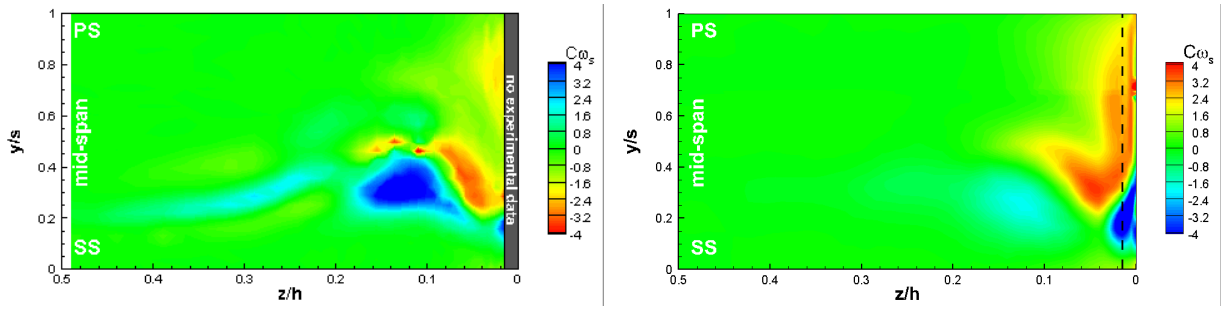

(a) Experiment (b) CFD

Figure 3.9: Contours of streamwise vorticity coefficient (C_{w_s}) at 0.4 c_x downstream plane for baseline

3.1.6 Reynolds Number Effect on Blade Pressure Coefficient

This section presents the experimental results carried out to determine the effect of Reynolds number on the surface pressure distribution for the baseline airfoil. The measurements were performed at Reynolds numbers 1.25×10^5, 1.5×10^5 and 1.75×10^5 based on the chord length. Figure 3.10 shows a comparison of mid-span loading distributions. It is observed that the extend of the suction surface laminar separation bubble gets smaller as the Reynolds number increases. This result indicates that higher Reynolds number decreases the length of the transition region and causes an earlier turbulent reattachment after laminar separation. The pressure distributions are observed to be almost the same for the pressure surface.

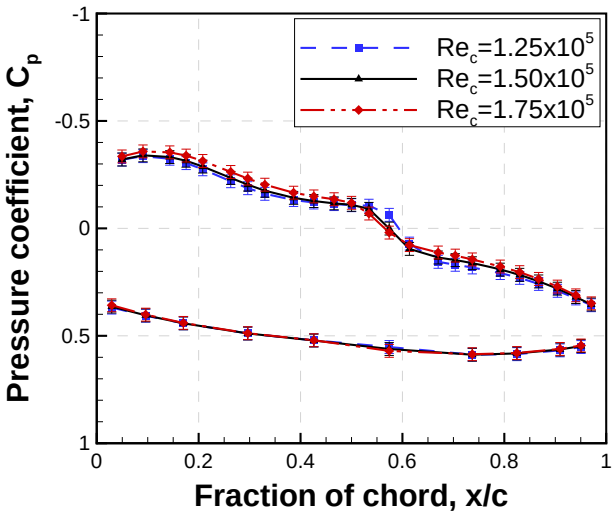

Figure 3.10: Experimental pressure coefficient distributions at various Reynolds numbers

3.2 Endwall Plasma Actuation Flow Control

The results presented for the baseline compressor cascade have shown the presence of highly three-dimensional corner stall region. Furthermore, the surface flow visualizations and computational 3-D streamlines revealed the existence of reversed flow around.

3.2.1 Computations to Determine Plasma Actuator Configuration

As presented in Section 2.2, three plasma actuators were used to assess plasma actuation flow control for the endwall corner separation. Figure 3.11 shows the plasma actuator body force vectors for each plasma actuator. The plasma actuators $F_{act,1}$ and $F_{act,2}$ are on the endwall at 0.5 chord and 0.75 chord locations, respectively. The plasma actuator $F_{act,3}$ is located on the suction surface at 0.5 chord. Therefore, the plasma actuator $F_{act,2}$ resides in the corner separation region and $F_{act,1}$ and $F_{act,3}$ is located at the upstream of the corner separation region. In all cases, the plasma actuation was applied in continuous mode with a plasma actuation strength of 125 mN/m.

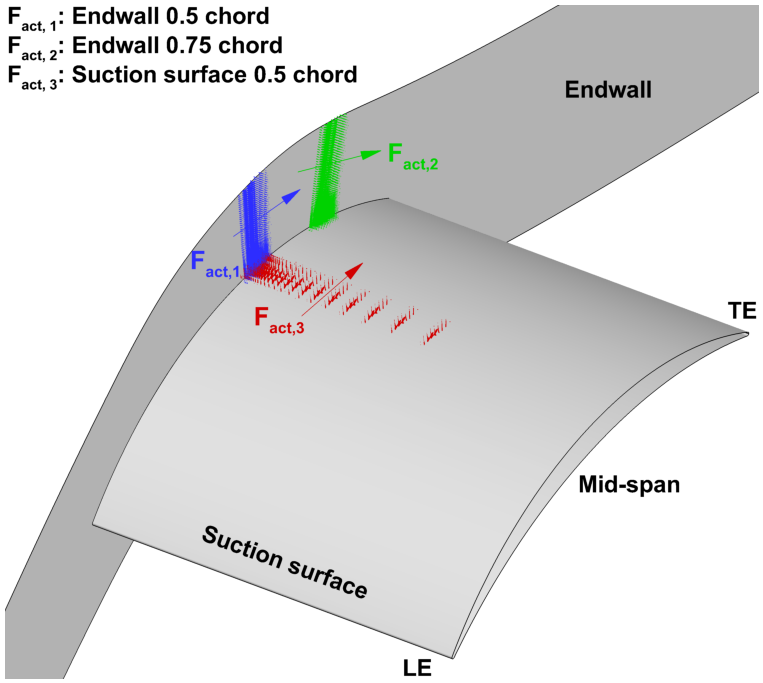

Figure 3.11: Plasma actuator body force vectors on the suction surface and endwall

Figure 3.12 shows the predicted total pressure loss coefficient distribution over five planes located at various chordwise locations. The plasma actuation endwall flow control cases are compared against baseline case (Figure 3.12(a)). Endwall plasma actuation results shown in Figure 3.12(b) and Figure 3.12(c) for $F_{act,1}$ and $F_{act,2}$ configurations show that the plasma actuation at 0.5 chord ($F_{act,1}$) is more effective compared to the plasma actuation at 0.75 chord ($F_{act,2}$) in

reducing the total pressure loss coefficient. The $F_{act,2}$ configuration causes a local total pressure loss reduction right after the plasma actuator, but it does not affect the total pressure loss coefficient at the trailing edge plane. The $F_{act,1}$ configuration creates a noticeable reduction in the corner stall close to the endwall. This result suggests that the plasma actuator should be located upstream of the low-momentum blockage region caused by the corner separation to achieve a reduction in the corner separation size. A plasma actuator inside the corner separation region will require larger plasma actuation strength to achieve the same effect. It can be seen from Figure 3.12(d) that the suction surface plasma actuation at 0.5 chord reduces the thickness of suction surface boundary layer loss (profile loss). However, it is not effective in reducing the losses arising from corner separation. The final configuration with $F_{act,1}$ & $F_{act,3}$ plasma actuators work together causes the most significant total pressure loss reduction as shown in Figure 3.12(e).

In an effort to have a more quantitative comparison, Figure 3.13 shows the chordwise distribution of overall total pressure loss coefficient (ω_0) calculated by mass flow averaging the total pressure loss on the suction surface planes. These planes, oriented normal to the suction surface, extend up to mid-span from the endwall as shown previously in Figure 3.12(a). In pitchwise direction, they cover the region between suction surface and symmetry plane. Overall, it can be seen that the overall total pressure loss coefficient starts to drop slightly after the plasma actuator location. Similar to the observations made earlier, the suction surface plasma actuator ($F_{act,1}$) causes the most significant overall total pressure loss coefficient reduction when the plasma actuators are used separately. The endwall plasma actuation at the upstream of the corner separation region ($F_{act,1}$) reduces ω_0 more effectively compared to the downstream endwall plasma actuation ($F_{act,2}$). Finally, $F_{act,1}$ & $F_{act,3}$ configuration has the most significant effect where the trailing edge ω_0 was reduced by 3% of inlet dynamic head (from 0.14 to 0.11).

Figure 3.14 compares the plasma actuation configurations based on the non-dimensional boundary layer displacement thickness (δ^*/c) distributions on the endwall and suction surface. As opposed to the previous comparisons, this comparison provides a way to determine the plasma actuation effectiveness based on the boundary layer flow properties around the corner stall region. The result for the baseline configuration shows that the δ^*/c becomes significantly large around the corner separation region. It can be seen that the $F_{act,1}$ configuration reduces the corner stall region displacement thickness noticeably. The $F_{act,2}$ has a negligible effect on the δ^*/c distribution. This can be attributed to the relatively large displacement thickness (δ^*/c) near the plasma actuator location. A large displacement thickness at the plasma actuator location will require a larger plasma actuation strength to achieve the same effect achieved with $F_{act,1}$ configuration. This result one more time suggests that the plasma actuator should be located at the upstream of the corner separation. It is interesting to note that the suction surface plasma actuation $F_{act,3}$ has a very small effect on the corner stall region displacement thickness although it was previously shown in Figure 3.12

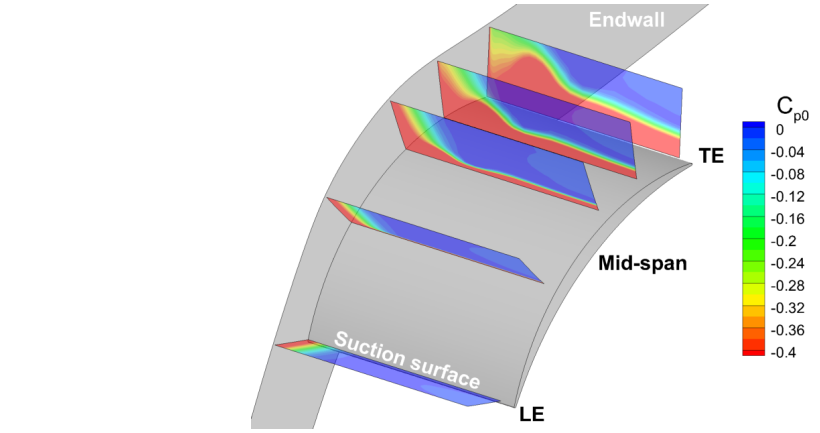

(a) Baseline

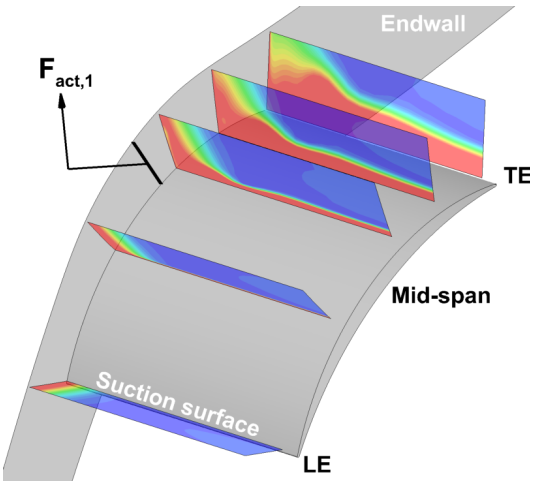

(b) $F_{act,1}$

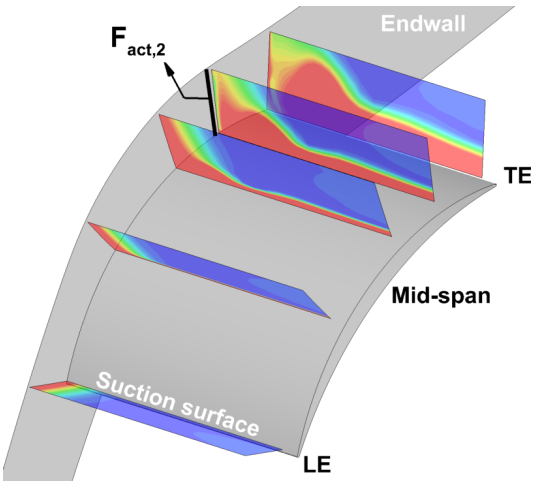

(c) $F_{act,2}$

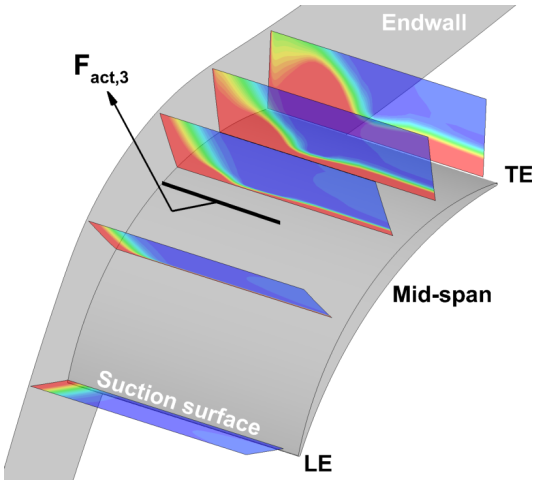

(d) $F_{act,3}$

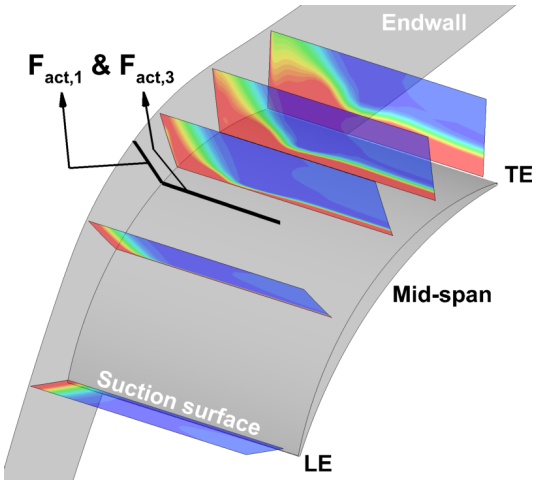

(e) $F_{act,1}$ & $F_{act,3}$

Figure 3.12: Predicted total pressure loss coefficient (C_{p_0}) contours at various chordwise planes

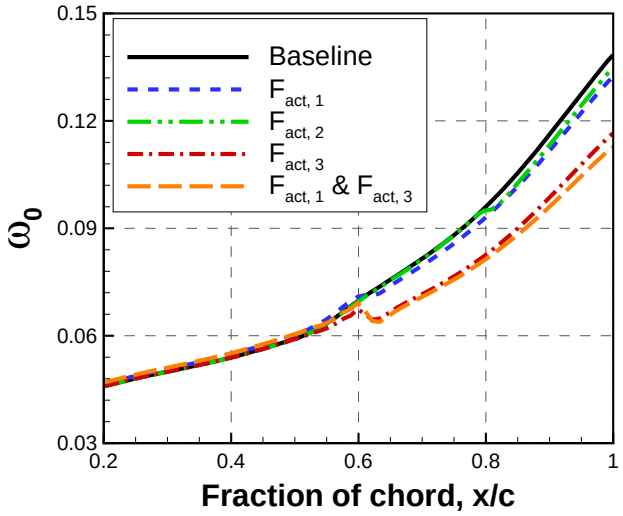

Figure 3.13: Predicted overall loss coefficient (ω_0) distributions in chordwise direction

that it suppresses the suction surface profile losses. Finally, the $F_{act,1}$ & $F_{act,3}$ configuration reduces the displacement thickness significantly compared to the other plasma actuator configurations.

3.2.2 Experimental Validation with Final Plasma Actuator Configuration

Computations have shown that the plasma actuation applied from endwall and suction surface at 0.5 chord ($F_{act,1}$ & $F_{act,3}$) was the most effective in reducing total pressure losses caused by the corner separation. Therefore, $F_{act,1}$ & $F_{act,3}$ configuration was used in the experiments in an effort to validate the computational results at a low plasma actuation strength. Once the computational method was validated for the corner separation plasma flow control, the computational tool was employed to achieve flow control at higher plasma actuation strength beyond presently achievable levels.

The plasma actuator configuration for the endwall corner separation control was described in Section 2.4.2. The plasma actuation force measurements for the SLA blade and Teflon piece are presented in Appendix B.6. A small plasma actuation strength (65 mN/m) was used in the endwall corner separation measurements to reduce the risk of deterioration/burnout of the dielectric material from long running time.

Downstream Flow Field Measurements

To determine the effect of (slightly protruding) plasma actuator located on the suction surface and endwall, seven-hole pressure probe measurements at 0.4 c_x downstream of the blade trailing edge were repeated for the baseline cascade. Figure 3.15 presents the downstream total pressure loss coefficient measurements. Figure 3.15(c) shows the change in total pressure coefficient con-

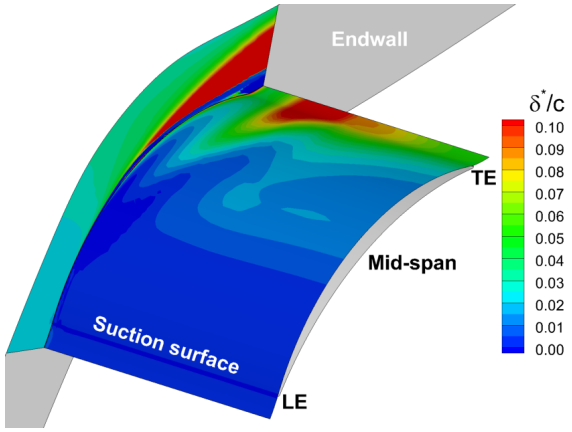

(a) Baseline

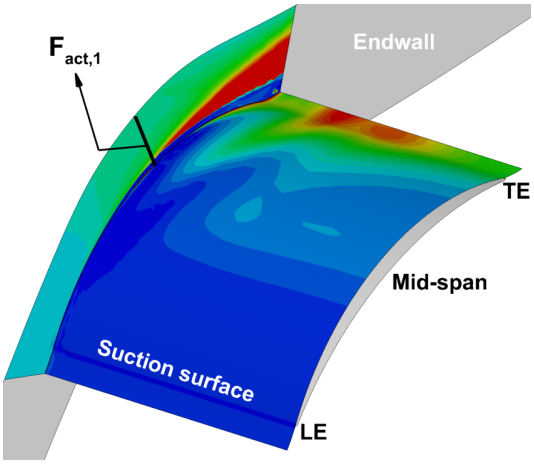

(b) $F_{act,1}$

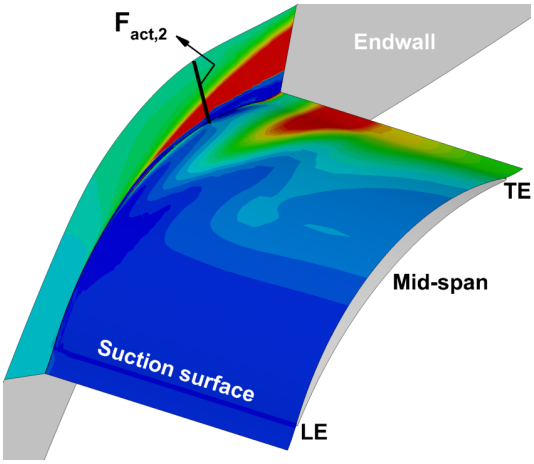

(c) $F_{act,2}$

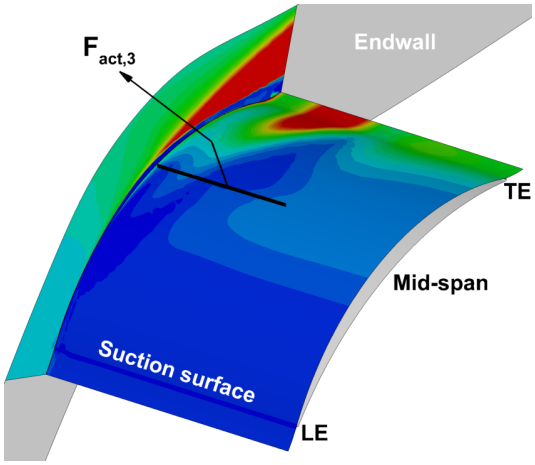

(d) $F_{act,3}$

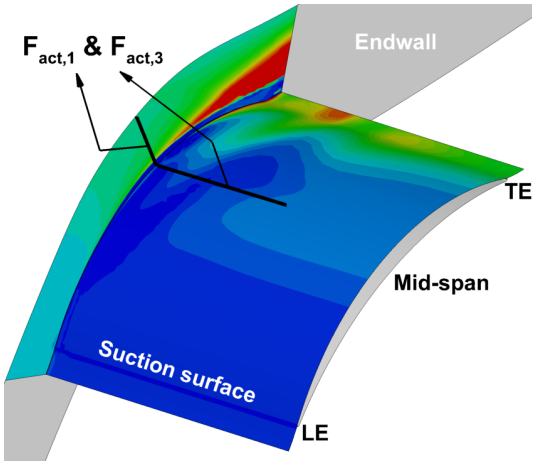

(e) $F_{act,1}$ & $F_{act,3}$

Figure 3.14: Predicted boundary layer displacement thickness (δ^*/c) distributions over the suction surface and endwall for plasma actuator configurations

tours between clean and plasma actuator mounted (unpowered) blades. It can be seen that the plasma actuation hardware moves the blade wake closer to the suction surface (where the datum of seven-hole probe kept the same) and increases the total pressure loss. Indeed, the overall loss coefficient (ω_0) was observed to increase from 0.0553 to 0.0616. To isolate the plasma actuation effect, the plasma actuation results were thus compared against the measurements performed for the baseline configuration with plasma actuator hardware.

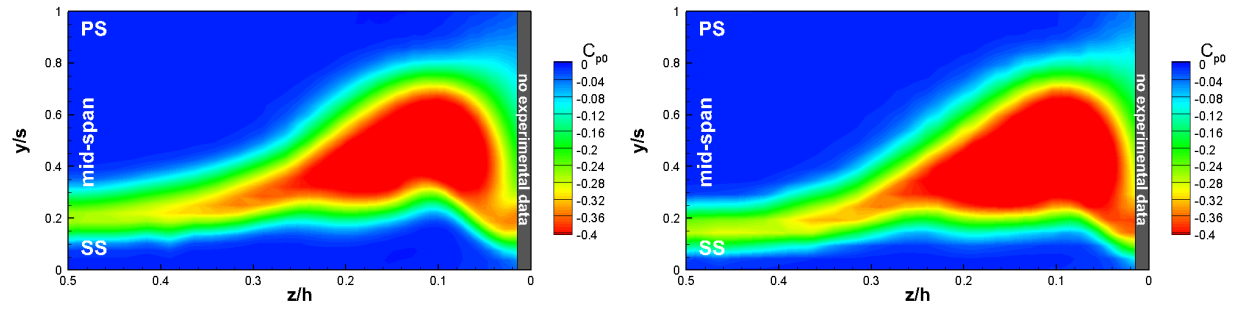

(a) Baseline blade without plasma actuator hardware (clean)

(b) Baseline blade with plasma actuator hardware (plasma mounted)

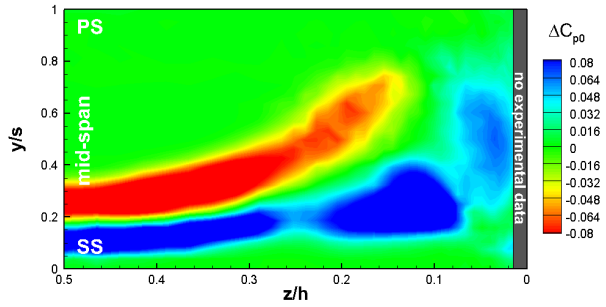

(c) Change in C_{p0} ($\triangle C_{p0}$)

Figure 3.15: Contours of total pressure loss coefficient (C_{p_0}) at 0.4 c_x downstream plane for plasma actuator hardware effect

Figure 3.16 shows the experimental and corresponding computational results for the total pressure loss coefficient distribution at 0.4 c_x downstream plane. The computations over-predict the wake total pressure losses close to the mid-span (i.e. higher profile losses) but underestimate the total pressure loss coefficient around the corner stall region. Figure 3.16(e) and Figure 3.16(f) show the change in total pressure coefficient contours for the experimental and computational data, respectively. The plasma actuation reduces the total pressure losses caused by corner separation and blade profile.

Table 3.2 shows that the plasma actuation reduces the overall total pressure loss coefficient by 0.67% of inlet dynamic head, in the corresponding CFD simulation the overall total pressure loss coefficient reduction was predicted as 0.79% of inlet dynamic head where the difference between experiment and CFD results is within the measurement uncertainties. Overall, the computational results and the experimental data shows a good agreement.

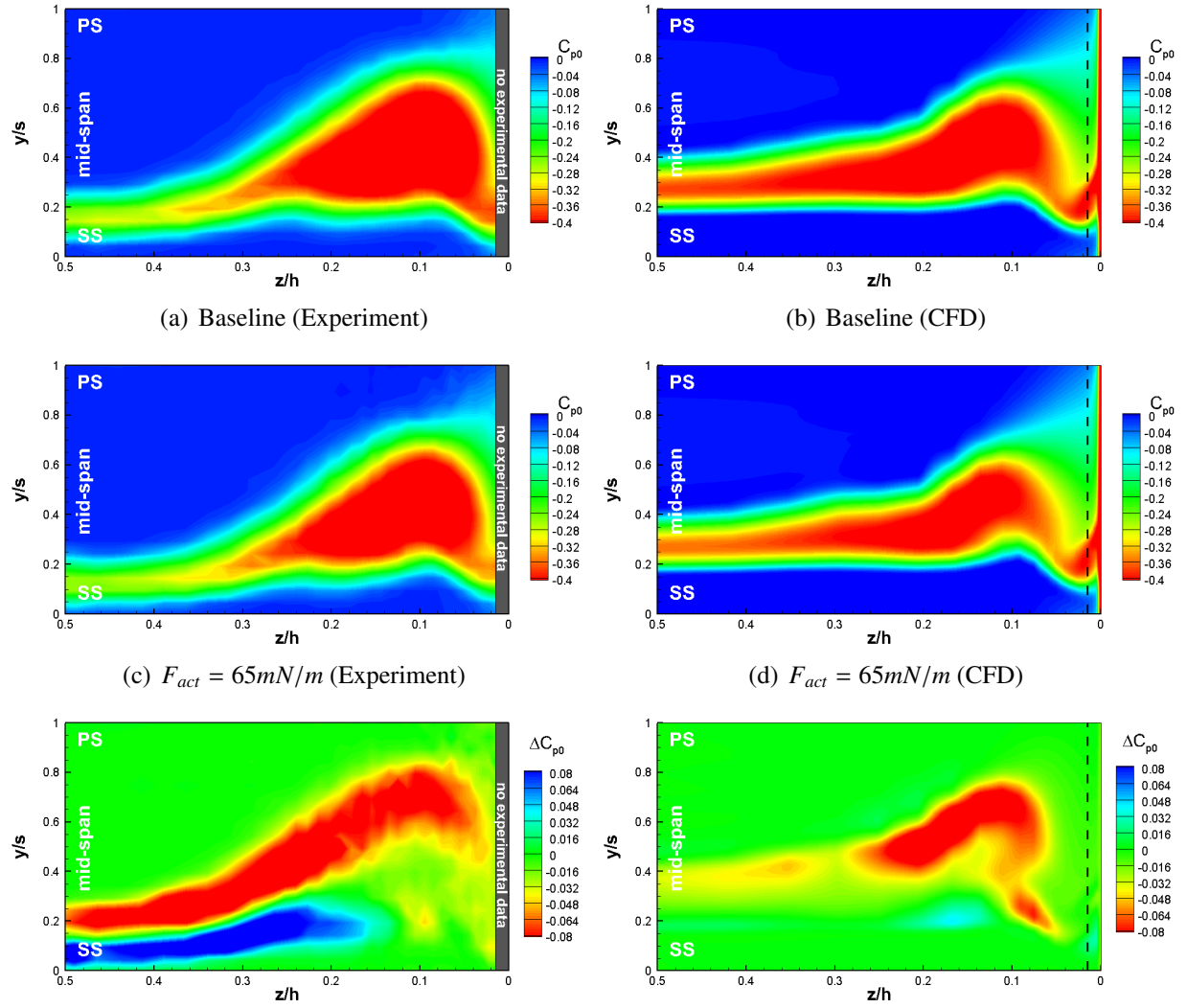

(a) Baseline (Experiment)

(b) Baseline (CFD)

(c) $F_{act} = 65mN/m$ (Experiment)

(d) $F_{act} = 65mN/m$ (CFD)

(e) Change in C_{p0} ($\triangle C_{p0}$) (Experiment)

(f) Change in C_{p0} ($\triangle C_{p0}$) (CFD)

Figure 3.16: Contours of total pressure loss coefficient (C_{p_0}) at 0.4 c_x downstream plane for endwall plasma actuation

Table 3.2: Experimental and computational results for overall total pressure loss coefficient (ω_0)

Configuration	ω_0		$\triangle(\omega_0)$	
	(Experiment)	(CFD)	(Experiment)	(CFD)
Baseline	0.0616±0.01	0.0528	-	-
$F_{act} = 65mN/m$	0.0549±0.01	0.0449	0.0067	0.0079

3.3 Endwall Boundary Layer Bleed/Suction Flow Control

In this section, experimental and computational results for the endwall boundary layer suction are presented. As discussed in Section 2.3.3, three boundary layer bleed mechanisms, suction surface holes (SSH), passage holes (PH) and inlet bleed (IB) were used. The endwall boundary layer bleed configurations are previously shown in Figure 2.8.

The cases studied are listed in Table 3.3 together with the bleed mass flow rate measurement results (details are given in Appendix C.1) at a tunnel operating Reynolds number of 1.5×10^5. m_{bleed}/m_{inlet} represents the bleed mass flow rate (for both sides of the endwall) in percentage of the inlet mass flow. As can be seen in Figure 2.8(b), EC-1 configuration corresponds to endwall boundary layer bleed flow control using SSH only. This configuration requires 1.32% of the inlet mass flow as the bleed air. In EC-2 configuration, PH is also used and the bleed mass flow rate increased to 1.60%. Finally, EC-3 configuration corresponds to the endwall boundary layer bleed case with all three suction surfaces (SSH, PH and IB) were opened as shown schematically in Figure 2.8(d). The bleed mass flow rate for EC-3 configuration was measured as 2.42%.

Table 3.3: Cases studied in endwall boundary layer suction flow control

Configuration	IB	SSH	PH	m_{bleed}/m_{inlet} [%]
Baseline	Closed	Closed	Closed	-
EC-1	Closed	Open	Closed	1.32±0.2
EC-2	Closed	Open	Open	1.60±0.2
EC-3	Open	Open	Open	2.42±0.2

Figure 3.17 shows the computationally predicted bleed mass flow rates through each suction surface and passage hole. It can be seen that the bleed rate through the holes increases in chordwise direction as a result of the passage pressure rise in chordwise direction.

The experimental oil-film flow visualization results and corresponding CFD simulations showing skin-friction coefficient plotted together with the limiting streamlines are shown in Figures 3.18-3.21. Overall, the endwall boundary layer suction configurations reduce the spanwise motion of the fluid near the endwall. The suction surface boundary layer fluid leaning away from the endwall observed to move in downstream direction having a relatively small spanwise velocity component compared to the baseline. Moreover, the reversed flow originating from the blade corner becomes less dominant. Among the endwall suction configurations, the EC-3 configuration improves the boundary layer flow the most. In this configuration, the laminar separation line moves slightly upstream. Based on the predicted skin friction coefficient distribution on the suction surface, EC-3 configuration moves the laminar separation line approximately from 0.29 chord to 0.27 chord. However, the size of the separation bubble is observed to remain unchanged. The flow patterns for

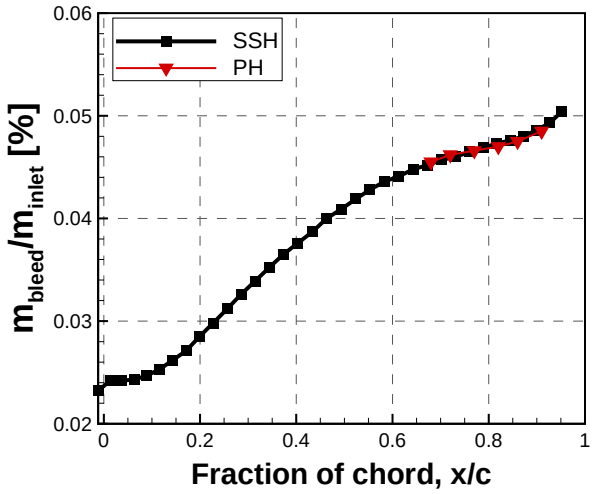

Figure 3.17: Predicted bleed mass flow rates through SSH and PH

EC-1 and EC-2 configurations are almost identical. Therefore, the addition of the passage holes does not have any significant effect on blade suction surface boundary layer flow. The CFD predictions capture the location of laminar separation fairly well. However, the size of the separation bubble over-predicted. The behavior of the suction surface flow near the endwall and corner region are also captured fairly well. Finally, the CFD predictions suggest an earlier turbulent separation compared to experimental data. Since the focus of that study was to obtain general behavior of the boundary layer flow for various endwall suction configurations, it can be concluded that there is a good agreement between experimental data and CFD predictions in terms of capturing the boundary layer flow structures especially around the corner separation region.

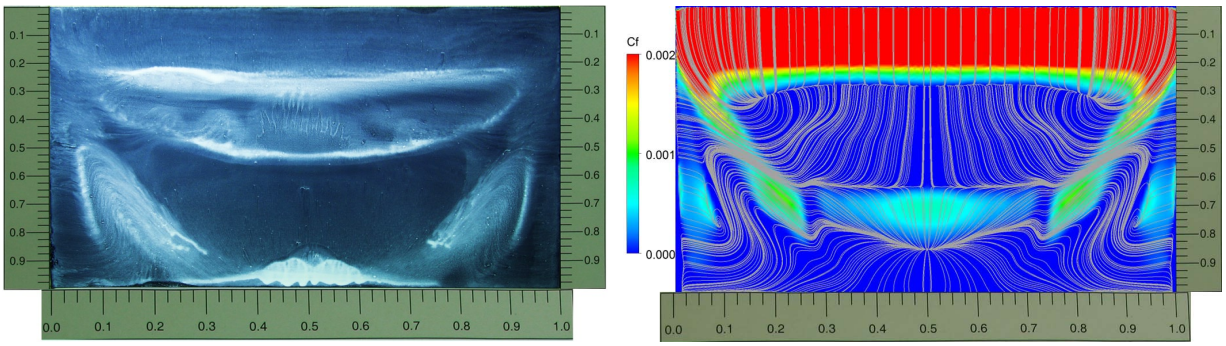

(a) Experiment (b) CFD

Figure 3.18: Baseline oil flow visualization results on the left; Streamwise skin-friction coefficient plotted together with the limiting streamlines for velocity on the right

For a further understanding of the effect of endwall suction surfaces, Figure 3.22 shows the predicted limiting streamlines on the endwall and suction surface. Figure 3.22(b) shows that the suction surface holes in EC-1 configuration pulls the endwall boundary layer streamlines toward

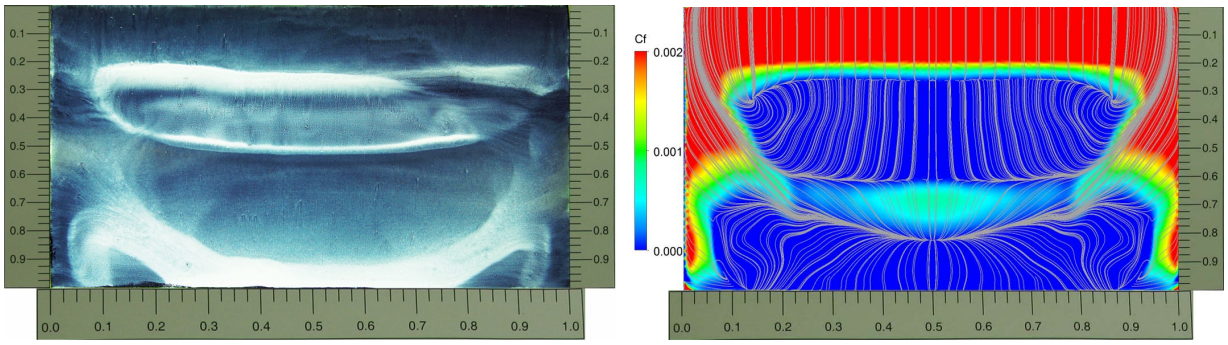

(a) Experiment (b) CFD

Figure 3.19: EC-1 oil flow visualization results on the left; Streamwise skin-friction coefficient plotted together with the limiting streamlines for velocity on the right

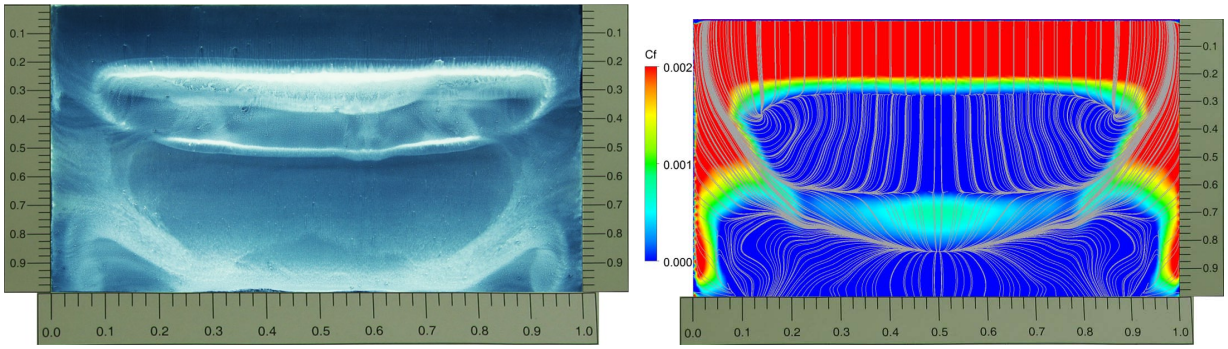

(a) Experiment (b) CFD

Figure 3.20: EC-2 oil flow visualization results on the left; Streamwise skin-friction coefficient plotted together with the limiting streamlines for velocity on the right

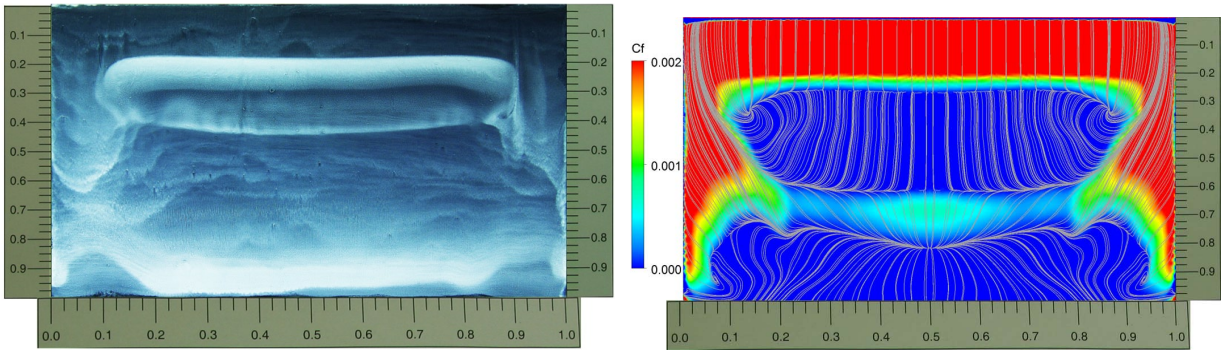

(a) Experiment (b) CFD

Figure 3.21: EC-3 oil flow visualization results on the left; Streamwise skin-friction coefficient plotted together with the limiting streamlines for velocity on the right

the suction surface and avoids endwall boundary layer flow separation observed in the baseline configuration. Moreover, the spanwise motion of the corner flow is significantly suppressed. The passage holes do not cause any significant change on the corner flow as shown in Figure 3.22(c). However, they reduce cross passage flow which moves towards to the suction surface. Finally, Figure 3.22(d) shows that the spanwise velocity component of the suction surface inlet boundary layer flow is reduced with the inlet bleed slot. This is a result of the reduced endwall boundary layer thickness which in turn reduces the endwall boundary layer blockage and reduces the contraction of passage flow.

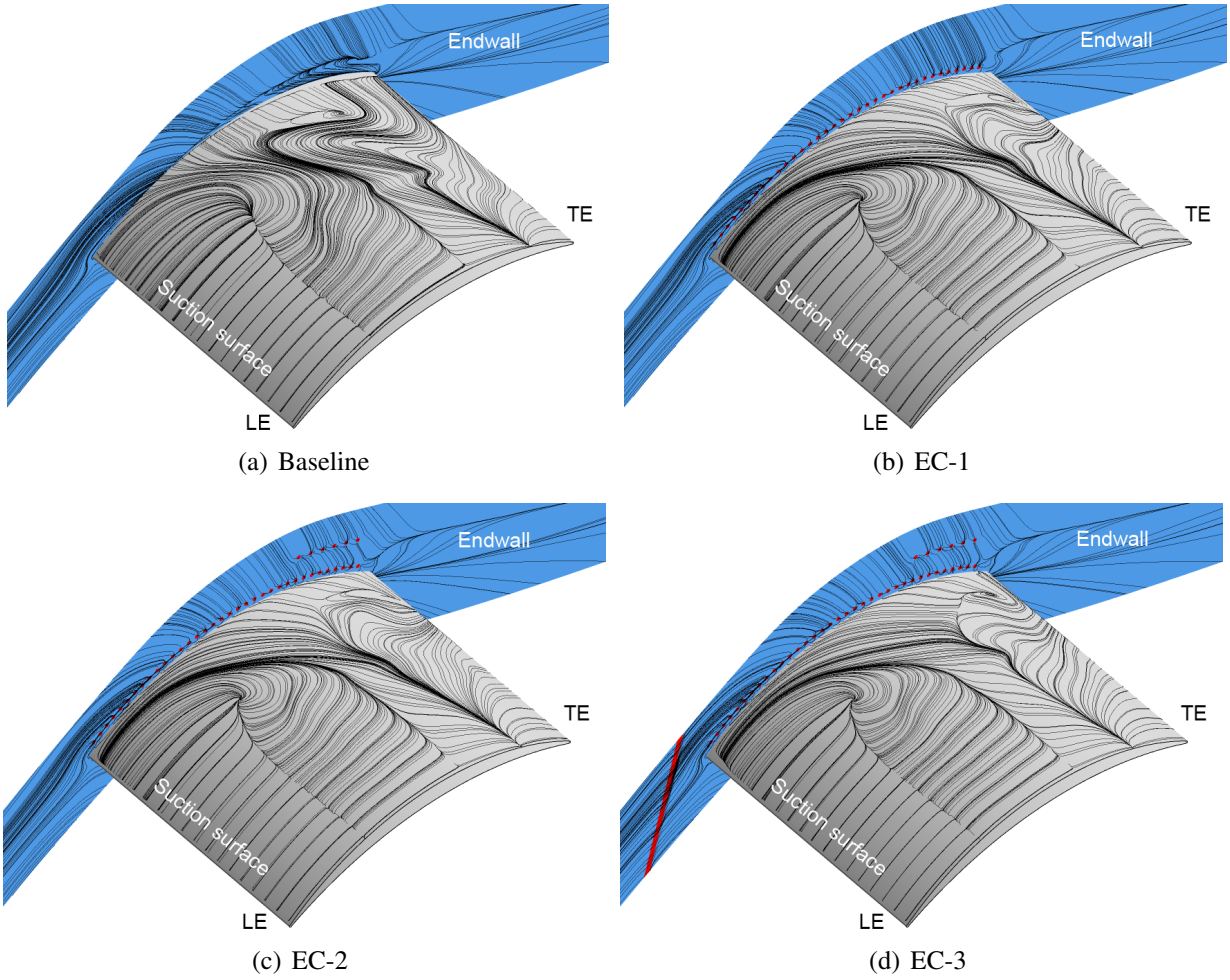

(a) Baseline (b) EC-1

(c) EC-2 (d) EC-3

Figure 3.22: Predicted limiting streamlines for the suction surface and endwall

Figure 3.23 shows the static pressure distribution coefficients for each configuration at 50%, 30%, 15% and 7.5% spanwise locations. The experiments and computations were in good agreement except for the suction configuration EC-3 where the experimental surface pressure distribution does not suggest a laminar separation bubble on the suction surface. However, the surface flow visualization given in Figure 3.21 shows the presence of a separation bubble on the suction surface. This result suggests that the separation bubble cannot always be inferred from the pressure distribu-

tion, especially when the separation bubble thickness is small. Both experiments and computations show that the separation bubble disappears close to the endwall as previously shown in oil-film flow visualizations. As expected, the pressure surface pressure distribution was not modified as much as suction surface pressure distribution.

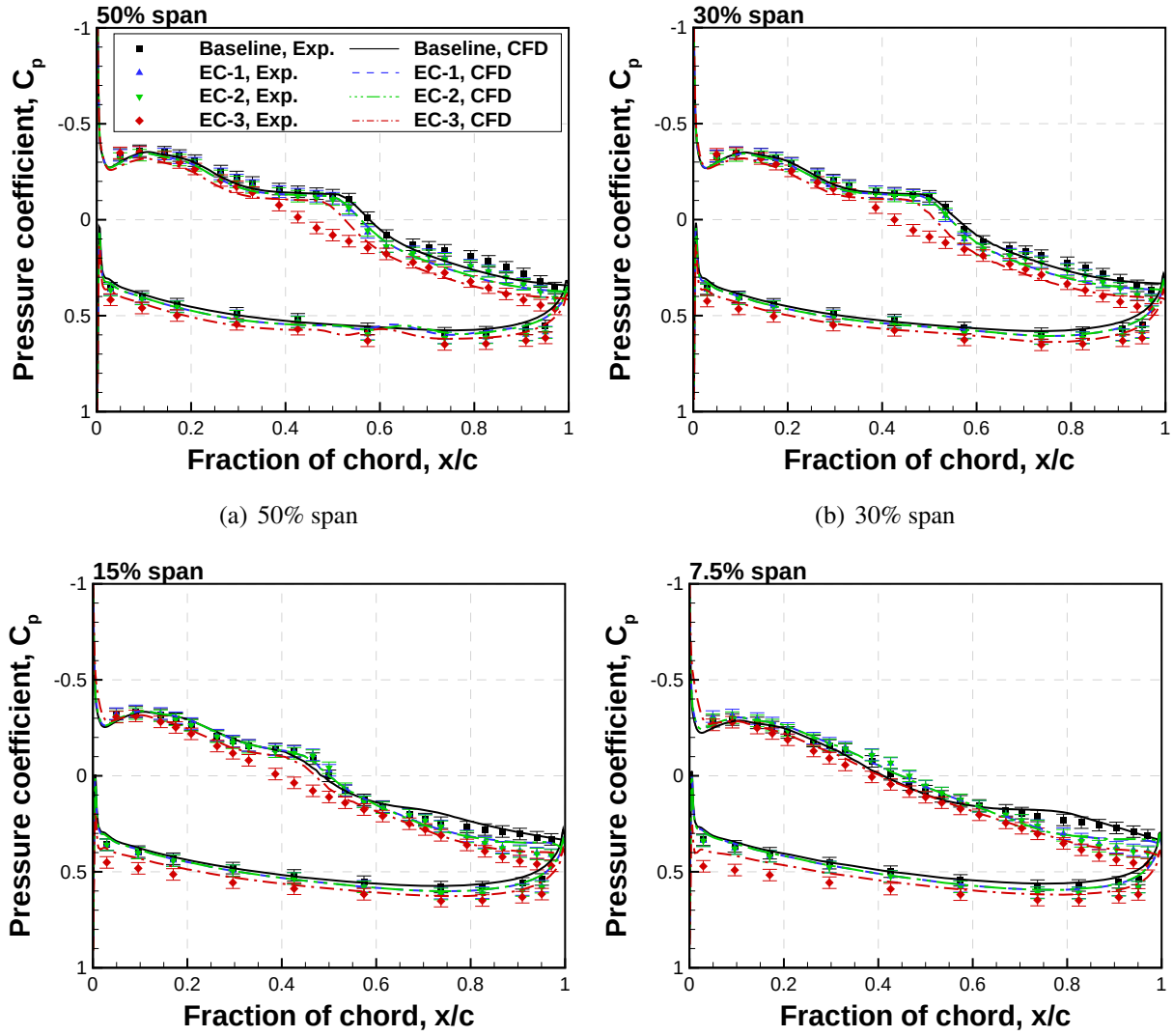

(a) 50% span

(b) 30% span

(c) 15% span

(d) 7.5% span

Figure 3.23: Experimental and computational surface pressure distributions for each endwall suction configuration at each spanwise location

The seven-hole probe measurements and computational results for total pressure loss coefficient at 0.4 c_x downstream of the blade trailing edge are shown in Figures 3.24-3.27. Overall, the size of the high total pressure loss region caused by corner separation diminishes with the endwall suction flow control. The EC-3 configuration caused the most significant reduction in total pressure loss at the corner separation region. It can be seen that the CFD simulations over-predict the profile losses in all endwall suction configurations. It is interesting to note that both the experimental and

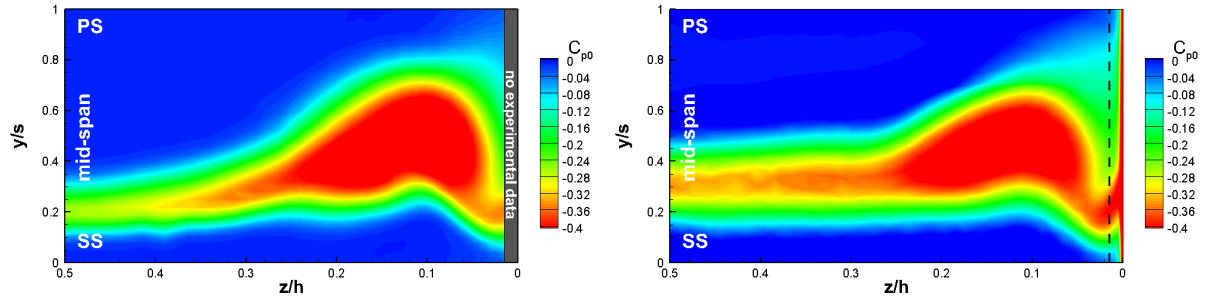

(a) Experiment (b) CFD

Figure 3.24: Contours of total pressure loss coefficient (C_{p_0}) at 0.4 c_x downstream plane for baseline

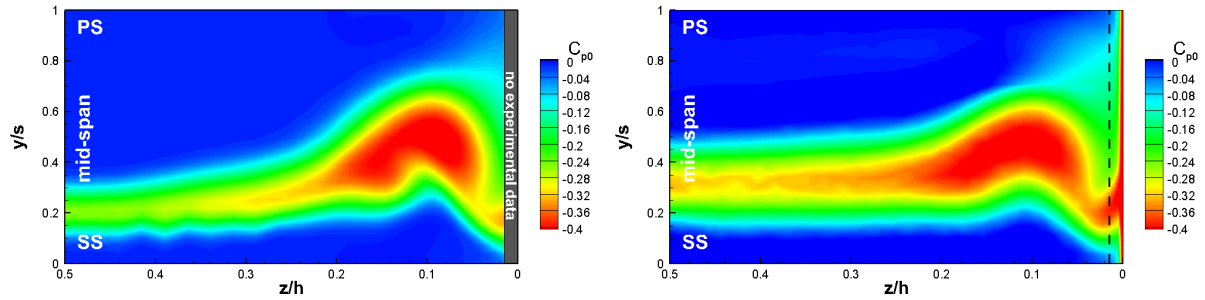

(a) Experiment (b) CFD

Figure 3.25: Contours of total pressure loss coefficient (C_{p_0}) at 0.4 c_x downstream plane for EC-1

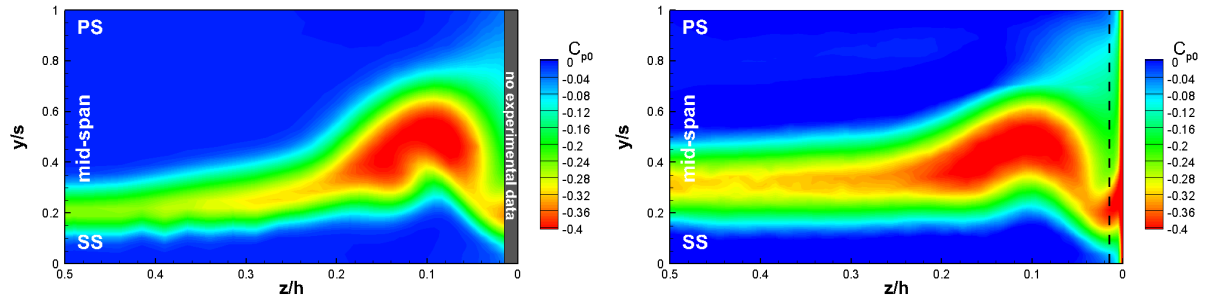

(a) Experiment (b) CFD

Figure 3.26: Contours of total pressure loss coefficient (C_{p_0}) at 0.4 c_x downstream plane for EC-2

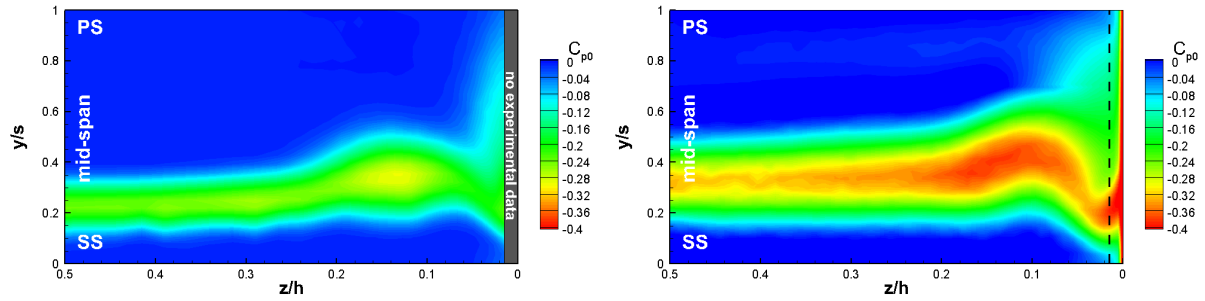

(a) Experiment (b) CFD

Figure 3.27: Contours of total pressure loss coefficient (C_{p_0}) at 0.4 c_x downstream plane for EC-3

computational data indicate that the mid-span wake size is almost unaffected.

To draw conclusions from quantitative comparisons, the overall total pressure loss coefficient values at 0.4 c_x downstream of the blade trailing edge are listed in Table 3.4. The measurements for EC-3 configuration show that the overall total pressure loss coefficient is reduced by 3.52% of inlet dynamic head. The experimental and computational result compared reasonable well for all cases except EC-3. For EC-3 configuration, the computations over-predicted the overall total pressure loss coefficient.

Table 3.4: Experimental and computational overall total pressure loss coefficient (ω_0)

Configuration	ω_0		$\triangle(\omega_0)$	
	(Experiment)	(CFD)	(Experiment)	(CFD)
Baseline	0.0553±0.01	0.0575	-	-
EC-1	0.0399±0.01	0.0446	0.0154	0.0129
EC-2	0.0397±0.01	0.0441	0.0156	0.0134
EC-3	0.0201±0.01	0.0371	0.0352	0.0204

Table 3.5 presents the experimental and computational AVR values for each configuration. For the baseline, the AVR was measured to be 1.071. The endwall suction with EC-3 configuration observed to reduce AVR to 0.985 in the experiments. Overall, the difference between the experimental and computational data is within measurement error which is stated in Section 2.3.6 as ±0.02 with 95% confidence. The difference between the experimental and computational results can be attributed to the experimental uncertainties in flow angle and velocity measurements both at the inlet and outlet planes.

Table 3.5: Experimental and computational AVR values

Configuration	AVR	
	(Experiment)	(CFD)
Baseline	1.071±0.02	1.060
EC-1	1.032±0.02	1.024
EC-2	1.030±0.02	1.023
EC-3	0.985±0.02	1.003

Both experimental and computational results show that the endwall corner separation can be suppressed with endwall boundary layer bleed. The effect of the endwall bleed becomes the maximum with the EC-3 configuration where 2.42% of the inlet mass flow was ingested to reduce the overall loss coefficient by 3.52% of inlet dynamic head.

The experimental and computational results in terms of surface pressure distribution, oil flow visualization and downstream plane total pressure loss contours were in good agreement except

for EC-3 configuration where inlet bleed (IB) slot was open. This result can be partially attributed to the over-estimated laminar separation bubble. In addition to that, the discrepancy between experimental and computational data can also be attributed to the possible interference of the inlet bleed adjusting plate with the endwall boundary layer fluid in the experiments. The adjusting plate shown in Figure 3.28(a) was used to adjust the width of the IB slot in an effort to control the bleed mass flow rate in the experiments. As depicted in Figure 3.28(b), the inlet bleed was accepted as a constant width slot (without adjusting plate) in the computational setup.

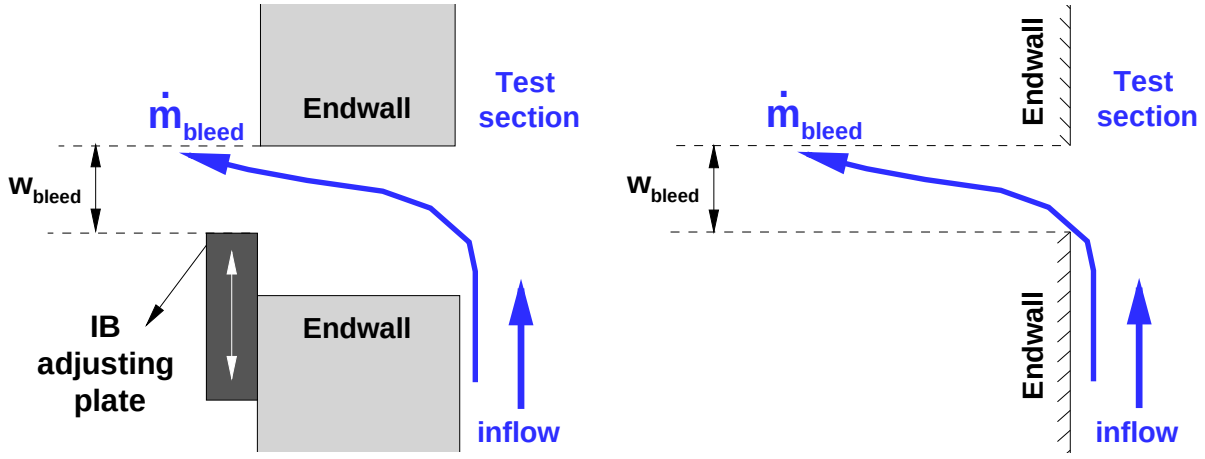

(a) Experimental setup (b) Computational setup

Figure 3.28: Schematic illustration of the difference between the experimental and computational configurations for inlet bleed (IB) slot

3.3.1 Endwall Suction at High Speed

After validating the computational model, the endwall boundary layer suction study was carried out at a Reynolds number of 3×10^5 (corresponding to an inlet velocity of 40 m/s). The endwall boundary layer suction was applied using EC-1 configuration by ingesting 1.32% of the inlet mass flow.

Figure 3.29 shows the streamwise skin friction coefficient plotted together with the limiting streamlines for velocity. For the baseline, the laminar separation bubble becomes smaller at high Reynolds number (Re_c=3.0×10^5) since the transition point moves upstream and turbulent reattachment takes place earlier as seen in Figure 3.29(b). Moreover, the turbulent boundary layer separation close to the trailing edge moves downstream. It can be seen that the endwall suction has a very similar effect on the suction surface boundary layer flow at high Reynolds number where the spanwise motion of the suction surface boundary layer fluid towards the mid-span is reduced and the corner separation is suppressed.

Figure 3.30 shows the total pressure loss coefficient at 0.4 c_x downstream of the blade trailing edge. Comparing the baseline cases at two Reynolds numbers, it can be seen that profile losses are

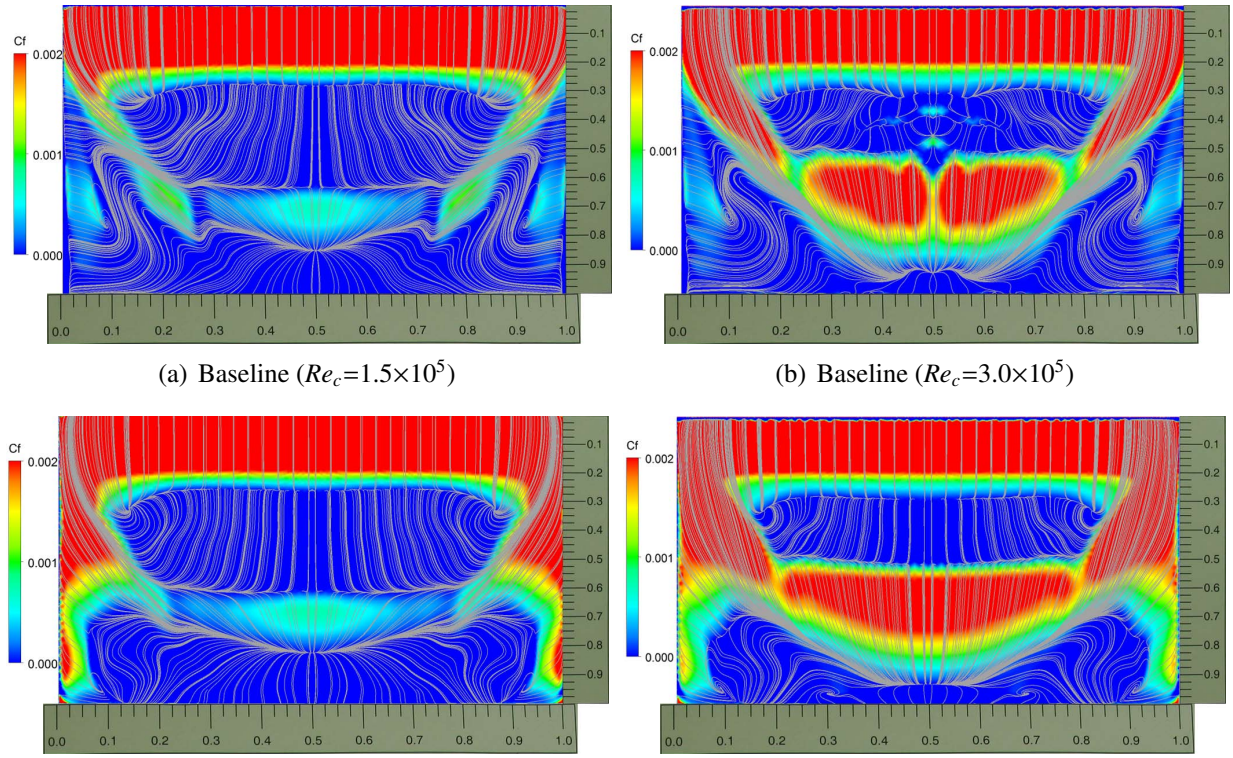

(a) Baseline (Re_c=1.5×10^5)

(b) Baseline (Re_c=3.0×10^5)

(c) EC-1 (Re_c=1.5×10^5)

(d) EC-1 (Re_c=3.0×10^5)

Figure 3.29: Predicted streamwise skin-friction coefficient plotted together with the limiting streamlines for velocity at high speed

reduced at high speed. Besides, the losses arising due to endwall corner separation stays almost the same at high speed. It can be seen that the size of the high total pressure loss corner separation region becomes smaller with the endwall suction.

The overall loss coefficients at 0.4 c_x downstream of the blade trailing edge are listed in Table 3.6. It can be seen that the overall loss coefficient reduces as the Reynolds number is increased from 1.5×10^5 to 3.0×10^5. It can be observed from Figure 3.30 that the reduction in overall total pressure loss coefficient at high Reynolds number is caused by the reduced profile losses. At Re_c=1.5×10^5, the endwall suction with EC-1 configuration reduces the overall total pressure loss coefficient by 1.29% of inlet dynamic head. At Re_c=3.0×10^5, the overall total pressure loss coefficient reduction is 1.37% of inlet dynamic head. The computations at high Reynolds number therefore show that the proposed endwall corner separation control method works efficiently in suppressing the endwall corner separation at a Reynolds number of 3.0×10^5.

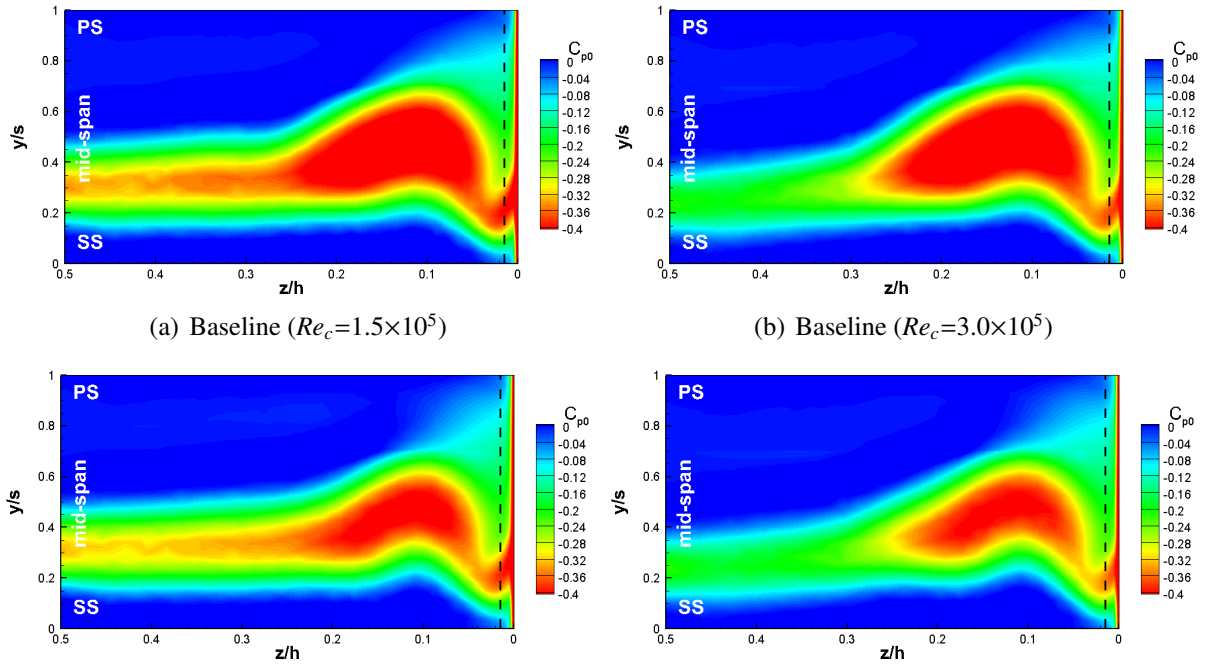

(a) Baseline (Re_c=1.5×10^5)

(b) Baseline (Re_c=3.0×10^5)

(c) EC-1 (Re_c=1.5×10^5)

(d) EC-1 (Re_c=3.0×10^5)

Figure 3.30: Predicted contours of total pressure loss coefficient (C_{p_0}) at 0.4 c_x downstream plane at high speed

Table 3.6: Predicted overall total pressure loss coefficient (ω_0) at high speed

Case	ω_0	$\triangle(\omega_0)$
Baseline (Re_c=1.5×10^5)	0.0575	-
Baseline (Re_c=3.0×10^5)	0.0464	-
EC-1 (Re_c=1.5×10^5)	0.0446	0.0129
EC-1 (Re_c=3.0×10^5)	0.0327	0.0137

3.4 Enhanced Plasma Actuation

In this section, the validated computational setup was used to assess plasma actuator requirements to achieve comparable results with EC-3 endwall suction case. The endwall plasma actuation was applied using $F_{act,1}$ & $F_{act,3}$ configuration at an actuation strength of 300 mN/m. Computations were performed at a Reynolds number of 1.5×10^5 corresponding to an inlet flow velocity of 20 m/s.

Figure 3.31(a) shows total pressure loss coefficient distributions at 0.4 c_x downstream of the blade trailing edge. The baseline results corresponding to the plasma actuation and endwall suction flow control are shown in the figure together with the flow control applied cases. It can be seen that the plasma actuation reduces both corner separation and profile losses. The endwall suction diminishes the corner separation losses, whereas the endwall suction mostly only affected corner separation losses. Table 3.7 presents the overall total pressure loss coefficient results at 0.4 c_x downstream of the blade trailing edge. As can be seen, the plasma actuation at 300 mN/m actuation

strength reduces the loss coefficient by 2.74% of the inlet dynamic head. On the other hand, the endwall suction reduces the loss coefficient by 2.04% of inlet dynamic head using 2.42% of the inlet mass flow in total as discharged mass flow.

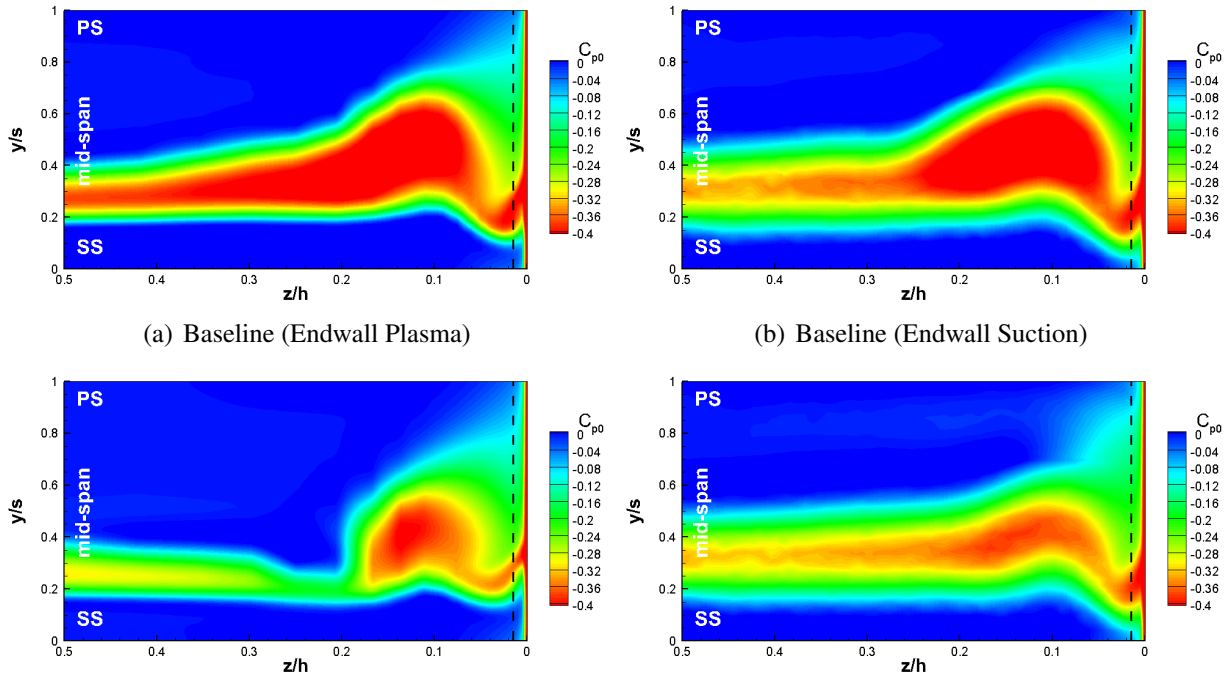

(a) Baseline (Endwall Plasma)

(b) Baseline (Endwall Suction)

(c) F_{act} = 300mN/m

(d) Suction, EC-3

Figure 3.31: Predicted contours of total pressure loss coefficient (C_{p_0}) at 0.4 c_x downstream plane for enhanced plasma actuation

Table 3.7: Predicted overall total pressure loss coefficient (ω_0) for enhanced plasma actuation

Case	ω_0	$\triangle(\omega_0)$
Baseline (Endwall plasma)	0.0528	-
Baseline (Endwall suction)	0.0575	-
F_{act} = 300mN/m	0.0254	0.0274
EC-3	0.0371	0.0204

To determine the plasma actuation effect on the overall passage flow, the total pressure loss coefficient distributions are shown in Figure 3.32. The plane located at the mid-chord shows that the plasma actuation at an actuation strength of 300 mN/m eliminates the total pressure losses arising from the endwall boundary layer and blade boundary layer significantly.

Figure 3.33 shows the non-dimensional boundary layer displacement thickness (δ^*/c) distributions on the endwall and suction surface. The high δ^*/c region caused by the corner stall on the blade suction surface seems to be diminished significantly by the plasma actuation. Plasma actuation observed to reduce the displacement thickness around 25% span of the blade trailing edge

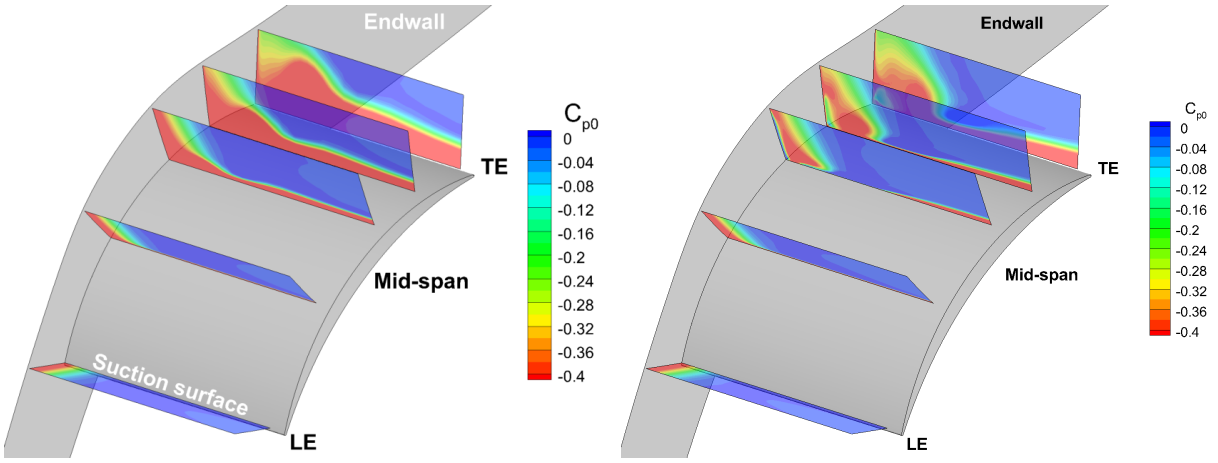

(a) Baseline (b) F_{act} = 300mN/m

Figure 3.32: Predicted total pressure loss coefficient (C_{p_0}) distributions at various chordwise planes for enhanced plasma actuation

significantly. It should be noted that the blue contour with δ^*/c=0 on the endwall (around 0.5 chord in Figure 3.33(b)) is caused by the plasma actuation. The flow accelerated by the plasma actuation excessively diminishes the boundary layer displacement thickness.

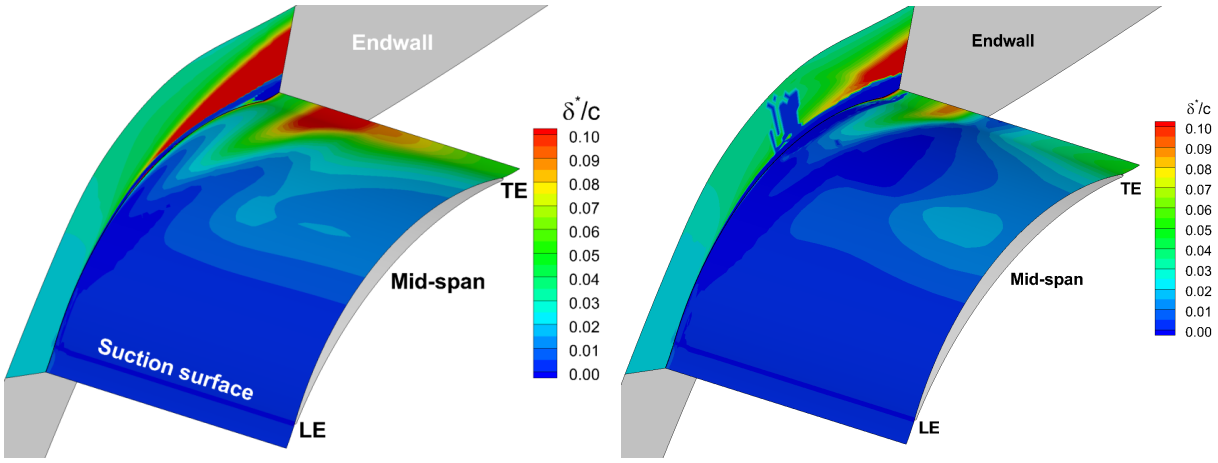

(a) Baseline (b) F_{act} = 300mN/m

Figure 3.33: Predicted boundary layer displacement thickness distributions over the suction surface and endwall for enhanced plasma actuation

3.4.1 Reynolds Number Scaling for Endwall Corner Separation Control

In this section, Reynolds number scaling study performed for the plasma actuation endwall flow control is presented. The Reynolds number scaling study was performed for a Reynolds number range between 1.5×10^5 and 7.5×10^5 using $F_{act,1}$ & $F_{act,3}$ plasma actuator configuration to achieve a 51.5%±0.5 reduction in overall total pressure loss coefficient. It can be observed in Figure 3.34 that the plasma actuation strength shows a non-linear increase with the Reynolds number and Mach

number increase to achieve the same overall total pressure loss coefficient reduction. It can also be seen that the best fit to this data was obtained using a 1.616 power-law function. The non-linear growth can be explained by the fact that the required plasma actuation strength is proportional to square of the flow velocity. It is computationally demonstrated in Appendix A.3 that the plasma actuation strength is proportional to $V^2_{induced}$. It must be noted that this scaling study is preliminary and limited in flow velocity because the nominal loss in total pressure reduces as the Reynolds number increases, as evidenced in Figure 3.35. The need for flow control on a particular geometry is thus decreased with rising Reynolds number such that a more accurate scaling would require the blade camber to be increased with Reynolds number to maintain the same value of total pressure loss coefficient.

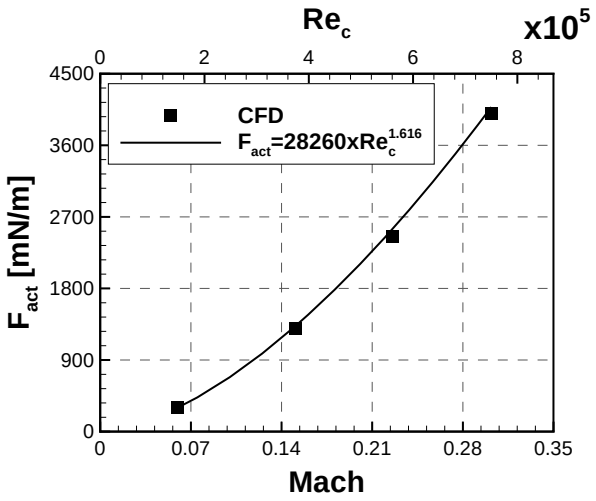

Figure 3.34: Reynolds number scaling for endwall corner separation control with plasma actuation

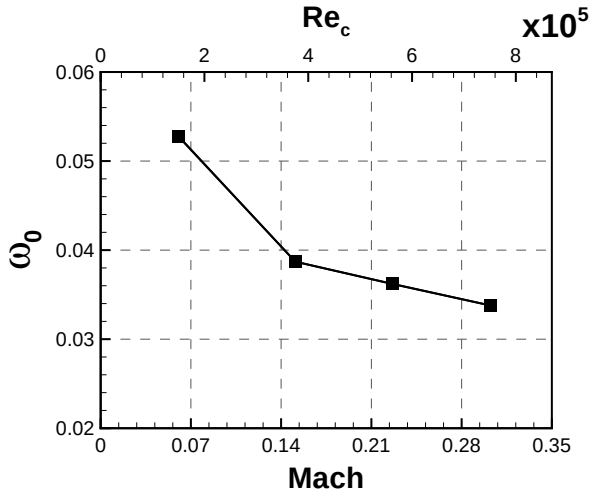

Figure 3.35: Reynolds number effect on the overall total pressure loss coefficient of unactuated blade (taken at 0.4 c_x downstream of the blade trailing edge)

3.5 Summary

In summary, the numerical simulations can capture the experimentally observed flow features and trends associated with corner separation and the effect of endwall suction and plasma actuation on this phenomenon. Simulations with this CFD setup show that a combination of plasma actuators located at the upstream of the separation point on the suction surface and endwall (both adding streamwise momentum) is the better option of the cases tested, with most of the improvement coming from the suction surface actuator. While the current endwall suction configuration provides the best performance yet in terms of corner separation reduction at very low suction mass flow, plasma actuation with high but near-term reachable actuator strength can rival this performance at the low-speed cascade conditions. Simulations at higher speeds indicate that the required actuation strength scales approximately with the square of the Reynolds number.

Chapter 4

Plasma Actuation Flow Control for Boundary Layer Separation

In this chapter, the experimental and computational studies, performed for the plasma actuation boundary layer flow control, are presented. Simulations and experiments with plasma actuation were carried out in continuous and pulsed modes. Unless otherwise stated, a Reynolds number of 1.5×10^5 (corresponding to a 20 m/s inlet velocity) was used. The effectiveness of plasma actuation is determined based on the pressure rise coefficient.

4.1 Parametric Study for Plasma Actuation Parameters

This section presents the computational results for the parametric study carried out in terms of plasma actuator location, actuation strength, pulsing frequency, duty cycle and actuation mode to determine the plasma actuation effectiveness in controlling the boundary layer flow separation.

4.1.1 Continuous Plasma Actuation

Continuous plasma actuation simulations were performed to assess the effect of plasma actuator location and strength on the boundary layer flow separation control.

Plasma Actuator Location Effect

Previously, it was shown in Section 3.1.3 that laminar boundary layer flow separation occurs on the suction surface at 0.29 chord. The plasma actuator location effect was assessed at actuator locations, namely 0.15 chord, 0.22 chord, 0.3 chord and 0.35 chord. Figure 4.1 shows the plasma actuation body force vectors at each location. Plasma actuation was applied in continuous mode with an actuation strength of 150 mN/m which is close to the maximum achievable plasma actuation strength in the literature (Thomas *et al*., 2009).

The pressure coefficient and skin friction coefficient distributions over the blade suction surface are shown in Figure 4.2. It can be seen that the plasma actuation moved the separation point downstream in all cases. The most aft plasma actuator location delayed the boundary layer flow

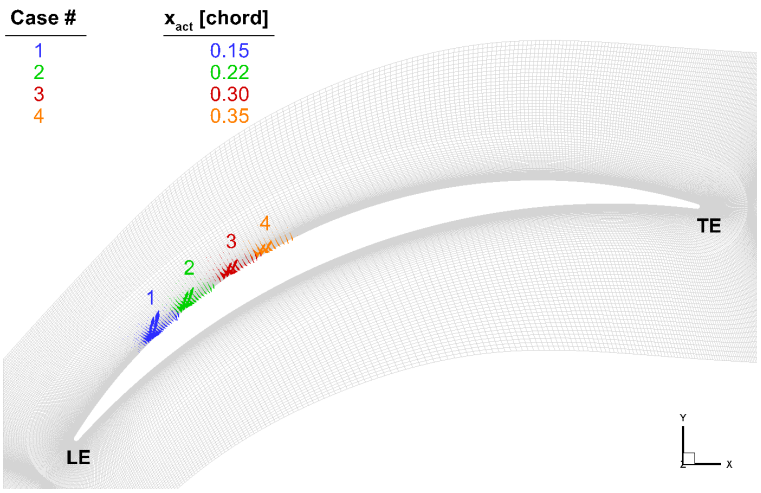

Figure 4.1: Plasma actuator locations on DCA-1 airfoil

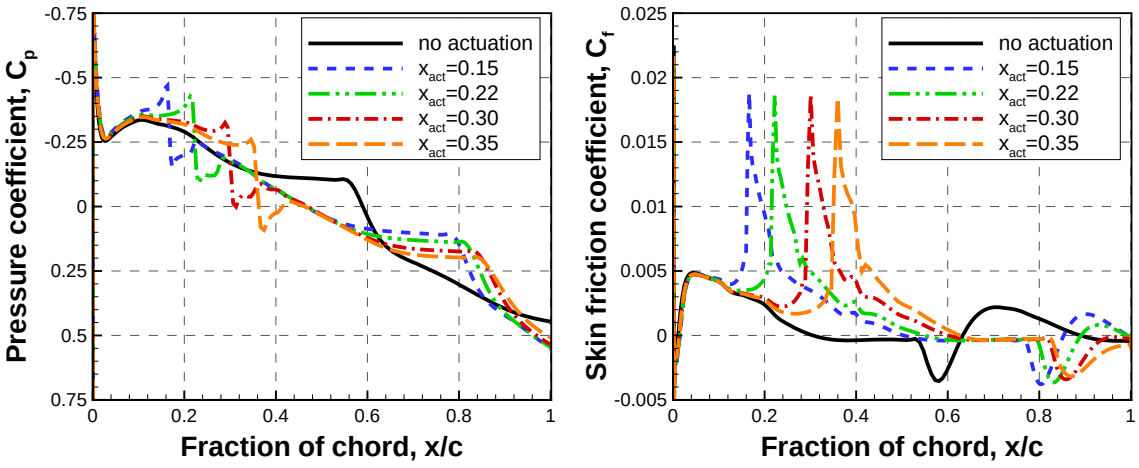

(a) Suction surface pressure distribution

(b) Suction surface skin friction coefficient distribution

Figure 4.2: Actuator location effect on suction surface pressure coefficient and skin friction coefficient distribution

separation the most from 0.29 chord to 0.63 chord. Figure 4.3 shows the plasma actuator location effect on suction surface momentum thickness distribution. The plasma actuation reduces the momentum thickness distribution significantly. The plasma actuators located at 0.3 chord and 0.35 chord have almost the same effect on momentum thickness. Note that the plasma actuator location has almost no effect on momentum thickness downstream of 0.42 chord for the cases studied here.

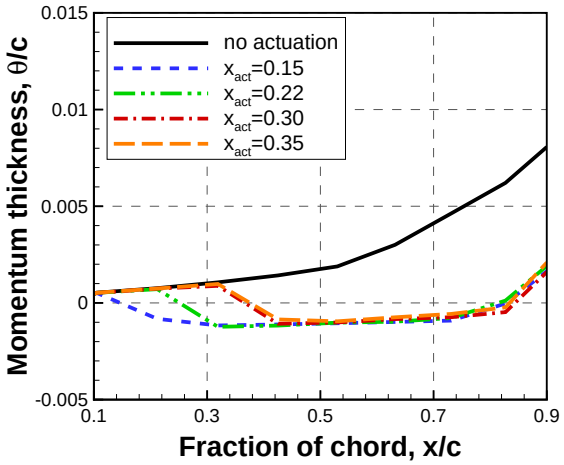

Figure 4.3: Actuator location effect on suction surface momentum thickness distribution

Figure 4.4 shows the plasma actuator location effect on cascade performance. The pressure rise coefficient (ψ) is increased by plasma actuation at all locations between 0.15 chord and 0.35 chord. It can be seen that a higher pressure rise coefficient is achieved as the plasma actuator moves upstream. The pressure rise coefficient improvement is based on three factors, namely, increased flow turning, reduced blockage and reduced boundary layer total pressure loss. The increase in flow turning can be inferred from the reduction in deviation angle (δ) shown in Figure 4.4(b). In addition, the reduction in trailing edge plane boundary layer displacement thickness (suggesting a lower blockage, hence higher diffusion) shown in Figure 4.4(c). Finally, the reduced boundary layer total pressure loss can be inferred from the reduction of overall total pressure loss coefficient (ω_0) in Figure 4.4(d). These factors explain the observed increase in pressure rise coefficient shown in Figure 4.4(a).

The effectiveness of plasma actuation reduces for the plasma actuators located far downstream (x_{act}=0.35). This can be explained by the delay of turbulent reattachment when the plasma actuators are located far downstream. It can be inferred from Figure 4.2(b) where the turbulent flow reattachment takes place just before the trailing edge for plasma actuators located at 0.30 chord and 0.35 chord.

From the point of view of power input, the plasma actuators located closer to the blade leading edge cause a larger increase in the rotor equivalent power ($\dot{W}_{req}$) as a result of high flow turning as shown in Figure 4.5(a). However, they require more plasma power ($\dot{W}_{plasma}$) where the power

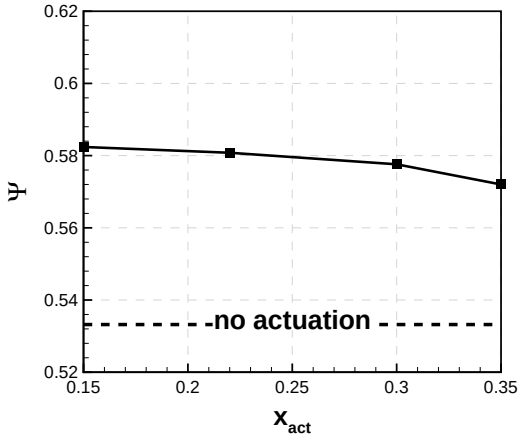

(a) Pressure rise coefficient

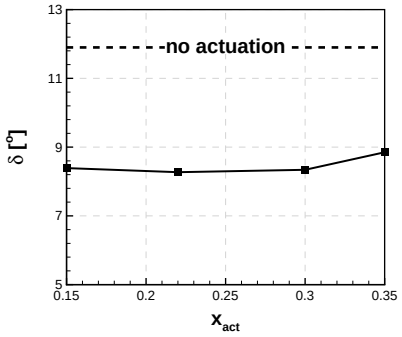

(b) Deviation angle

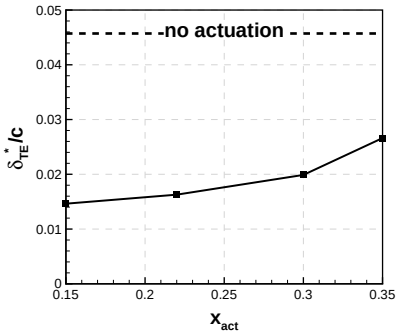

(c) Trailing edge displacement thickness at suction surface

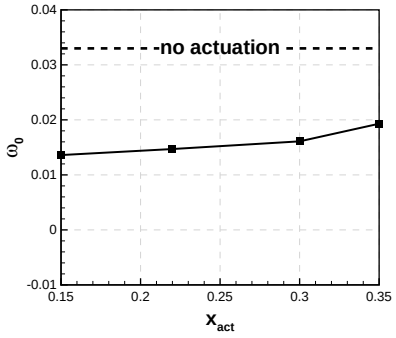

(d) Overall loss coefficient

Figure 4.4: Actuator location effect on cascade performance

ratio ($R_p = \frac{\dot{W}_{plasma}}{\dot{W}_{req}} \times 100$) becomes the maximum for plasma actuation at 0.15 chord as presented in Figure 4.5(c). While the power ratio for the plasma actuation at 0.15 chord is 1.41%, this value reduces down to 1.21% for the plasma actuation at 0.35 chord. The boundary layer is more developped (δ^* is high) at 0.35 chord compared to 0.15 chord. Therefore, the velocity near the actuator is smaller than at 0.15 chord which explains the smaller power ratio (R_p) at 0.35 chord. Finally, the plasma actuator location seems to have a very little effect on the plasma actuation efficiency (η_p) as presented in Figure 4.5(d) where the plasma actuation efficiency is the ratio of rotor equivalent and plasma power difference to plasma power in percentage.

Although the plasma actuation at 0.15 chord requires slightly more plasma power due to higher flow velocity, this location is superior compared to 0.22 chord location in terms of performance where the pressure rise coefficient increased the most. Based on these results, the plasma actuation simulations for the other remaining plasma actuation parameters were carried out using the plasma actuator located at 0.15 chord.

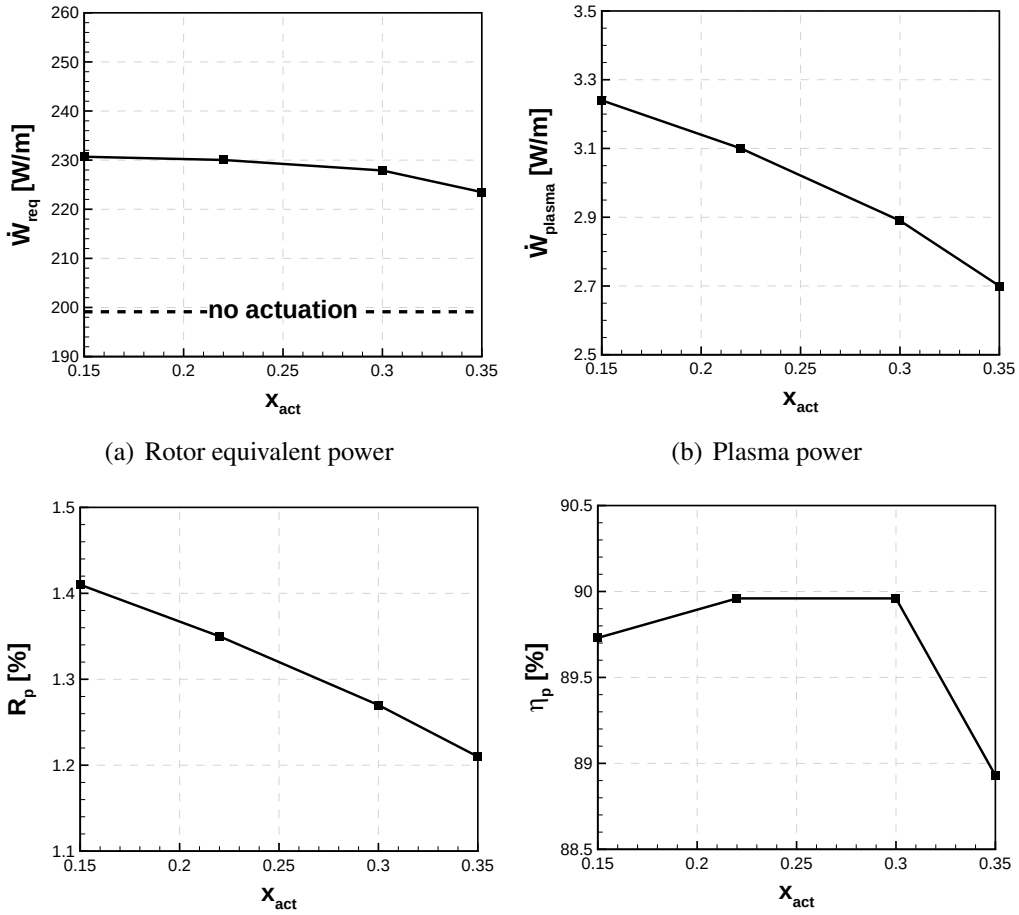

(a) Rotor equivalent power

(b) Plasma power

(c) Power ratio

(d) Plasma actuation efficiency

Figure 4.5: Actuator location effect on power parameters

Actuation Strength Effect

Four simulations were performed to evaluate the effect of plasma actuation strength. The plasma actuation was applied in continuous mode at 0.15 chord with actuation strengths between 50 and 400 mN/m. The pressure and skin friction coefficient distributions, shown in Figure 4.6, reveal that the actuation strength has a major effect on the development of the suction surface boundary layer flow. The separation point moves further downstream as the actuation strength increases. Furthermore, Figure 4.7 shows that the momentum thickness is reduced significantly over the blade surface as actuation strength increases, becoming even negative for all actuation strengths above 50 mN/m. The negative momentum thickness implies a momentum surplus instead of momentum deficiency in the boundary layer.

Figure 4.8 shows the effect of actuation strength on the cascade performance. It can be seen that as the actuation strength increases the pressure rise coefficient increases significantly. However, these plots also show a non-linear increase in pressure rise with diminishing effect as actuation strength increases. This asymptotic trend can be attributed to the variation of induced flow velocity

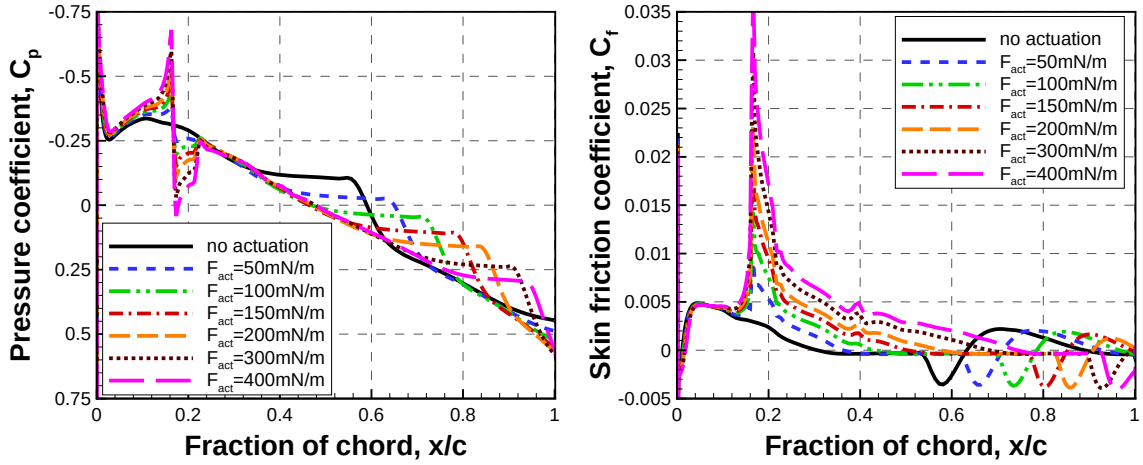

(a) Suction surface pressure distribution

(b) Suction surface skin friction coefficient distribution

Figure 4.6: Actuation strength effect on suction surface pressure coefficient and skin friction coefficient distributions

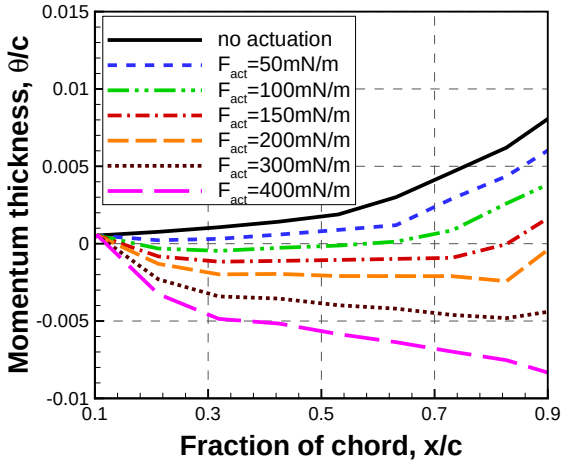

Figure 4.7: Actuation strength effect on suction surface momentum thickness distribution

with plasma actuation strength. The increase of pressure rise coefficient comes from a reduction in deviation angle (i.e. increased flow turning) and boundary layer displacement thickness (reduced blockage), combined with a reduction in overall total pressure loss. It can seen that the deviation angle levels off after 300 mN/m and becomes closer to the minimum deviation angle as determined from inviscid flow solution. The reduction in total pressure loss can be attributed to a delay in boundary layer transition (reduced losses associated with delayed turbulent boundary layer) with increased actuation strength as can be seen from TKE contours in Figure 4.9. The levelling off in deviation angle δ and displacement thickness δ^*/c above 300 mN/m can be explained by the delayed boundary layer transition. Therefore, the higher plasma actuation strength causes a boundary layer separation closer to the trailing edge which can be inferred from skin friction coefficient previously shown in Figure 4.6(b).

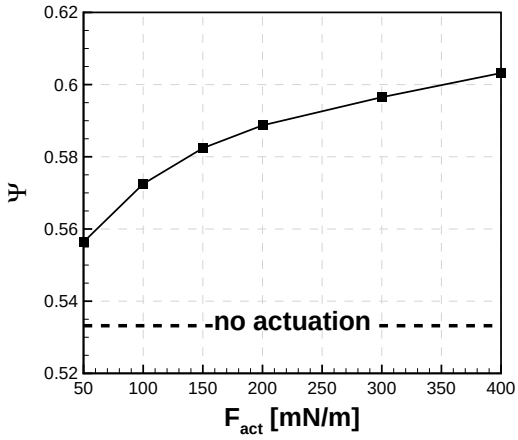

(a) Pressure rise coefficient

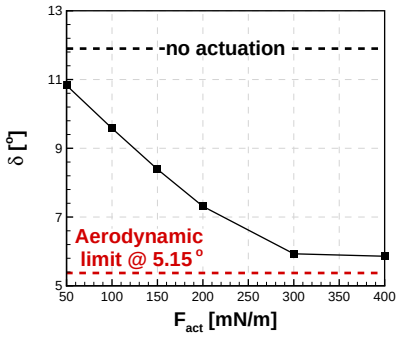

(b) Deviation angle

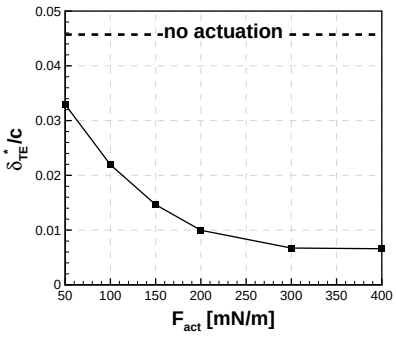

(c) Trailing edge displacement thickness at suction surface

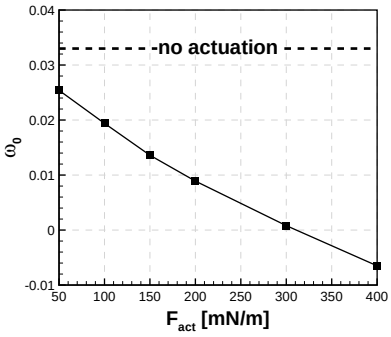

(d) Overall loss coefficient

Figure 4.8: Actuation strength effect on cascade performance

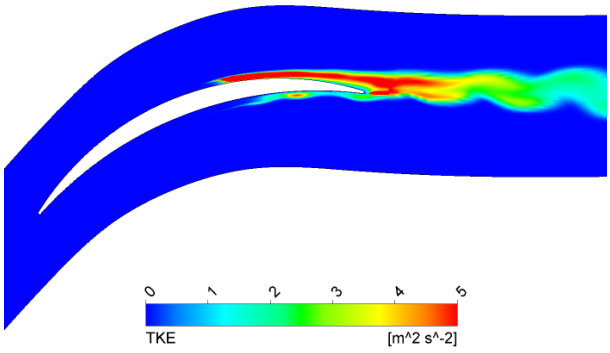

(a) F_{act}=50 mN/m

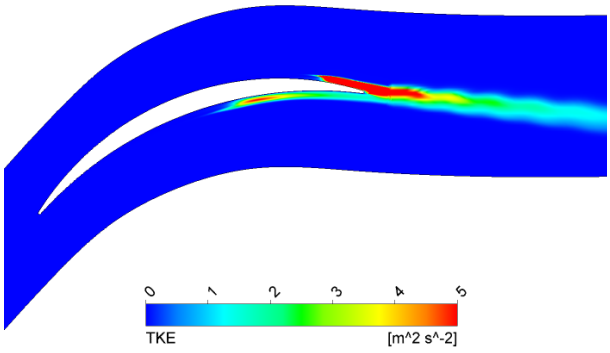

(b) F_{act}=400 mN/m

Figure 4.9: TKE contours for plasma actuation strengths of 50 mN/m and 200 mN/m

The power analysis for the plasma actuation strength effect is shown in Figure 4.10. As stated earlier, the rate of improvement on the cascade performance reduces as the plasma actuation strength increases. A similar trend is observed in rotor equivalent power ($\dot{W}_{req}$). Moreover, the plasma power ($\dot{W}_{plasma}$) and plasma power ratio (R_p) increases almost linearly with actuation strength. As a result, the plasma actuation efficiency (η_p) decreases as actuation strength increases.

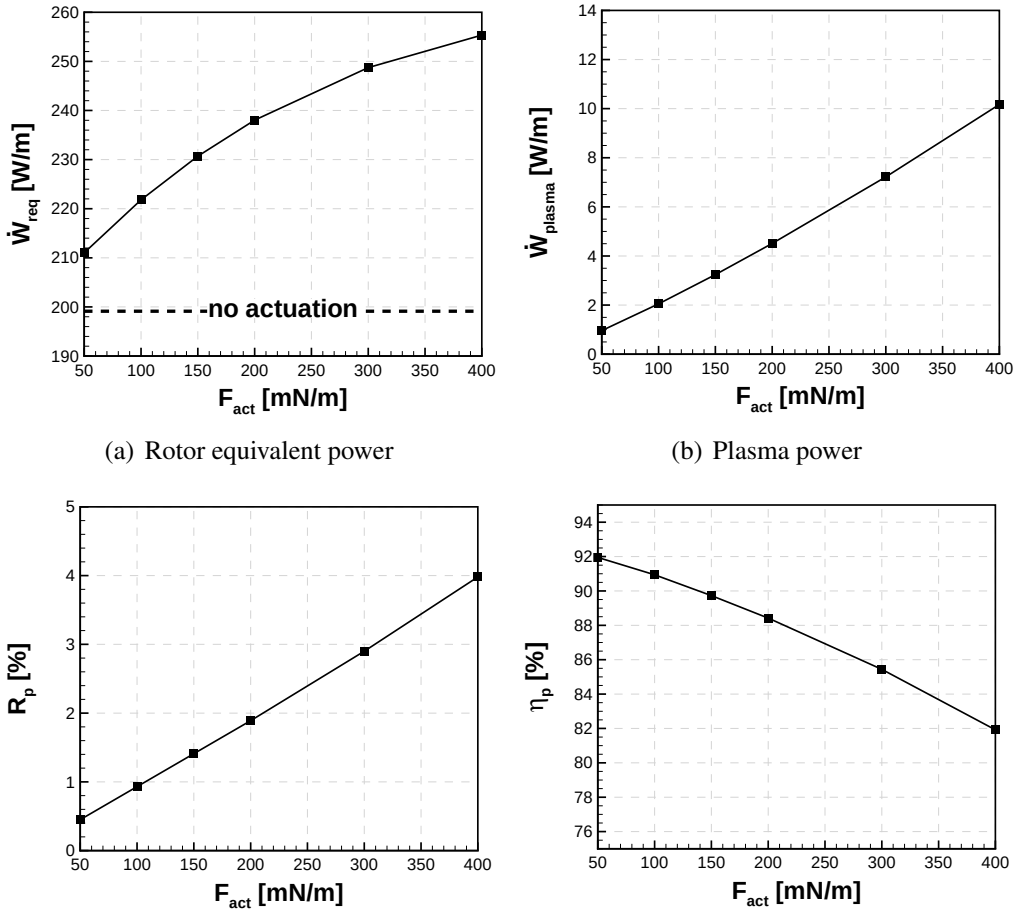

(a) Rotor equivalent power

(b) Plasma power

(c) Power ratio

(d) Plasma actuation efficiency

Figure 4.10: Actuation strength effect on power parameters

4.1.2 Pulsed Plasma Actuation

The pulsed actuation simulations were performed to assess the effect of pulsing frequency and duty cycle on the boundary layer flow separation control.

Pulsing Frequency Effect

The resonant frequencies for turbulent structures within the boundary layer were determined by performing a discrete Fourier Transform (DFT) on time history of velocity. The velocity signal was obtained using numerical probes shown in Figure 4.11. Three probes reside inside the boundary layer and located downstream of the laminar separation point. The other probe is placed just outside the boundary layer. Figure 4.12 shows the spectral analysis of the velocity data for probe number 1. The frequencies with the highest amplitudes represent the resonant frequencies. The resonant frequencies were observed to be similar for the other probes. The first two frequencies, 388 Hz and 776 Hz (the latter being a harmonic of the former), were chosen to determine the pulsing frequency effect. The Strouhal numbers corresponding to these frequencies were 0.72 and 1.44, respectively.

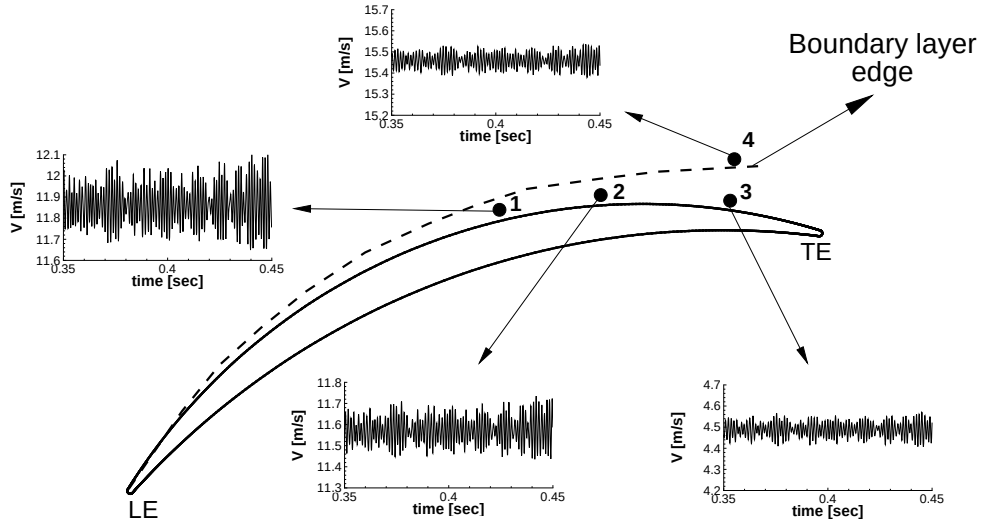

Figure 4.11: Numerical probes located on the suction side of the DCA-1 airfoil

In addition to resonant frequencies estimated from the velocity signal, the simulations were also carried out at a frequency of 530 Hz corresponding to a Strouhal number of unity, which has been reported as the optimum pulsing frequency by Huang (2005); Huang *et al*. (2006); Little and Samimy (2010); Corke *et al*. (2011). The plasma actuator with an actuation strength of 150 mN/m was located at 0.15 chord. The duty cycle was held constant at 0.3 which is a reasonable value of duty cycle based on the literature (Huang, 2005).

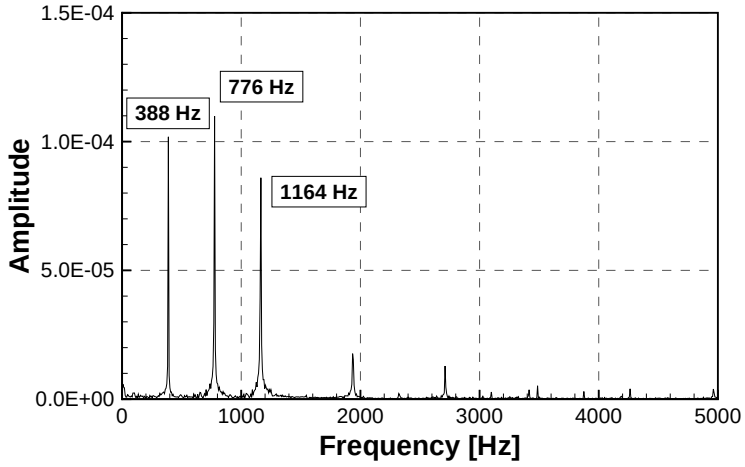

Figure 4.12: Spectral analysis for the velocity signal of probe 1 (similar results for other probes)

Comparisons are made with reference to the no-actuation and continuous actuation cases. Figure 4.14 shows that the pulsing frequency has little effect on boundary layer momentum thickness distribution, the pressure coefficient and skin friction coefficient distributions shown in Figure 4.13(a) and Figure 4.13(b) indicate that the pulsed actuation at a Strouhal number of 1 results in a smaller separation bubble. To demonstrate the separation bubble length variation clearly, the suction surface separation bubble lengths, calculated based on the skin friction coefficient, are listed in Table 4.1. The pulsed actuation with a Strouhal number of 1 delays the separation point the most with the separation bubble length reduced from 0.34 to 0.06 chord. This result suggests that at a Strouhal number of 1, the turbulent flow structures in the boundary layer are excited more effectively compared to other pulsing frequencies. The high-momentum transferred from the fluid outside the boundary layer to the boundary layer fluid may be the reason for boundary layer separation suppression.

Table 4.1: Pulsing frequency effect on suction surface separation bubble properties

Case	f_{act} [Hz]	St	$x_{Separation}$ [x/c]	$x_{Reattachment}$ [x/c]	$l_{Separation}$ [x/c]
No actuation	-	-	0.29	0.63	0.34
Continuous actuation	-	-	0.50	0.85	0.35
Frequency1	388	0.72	0.47	0.64	0.17
Frequency2	530	1.0	0.48	0.54	0.06
Frequency3	776	1.44	0.44	0.58	0.14

The effect of pulsing frequency on the cascade performance is shown in Figure 4.15. The plasma actuation frequency range was extended by performing additional simulations to observe the correct trend. It can be seen that the pulsing frequency has negligible effect on pressure rise

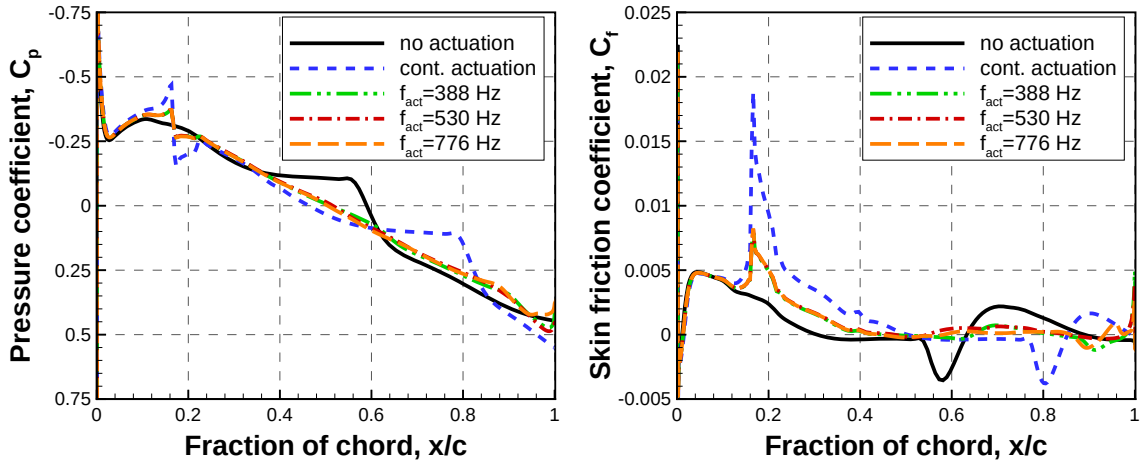

(a) Suction surface pressure distribution

(b) Suction surface skin friction coefficient distribution

Figure 4.13: Pulsing frequency effect on suction surface pressure coefficient and skin friction coefficient distributions

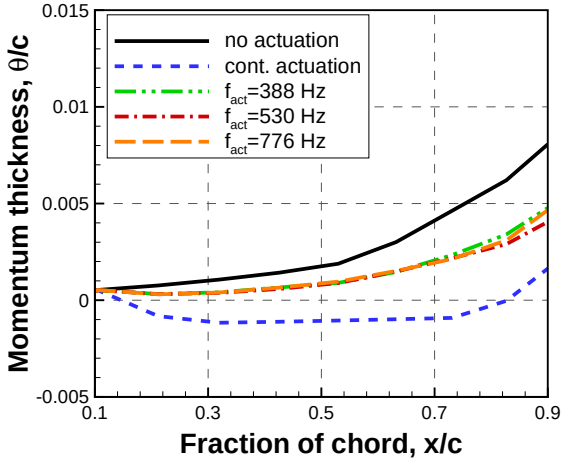

Figure 4.14: Pulsing frequency effect on suction surface momentum thickness distribution

coefficient and the total pressure loss coefficient. At pulsing frequencies of 50 Hz, the pressure rise coefficient is relatively smaller. This result can be explained by high deviation angle (i.e. low flow turning) shown in Figure 4.15(b) and relatively thicker boundary layer displacement thickness shown in Figure 4.15(c).

Figure 4.16 shows the power analysis for the pulsing frequency effect. Similar to the behavior observed in cascade performance, pulsing frequency has a minor effect on compressor and plasma actuation power. Although very small, the plasma actuation efficiency (η_p) observed to have a peak around 350 Hz which is close to the flow frequency predicted from the simulations.

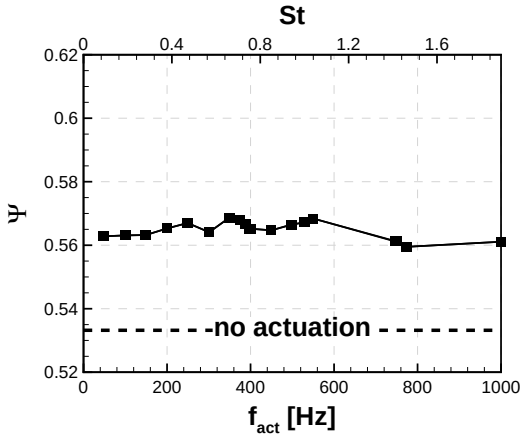

(a) Pressure rise coefficient

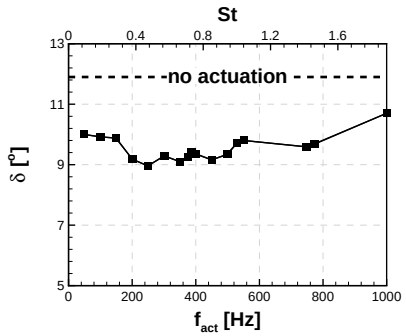

(b) Deviation angle

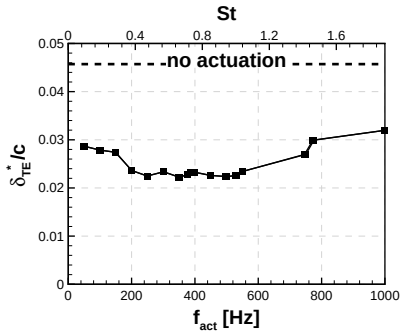

(c) Trailing edge displacement thickness at suction surface

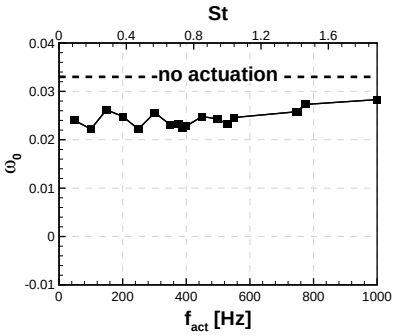

(d) Overall loss coefficient

Figure 4.15: Pulsing frequency effect on cascade performance

Duty Cycle Effect

The duty cycle effect was investigated with five simulations at a pulsing frequency of 530 Hz with an actuation strength of 150 mN/m. Duty cycle values of 0.1, 0.3, 0.5, 0.7 and 0.9 were used for the plasma actuator located at 0.15 chord.

Figure 4.17 shows the pressure and skin friction distributions. It can be seen that the pulsed actuation reduces the size of the separation bubble at all duty cycle values studied. It should be noted that the plasma actuation with a 0.9 duty cycle reduces the size of the laminar separation bubble, however, it causes a boundary separation closer to the blade trailing edge.

The results for the duty cycle effect on suction surface separation bubble are listed in Table 4.2. It is observed that the separation point moves downstream as the duty cycle increases. The continuous and pulsed actuation at 0.5 duty cycle moves the separation point to the same point (0.5 chord). However, the pulsed actuation moves the reattachment point further upstream compared to continuous actuation, from 0.85 chord to 0.54 chord. The separation bubble length is minimized in a duty cycle range of 0.3 to 0.5. The boundary layer momentum thickness distributions shown in Figure 4.18 show that the momentum thickness becomes smaller as the duty cycle increases.

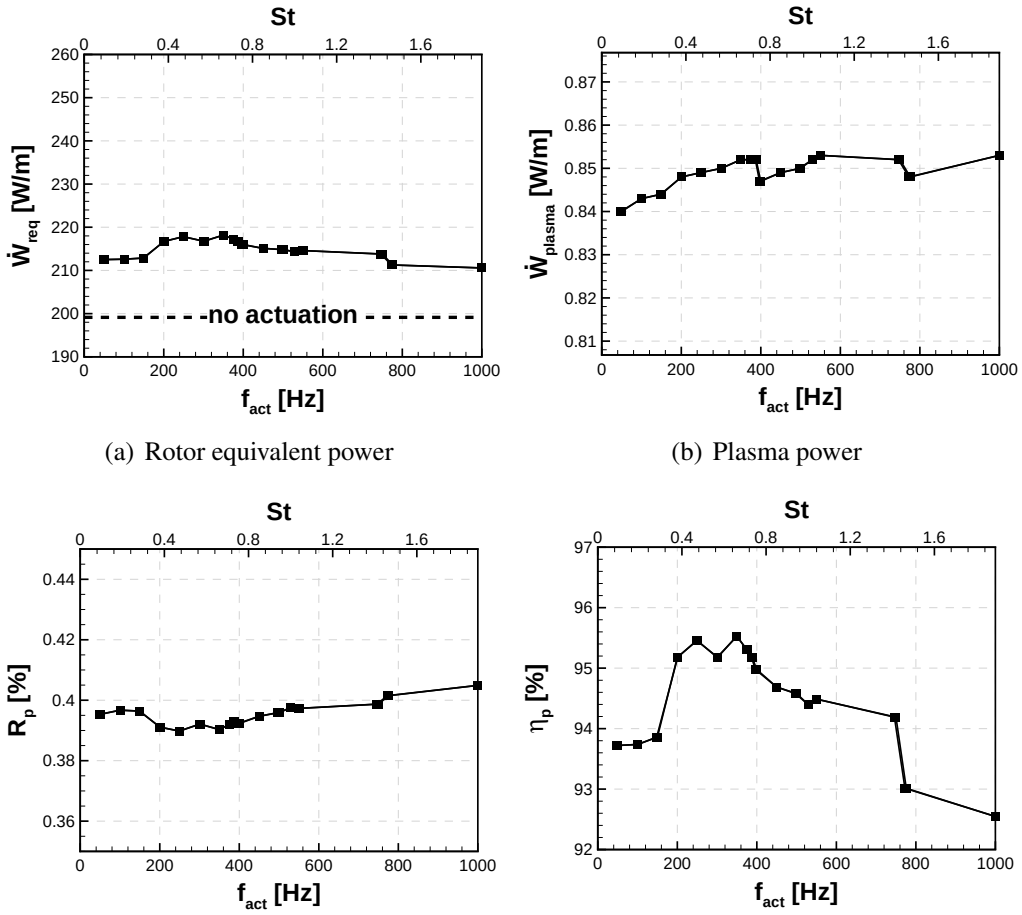

(a) Rotor equivalent power (b) Plasma power

(c) Power ratio (d) Plasma actuation efficiency

Figure 4.16: Pulsing frequency effect on power parameters

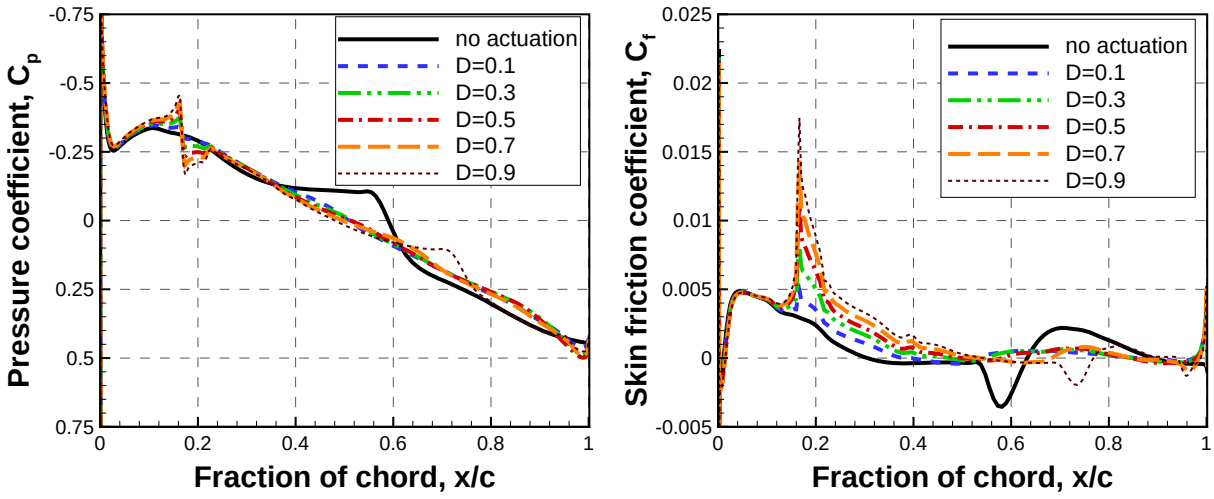

(a) Suction surface pressure distribution (b) Suction surface skin friction distribution

Figure 4.17: Duty cycle effect on suction surface pressure coefficient and skin friction coefficient distributions

Table 4.2: Duty cycle effect on suction surface separation bubble properties

Case	D	$x_{Separation}$ [x/c]	$x_{Reattachment}$ [x/c]	$l_{Separation}$ [x/c]
No actuation	-	0.29	0.63	0.34
Continuous actuation	-	0.50	0.85	0.35
Duty1	0.1	0.39	0.53	0.14
Duty2	0.3	0.47	0.54	0.07
Duty3	0.5	0.50	0.58	0.08
Duty4	0.7	0.53	0.68	0.15
Duty5	0.9	0.54	0.77	0.23

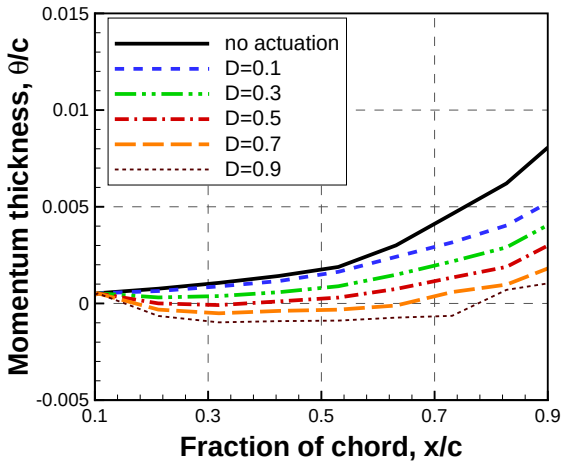

Figure 4.18: Duty cycle effect on suction surface momentum thickness distribution

Figure 4.19 presents the cascade performance parameters for duty cycle effect. It can be seen from Figure 4.19(a) that the pressure rise coefficient increases with the duty cycle. However, rate of improvement becomes smaller as the duty cycle increases. As shown in Figure 4.19(b), the deviation angle stays almost the same for a duty cycle range between 0.5 and 0.9. Moreover, the boundary layer displacement thickness at the trailing edge becomes almost the same for duty cycle values above 0.5. The reason of pressure rise enhancement for duty cycle values between 0.5 and 0.9 can be explained by the linear reduction of overall total pressure loss coefficient shown in Figure 4.19(d). This result confirms that increase of flow turning (reduced deviation angle and displacement thickness) and reduction of total pressure loss add up to create pressure rise coefficient enhancement. Overall, the continuous actuation performs better in terms of improving cascade performance parameters compared to pulsed actuation for the same plasma actuation strength.

Figure 4.20 shows the power analysis for the duty cycle effect. The rotor equivalent power (Figure 4.20(a)) shows the same behaviour with the pressure rise coefficient (Figure 4.19(a)). The longer plasma actuation time with increasing duty cycle clearly causes higher plasma power re-

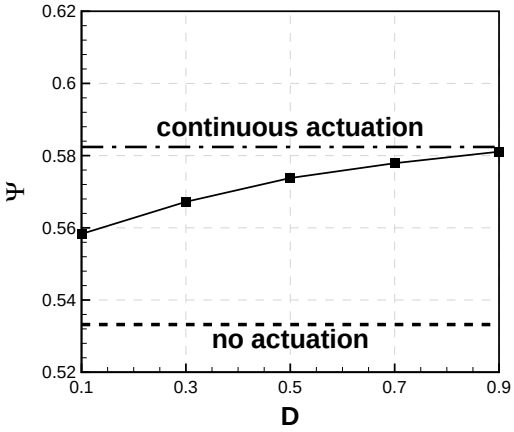

(a) Pressure rise coefficient

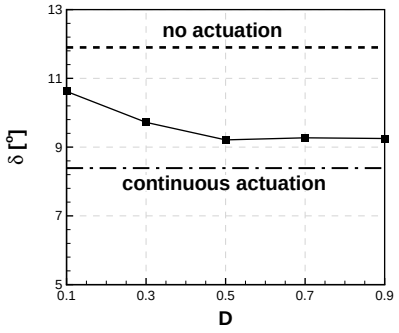

(b) Deviation angle

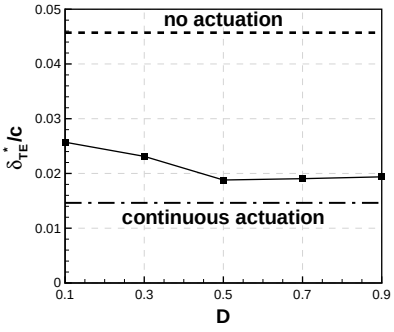

(c) Trailing edge displacement thickness at suction surface

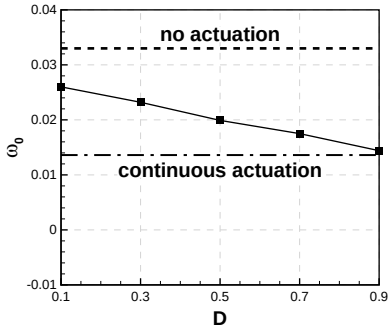

(d) Overall loss coefficient

Figure 4.19: Duty cycle effect on cascade performance

quirement (R_p) as presented in Figure 4.20(c). The plasma actuation efficiency reduces almost linearly as duty cycle increases from 0.1 to 0.9.

4.1.3 Actuation Mode Effect

Finally, the continuous and pulsed plasma actuation flow control effectiveness was compared for the same plasma power, 0.9 W/m. The simulations performed for the pulsed and continuous plasma actuations are summarized in Table 4.3. Pulsed actuation simulation was carried out for an actuation strength of 150 mN/m, a pulsing frequency of 530 Hz and a duty cycle of 0.3. Continuous plasma actuation was performed for an actuation strength of 45 mN/m. The plasma actuators were located at 0.15 chord for both cases. Table 4.3 also illustrates power calculations which reveal that the rotor equivalent power improvement achieved by pulsed actuation is larger than continuous actuation. Moreover, the pulsed actuation works more efficiently in other words plasma actuation efficiency (η_p) is larger.

Suction surface pressure and skin friction coefficient distributions shown in Figure 4.21 show that pulsed actuation moves the separation point further downstream compared to the continuous

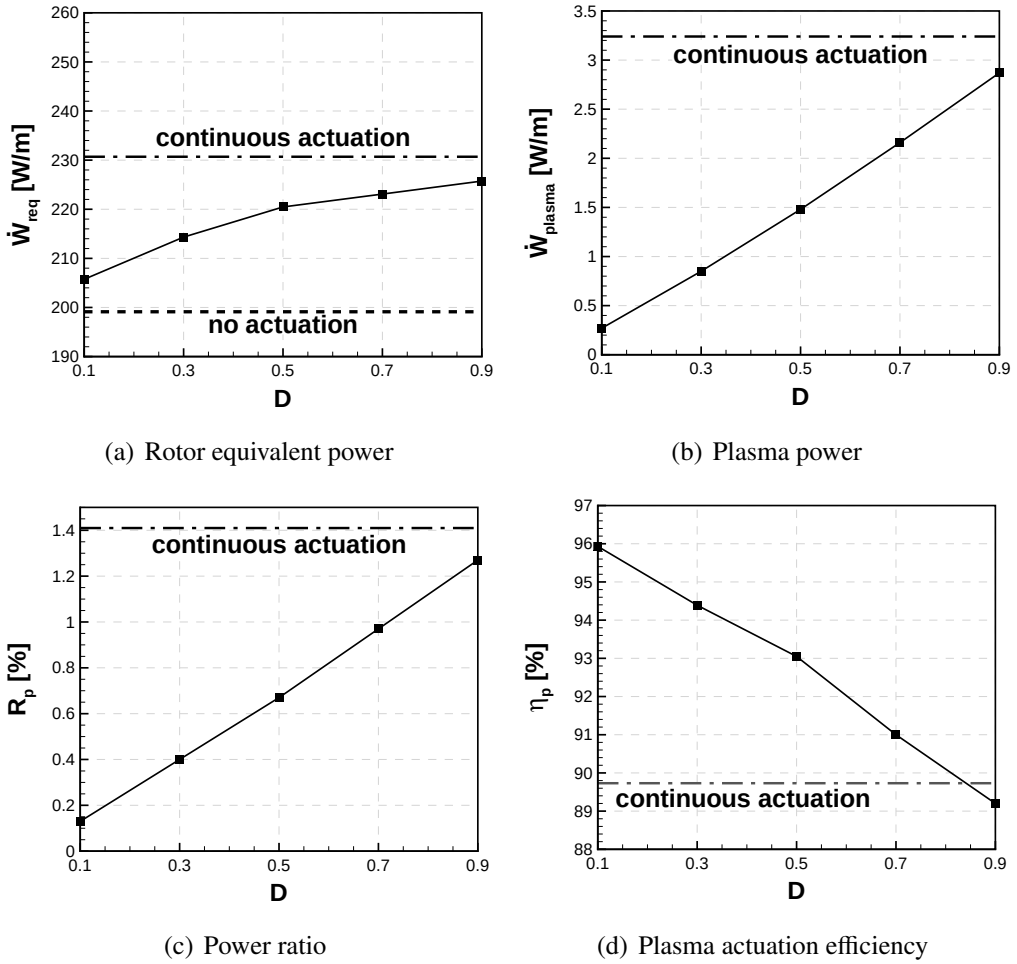

(a) Rotor equivalent power

(b) Plasma power

(c) Power ratio

(d) Plasma actuation efficiency

Figure 4.20: Duty cycle effect on power parameters

actuation. Furthermore, the boundary layer momentum thickness is further reduced with the pulsed actuation as shown in Figure 4.22.

The pulsed actuation performed better than continuous actuation in terms of pressure rise coefficient increase as shown in Table 4.4. The enhancement in the pressure rise coefficient can be attributed to the higher flow turning (smaller deviation angle), smaller blockage (due to smaller displacement thickness) and reduced total pressure loss.

The effectiveness of pulsed actuation can be explained by instantaneous TKE and vorticity contours presented in Figure 4.23. TKE contours indicate that the pulsed actuation suppresses the transition and the blade experiences a fully laminar flow. On the other hand, the continuous actuation only moves the transition onset slightly downstream and reduces the turbulent boundary layer thickness. This explains the higher total pressure loss reduction achieved by the pulsed actuation. The vorticity contours for no actuation case (Figure 4.23(b)) prove that the suction surface boundary layer experiences a negative vorticity. Although hard to notice, the suction surface laminar separation bubble is characterized by a thin positive vorticity region near the surface at the

Table 4.3: Actuation mode effect on power

Case	x_{act}	F_{act} [mN/m]	f_{act} [Hz]	D	$\dot{W}_{req}$ [W/m]	η_p [%]
No actuation	-	-	-	-	199.1	-
Pulsed actuation	0.15	150	530	0.3	214.3	94.39
Continuous actuation	0.15	45	-	-	209.9	92.02

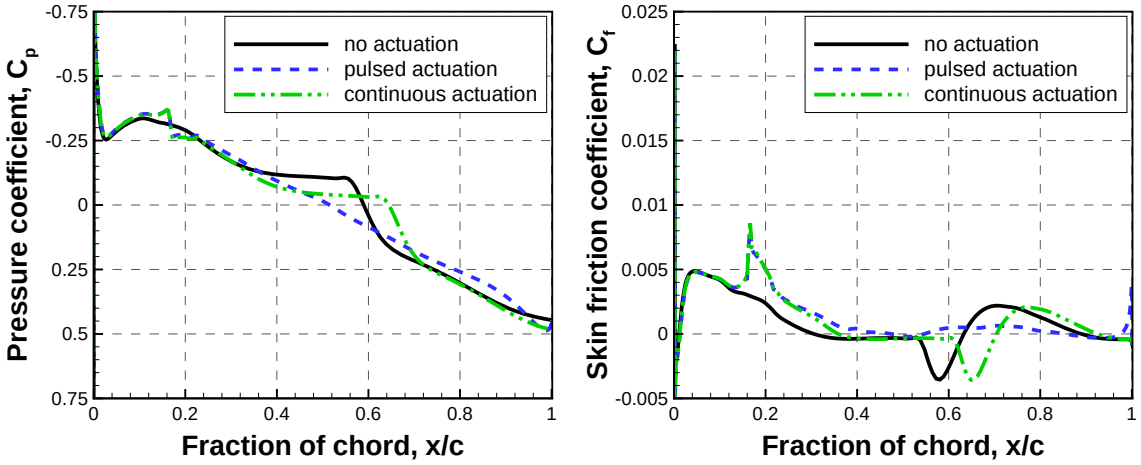

(a) Suction surface pressure distribution

(b) Suction surface skin friction coefficient distribution

Figure 4.21: Actuation mode effect on suction surface pressure coefficient and skin friction coefficient distributions

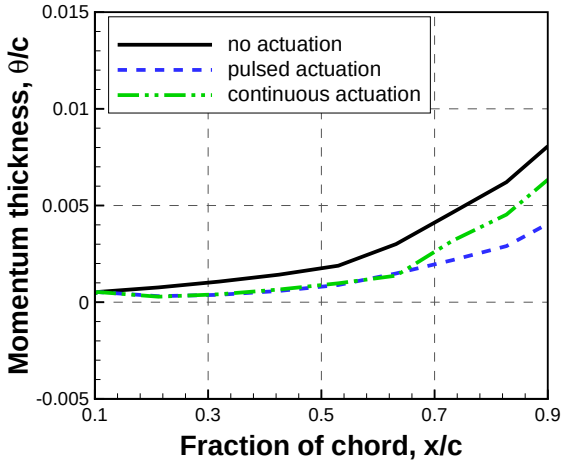

Figure 4.22: Actuation mode effect on suction surface momentum thickness distribution

Table 4.4: Actuation mode effect on cascade performance parameters

Case	ψ	δ [°]	δ^*_{TE}/c	ω_0
No actuation	0.5332	11.9	$4.6\times10^{-}2$	0.0330
Pulsed actuation	0.5672	9.7	$2.3\times10^{-}2$	0.0232
Continuous actuation	0.5544	10.9	$3.4\times10^{-}2$	0.0273

mid-chord. The pulsed plasma actuation induces train of positive vortices which interact with the negative vorticity boundary layer fluid. The continuous plasma actuation (Figure 4.23(f)) induces a continuous but thinner positive vorticity fluid over the negative vorticity boundary layer fluid compared to pulsed plasma actuation. The higher interaction between the negative and positive vorticity in pulsed actuation may be the reason for the suppression of transition.

Finally, axial pressure gradient contours are shown in Figure 4.24. Similar to the behavior observed for TKE contours (Figure 4.23), the continuous plasma actuation noted to delay adverse pressure gradient on the suction surface. The effect of negative and positive vorticity interaction can be observed more clearly in axial pressure gradient contours of pulsed plasma actuation. The interaction of these counter rotating vortices overcomes the adverse pressure gradient region locally and forms favourable pressure gradient pockets. Therefore, the boundary layer flow under the presence of consecutive adverse and favourable pressure gradient does not experience boundary layer transition.

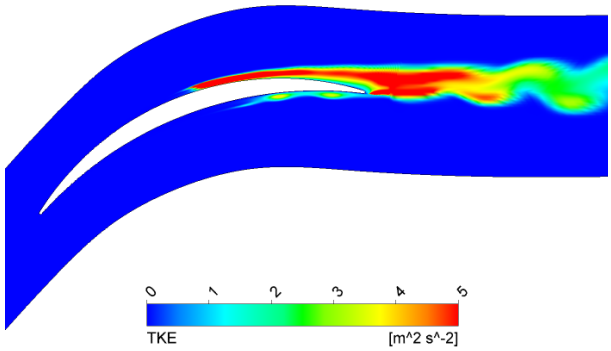

(a) TKE (No actuation)

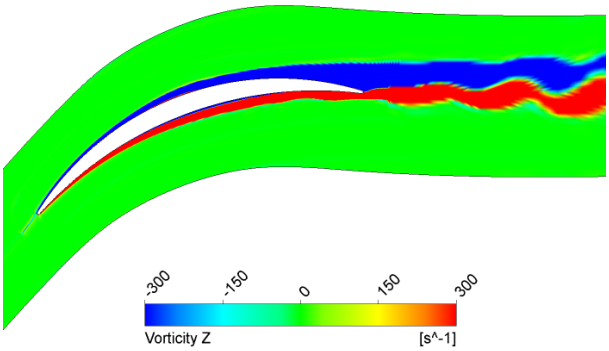

(b) Vorticity-z (No actuation)

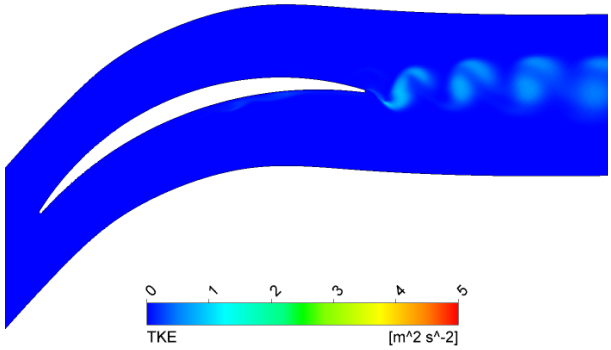

(c) TKE (Pulsed actuation)

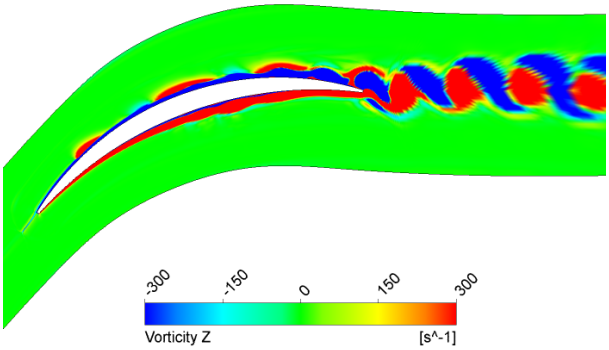

(d) Vorticity-z (Pulsed actuation)

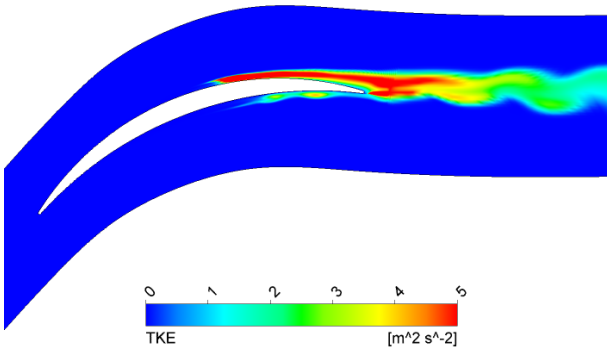

(e) TKE (Continuous actuation)

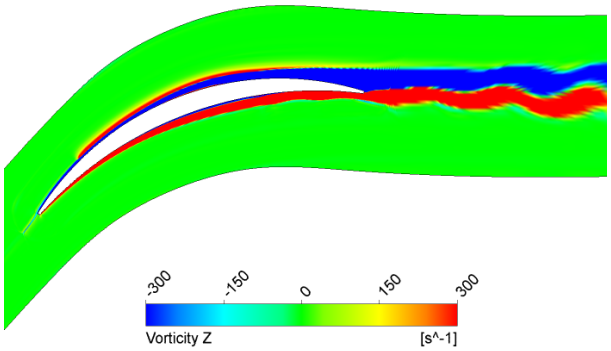

(f) Vorticity-z (Continuous actuation)

Figure 4.23: Instantaneous TKE and vorticity contours for actuation mode effect

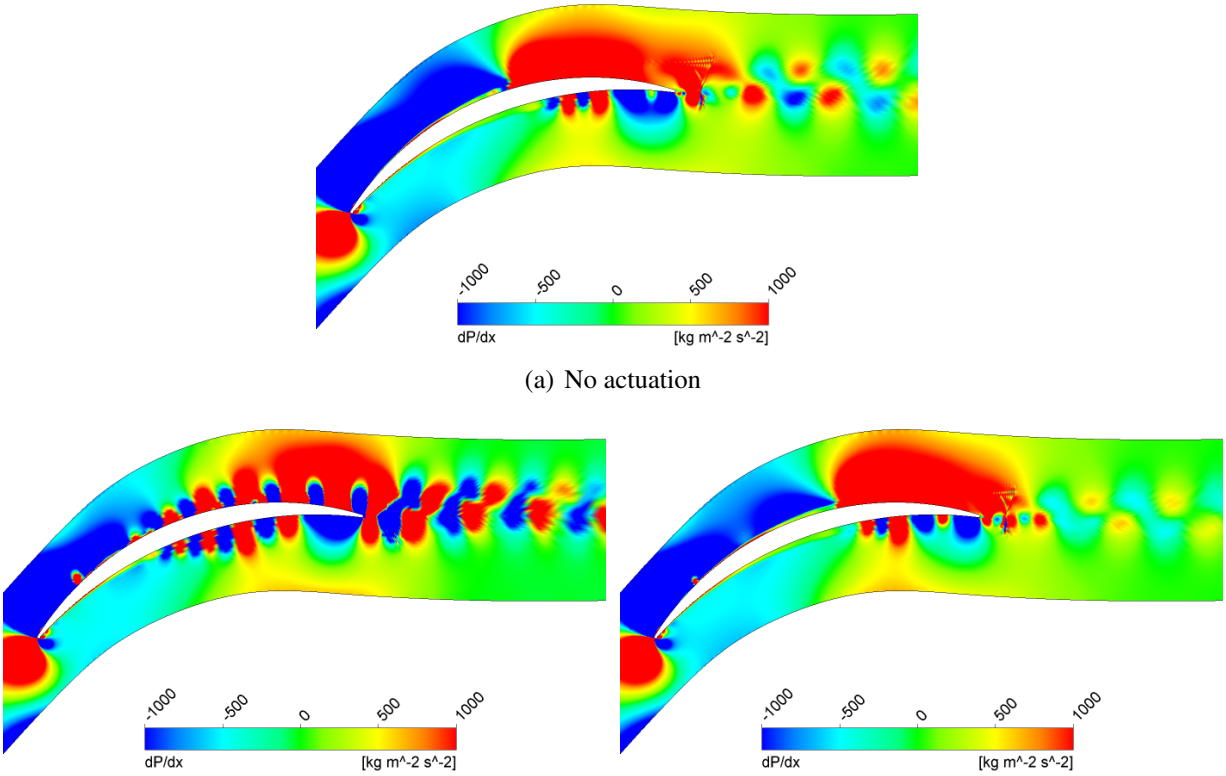

(a) No actuation

(b) Pulsed actuation

(c) Continuous actuation

Figure 4.24: Actuation mode effect on axial pressure gradient contours

4.2 Experimental Validation

Following the computational parametric study, wind tunnel cascade tests were carried out with the plasma actuator located at 0.25 chord on the suction surface of the cascade blade. The suction surface static pressure measurements were carried out to determine plasma actuation effectiveness. The experiments were performed at a Reynolds number of 1.5×10^5 corresponding to an inlet velocity of 20 m/s. The plasma actuation was applied both in continuous and pulsed modes at various actuation strengths and pulsing frequencies.

In an effort to assess the effect of the slightly protruding plasma actuator located on the suction surface, surface pressure measurements were performed for clean and plasma actuator mounted (unpowered) blades. As explained in Section 2.4.2, two grooves were used to reduce the effect of plasma actuator hardware based on the parametric study performed for boundary layer trip effect in Appendix C.4. Figure 4.25 compares the pressure distributions for clean and plasma actuator mounted (unpowered) blades. Measurements show that the plasma actuator hardware effect is reduced on the surface pressure distribution, yet the plasma actuator trips the boundary layer flow which can be seen from the pressure coefficient slope between 0.3 and 0.55 chord. Boundary layer separation, inferred from plateau region, becomes less pronounced for the plasma actuator instrumented blade. This configuration is thus used as the reference (no actuation) case to isolate

the effect of plasma actuation. Therefore, the compressor cascade in experiments experienced a weaker boundary layer separation.

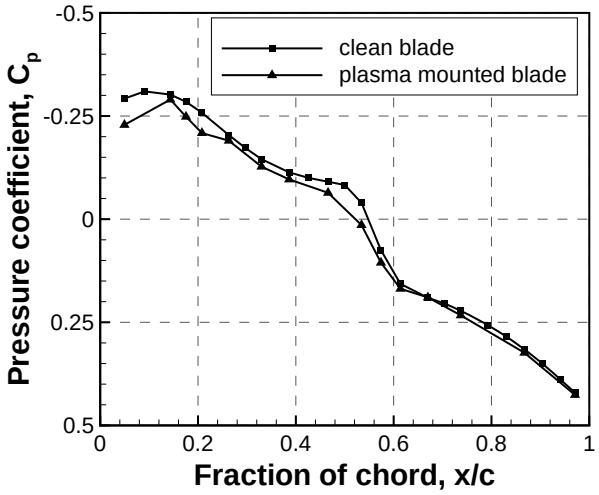

Figure 4.25: Suction surface pressure coefficient distribution with/without plasma actuator setup

4.2.1 Plasma Actuation Results

Figure 4.26 presents the experimental and corresponding computational surface pressure distributions. The plasma actuation was applied at an actuation strength of 40 mN/m. The computational data predicts a stronger separation bubble compared to the experimental data since actuator protrusion effect is not simulated. Therefore, it should be stated that the comparison of experimental and computational results were based on the change (trend) rather than the absolute value of performance parameters. The experimental data shows that the plasma actuation eliminates the boundary layer flow separation (indicated by the plateau region) observed approximately between 0.3 chord and 0.55 chord. The computations reveal that the plasma actuation moves the separation bubble downstream without altering the size of the bubble. This discrepancy can be attributed to the fact that the plasma actuator setup trips the boundary layer flow in the experiments. The tripped boundary layer flow results in a smaller separation bubble which can be suppressed with a comparatively smaller plasma actuation. It should be noted that although the experimental surface pressure coefficient distribution does not indicate a separation bubble, there may exist a very small separation bubble. Indeed, the surface pressure measurements performed for endwall boundary layer suction (Section 3.3) have proved that the separation bubble observed in oil flow visualization could not be inferred from surface pressure measurements.

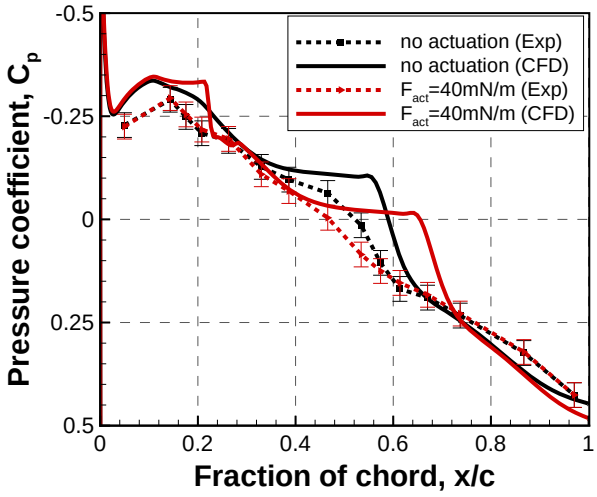

Figure 4.26: Experimental and computational pressure coefficient distributions with/without plasma actuation

Actuation Strength Effect

Figure 4.27 presents the experimental and computational surface pressure distributions for continuous plasma actuation performed at three actuation strengths, 40 mN/m, 65 mN/m and 90 mN/m. The experimental measurements shown in Figure 4.27(a) reveal that plasma actuation at an actuation strength of 90 mN/m causes a significant pressure recovery at around 0.27 chord. The surface pressure measurements show that the stronger plasma actuation changes the size and location of the laminar separation bubble or even eliminates it. Figure 4.27(b) presents the computational results. The pressure recovery due to plasma actuation increases with actuation strength. As opposed to the experimental data, the computational data show that the separation region (plateau region) is still present and it moves further downstream as the actuation strength increases. As stated earlier, the discrepancy between experimental and computational results can be attributed to the presence of a weaker separation bubble in the experiments.

Pulsing Frequency Effect

To determine the pulsing frequency effect, three actuation frequencies were tested at an actuation strength of 65 mN/m. The first pulsing frequency tested was 388 Hz which was based on the on resonant flow frequency extracted from the unsteady flow simulations for the no actuation case. The second pulsing frequency, 300 Hz, was based on the Tollmien-Schlichting (T-S) wave frequency. As discussed in further detail in Appendix C.5, the T-S wave frequency was approximated based on the momentum thickness, boundary layer edge velocity and viscosity obtained from computations. The third pulsing frequency, 530 Hz, was based on the Strouhal number where a value of unity shown from the literature and earlier simulations in Section 4.1.2 to be most effective.

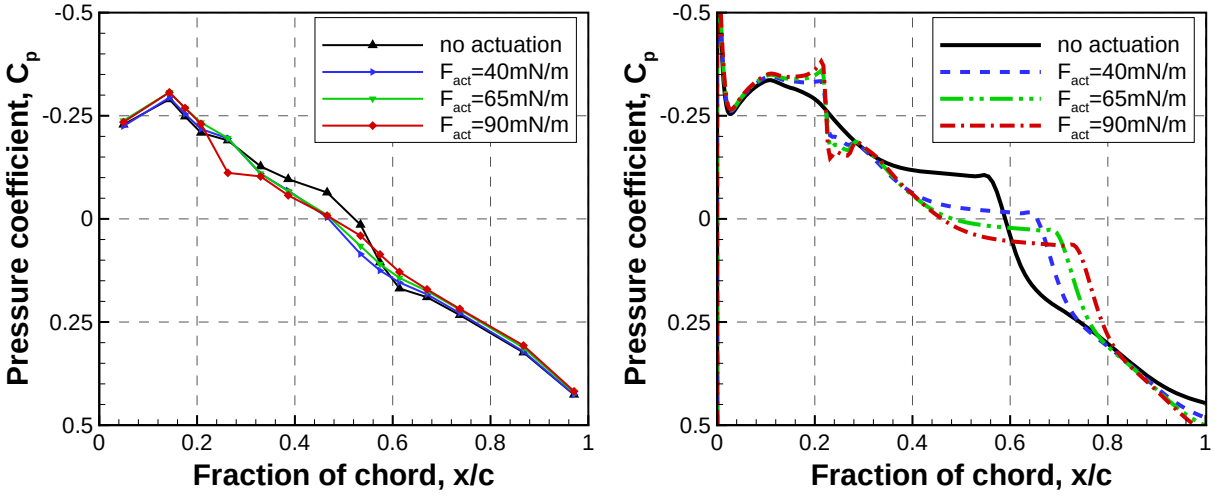

(a) Experiment (b) CFD

Figure 4.27: Actuation strength effect on suction surface pressure coefficient distribution

Figure 4.28(a) shows the experimental surface pressure coefficient distribution. The pulsed actuation eliminated the flow separation on the suction surface. However, the pressure distributions at the three pulsing frequencies show almost no difference. Similar to the experiments, the computational results shown in Figure 4.28(b) also suggest that pulsed actuation eliminates the boundary layer separation. Note also that the pulsed actuation simulation at 300 Hz shows the presence of a plateau suggesting a separation bubble close to the blade trailing edge. Since the resonant experimental frequency may not match the theoretical and CFD frequencies exactly, the pulsing frequency was varied around the nominal predicted values to find the optimum frequency. However, the pressure distribution measurements did not show any significant effect at these frequencies.

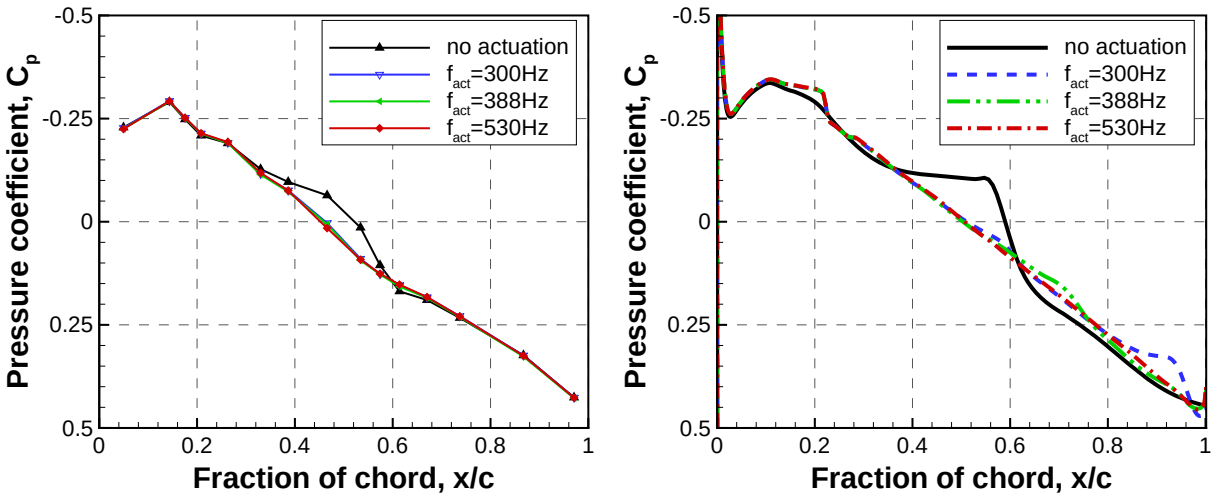

(a) Experiment (b) CFD

Figure 4.28: Pulsing frequency effect on suction surface pressure coefficient distribution

Pulsed Actuation Duty Cycle Effect

The duty cycle effect was tested at five duty cycle values (0.1, 0.3, 0.5 0.7 and 0.9). Figure 4.29 shows the experimental and computational results for duty cycle effect on the pressure coefficient distribution. Both experimental and computational data show that duty cycle has a minor effect on pressure distribution. Close inspection of the pressure distribution curves show that the leading edge pressure drop becomes stronger at high duty cycle values for both experimental and computational data. A duty cycle of 0.9 has the lowest pressure recovery at around 0.55 chord. Moreover, the computational data suggests a flow separation after 0.5 chord for a duty cycle of 0.9.

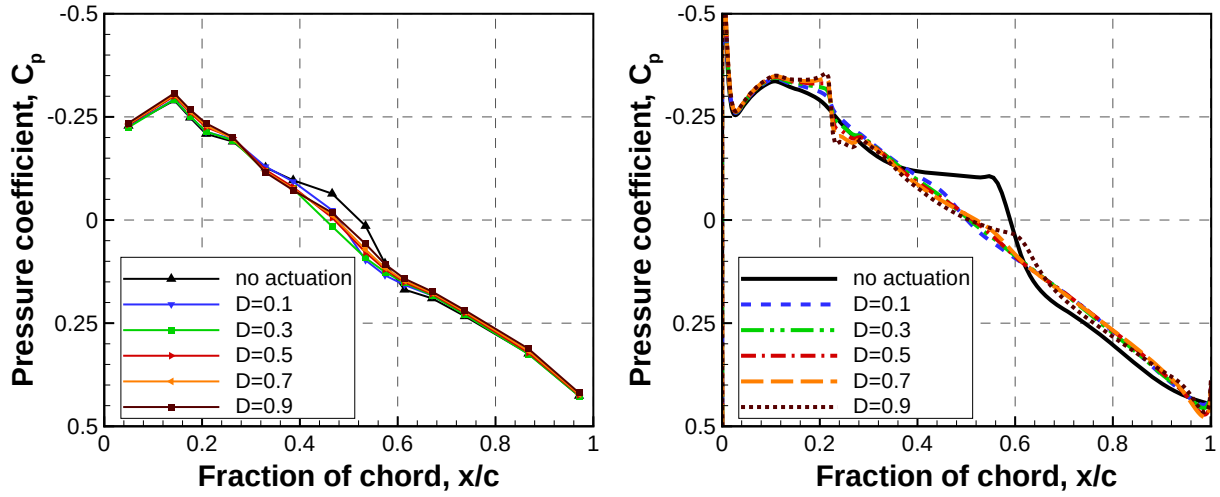

(a) Experiment (b) CFD

Figure 4.29: Duty cycle effect on suction surface pressure coefficient distribution

Actuation Mode Effect

After determining the strength and pulsing frequency effects, the continuous and pulsed plasma actuations were compared. While assessing the effect of actuation mode in simulations in Section 4.1.3, the continuous and pulsed plasma actuations were applied for the same plasma power. However, the maximum achievable plasma strength was small in the experiments. For the same plasma power, the equivalent continuous actuation strength (the actuation strength varies almost linearly with duty cycle) would be significantly small to measure the resultant effect on the pressure coefficient. Therefore, the pulsed actuation plasma experiments were carried out at the same actuation strength instead of same plasma power.

For the continuous actuation, the plasma actuation was applied at an actuation strength of F_{act}=65 mN/m. For the pulsed actuation, the same plasma strength was used with a pulsing frequency of 530 Hz and a duty cycle of 0.3. The corresponding experimental and computational pressure distributions are shown in Figure 4.30. Figure 4.30(a) indicates that pulsed actuation per-

forms slightly better in eliminating the plateau region with a stronger pressure recovery between 0.3 chord and 0.5 chord. Computational results presented in Figure 4.30(b) clearly shows that the pulsed actuation suppressed the boundary layer separation more effectively. Thus, the CFD simulation reproduces the same trend as seen in the experiment (except the effect of plasma actuator protrusion).

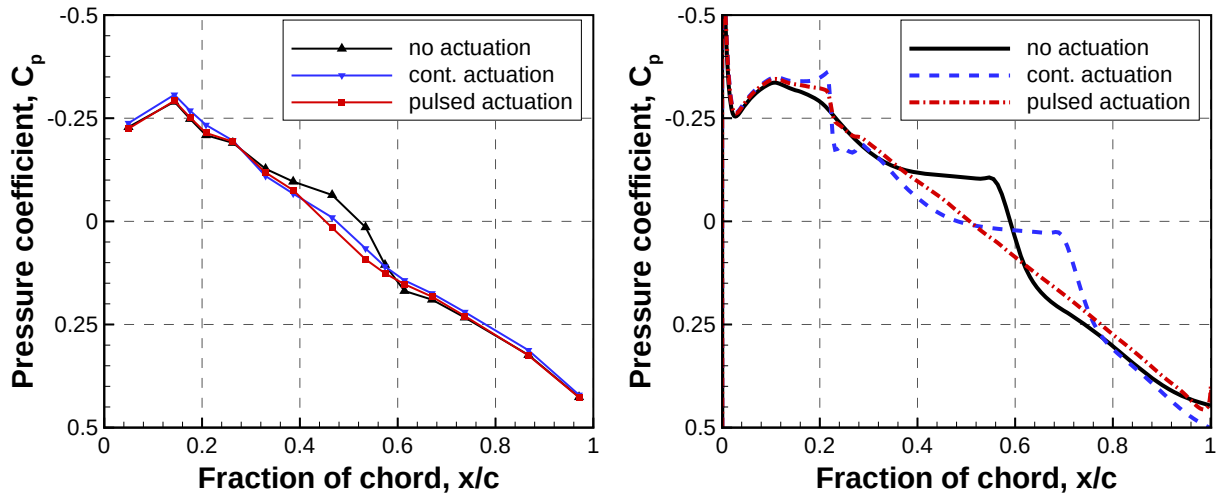

(a) Experiment (b) CFD

Figure 4.30: Actuation mode effect on suction surface pressure coefficient distribution

Pulsed Actuation Repeatability

After carrying out plasma actuation experiments, a thin layer of powder was observed near the regions where the plasma was formed. Considering the possible degradation of dielectric material addressed by many studies (Pons *et al.*, 2008; Rigit *et al.*, 2009), the continuous plasma actuation at 65 mN/m was repeated to assess the repeatability of the plasma actuation experiments. Figure 4.31 shows that there is a small difference between the two measurements. This result suggests that the dielectric material degradation was not severe enough yet to cause a large discrepancy in the plasma actuation surface pressure measurements.

4.3 Reynolds Number Scaling for Compressor Cascade Pressure Rise Enhancement

In this section, the Reynolds number scaling study for plasma actuation boundary layer separation control is presented. The plasma actuation was applied at 0.25 chord on the suction surface in continuous mode. The actuation strength was adjusted to achieve a 9.2%±0.25 increase in pressure rise coefficient at each Reynolds number. Figure 4.32 presents the Reynolds number scaling

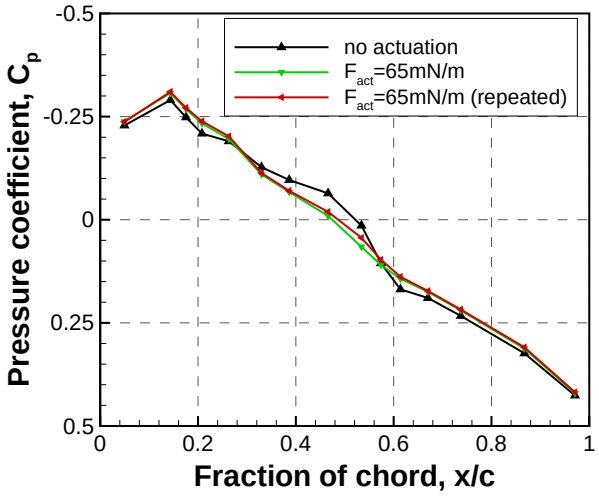

Figure 4.31: Suction surface pressure coefficient distribution for dielectric material degradation and repeatability (continuous actuation)

study results performed for a Reynolds number range between 1.5×10^5 and 7.5×10^5. A non-linear increase of plasma actuation strength is observed as the Reynolds number (and Mach number) increases to achieve the same pressure rise coefficient enhancement. The best fit to this data was obtained with a 2.361 power-law function. Similar to the Reynolds number scaling study for the corner separation, the exponential growth of plasma actuation strength can be attributed to proportionality of plasma actuation strength with the square of the induced velocity computationally shown in Appendix A.3. Similar to the case with corner stall, Figure 4.33 shows that pressure rise coefficient increases with Reynolds number for the same blade geometry as the boundary layer behaviour improves, eventually making flow control unneccessary. Thus, while the scaling study can be extended to higher flow velocities, the blade camber should be increased with Reynolds number for the results to be physically meaningful.

4.4 Summary

As expected, CFD simulations show that suction side plasma actuation increases pressure rise and rotor equivalent power through an increase in flow turning (reduced deviation) a reduction in blockage (boundary layer displacement thickness) and total pressure loss. However, the performance of the concept decreases as the actuator moves downstream due to a shift in the laminar separation bubble towards the trailing edge which causes adverse effects on the deviation and trailing edge displacement thickness. The optimum actuator location in terms of pressure rise and actuator effectiveness is just upstream of the separation point. On the other hand, while the performance increases with actuation strength, this increase is asymptotic and decreases with actuation

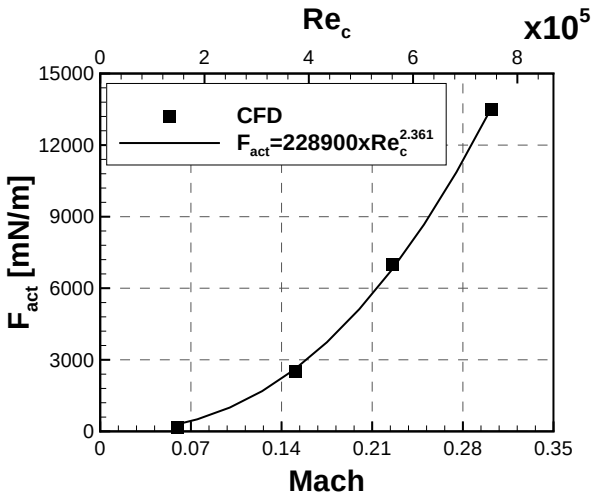

Figure 4.32: Reynolds number scaling for compressor pressure rise enhancement with plasma actuation

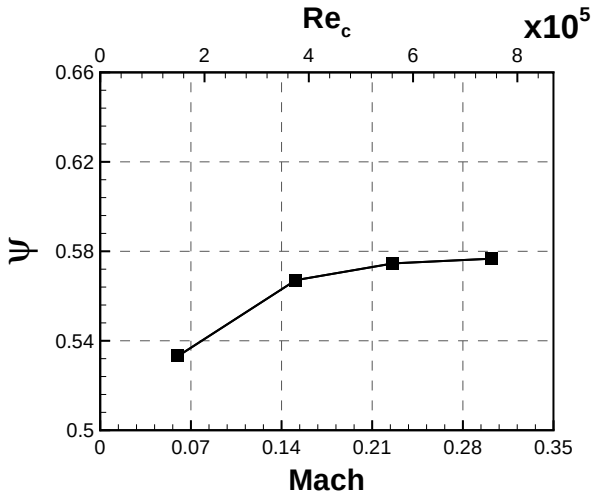

Figure 4.33: Reynolds number effect on the pressure rise coefficient

strength. Pulsed actuation performed less effectively than continuous actuation for the same actuation strength but better for the same input plasma power. Pulsing frequency and duty cycle do not have a large impact on pressure rise and rotor equivalent power increase but simulations point out a better performance with pulsing frequency near the fundamental boundary layer flow oscillation frequency and at lower duty cycles. While the actuator protrusion on the experimental cascade blade changed the nominal performance of the blade, comparison of experimental pressure suction surface pressure distribution with corresponding CFD simulations showed the same previously described trends from plasma actuation. Simulations at higher speeds indicate that the required plasma actuation strength scales approximately with the square of the Reynolds number.

Chapter 5

Plasma Actuation Flow Control for Noise Reduction

In this chapter, the 2-D computational results for blade wake plasma actuation flow control are presented. Unless otherwise stated, simulations over DCA-2 airfoil were carried at a Reynolds number of 3.5×10^5 (corresponding to 20 m/s inlet velocity). The plasma actuators were located both on suction side and pressure side close to the blade trailing edge in an effort to reduce blade wake momentum deficit. The effectiveness of plasma actuation was determined based on the wake momentum thickness at 0.2 chord downstream of blade trailing edge.

5.1 Parametric Study for Plasma Actuation Parameters

In order to show boundary layer flow behavior, the suction and pressure side axial skin friction coefficients are shown in Figure 5.1 together with the turbulent kinetic energy contours. This figure reveals that the blade encounters a laminar flow separation at 0.7 and 0.57 chord on the suction and pressure sides, respectively. Then, a turbulent reattachment takes place at 0.93 chord on the suction side and a laminar reattachment takes place at 0.87 chord on pressure side. Results show that the pressure side experiences an earlier laminar boundary layer separation compared to suction side. This can be explained by the fact that an incidence angle of -1° was used to minimize the undesired boundary layer separation on the suction side (in an effort to minimize the suction surface boundary layer separation and therefore to concentrate on blade wake suppression only).

5.1.1 Continuous Plasma Actuation

Plasma Actuator Location Effect

The continuous plasma actuation was applied over suction and pressure surfaces at five locations (0.65, 0.70, 0.75, 0.80 and 0.85 chord) with an actuation strength of 150 mN/m (which is a reasonable plasma actuator strength based on the literature (Thomas *et al*., 2009)) as shown in Figure 5.2(a). The plasma actuation body force vectors at 0.8 chord are shown in Figure 5.2(b).

The time-averaged streamwise velocity profiles at various chordwise locations are shown in

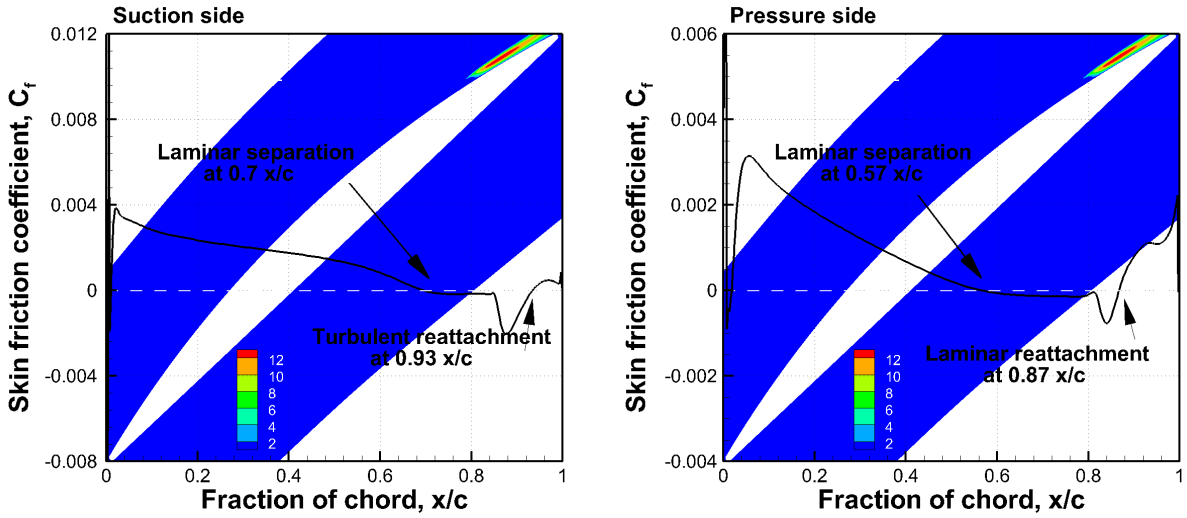

(a) Suction side (b) Pressure side

Figure 5.1: Skin friction coefficient distributions plotted together with the TKE contours

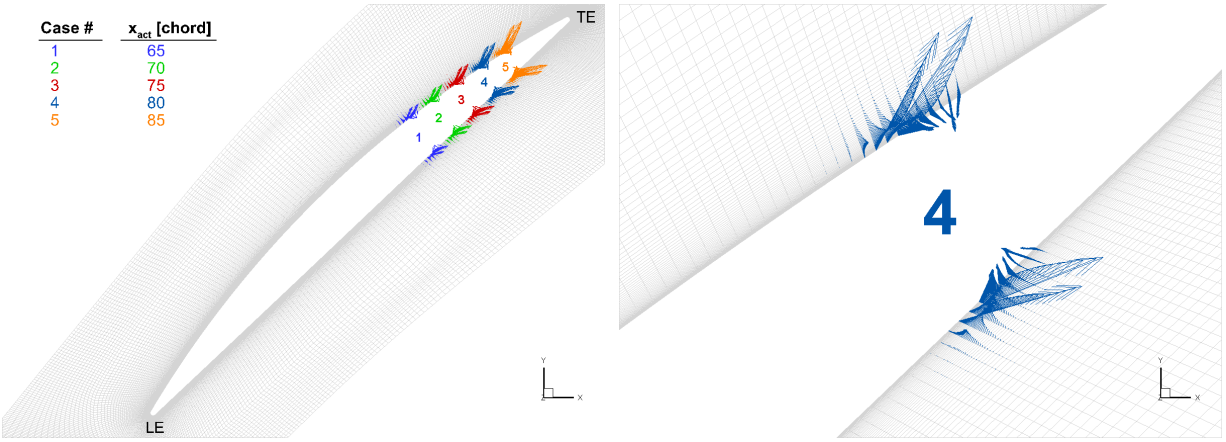

(a) Plasma actuator locations (b) Body force vectors at 0.8 chord chord location

Figure 5.2: Plasma actuator body force vectors on DCA-2 airfoil

Figure 5.3. The velocity profiles show that the plasma actuators located closer to the trailing edge reduce the trailing edge boundary layer velocity deficit more effectively. The reversed flow at 0.913 chord, observed in Figure 5.3(a) for the no actuation case, was totally eliminated and the velocity deficit was reduced significantly when the plasma actuators are located at 0.80 chord and 0.85 chord as shown in Figure 5.3(e) and Figure 5.3(f), respectively. The more upstream plasma actuator locations (0.65 chord, 0.70 chord and 0.75 chord) reduce the suction surface boundary layer velocity deficit at the 0.73 chord and 0.822 chord, i.e. just downstream of the suction surface boundary layer separation point. However, a larger boundary layer velocity deficit is introduced close to the trailing edge as a results of the suction surface boundary layer separation observed at 0.913 chord. As opposed to the suction surface, all plasma actuators observed to reduce the trailing edge velocity deficit on the pressure surface. The velocity deficit was minimized most effectively

by the plasma actuator located at 0.85 chord on the pressure surface.

Figure 5.4 presents the variation of wake momentum thickness at 0.2 chord downstream of blade trailing edge ($\theta_{wake,0.2c}/c$) with plasma actuator location. It can be seen that plasma actuators located at 0.80 chord and 0.85 chord reduce wake momentum thickness more effectively compared to the plasma actuators located far upstream. Figure 5.5 illustrates the effect by plotting the pitchwise distribution of wake total pressure loss coefficient at 0.2 chord downstream of blade trailing edge. It can be observed that the wake total pressure loss coefficient becomes smaller as the plasma actuator moves downstream, with the plasma actuators located at 0.8 chord and 0.85 chord showing similar performance. It should be noted that the plasma actuation moves the pitchwise location of the wake peak towards to the suction surface. This result is consistent with Figure 5.3 which suggests that the pressure surface plasma actuation works more efficiently in terms of total pressure loss reduction compared to the suction surface plasma actuation. This result can be attributed to the presence of larger adverse pressure gradient on the suction surface as indicated by Figure 5.6(b) which shows the symmetry plane axial pressure gradient contours for the no actuation case. Moreover, TKE contours shown in Figure 5.6(a) indicate that the blade suction surface has a turbulent boundary layer near the trailing edge which causes higher total pressure loss and therefore plasma actuator works less efficiently.

Figure 5.7 presents the rotor equivalent power results for the actuator location effect. The rotor equivalent power (Figure 5.7(a)) is observed to be first decreasing and then increasing as the plasma actuator moves downstream. This can be explained by the deviation angle plot illustrated in Figure 5.7(b) which shows an opposite trend with respect to rotor equivalent power. In other words increasing flow turning directly improves rotor equivalent power or vice versa. The plasma power (Figure 5.7(c)) is observed to be decreasing as the plasma location moves downstream. This can be explained due to fact that the flow velocity becomes smaller close to the trailing edge. This is very promising since the plasma actuator becomes more effective in reducing the wake size as it moves closer to the trailing edge. From Figure 5.7(d), it can be seen that the plasma actuation at 0.85 chord requires the minimum power ratio while reducing the wake momentum thickness at 0.2 chord downstream of blade trailing edge the most.

A last observation concerns the rotor equivalent power change with plasma actuation. The rotor equivalent power observed to be decreasing with the plasma actuation as opposed to the DCA-1 cascade. This can be attributed to the fact that the plasma actuation increases the deviation angle with respect to the no actuation case at all plasma actuation cases. The higher deviation angle causes trailing edge flow to under-turn. Consequently, the work done on the cascade fluid ($\dot{W}_{req}$) decreases with the plasma actuation. In addition to low power requirement and high wake reduction, the plasma actuation at 0.85 chord causes the minimum reduction in the rotor equivalent power. Consequently, the plasma actuation at 0.85 chord proved to be the most effective in terms

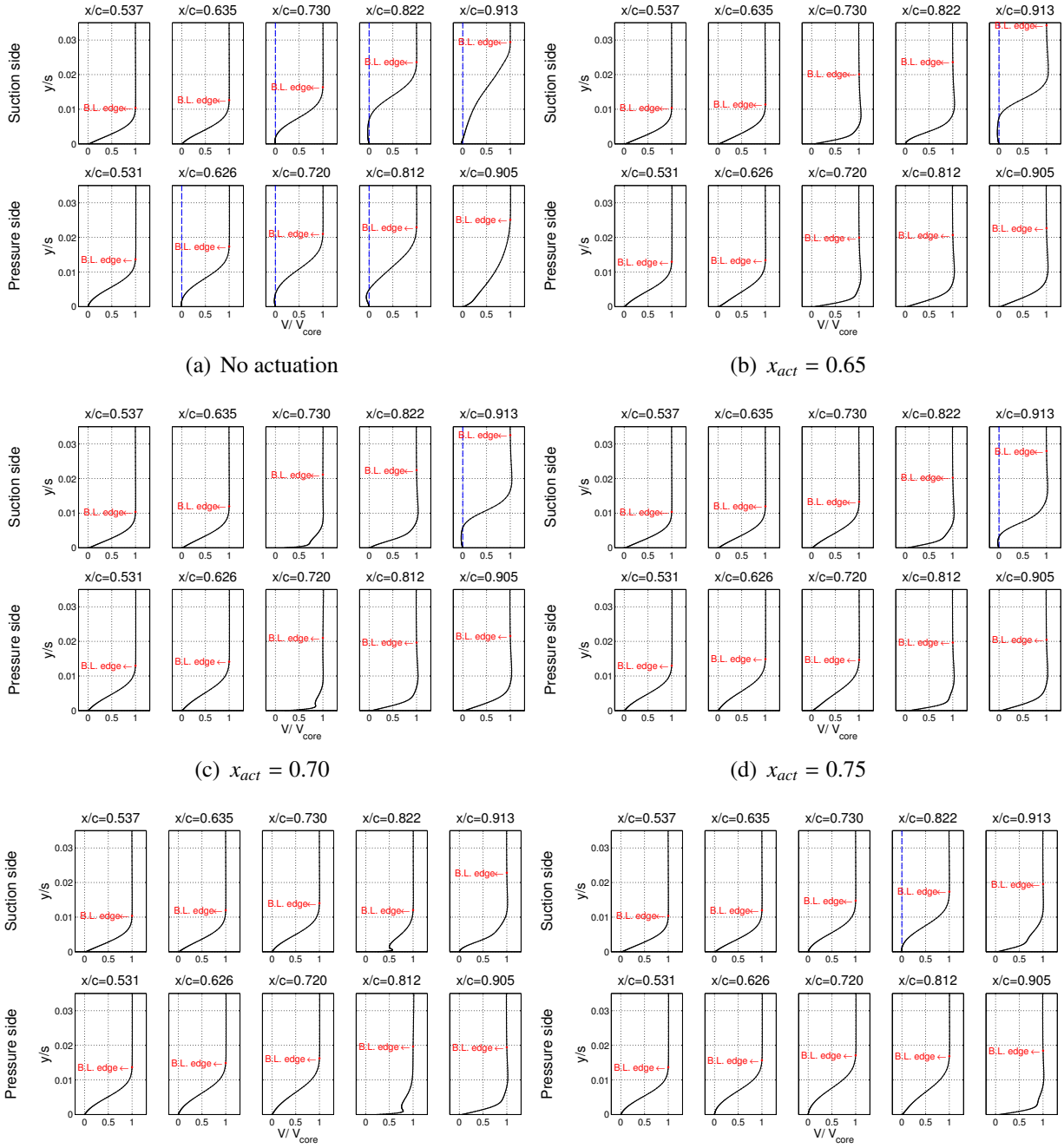

(a) No actuation

(b) $x_{act} = 0.65$

(c) $x_{act} = 0.70$

(d) $x_{act} = 0.75$

(e) $x_{act} = 0.80$

(f) $x_{act} = 0.85$

Figure 5.3: Actuator location effect on boundary layer profiles of time-averaged velocity

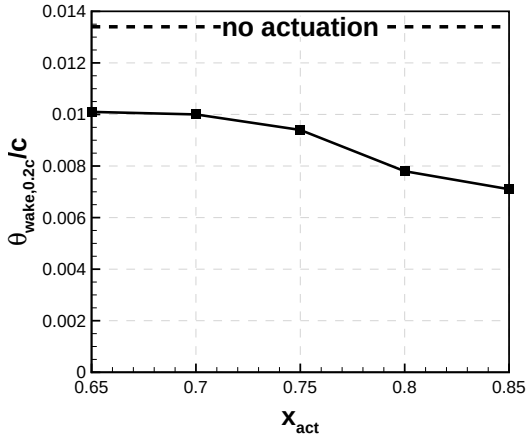

Figure 5.4: Actuator location effect on wake momentum thickness at 0.2 chord downstream of blade trailing edge

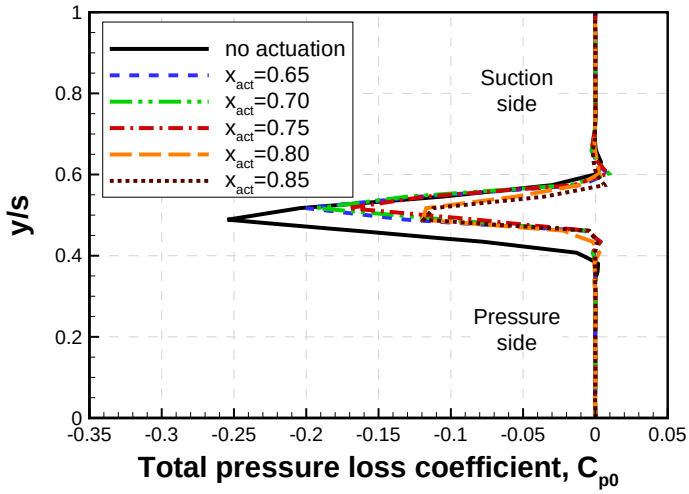

Figure 5.5: Actuator location effect on pitchwise profile wake total pressure loss coefficient at 0.2 chord downstream of blade trailing edge

of wake reduction and power requirement.

In an eventual experimental validation, the blade thickness at the locations of the actuators needs to be thick enough to accommodate the required plasma actuators on both sides of the airfoil. Although the parametric study for actuator location has shown that the plasma actuation from the most downstream location (0.85 chord) is more effective in reducing the wake with the minimum power ratio, the remaining part of the parametric study was carried out using plasma actuators at 0.8 chord considering the constraint set by the blade thickness.

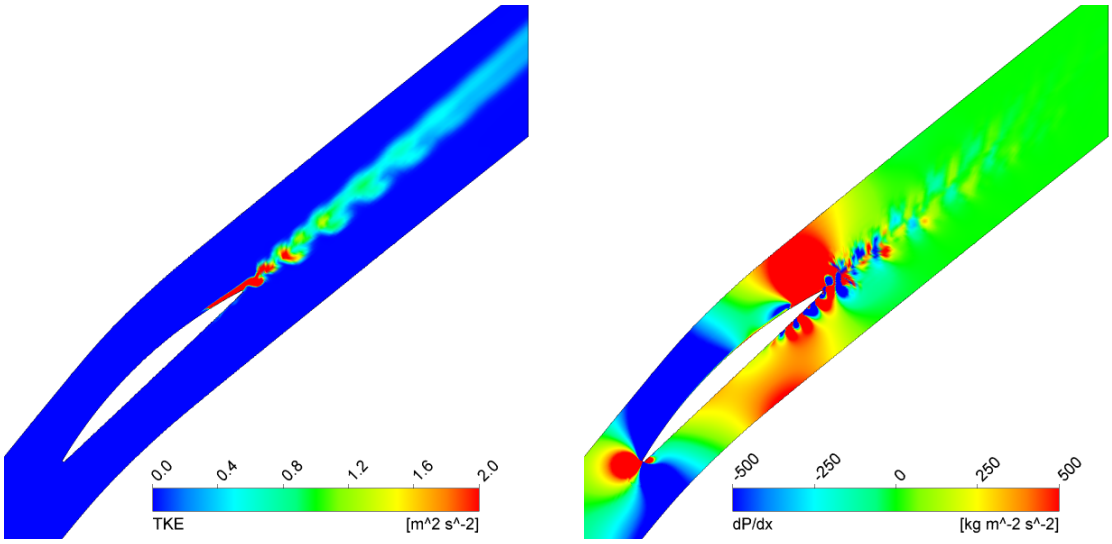

(a) TKE (b) Axial pressure gradient

Figure 5.6: Contours of symmetry plane TKE and axial pressure gradient for no actuation case

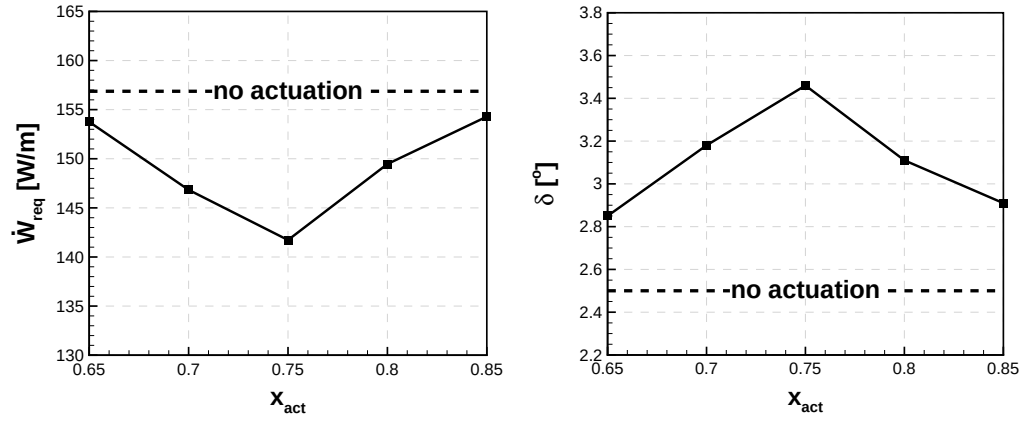

(a) Rotor equivalent power (b) Deviation angle

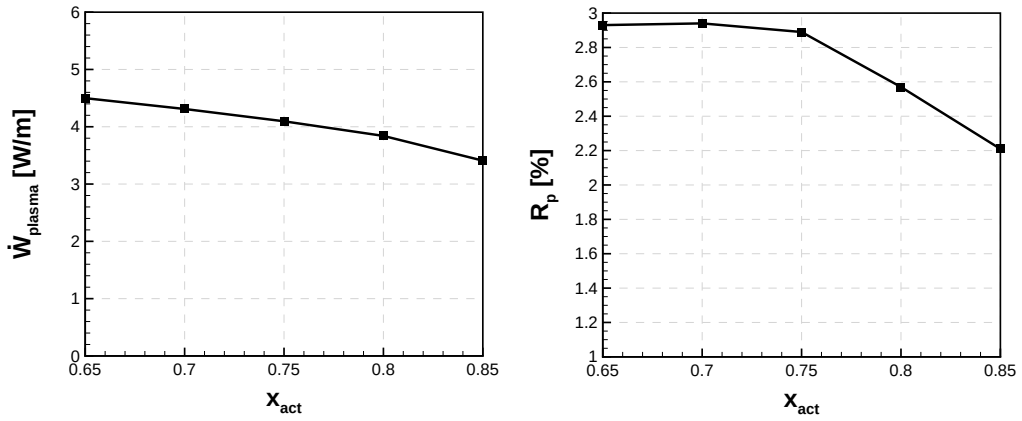

(c) Plasma power (d) Power ratio

Figure 5.7: Actuator location effect on cascade performance and power

Actuation Strength Effect

The continuous plasma actuation was applied at 0.8 chord with actuation strengths of 50, 100, 150 and 200 mN/m. The time-averaged streamwise velocity profiles at various chordwise locations are shown in Figure 5.8. The velocity profiles presented in Figure 5.8(a) for the no actuation case show that the suction surface boundary layer experiences a flow separation close to the trailing edge. Although plasma actuation at a plasma strength of 50 mN/m avoids the boundary layer separation at 0.822 chord, the flow separation close to the trailing edge (0.913 chord) becomes more significant with the plasma actuation. For further understanding the reason of behind the negative effect of the plasma actuation at 50 mN/m, Figure 5.9 shows the symmetry plane TKE contours. Comparing Figure 5.9(a) and Figure 5.9(b) reveals that plasma actuation at a 50 mN/m strength increases turbulent boundary layer thickness which in turn increases the total pressure loss. Figure 5.8 further shows that the plasma actuation at higher actuation strengths, 100, 150 and 200 mN/m, eliminates the suction surface boundary layer separation near the trailing edge and reduces the velocity deficit both on the suction and pressure surfaces.

The effect of actuation strength can be observed from the variation of wake momentum thickness at 0.2 chord downstream of the blade trailing edge with plasma actuation strength as shown in Figure 5.10. The plasma actuation becomes more effective with increasing actuation strength in reducing wake momentum thickness. Although the wake momentum thickness reduction with actuation strength increase starts to level off after 150 mN/m, increasing the actuation strength to 200 mN/m causes a significant reduction in the wake momentum thickness.

The pitchwise distribution of the wake total pressure loss coefficient at 0.2 chord downstream of blade trailing edge is shown in Figure 5.11. It is interesting to note that the plasma actuation with a 50 mN/m actuation strength increases the depth of the blade wake which may be attributed to the higher losses associated with a thicker turbulent boundary layer close to the trailing edge (Figure 5.9(b)). Above that actuation strength, the losses associated with turbulent boundary layer becomes smaller (Figure 5.9(c)) and the plasma actuation reduces both width and depth of the blade wake.

The power calculations are presented in Figure 5.12. The rotor equivalent power initially drops with plasma actuation strength increase and then increases. The deviation angle shows an opposite behavior with the rotor equivalent power. As expected, increasing the plasma actuation strength increases the plasma power linearly. The power ratio increases significantly with the actuation strength. The reason is the substantial increase of flow velocity in the plasma actuator region with increasing plasma actuation strength, as power input is the product of actuation strength and flow velocity.

Consequently, it is noted that the plasma actuation with 200 mN/m is the most effective in terms of wake momentum reduction (56.4%) at a cost of 3.70% the rotor equivalent power. On the

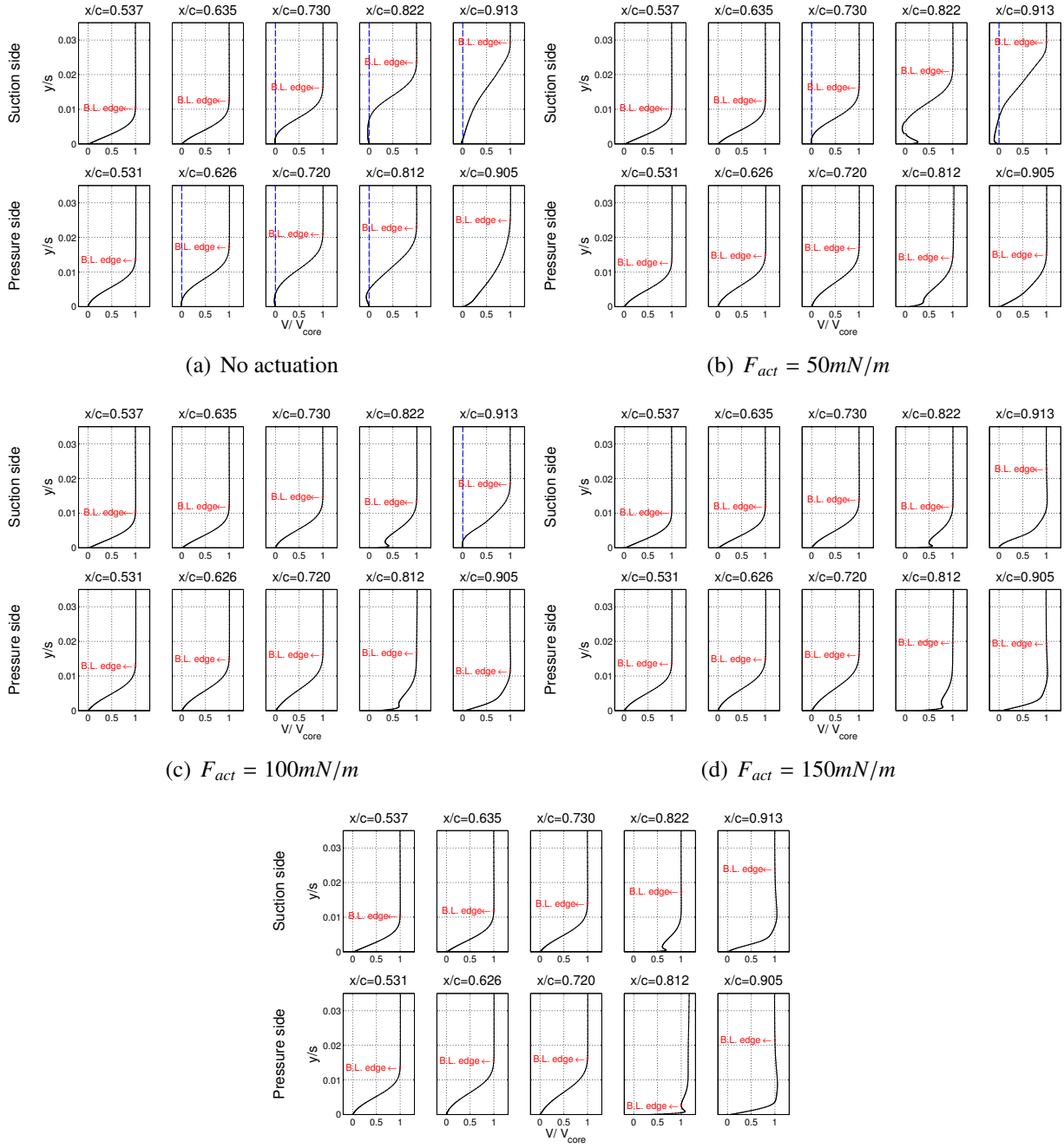

(a) No actuation

(b) $F_{act} = 50mN/m$

(c) $F_{act} = 100mN/m$

(d) $F_{act} = 150mN/m$

(e) $F_{act} = 200mN/m$

Figure 5.8: Actuation strength effect on boundary layer profiles of time-averaged velocity

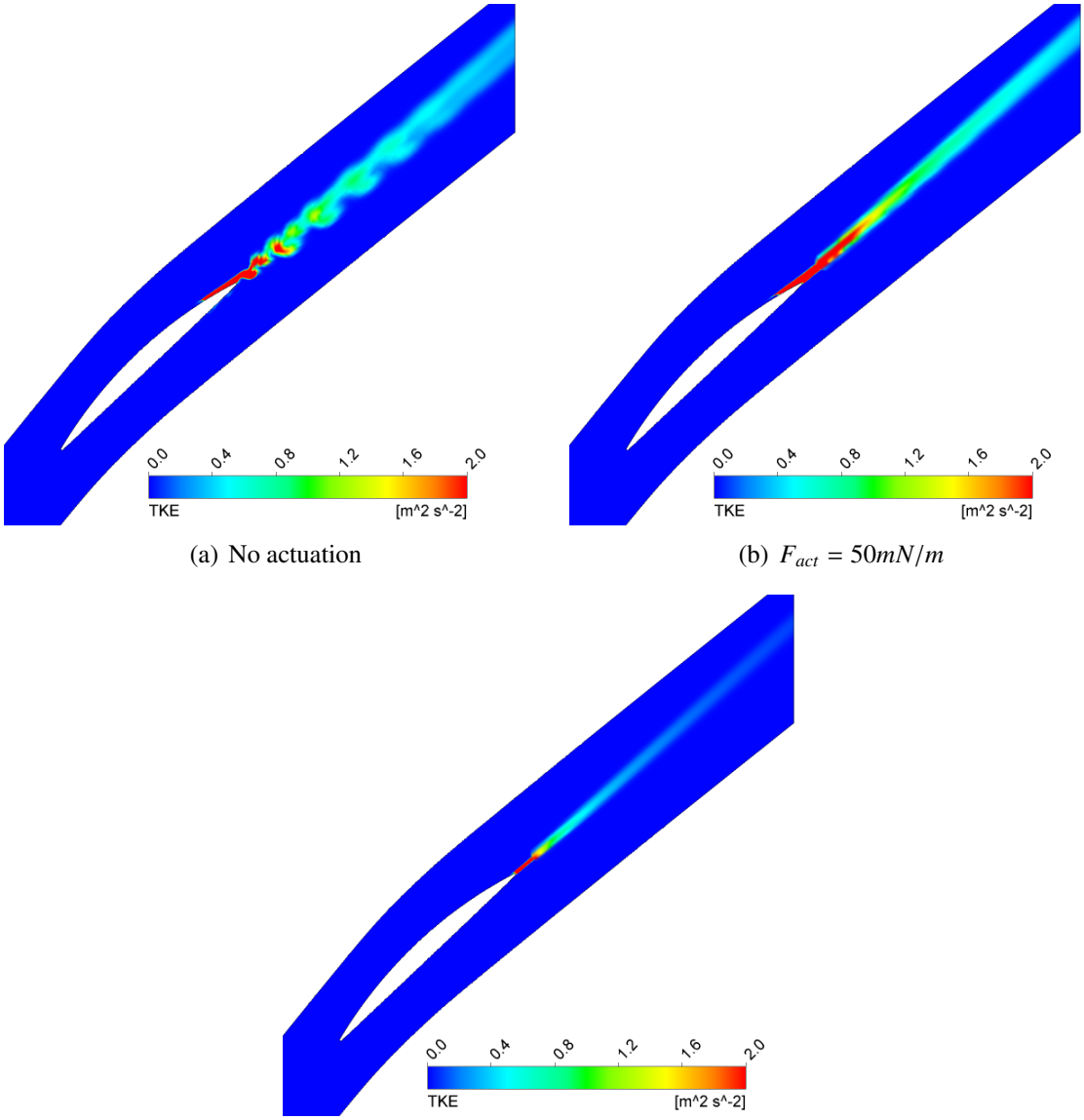

(a) No actuation

(b) $F_{act} = 50mN/m$

(c) $F_{act} = 200mN/m$

Figure 5.9: Actuation strength effect on symmetry plane TKE contours

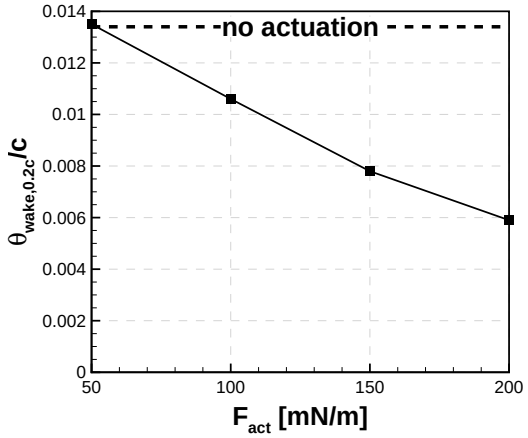

Figure 5.10: Actuation strength effect on wake momentum thickness at 0.2 chord downstream of blade trailing edge

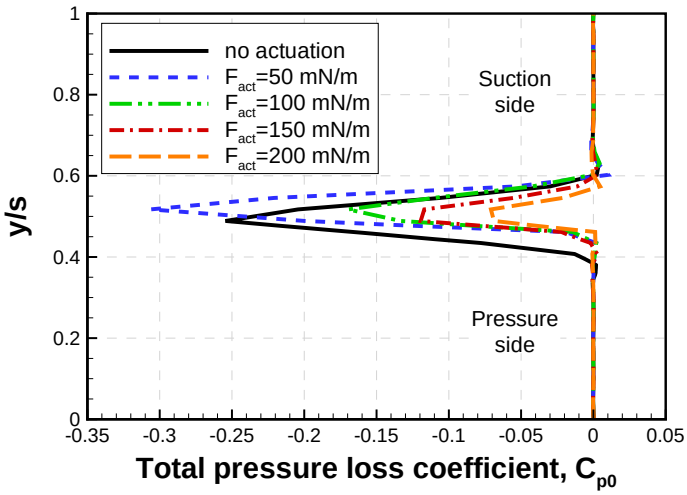

Figure 5.11: Actuation strength effect on pitchwise profile wake total pressure loss coefficient at 0.2 chord downstream of blade trailing edge

other hand, the plasma actuation at a strength of 150 mN/m reduces wake momentum reduction by 41.7% with a rotor equivalent power of 2.57%, which is proportionally more efficient. A leveling off effect of the plasma actuation strength was observed to start after 150 mN/m in wake momentum thickness as shown in Figure 5.10. A plasma actuation strength of 150 mN/m is thus chosen as the nominal value for the pulsed actuation study.

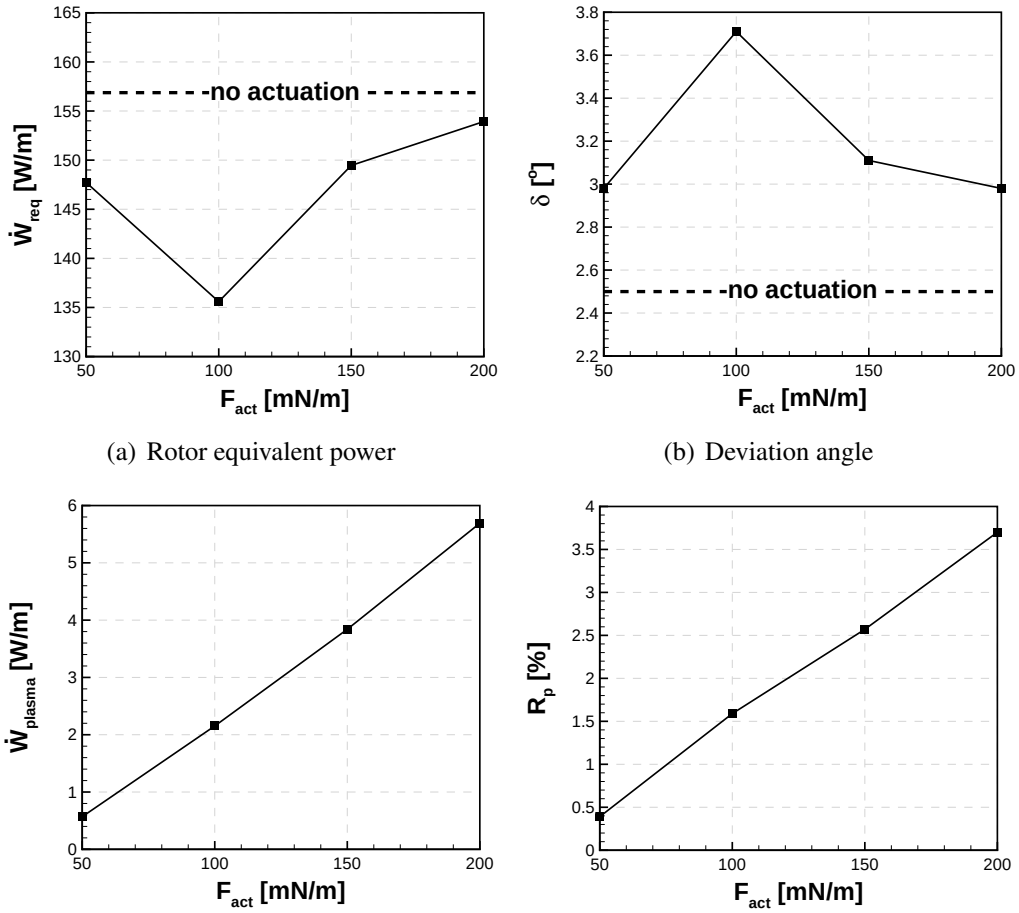

(a) Rotor equivalent power (b) Deviation angle

(c) Plasma power (d) Power ratio

Figure 5.12: Actuation strength effect on cascade performance and power

5.1.2 Pulsed Plasma Actuation

Unsteady flow simulations were performed for the no actuation case to determine the time history of flow velocity inside the blade wake. The numerical probes were located 0.05 chord downstream of blade trailing edge as schematically shown in Figure 5.13. The locations of the probes were determined such that the frequency of vortex shedding within the blade wake could be captured. The dominant flow frequencies obtained from the spectral analysis for these probe locations were exactly the same. Figure 5.14 shows spectral analysis performed for the probe number 2. The spectral analysis suggested that the vortex shedding frequency was 304 Hz.

Pulsing Frequency Effect

The pulsed plasma actuation was applied over a range of pulsing frequencies at 0.8 chord with an actuation strength of 150 mN/m and a duty cycle of 0.5. To determine the pulsing frequency effect on the blade wake momentum thickness, Figure 5.15 shows the variation of wake momentum thickness at 0.2 chord downstream of the trailing edge. It is observed that pulsed actuation at a

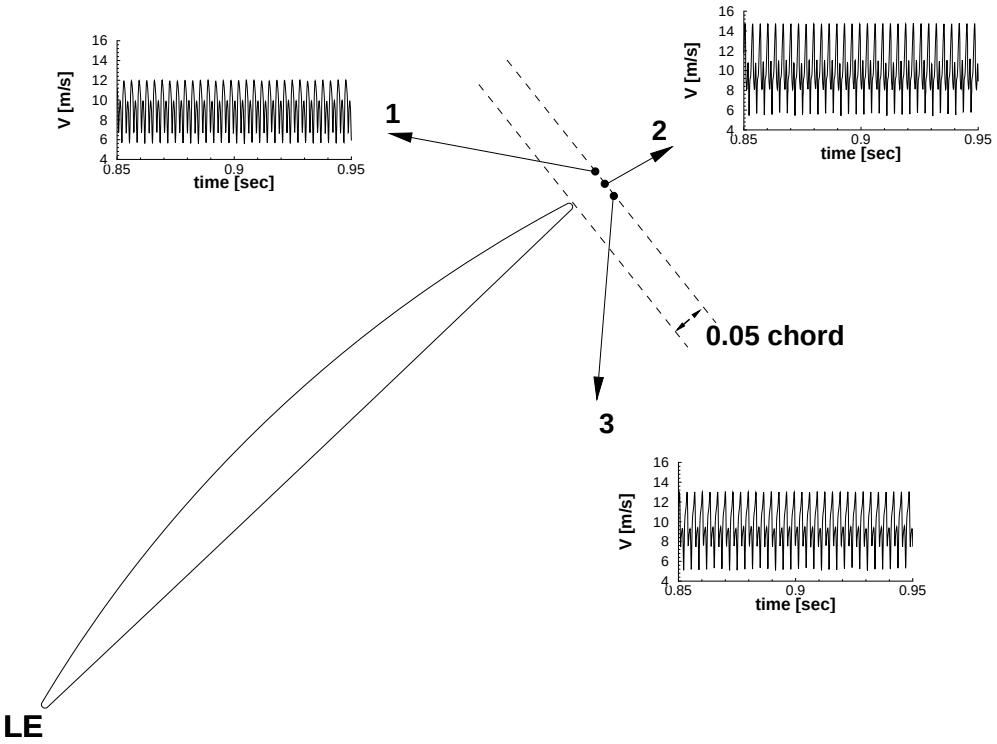

Figure 5.13: Numerical probes located at the downstream of the DCA-2 airfoil trailing edge

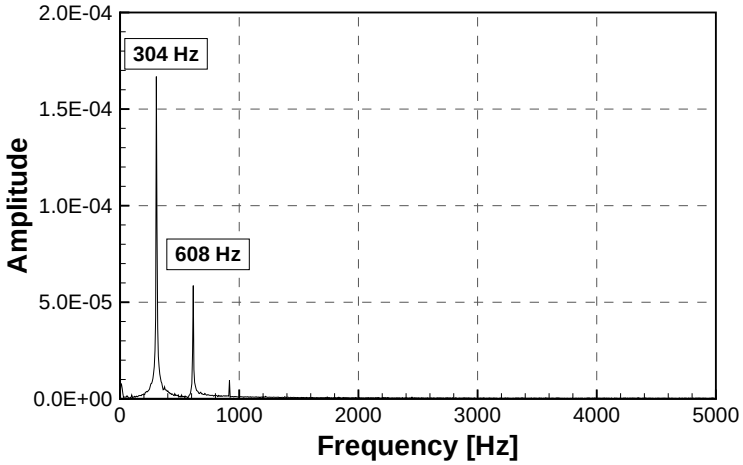

Figure 5.14: Spectral analysis for the velocity signal of probe 2

pulsing frequency of 650 Hz reduces the wake momentum thickness the least. In addition, it is seen that there is a minimum around the vortex shedding frequency (304 Hz), perhaps indicating some resonance effect.

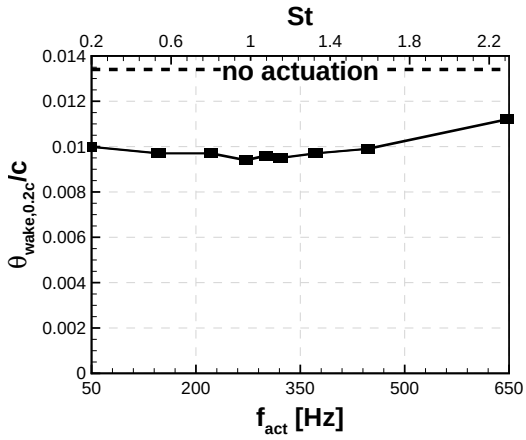

Figure 5.15: Pulsing frequency effect on wake momentum thickness at 0.2 chord downstream of blade trailing edge

The power calculations presented in Figure 5.16 reveals that the rotor equivalent power becomes close to no actuation case for a pulsing frequency range of 150 Hz and 450 Hz. This observation is also confirmed by the deviation angle plot shown in Figure 5.16(b). It is also observed that the plasma power increases with pulsing frequency and this effect levels off after the vortex shedding frequency (304 Hz). The power ratio increases in a similar trend; however, the leveling off effect is not present. This can be explained by the reduction observed in rotor equivalent power after 375 Hz.

Plasma Actuator Duty Cycle Effect

The effect of duty cycle was investigated (for D=0.1, 0.3, 0.5, 0.7 and 0.9) using plasma actuators at 0.8 chord at an actuation strength of 150 mN/m and a pulsing frequency of 304 Hz. Figure 5.17 shows the wake momentum thickness at 0.2 chord downstream of blade trailing edge. It can be seen that the wake momentum thickness reduction reaches to an asymptote at around D=0.7, which suggests that the duty cycle in a pulsed actuation should be no more than 0.7. It can be seen that the continuous actuation performs better in terms of reducing the wake momentum thickness compared to pulsed actuation for the same plasma actuation strength.

The pitchwise total pressure loss coefficient at 0.2 chord away downstream of blade trailing edge is shown in Figure 5.18. It is interesting to note that wake depth was significantly reduced by pulsing actuation at duty cycles of 0.5 and 0.7. On the other hand, the pulsed actuation at a duty cycle of 0.9 is observed to reduce the wake width the most.

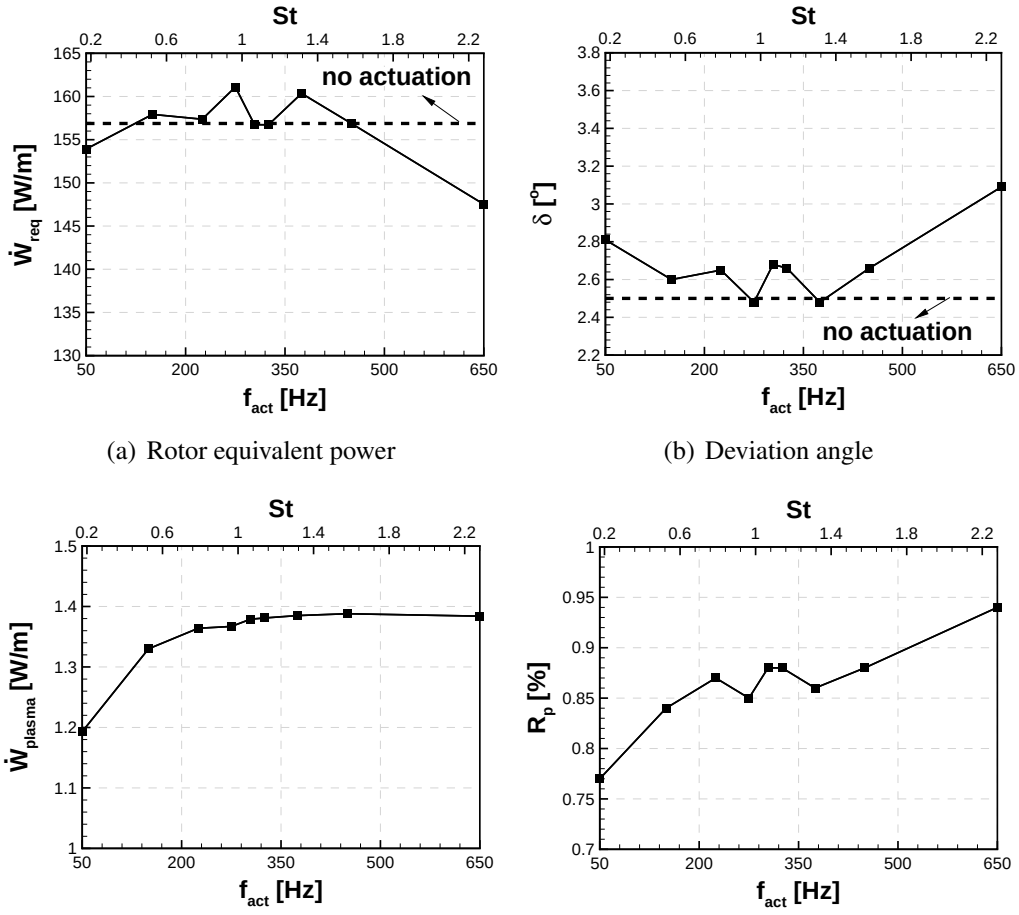

(a) Rotor equivalent power (b) Deviation angle

(c) Plasma power (d) Power ratio

Figure 5.16: Pulsing frequency effect on cascade performance and power

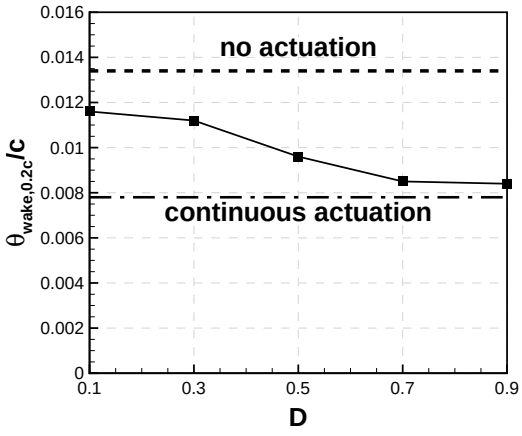

Figure 5.17: Duty cycle effect on wake momentum thickness at 0.2 chord downstream of blade trailing edge

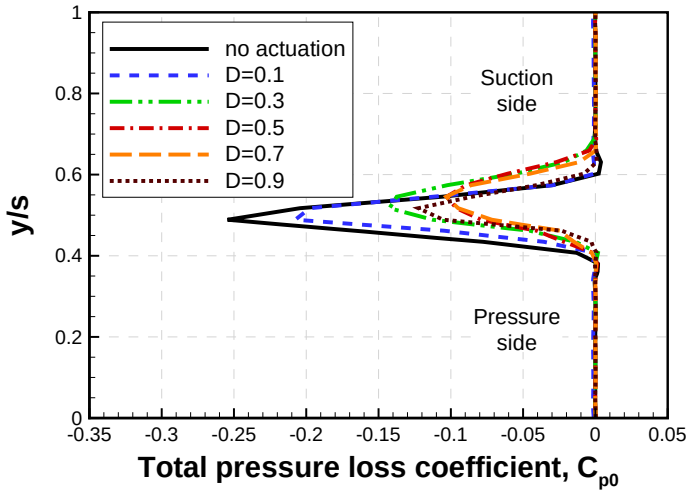

Figure 5.18: Duty cycle effect on pitchwise profile wake total pressure loss coefficient at 0.2 chord downstream of blade trailing edge

The actuation duty cycle effect on the actuation power is presented in Figure 5.19. The oscillating behavior of the rotor equivalent power can be attributed to the deviation angle. Figure 5.19(c) and Figure 5.19(d) show that the plasma power and power ratio increase with the duty cycle increase. As observed previously from Figure 5.17, duty cycles 0.7 and 0.9 have almost the same effect on wake momentum thickness. This results also suggests the plasma actuator that requires more plasma power without any wake momentum thickness reduction as the duty cycle increases between a range of 0.7 and 0.9.

5.1.3 Actuation Mode Effect

To investigate the effectiveness of pulsed and continuous plasma actuations, the plasma actuation was applied for the same plasma power of 1.38 W/m. The plasma actuation parameters for the continuous and pulsed actuation cases are listed in Table 5.1. The continuous plasma actuation was applied with an actuation strength of 77 mN/m. The pulsed actuation was applied with an actuation strength of 150 mN/m at a pulsing frequency of 304 Hz and a duty cycle of 0.5.

Table 5.1: Cases studied for the actuation mode effect

Actuation type	x_{act}	F_{act} [mN/m]	f_{act} [Hz]	D
Pulsed	0.8	150	304	0.5
Continuous	0.8	77	-	-

The boundary layer profiles are shown in Figure 5.20. As shown in Figure 5.20(a) for the no actuation case, the suction surface boundary layer flow at 0.913 chord reversed its direction.

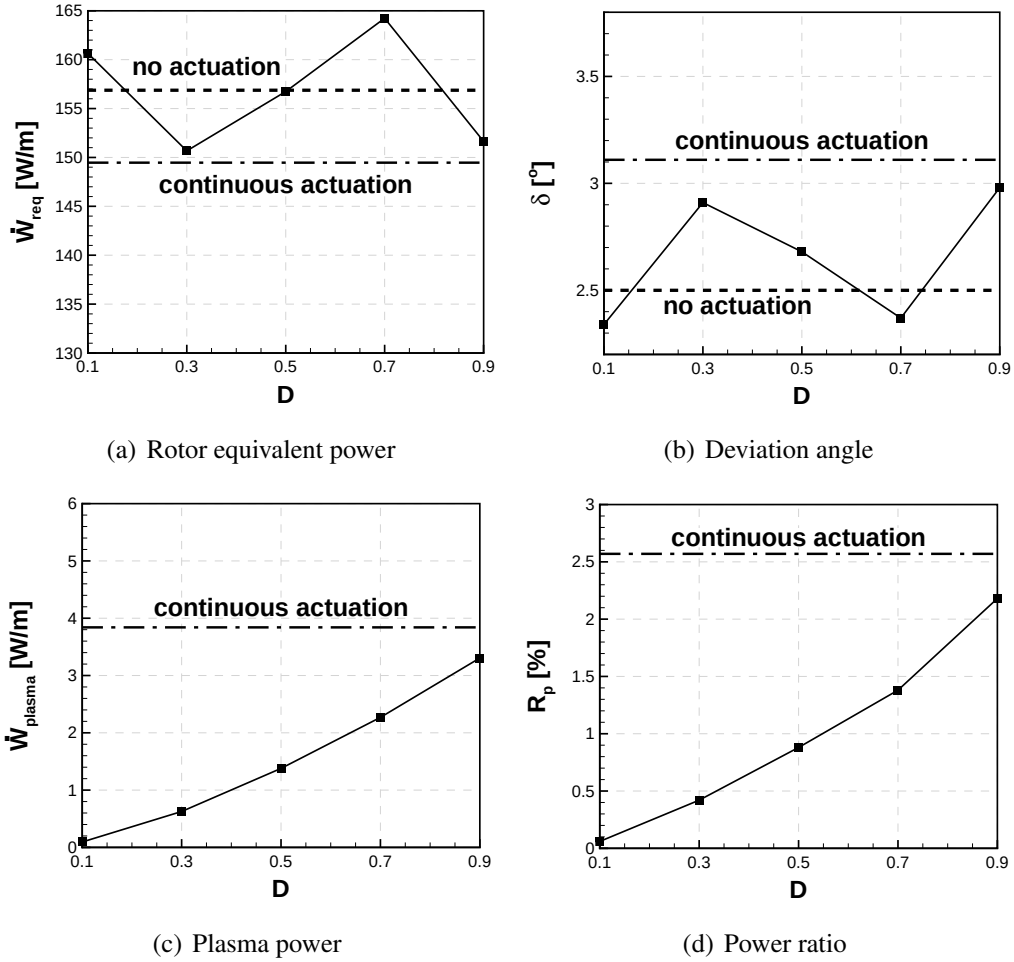

(a) Rotor equivalent power

(b) Deviation angle

(c) Plasma power

(d) Power ratio

Figure 5.19: Duty cycle effect on cascade performance and power

The continuous actuation causes a more severe boundary layer flow reversal. Whereas, the pulsed actuation eliminates the boundary layer flow separation both on the suction and pressure surfaces. Figure 5.21 shows that the pulsed actuation laminarize the boundary layer. However, the continuous actuation delays the transition.

The pitchwise wake total pressure loss coefficient is shown in Figure 5.22. The profiles show that the pulsed actuation significantly reduces the wake depth compared to the no actuation case. Even though the continuous actuation reduces the wake width, the wake depth stays almost the same. In fact, the pulsed actuation increases the wake width slightly. This result could explain the reduced wake depth with plasma actuation such that the pulsed actuation brings in outer layer high-momentum into the wake. The high-momentum fluid addition to the blade wake reduces to the wake depth. Table 5.2 presents the power calculations together with the blade wake thickness at 0.2 chord downstream of blade trailing edge. It can be seen that the pulsed actuation reduces the wake momentum thickness at 0.2 chord downstream of the blade trailing edge more effectively compared to the continuous actuation. Therefore, it can be concluded that the pulsed actuation

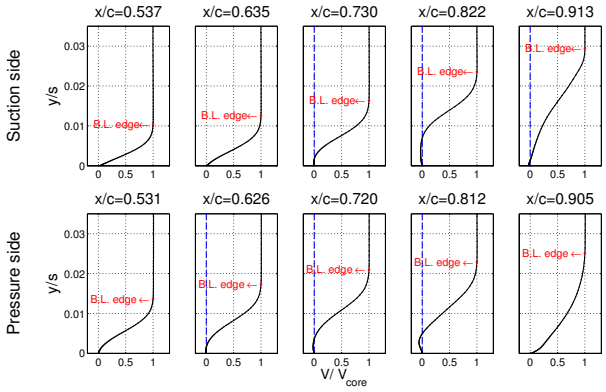

(a) No actuation

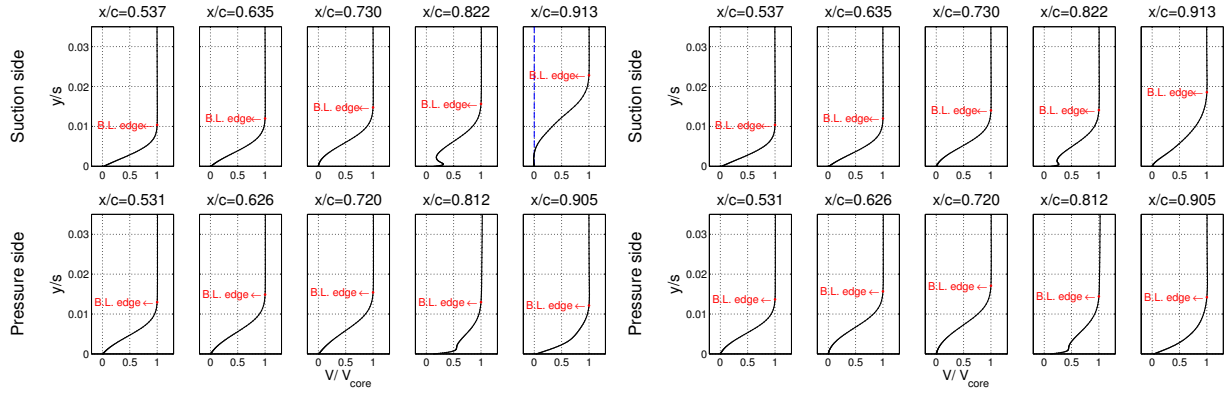

(b) Continuous actuation

(c) Pulsed actuation

Figure 5.20: Actuation mode effect on boundary layer profiles of time-averaged velocity

reduces the wake size by bringing in high-momentum fluid from outer layer to the wake. It can be seen that the rotor equivalent power stays almost the same in pulsed actuation. However, the continuous plasma actuation reduces the rotor equivalent power significantly. This result can be attributed to the relatively higher flow turning achieved (relatively smaller deviation angle) with pulsed actuation case.

Table 5.2: Actuation mode effect on blade wake and rotor equivalent power

Case	$\theta_{wake,0.2c}/c$	$\triangle(\theta_{wake,0.2c}/c)$ [%]	$\dot{W}_{req}$ [W/m]	δ [°]	$\dot{W}_{plasma}$ [W/m]	R_p [%]
No actuation	0.0134	-	156.9	2.50	-	-
Pulsed actuation	0.0096	-28.7	156.7	2.68	1.38	0.88
Continuous actuation	0.0128	-5.1	128.4	4.07	1.38	1.09

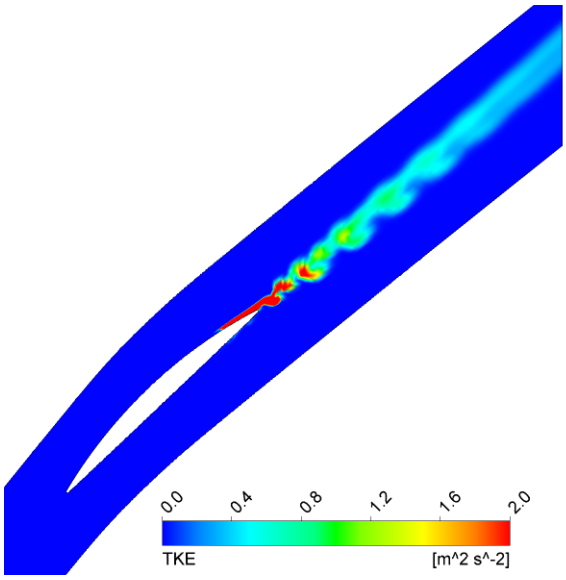

(a) No actuation

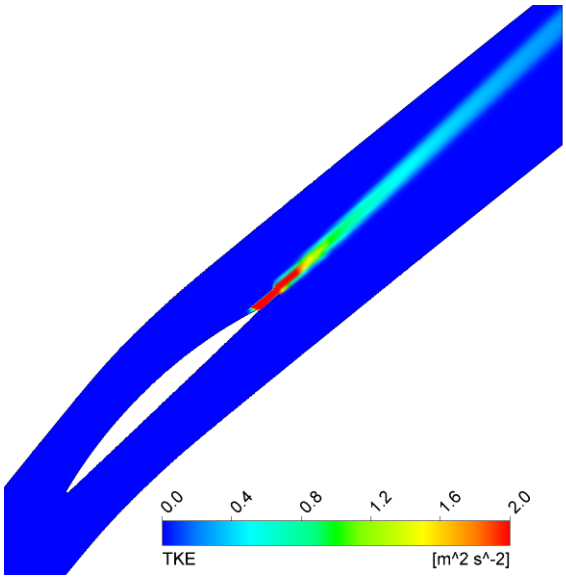

(b) Continuous actuation

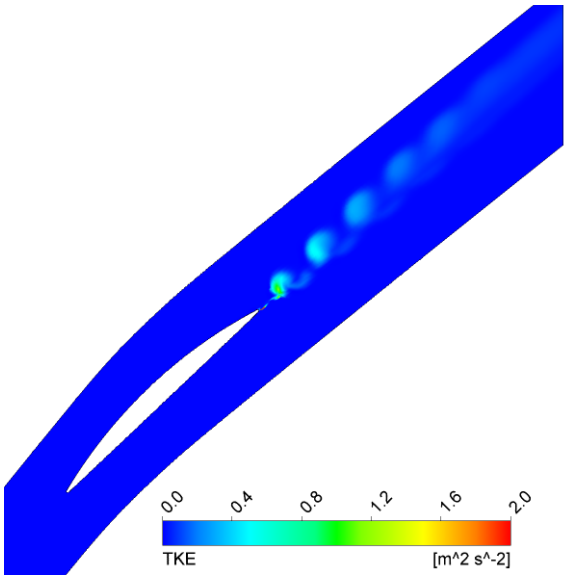

(c) Pulsed actuation

Figure 5.21: Actuation mode effect on symmetry plane TKE contours

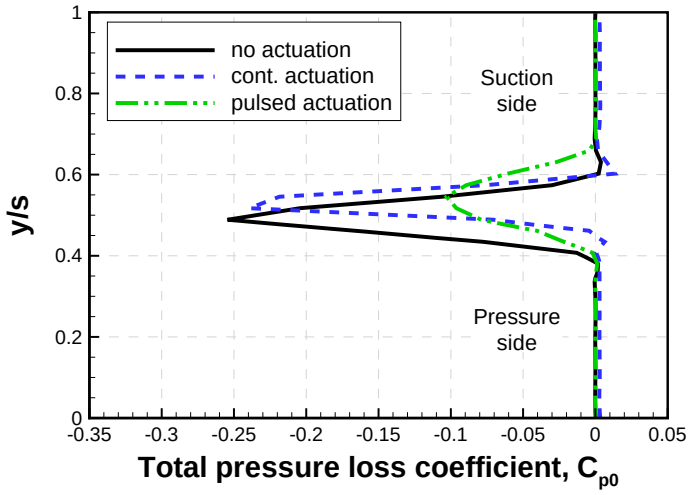

Figure 5.22: Actuation mode effect on pitchwise profile wake total pressure loss coefficient at 0.2 chord downstream of blade trailing edge

5.2 Reynolds Number Scaling for Wake/Noise Suppression

The Reynolds number scaling study was performed at a Reynolds number range between 3.5×10^5 and 1.75×10^6 for wake/noise control. To determine the required plasma actuation strength to achieve a 29.25%±0.25 reduction in blade wake momentum thickness at 0.2 chord downstream of blade trailing edge, the plasma actuators were located at 0.8 chord and plasma actuation was applied in continuous mode at each Reynolds number. Figure 5.23 shows that the required plasma actuation strength increases non-linearly with Reynolds number and Mach number. The best fit to this data was obtained with a 1.239 power-law function. As with the first two flow control concepts, this scaling study can be considered preliminary. Figure 5.24 shows that the wake momentum thickness (without actuation) reduces as flow velocity increases for the same blade geometry due to improved boundary layer behaviour with rising Reynolds number. Thus, a more accurate scaling study that extends to higher flow velocities would involve changing the blade thickness with Reynolds number to maintain the same nominal value of wake momentum thickness.

5.3 Summary

For the blade wake/noise attenuation concept, the reduction in wake displacement thickness improves with the placement of the actuator closer to the blade trailing edge and with an increase in actuation strength. Since plasma actuation delays boundary layer transition, an actuator position too far from the trailing edge or an insufficient actuation strength could be detrimental to wake displacement thickness if the boundary layer remains laminar and separates at the trailing edge instead

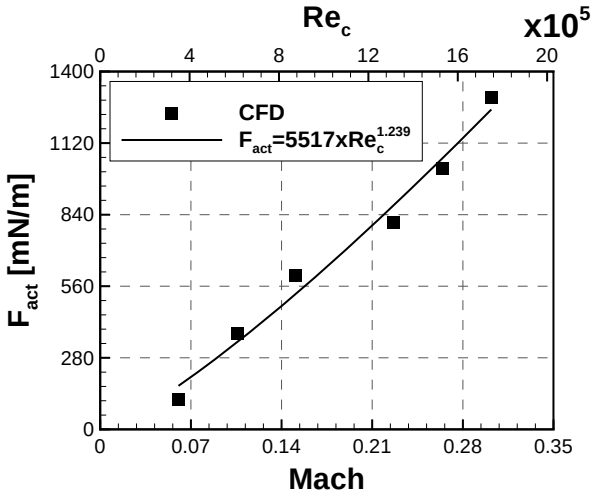

Figure 5.23: Reynolds number scaling for blade wake/noise control with plasma actuation

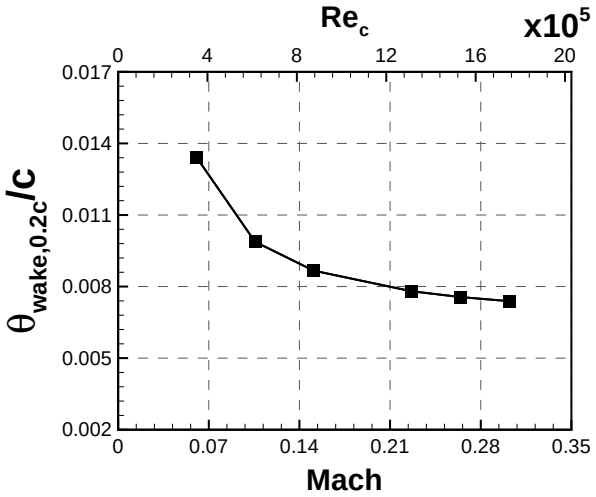

Figure 5.24: Reynolds number effect on wake momentum thickness at 0.2 chord downstream of blade trailing edge

of exhibiting an earlier laminar separation followed by a turbulent reattachment prior to reaching the trailing edge as in the nominal case. In all cases, continuous plasma actuation with the same actuator strength on both pressure and suction side increases deviation slightly and thus decreases equivalent rotor power. Pulsed actuation is less effective than continuous actuation at the same actuator strength but is superior for the same input power. In terms of pulsing parameters, although the variation of effectiveness with pulsing frequency is small, an optimum frequency occurs at a Strouhal number around 1. In terms of duty cycle, the effectiveness of pulsed actuation reaches a ceiling above a duty cycle of 0.7. Scaling simulations indicate that the plasma actuation strength requirement for this concept increases non-linearly (power-law of 1.239) with the Reynolds number.

Conclusions and Recommendations

This research investigated three flow control concepts using plasma actuators in the context of a low-speed linear compressor blade cascade. The first two concepts aim to reduce corner separation and to suppress blade boundary layer separation for increasing compressor stage pressure ratio with placement of plasma actuators on the suction side and endwall. The last concept consists of putting plasma actuators on both blade pressure and suction sides to attenuate the blade wake to reduce the compressor/fan noise. The methodology consists of computational (CFD) assessment of each concept and cascade tests for first two concepts for experimental demonstration as well as validation of the computational tool and extension of the detailed results obtained from simulations. For each concept, the validated CFD tool was also used for a preliminary scaling study with Reynolds number for a rough estimate of actuation requirements at realistic operating conditions.

For the concept to reduce corner separation with suction side and endwall plasma actuators, the main conclusions/findings are:

1. The computational tool can capture reasonably well the measured flow features and trends associated with corner separation and the effect of endwall suction and plasma actuation on this phenomenon.
2. The new endwall suction scheme developed in this project can reduce corner separation significantly with little suction mass flow to provide a target for plasma actuation and improve flow two-dimensionality for the blade boundary layer separation suppression study.
3. Simulations and tests show that a combination of the suction surface and endwall plasma actuators located near the separation region and arranged to induce streamwise momentum can have a noticeable impact on corner separation. Simulations with higher but achievable plasma actuator strength in the short-term showed comparable reduction in total pressure losses associated with corner separation.
4. Simulations at higher speeds indicate that the required actuator strength scales approximately with the square of the Reynolds number, a fact likely explained by the quadratic relationship between the induce velocity and actuator strength demonstrated analytically and computationally in the present work.

For the concept to suppress blade boundary layer separation with suction side plasma actuation, the main conclusions/findings are:

5. Suction side plasma actuation increases pressure rise and rotor equivalent power through a decrease in deviation (increased flow turning), boundary layer displacement thickness (blockage) and total pressure loss.
6. The optimum actuator location in terms of pressure rise is just upstream of the separation point. The improvement in the pressure rise reduces as the actuator moves downstream due to a shift in the laminar separation bubble towards the trailing edge which has adverse effects on the deviation and trailing edge displacement thickness.
7. The rate of improvement in pressure rise with actuator strength decreases with increasing actuator strength.
8. Pulsed actuation performed less effectively than continuous actuation for the same actuator strength but better for the same input power. Pulsing frequency only have small impacts on the increase in pressure rise and equivalent rotor power but pulsing frequency near the fundamental flow oscillation frequency in the boundary layer.
9. The variation in experimental suction surface pressure distribution with actuator strength, actuation mode (continuous versus pulsed) and pulsing frequency and duty cycle exhibit the same general trends seen in the simulations in spite of differences in the nominal flow field from actuator protrusion in the test setup.
10. Simulations at higher speeds indicate that the required actuator strength scales approximately with the square of the Reynolds number, again likely linked to the quadratic relationship between the induced velocity and actuator strength.

For the concept to reduce wake momentum deficiency with suction and pressure side plasma actuation, the main conclusions/findings are:

11. Wake displacement thickness improves with the placement of the actuator closer to the blade trailing edge and with an increase in actuator strength.
12. Plasma actuation delays boundary layer transition. Consequently, an actuator position too far from the trailing edge or insufficient actuator strength could be detrimental to wake displacement thickness if the boundary layer remains laminar and separates at the trailing edge instead of exhibiting an earlier laminar separation followed by a turbulent reattachment prior to reaching the trailing edge as in the nominal case.
13. Continuous plasma actuation with the same actuator strength on both pressure and suction side increases deviation slightly and thus decreases equivalent rotor power.

14. Pulsed actuation is less effective than continuous actuation at the same actuator strength but is superior for the same input power. The variation of effectiveness with pulsing frequency is small but an optimum frequency occurs at a Strouhal number around 1. The actuation effectiveness increases with duty cycle but reaches a ceiling above a duty cycle of 0.7.
15. Scaling simulations indicate that the plasma actuation strength requirement for this concept increases with the Reynolds number with a 1.239 power-law function. Therefore, wake suppression is the most promising concept among the three plasma actuation concepts.

The contributions of this project are:

1. First experimental demonstration with detailed measurements showing reduction of corner separation loss with plasma actuation.
2. Design and implementation of an endwall suction scheme that is more effective than other systems in the literature with equivalent low mass suction.
3. First experimental demonstration of plasma actuation on a high camber compressor blade showing the influence of actuation parameters on suction side boundary layer.
4. Use of experimentally validated CFD setup to carry out a detailed assessment of the plasma actuator's effect on the blade performance and flow field for each flow control concept and preliminary determination of best location and operating parameters.
5. Determination of preliminary scaling laws for actuation requirements at real operating conditions.

Although plasma actuation flow control was shown to be effective, here are some of the limitations for real applications of these concepts:

1. Requirement for significantly larger actuator strengths for operation at realistic flow velocities.
2. Influence of temperature, pressure and humidity/rain on actuator performance must be assessed.
3. Robustness of the actuator in terms of resisting degradation of the dielectric material with usage (which occurred on the actuators used in this research).
4. Integration of plasma actuators on small compressor blades.

Based on this research, the recommendations for future work include:

1. Perform tests on larger cascade blades with flush mounted actuators and accessories to minimize their effect on the nominal flow field.
2. Investigate spatial variation of actuator strength to optimize the effect on the flow field.
3. Carry out a more accurate Reynolds number scaling study that extends to higher flow velocities by changing the blade geometry with Reynolds number to keep the nominal blade performance the same as the Reynolds number increases.

References

ANSYS (2009). *CFX-Solver Modeling Guide*. ANSYS Inc, 12th edition.

BLOXHAM, M. and BONS, J. (2010). Leading-Edge Endwall Suction and Midspan Blowing to Reduce Turbomachinery Losses. *Journal of Propulsion and Power*, 26, 1268–1275.

BROOKFIELD, J. and WAITZ, I. (2000). Trailing-Edge Blowing for Reduction of Turbomachinery Fan Noise. *Journal of Propulsion and Power*, 16, 57–64.

CAROLUS, T., SCHNEIDER, M. and REESE, H. (2007). Axial Flow Fan Broad-Band Noise and Prediction. *Journal of Sound and Vibration*, 300, 50–70.

CHEN, W., LIEN, F. and LESCHZINER, M. (1998). Computational Prediction of Flow Around Highly Loaded Compressor-Cascade Blades with Non-Linear Eddy-Viscosity Models. *International Journal of Heat and Fluid Flow*, 19, 307–319.

CLARK, J. and GROVER, E. (2007). Assessing Convergence in Predictions of Periodic-Unsteady Flowfields. *Journal of Turbomachinery*, 129, 740–749.

CORKE, T., BOWLES, P., HE, C. and MATLIS, E. (2011). Sensing and Control of Flow Separation Using Plasma Actuators. *Philosophical Transactions of the Royal Society A: Mathematical, Physical and Engineering Sciences*, 369, 1459–1475.

CORKE, T., ENLOE, C. and WILKINSON, S. (2010). Dielectric Barrier Discharge Plasma Actuators for Flow Control. *Annual Review of Fluid Mechanics*, 42, 505–529.

CORKE, T., POST, M. and ORLOV, D. (2009). Single Dielectric Barrier Discharge Plasma Enhanced Aerodynamics: Physics, Modeling and Applications. *Experiments in Fluids*, 46, 1–26.

CUMPSTY, N. (1989). *Compressor Aerodynamics*. Halsted Press.

DEUTSCH, S. and ZIERKE, W. (1987). The Measurement of Boundary Layers on a Compressor Blade in Cascade: Part 1-A Unique Experimental Facility. *Journal of Turbomachinery*, 109, 520–526.

DONG, Y., GALLIMORE, S. and HODSON, H. (1987). Three-Dimensional Flows and Loss Reduction in Axial Compressors. *Journal of Turbomachinery*, 109, 354–361.

DRING, R., JOSLYN, H. and HARDIN, L. (1982). Investigation of Axial Compressor Rotor Aerodynamics. *Journal of Engineering Power*, 104, 84–96.

DYSON, R., HIXON, R., NALLASAMY, M. and SAWYER, S. (2004). Simulating Nonlinear Stator Noise for Active Control. TM 2003-212338, NASA.

ENLOE, C., MCLAUGHLIN, T., FONT, G. and BAUGHN, J. (2006). Parameterization of Temporal Structure in the Single-Dielectric-Barrier Aerodynamic Plasma Actuator. *AIAA journal*, 44, 1127–1136.

ENLOE, C., MCLAUGHLIN, T., VANDYKEN, R., KACHNER, K., JUMPER, E., CORKE, T., POST, M. and HADDAD, O. (2004). Mechanisms and Responses of a Single Dielectric Barrier Plasma Actuator: Geometric Effects. *AIAA journal*, 42, 595–604.

ENVIA, E. (2001). Fan Noise Reduction: An Overview. *39th Aerospace Sciences Meeting and Exhibit*. Reno, Nevada, AIAA 2001–0661.

FITE, E., WOODWARD, R. and PODBOY, G. (2006). Effect of Trailing Edge Flow Injection on Fan Noise and Aerodynamic Performance. *3rd Flow Control Conference*. San Francisco, USA, AIAA 2006–2844.

FONT, G., ENLOE, C. and MCLAUGHLIN, T. (2010). Plasma Volumetric Effects on the Force Production of a Plasma Actuator. *AIAA journal*, 48, 1869–1874.

FORTE, M., JOLIBOIS, J., PONS, J., MOREAU, E., TOUCHARD, G. and CAZALENS, M. (2007). Optimization of a Dielectric Barrier Discharge Actuator by Stationary and Non-Stationary Measurements of the Induced Flow Velocity: Application to Airflow Control. *Experiments in Fluids*, 43, 917–928.

GAITONDE, D., VISBAL, M. and ROY, S. (2006a). A Coupled Approach for Plasma-Based Flow Control Simulations of Wing Sections. *44th Aerospace Sciences Meeting and Exhibit*. Reno, Nevada, AIAA 2006–1205.

GAITONDE, D., VISBAL, M. and ROY, S. (2006b). A Coupled Approach for Plasma-Based Flow Control Simulations of Wing Sections. *44th Aerospace Sciences Meeting and Exhibit*. Reno, Nevada, AIAA 2006–1205.

GANZ, U., JOPPA, P., PATTEN, T. and SCHARPF, D. (1998). Boeing 18-Inch Fan Rig Broadband Noise Test. CR 208704, NASA.

GBADEBO, S., CUMPSTY, N. and HYNES, T. (2005). Three-Dimensional Separations in Axial Compressors. *Journal of Turbomachinery*, 127, 331–339.

GBADEBO, S., CUMPSTY, N. and HYNES, T. (2008). Control of Three-Dimensional Separations in Axial Compressors by Tailored Boundary Layer Suction. *Journal of Turbomachinery*, 130.

GERNER, A., MAURER, C. and GALLINGTON, R. (1984). Non-Nulling Seven-Hole Probes for High Angle Flow Measurement. *Experiments in Fluids*, 2, 95–103.

GMELIN, C., THIELE, F., LIESNER, K. and MEYER, R. (2011). Investigations of Secondary Flow Suction in a High Speed Compressor Cascade. *Proceedings of ASME Turbo Expo 2011*. Vancouver, Canada, GT2011–46479.

GREGORY-SMITH, D., GRAVES, C. and WALSH, J. (1988). Growth of Secondary Losses and Vorticity in an Axial Turbine Cascade. *Journal of Turbomachinery*, 110, 1–8.

GÜMMER, V., GOLLER, M. and SWOBODA, M. (2008). Numerical Investigation of Endwall Boundary Layer Removal on Highly Loaded Axial Compressor Blade Rows. *Journal of Turbomachinery*, 130, 151–159.

GUO, S., CHEN, S., SONG, Y. and CHEN, F. (2010a). Effects of Boundary Layer Suction on Aerodynamic Performance in a High-load Compressor Cascade. *Chinese Journal of Aeronautics*, 23, 179–186.

GUO, S., CHEN, S. W., LU, H. W., SONG, Y. P. and CHEN, F. (2010b). Enhancing Aerodynamic Performances of a High-Turning Compressor Cascade via Boundary Layer Suction. *Science China Technological Sciences*, 53, 2748–2755.

HAH, C. and LOELLBACH, J. (1999). Development of Hub Corner Stall and Its Influence on the Performance of Axial Compressor Blade Rows. *Journal of Turbomachinery*, 121, 67–77.

HALASZ, C. (2005). *Advanced Trailing Edge Blowing Concepts for Fan Noise Control: Experimental Validation*. Master thesis, Virginia Polytechnic Institute and State University.

HALASZ, C., ARNTZ, D., BURDISSO, R. and NG, W. (2005). Fan Flow Control for Noise Reduction Part 1: Advanced Trailing Edge Blowing Concepts. *11th Aeroacoustics Conference*. Monterey,California, AIAA 2005–3025.

HALL, C. and CRICHTON, D. (2007). Engine Design Studies for a Silent Aircraft. *Journal of Turbomachinery*, 129, 479–487.

HECKLAU, M., ZANDER, V., PELTZER, I., NITSCHE, W., HUPPERTZ, A. and SWOBODA, M. (2010). Experimental AFC Approaches on a Highly Loaded Compressor Cascade. *Active Flow Control II*, 108, 171–186.

HERGT, A., DORFNER, C., STEINERT, W., NICKE, E. and SCHREIBER, H. (2009). Advanced Non-Axisymmetric Endwall Contouring for Axial Compressors by Generating an Aerodynamic Separator- Part II: Experimental and Numerical Cascade Investigation. *Proceedings of ASME Turbo Expo 2009*. Orlando, Florida, GT2009–59384.

HERGT, A., MEYER, R. and ENGEL, K. (2006). Experimental Investigation of Flow Control in Compressor Cascades. *Proceedings of ASME Turbo Expo 2006*. Barcelona, Spain, GT2006–90415.

HERZIG, H., HANSEN, A. and COSTELLO, G. (1953). A visualization Study of Secondary Flows in Cascades. Technical Report 1163, NACA.

HO, C. and HUERRE, P. (1984). Perturbed Free Shear Layers. *Annual Review of Fluid Mechanics*, 16, 365–422.

HORLOCK, J., LOUIS, J., PERCIVAL, P. and LAKSHMINARAYANA, B. (1966). Wall Stall in Compressor Cascades. *Journal of Basic Engineering*, 88, 637–648.

HOSKINSON, A. and HERSHKOWITZ, N. (2010). Differences Between Dielectric Barrier Discharge Plasma Actuators with Cylindrical and Rectangular Exposed Electrodes. *Journal of Physics D: Applied Physics*, 43, 1–8.

HOSKINSON, A., HERSHKOWITZ, N. and ASHPIS, D. (2008). Force Measurements of Single and Double Barrier DBD Plasma Actuators in Quiescent Air. *Journal of Physics D, Applied Physics*, 41, 1–9.

HOWELL, R., RAMESH, O., HODSON, H., HARVEY, N. and SCHULTE, V. (2001). High lift and Aft-Loaded Profiles for Low-Pressure Turbines. *Journal of Turbomachinery*, 123, 181–188.

HUANG, J. (2005). *Separation Control Over Low Pressure Turbine Blades Using Plasma Actuators*. Doctoral thesis, University of Notre Dame.

HUANG, J., CORKE, T. and THOMAS, F. (2006). Unsteady Plasma Actuators for Separation Control of Low-Pressure Turbine Blades. *AIAA Journal*, 44, 1477–1487.

HUANG, J. and LEXINGTON, K. (1997). Turbulence Modeling Validation, Testing and Development. TM 110446, NASA.

HUFF, D. (2007). Noise Reduction Technologies for Turbofan Engines. TM 2007-214495, NASA.

INC., A. (2006). ANSYS CFX-Solver. Theory Guide Release 11, ANSYS CFX.

JAYARAMAN, B., THAKUR, S. and SHYY, W. (2006). Modeling of Dielectric Barrier Discharge and Resulting Fluid Dynamics. *44th Aerospace Sciences Meeting and Exhibit*. Reno, Nevada, AIAA 2006–688.

JOSLYN, H. and DRING, R. (1985). Axial Compressor Stator Aerodynamics. *Journal of Engineering for Gas Turbines and Power*, 107, 485–493.

KANG, S. and HIRSCH, C. (1991). Three Dimensional Flow in a Linear Compressor Cascade at Design Conditions. *International Gas Turbine and Aeroengine Congress and Exposition*. Orlando, FL, USA, 91–GT–114.

KLINE, S. and MCCLINTOCK, F. (1953). Describing Uncertainties in Single-Sample Experiments. *Mechanical Engineering*, 75, 3–8.

KOZLOV, A. and THOMAS, F. (2011a). Bluff-Body Flow Control via Two Types of Dielectric Barrier Discharge Plasma Actuation. *AIAA journal*, 49, 1919–1931.

KOZLOV, A. and THOMAS, F. (2011b). Plasma Flow Control of Cylinders in a Tandem Configuration. *AIAA Journal*, 49, 2183–2193.

LANGTRY, R., MENTER, F., LIKKI, S., SUZEN, Y., HUANG, P. and VÖLKER, S. (2006). A Correlation-Based Transition Model Using Local Variables: Part 2: Test Cases and Industrial Applications. *Journal of Turbomachinery*, 128, 423–434.

LEI, V. M., SPAKOVSZKY, Z. and GREITZER, E. (2008). A Criterion for Axial Compressor Hub-Corner Stall. *Journal of turbomachinery*, 130.

LEMIRE, S. and VO, H. (2008). Reduction of Fan and Compressor Wake Defect Using Plasma Actuation for Tonal Noise Reduction. *Proceedings of ASME Turbo Expo 2008*. Berlin, Germany, GT2008–50821.

LEMIRE, S., VO, H. and BENNER, M. (2009). Performance Improvement of Axial Compressors and Fans with Plasma Actuation. *International Journal of Rotating Machinery*, 2009, 1–13.

LEWIS, W. (1965). Fixed-Direction Probes for Aerodynamic Measurements. *Proceedings of the Institution of Mechanical Engineers*, 180, 141–152.

LI, Y., WU, Y., ZHOU, M., SU, C., ZHANG, X. and ZHU, J. (2010a). Control of the Corner Separation in a Compressor Cascade by Steady and Unsteady Plasma Aerodynamic Actuation. *Experiments in Fluids*, 48, 1015–1023.

LI, Y., ZHANG, X. and HUANG, X. (2010b). The Use of Plasma Actuators for Bluff Body Broadband Noise Control. *Experiments in Fluids*, 49, 367–377.

LIST, J., BYERLEY, A., MCLAUGHLIN, T. and VAN DYKEN, R. (2003). Using a Plasma Actuator to Control Laminar Separation on a Linear Cascade Turbine Blade. *41st Aerospace Sciences Meeting and Exhibit*. Reno, Nevada, AIAA 2003–1026.

LITTLE, J. and SAMIMY, M. (2010). High-Lift Airfoil Separation with Dielectric Barrier Discharge Plasma Actuation. *AIAA journal*, 48, 2884–2898.

LIU, Z., WANG, L. and FU, S. (2011). Study of Flow Induced by Sine Wave and Sawtooth Plasma Actuators. *Science Physics, Mechanics & Astronomy*, 54, 2033–2039.

LU, J., CHU, W. and WU, Y. (2009). Effects of Endwall Profiling on Axial Flow Compressor Stage. *Proceedings of ASME Turbo Expo 2009*. Florida, USA, GT2009–59418.

MAHALLATI, A. (2003). *Aerodynamics of a Low-Pressure Turbine Airfoil Under Steady and Periodically Unsteady Conditions*. Doctoral thesis, Carleton University.

MALAN, P., SULUKSNA, K. and JUNTASARO, E. (2009). Calibrating the γ-Re_θ Transition Model for Commercial CFD. *47th Aerospace Sciences Meeting*. Orlando,Florida, AIAA 2009–1142.

MAYLE, R. (1991). The role of Laminar-Turbulent Transition in Gas Turbine Engines. *Journal of Turbomachinery*, 113, 509–537.

MERCHANT, A., DRELA, M., KERREBROCK, J., ADAMCZYK, J. and CELESTINA, M. (2000). Aerodynamic Design and Analysis of a High Pressure Ratio Aspirated Compressor Stage. *Proceedings of ASME Turbo Expo 2000*. Munich, Germany, GT2000–619.

MERZKIRCH, W. (1987). Techniques of Flow Visualization. Report AG-302, AGARD.

MINTON, C. (2005). *Wake Filling Techniques for Reducing Rotor-Stator Interaction Noise*. Master thesis, Virginia Polytechnic Institute and State University.

MOFFAT, R. (1982). Contributions to the Theory of Single-Sample Uncertainty Analysis. *Transactions, Journal of Fluids Engineering*, 104, 250–258.

MURTHY, K. and LAKSHMINARAYANA, B. (1987). Hub Wall Boundary Layer Development and Losses in an Axial Flow Compressor Rotor Passage. *Zeitschrift fur Flugwissenschaften und Weltraumforschung*, 11, 1–11.

ORLOV, D. (2006). *Modelling and Simulation of Single Dielectric Barrier Discharge Plasma Actuators*. Doctoral thesis, University of Notre Dame.

ORLOV, D., APKER, T., HE, C., OTHMAN, H. and CORKE, T. (2007). Modeling and Experiment of Leading Edge Separation Control Using SDBD Plasma Actuators. *45th Aerospace Sciences Meeting and Exhibit*. Reno, Nevada, AIAA 2007–0877.

ORLOV, D. and CORKE, T. (2005). Numerical Simulation of Aerodynamic Plasma Actuator Effects. *43rd Aerospace Sciences Meeting and Exhibit*. Reno, Nevada, AIAA 2005–1083.

PALMEIRO, D. and LAVOIE, P. (2011). Comparative Analysis on single Dielectric Barrier Discharge Plasma Actuator Models. *7th International Symposium on Turbulence and Shear Flow Phenomena*. Ottawa, Canada.

PEACOCK, R. (1971). Boundary-Layer Suction to Eliminate Corner Separation in Cascades of Aerofoils. Report and Memoranda 3663, Ministry of Defence.

PÖNICK, S., KOZULOVIC, D., RADESPIEL, R., BECKER, B. and GÜMMER, V. (2011). Numerical and Experimetal Investigations of a Compressor Cascade Flow with Secondary Air Removal. *Proceedings of ASME Turbo Expo 2011*. Vancouver, Canada, GT2011–45202.

PONS, J., OUKACINE, L., MOREAU, E. and TATIBOUET, J. (2008). Observation of Dielectric Degradation After Surface Dielectric Barrier Discharge Operation in Air at Atmospheric Pressure. *IEEE Transactions on Plasma Science*, 36, 1342–1343.

POST, M. (2004). *Plasma Actuators for Separation Control on Stationary and Unstationary Airfoils*. Doctoral thesis, University of Notre Dame.

POST, M. and CORKE, T. (2003). Separation Control on High Angle of Attack Airfoil Using Plasma Actuators. *41st Aerospace Sciences Meeting and Exhibit*. Reno, Nevada, AIAA 2003–1024.

PRANDTL, L. (1904). Motion of Fluids with Very Little Viscosity. Technical Memorandum 452, NACA.

PRANDTL, L. (1927). *Motion of Fluids with Very Little Viscosity*. NACA.

RIGIT, A., LAI, K. and BONG, D. (2009). Degradation of a Dielectric Barrier Discharge Plasma Actuator. *Proceedings of the 9th International Conference on Properties and Applications of Dielectric Materials*. Harbin, China, 569–572.

RODGER, P., SJOLANDER, S. and MOUSTAPHA, S. (1992). Establishing Two-Dimensional Flow in a Large-Scale Planar Turbine Cascade. *28th Joint Propulsion Conference and Exhibit*. Nashville, TN, AIAA 92–3066.

ROTH, J. (2003). Aerodynamic Flow Acceleration Using Paraelectric and Peristaltic Electrohydrodynamic Effects of a One Atmosphere Uniform Glow Discharge Plasma. *Physics of Plasmas*, 10, 2117–2126.

ROTH, J. and DAI, X. (2006). Optimization of the Aerodynamic Plasma Actuator as an Electrohydrodynamic (EHD) Electrical Device. *44th Aerospace Sciences Meeting and Exhibit*. Reno, Nevada, AIAA 2006–1203.

ROY, S., SINGH, K., KUMAR, H., GAITONDE, D. and VISBAL, M. (2006). Effective Discharge Dynamics for Plasma Actuators. *44th Aerospace Sciences Meeting and Exhibit*. Reno, Nevada, AIAA 2006–374.

SANTHANAKRISHNAN, A. and JACOB, J. (2007). Flow Control with Plasma Synthetic Jet Actuators. *Journal of Physics D: Applied Physics*, 40, 637–651.

SCHATZMAN, D. and THOMAS, F. (2008). Turbulent boundary layer separation control with plasma actuators. *4th AIAA Flow Control Conference*. Seattle, Washington, AIAA 2008–4199.

SCHLICHTING, H. and GERSTEN, K. (2000). *Boundary-Layer Theory*. Springer Verlag.

SCHULZ, H. and GALLUS, H. (1988). Experimental Investigation of the Three-Dimensional Flow in an Annular Compressor Cascade. *Journal of Turbomachinery*, 110, 467–478.

SCHULZ, H., GALLUS, H. and LAKSHMINARAYANA, B. (1990). Three-Dimensional Separated Flow Field in the Endwall Region of an Annular Compressor Cascade in the Presence of Rotor-Stator Interaction: Part 1-Quasi-Steady Flow Field and Comparison With Steady-State Data. *Journal of Turbomachinery*, 112, 669–678.

SINNETTE, J. and COSTELLO, G. (1951). Possible Application of Blade Boundary-Layer Control to Improvement of Design and Off-Design Performance of Axial-Flow Turbomachines. Technical Note 2371, NACA.

SONG, B. (2003). *Experimental and Numerical Investigations of Optimized High-Turning Supercritical Compressor Blades*. Doctoral thesis, Virginia Polytechnic Institute and State University.

SUZEN, Y., HUANG, P., JACOB, J. and ASHPIS, D. (2005). Numerical Simulations of Plasma Based Flow Control Applications. *35th Fluid Dynamics Conference and Exhibit*. Toronto, Canada, AIAA 2005–4633.

SVENINGSSON, A. (2006). Transition Modelling-A Review. Technical report, Chalmers University of Technology.

THIAM, A., WHITTLESEY, R., WARK, C. and WILLIAMS, D. (2008). Corner separation and the onset of stall in an axial compressor. *38th AIAA Fluid Dynamics Conference and Exhibit*. Seattle, Washington, AIAA 2008–4299.

THIART, G. (1991). A Numerical Procedure for Predicting the Effects of Distorted Inflow Conditions on the Performance of Axial Flow Fans. *Journal of Turbomachinery*, 113, 198–206.

THOMAS, F., CORKE, T., IQBAL, M., KOZLOV, A. and SCHATZMAN, D. (2009). Optimization of Dielectric Barrier Discharge Plasma Actuators for Active Aerodynamic Flow Control. *AIAA Journal*, 47, 2169–2178.

THOMAS, F., KOZLOV, A. and CORKE, T. (2008). Plasma Actuators for Cylinder Flow Control and Noise Reduction. *AIAA Journal*, 46, 1921–1931.

TYLER, J. and SOFRIN, T. (1962). Axial Flow Compressor Noise Studies. *SAE Transactions*, 70, 309–332.

VERSAILLES, P., GINGRAS-GOSSELIN, V. and VO, H. (2010). Impact of Pressure and Temperature on the Performance of Plasma Actuators. *AIAA Journal*, 48, 859–863.

VO, H. (2007). Control of Rotating Stall in Axial Compressors Using Plasma Actuators. *37th Fluid Dynamics Conference and Exhibit*. Miami, Florida, AIAA 2007–3845.

WALKER, G. (1968). The Prediction of Boundary Layer Development on Axial Flow Turbomachine Blades. *Conference on Hydraulics and Fluid Mechanics*. The Institution of Engineers, Australia, 2596.

WALKER, G. (1989). Transitional Flow on Axial Turbomachine Blading. *AIAA*, 27, 595–602.

WEBBER, M. (1993). *Determining the Effect of Endwall Boundary Layer Suction in a Large Scale Subsonic Compressor Cascade*. Master thesis, Naval Postgraduate School, Monterey, California.

WHITE, F. (1998). *Fluid Mechanics*. McGraw-Hill.

WILLIAMSON, C. (2008). *Compressor Blade Flow Control in an Axial Compressor with Plasma Actuators*. Doctoral thesis, Oklahoma State University.

WOODWARD, R., ELLIOTT, D., HUGHES, C. and BERTON, J. (2001). Benefits of Swept and Leaned Stators for Fan Noise Reduction. *Journal of Aircraft*, 38, 1130–1138.

WOODWARD, R., FITE, E. and PODBOY, G. (2007). Noise Benefits of Rotor Trailing Edge Blowing for a Model Turbofan. TM 2007-214666, NASA.

WU, Y., ZHAO, X., LI, Y. and LI, J. (2012). Corner Separation Control in a Highly Loaded Compressor Cascade Using Plasma Aerodynamic Actuation. *Proceedings of ASME Turbo Expo 2012*. Copenhagen, Denmark, GT2012–69196.

YARAS, M. and SJOLANDER, S. (1990). Development of the Tip-Leakage Flow Downstream of a Planar Cascade of Turbine Blades: Vorticity Field. *Journal of Turbomachinery*, 112, 609–617.

ZHANG, X. (2005). *Separation and Transition Control on Ultra-High-Lift Low Pressure Turbine Blades in Unsteady Flow*. Doctoral thesis, Cambridge University.

ZHANG, Y. (2011). Personal communication.

ZHENG, X., ZHOU, S., HOU, A., JIANG, Z. and LING, D. (2006). Separation Control Using Synthetic Vortex Generator Jets in Axial Compressor Cascade. *Acta Mech Sin*, 22, 521–527.

ZIERKE, W. and DEUTSCH, S. (1989). The Measurement of Boundary Layers on a Compressor Blade in Cascade Volume 1-Experimental Technique, Analysis and Results. Technical report CR-185118, NASA.

Appendix A

Details of Computational Approach

A.1 Convergence Assessment

The level of convergence was determined using the method defined by Clark and Grover (2007). The method is based on the comparison of two consecutive periodic signal intervals. To determine the flow frequency, pressure rise coefficient (ψ) was used. Then, the discrete pressure rise coefficient data in time domain was transformed into the frequency domain using the Discrete Fourier transform (DFT) as follows;

$$P_{overall}(k+1) = \sum_{n=0}^{N-1} p(n+1)e^{-i(2\pi kn/N)} \tag{A.1}$$

where p represents the ψ for this study with k=0,...,N-1. The DFT was calculated at integers multiples, (k+1), of the signal sampling frequency, $\Delta f = (N\Delta t)^{-1}$ with Δt being the time step.

Then, the frequency with the highest DFT amplitude was determined to be frequency of vortex shedding. After approximating the flow frequency, the last two intervals of the periodic signal were compared. The comparisons between the two periodic signal intervals with zero lag difference were based on the signals' time mean values, DFT magnitudes, phase angles and cross correlation factors. The time mean of the ψ over a period of cycle is given as:

$$p = \frac{1}{N}\sum_{n=0}^{N-1} p(n+1) \tag{A.2}$$

where N is the number of time steps per period and p(n+1) is the ψ calculated for each time step. It should be noted that the time mean of the signal should be same for perfectly periodic signals.

The discrete Fourier transform (DFT) of the static pressure signal is calculated as follows:

$$P(k+1) = \sum_{n=0}^{N-1} p'(n+1)e^{-i(2\pi kn/N)} \tag{A.3}$$

with k=0,....,N-1 and p' is the fluctuating pressure signal $p' = (p - \bar{p})$. Fourier components for each k can be represented in the following form:

$$P(k+1) = Re + Imi \tag{A.4}$$

Using the real (Re) and imaginary (Im) components of the DFT of the fluctuating ψ signal, a normalized DFT magnitude can be calculated as follows:

$$A(k+1) = 2\sqrt{Re^2 + Im^2}/N \tag{A.5}$$

Similarly the phase angle (ϕ) defined as follows:

$$\phi(k+1) = tan^{-1}(Im/Re) \tag{A.6}$$

The normalized DFT and phase angle should give the same value for perfectly periodic signals at frequency of interest. The cross-correlation coefficient (CCF) of a periodic interval is calculated as follows:

$$CCF(L) = \frac{\frac{1}{N}\sum_{n=0}^{N-1} p'\left((n+1)+L\right) p'\left((n+1)+N\right)}{\frac{1}{N}\left[\sum_{n=0}^{N-1} p'^2(n+1) \sum_{n=0}^{N-1} p'^2\left((n+1)+N\right)\right]^{1/2}} \tag{A.7}$$

where L is the time lag. At zero lag difference, the CCF of a perfectly periodic signal should be 1. After calculating the time mean levels, DFT magnitudes and phase angles and CCF at zero lag; the fuzzy sets are defined as follows:

$$f_M = 1 - \left|1 - \frac{\bar{p}_2}{\bar{p}_1}\right|; \qquad f_A = 1 - \left|1 - \frac{A_2}{A_1}\right|; \tag{A.8}$$

$$f_\phi = 1 - \left|\frac{\phi_2 - \phi_1}{\pi}\right|; \qquad f_S = |CCF(0)| \tag{A.9}$$

where subscripts 1 and 2 refer to one previous and current periodic cycles. The overall convergence level f_C is evaluated using the minimum membership grade in fuzzy sets:

$$f_C = min(f_M, f_A, f_\phi, f_S) \tag{A.10}$$

For a periodic-unsteady flow field, Clark and Grover (2007) suggest that an overall convergence level ≤ 0.95 shows the convergence in unsteady periodic signal. Flow variables (such as static pressure and velocity) and integral variables (such as pressure rise coefficient) were used to determine flow frequency. It was observed that the estimated flow frequency is independent of the choice of variable.

To illustrate preceding arguments, Figure A.1 shows the convergence assessment results for

unsteady flow field simulations performed for DCA-1 cascade. The fuzzy sets were calculated for the pressure rise coefficient signal. The original pressure rise coefficient signal is shown in Figure A.1(a). The last two intervals and percent fluctuations of signal are shown in Figure A.1(b and c). The fluctuations in the signal are observed to be on the order of 0.01%. The simulation time was non-dimensionalized with inlet axial flow velocity and axial length of computational domain. The signal is plotted in frequency domain as shown in Figure A.1(d and e). The first 3 peak frequencies are found to be 776.3 Hz, 338.15 Hz and 1164.6 Hz. The peak signal was determined to be flow frequency. In this example, the second peak frequency was determined to be flow frequency where periodicity of the intervals can be observed in Figure A.1(b). Figure A.1(f) shows the corresponding fuzzy sets in 40 periodic cycles. In that study, an overall convergence level of 0.9 was used. It can be observed from Table A.1 that all fuzzy sets are above the convergence level.

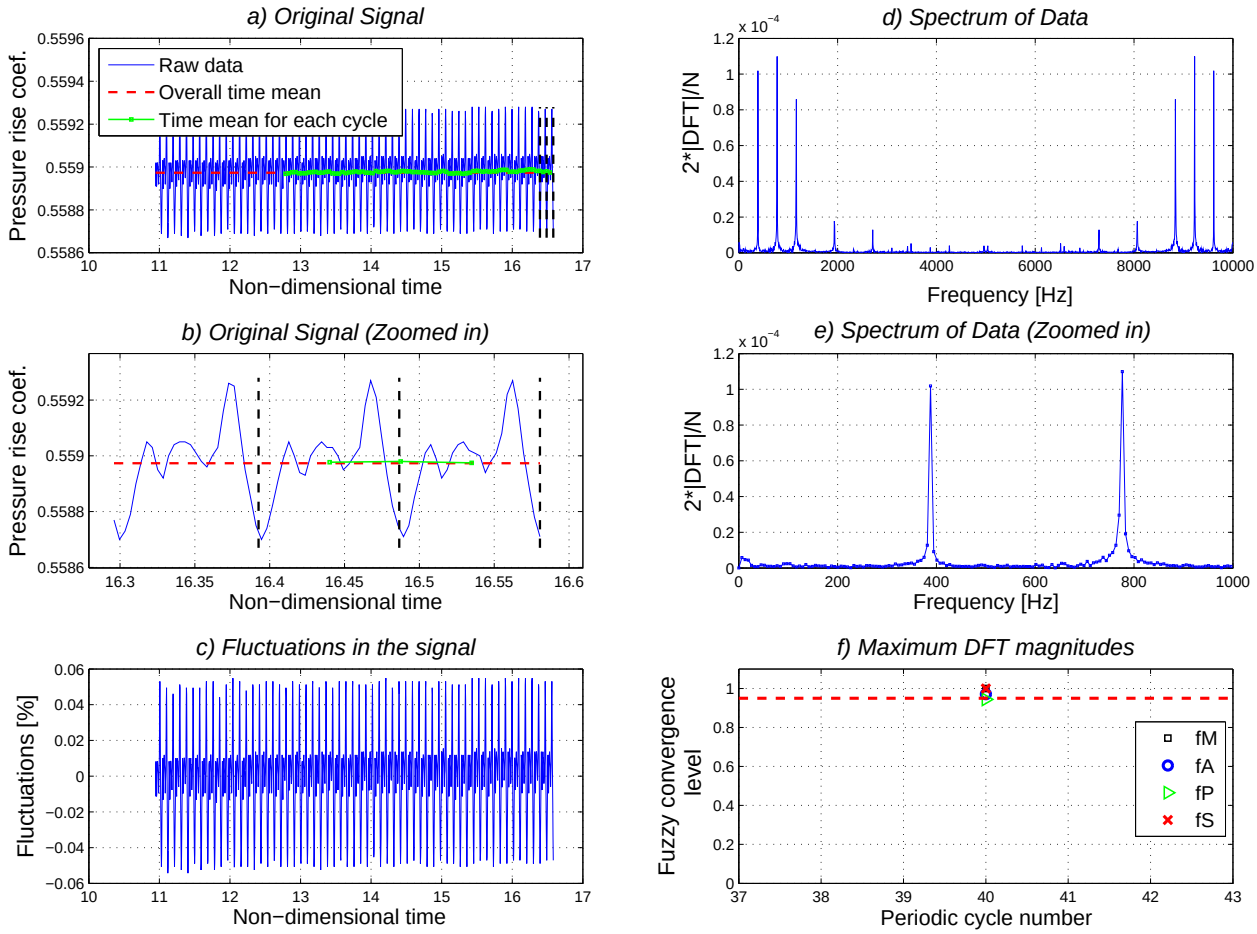

Figure A.1: Signal analysis and convergence behavior

Table A.1: Results of fuzzy-set convergence analysis

Fuzzy sets	Membership grades
f_M	1
f_A	0.9705
f_ϕ	0.9440
f_S	0.9999
f_C	0.9440

A.2 Mesh Convergence

A.2.1 Mesh Convergence for DCA-1 Cascade

The mesh convergence study performed by ANSYS (2009) for flat plate test case (T3A) has shown that the boundary layer should be defined at least using 10 points to solve the boundary layer flows accurately. Simulations performed on a compressor cascade has shown that y^+ should be less than 1. However, y^+ values less than 0.001 should be avoided to reduce the computational cost. A wall normal expansion ratio should be less than 1.1 and 75-100 grid points should be used in the streamwise direction. Although, the grid dependency may vary for various Reynolds numbers and turbulence levels, these criteria were considered in the generation of computational mesh for this study.

Initially, a mesh convergence study was performed for the DCA-1 cascade by varying the cell numbers in streamwise and pitchwise directions to determine the optimum two-dimensional mesh resolution. The numbers of nodes used in the mesh convergence study are listed in Table A.2. The boundary layer at 0.5 chord was resolved using 25 and 56 grid points in coarse mesh and fine mesh, respectively. In all mesh densities, the thickness of the first cell was kept sufficiently small to ensure a non-dimensional wall distance of $y^+ \approx O(1)$.

Figure A.2 shows the pressure distributions for each mesh density. It can be seen that the medium mesh gives a grid independent solution both on the suction surface and pressure surface. Although computationally more expensive, the fine mesh was chosen for the two-dimensional plasma actuation simulations. This selection would be helpful during plasma actuation force mapping from the linear plasma actuation mesh to the curvilinear CFD mesh over the blade surface as discussed in Section 2.1.4.

Then, a mesh convergence study was performed for the spanwise mesh density using a circumferential mesh density very similar to the fine mesh selected for two-dimensional solutions previously. Table A.3 shows the numbers of nodes used to resolve half span of the cascade. In all cases, the first cell high was kept constant.

The pressure coefficient distributions at 7.5% and 50% span locations are shown in Figure A.3.

Table A.2: Circumferential mesh properties used in DCA-1 mesh convergence study

Mesh density	Node # around blade	Node # normal to blade	Node # in BL at 0.5 chord on SS	Total cell #
Coarse mesh	280	44	25	n=14528
Medium mesh	420	66	39	1.5^2n=32688
Fine mesh	630	99	56	1.5^4n=73548

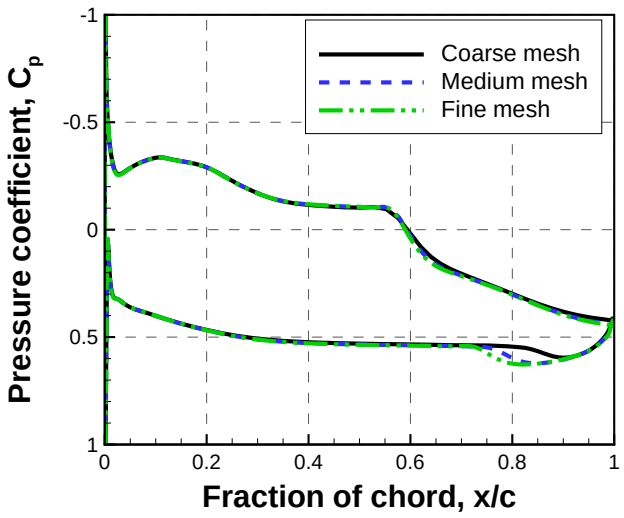

Figure A.2: Pressure coefficient distributions for circumferential mesh density effect

Table A.3: Spanwise mesh properties used in DCA-1 mesh convergence study

Mesh density	Spanwise node #	Total cell #
Coarse mesh	40	n=2671920
Medium mesh	60	1.5n=4007880
Fine mesh	90	1.5^2n=6011820

The coarse mesh with 40 points in spanwise direction observed to give grid independent solutions for pressure coefficients at both span locations. Considering the computational advantage, the coarse mesh density was chosen for the spanwise mesh distribution. This would not create any problem during the mapping of plasma actuator force on to the endwall since the endwall CFD mesh was linear. Figure A.4 shows the resultant mesh around the DCA-1 cascade together with the y^+ distribution. The total number of cells was 1.9 million. The maximum y^+ was 1.38 which resides around the blade leading edge and endwall junction.

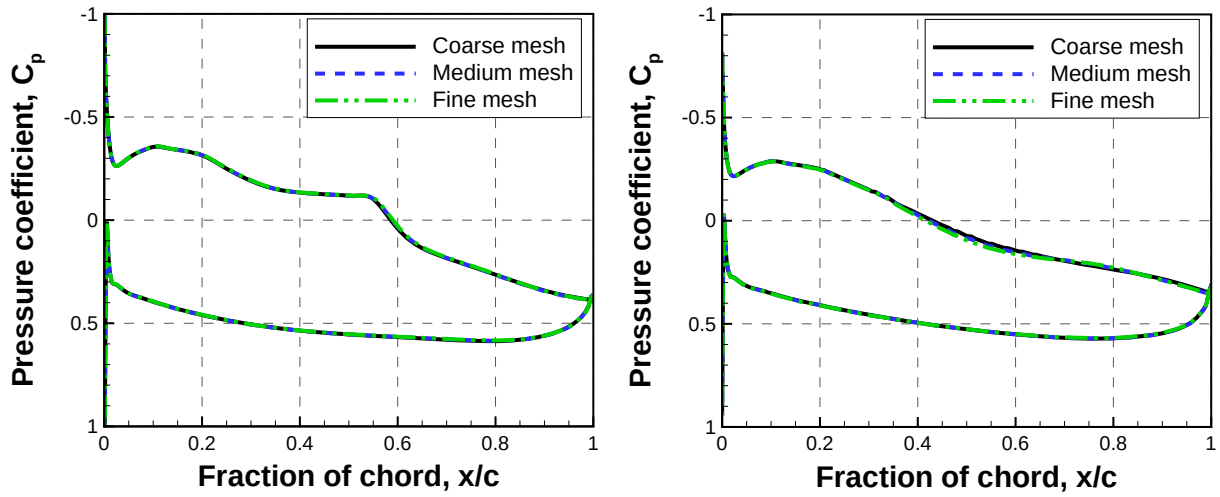

(a) Pressure coefficient distribution at 50% span (b) Pressure coefficient distribution at 7.5% span

Figure A.3: Pressure coefficient distributions at 50% and 7.5% span

A.2.2 Mesh Convergence for DCA-2 Cascade

Using a similar approach followed for DCA-1 cascade, a mesh convergence study for DCA-2 cascade was performed by varying the cell numbers in streamwise and pitchwise directions to determine the optimum two-dimensional mesh resolution. Table A.2 presents the properties of each grid density. The boundary layer was resolved using 19 and 54 nodes inside the boundary layer at 0.54 chord for the coarse mesh and finest mesh, respectively.

Table A.4: Mesh properties used in DCA-2 mesh convergence study

Mesh density	Node # around blade	Node # normal to blade	Node # in BL at 0.54 chord on SS	Total cell #
Coarse mesh	256	32	19	n=11776
Medium mesh	384	48	25	1.5^2n=26496
Fine mesh	576	72	32	1.5^4n=59616
Finest mesh	864	108	54	1.5^6n=134136

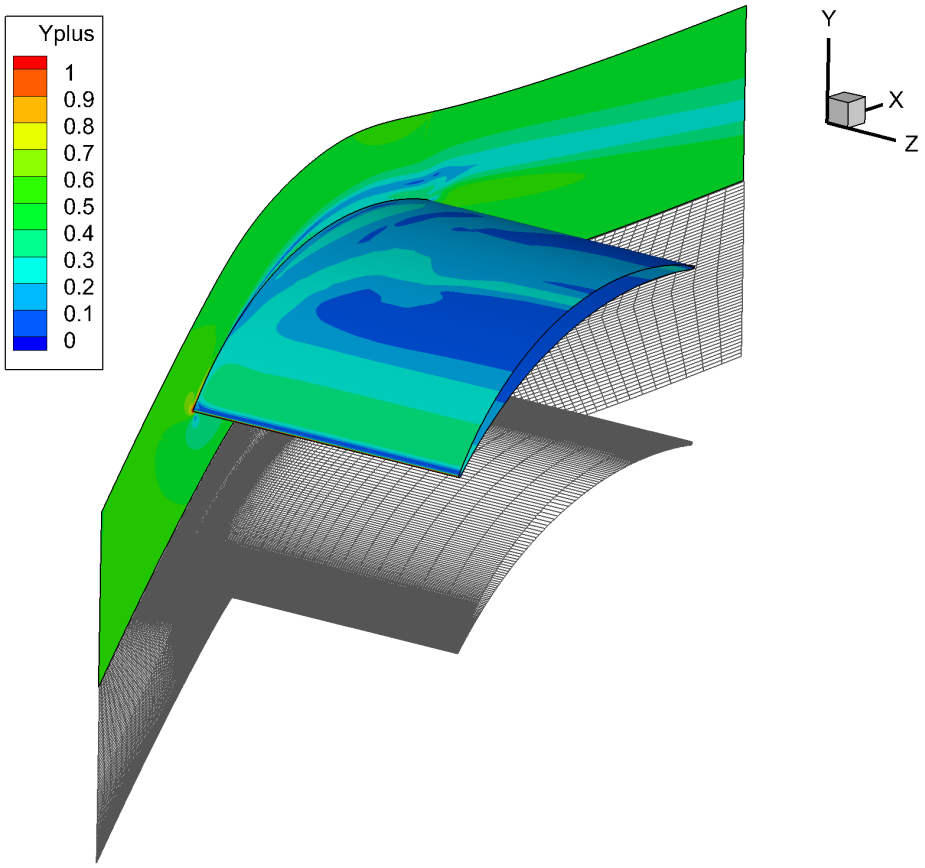

Figure A.4: Overview of the computational mesh and y^+ distribution over the wall

The pressure coefficient distributions for each mesh are shown in Figure A.5. For the suction surface pressure distribution, the medium mesh gave a mesh independent solution. For the pressure surface, the pressure distribution obtained with fine mesh was grid independent. To decrease the computational time, the fine mesh shown in Figure A.6, was chosen for the plasma actuation wake suppression flow control simulations. The boundary layer mesh was resolved with 32 nodes which ensures a non-dimensional wall distance of $y^+ \approx O(1)$.

A.2.3 Unstructured Mesh for Endwall Boundary Layer Suction

The unstructured mesh was generated using Gambit and TGrid. Initially, a triangular surface mesh was generated in Gambit. Then, the boundary layer mesh was formed in TGrid using prism layers over the solid walls. Finally, the remaining part of the computational domain was filled with tetrahedral elements. A good mesh quality was ensured by using the size function and mesh refinement options. The size function provided control over the surface and volume mesh size and their distributions by defining maximum and minimum sizes as well as growth rate. Figure A.7 shows the unstructured mesh, consisting of 5.4 million cells, used for endwall suction flow control.

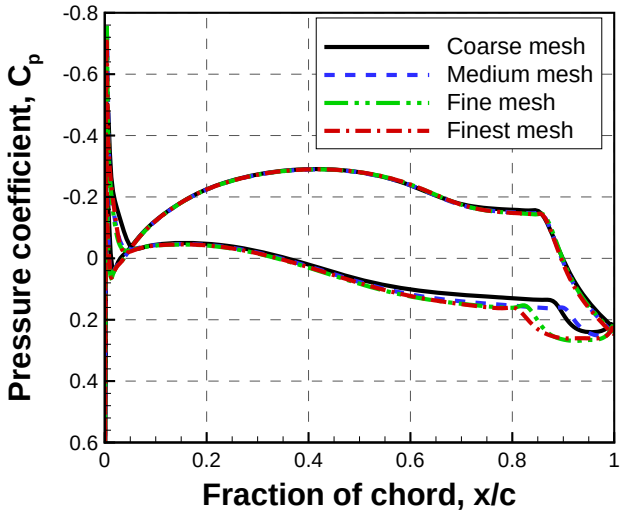

Figure A.5: Pressure coefficient distributions for DCA-2 blade mesh convergence study

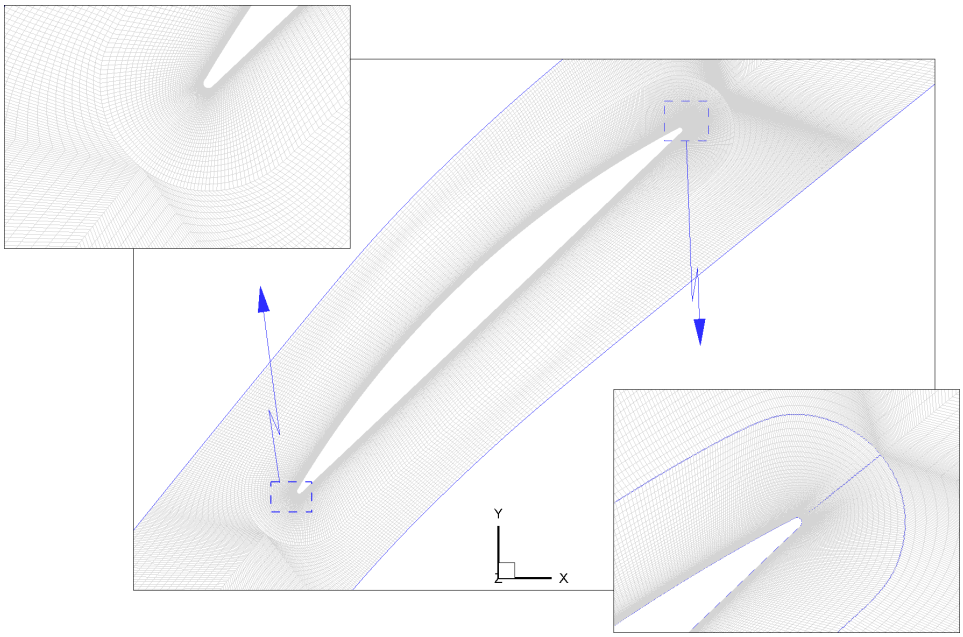

Figure A.6: Fine mesh for DCA-2 cascade

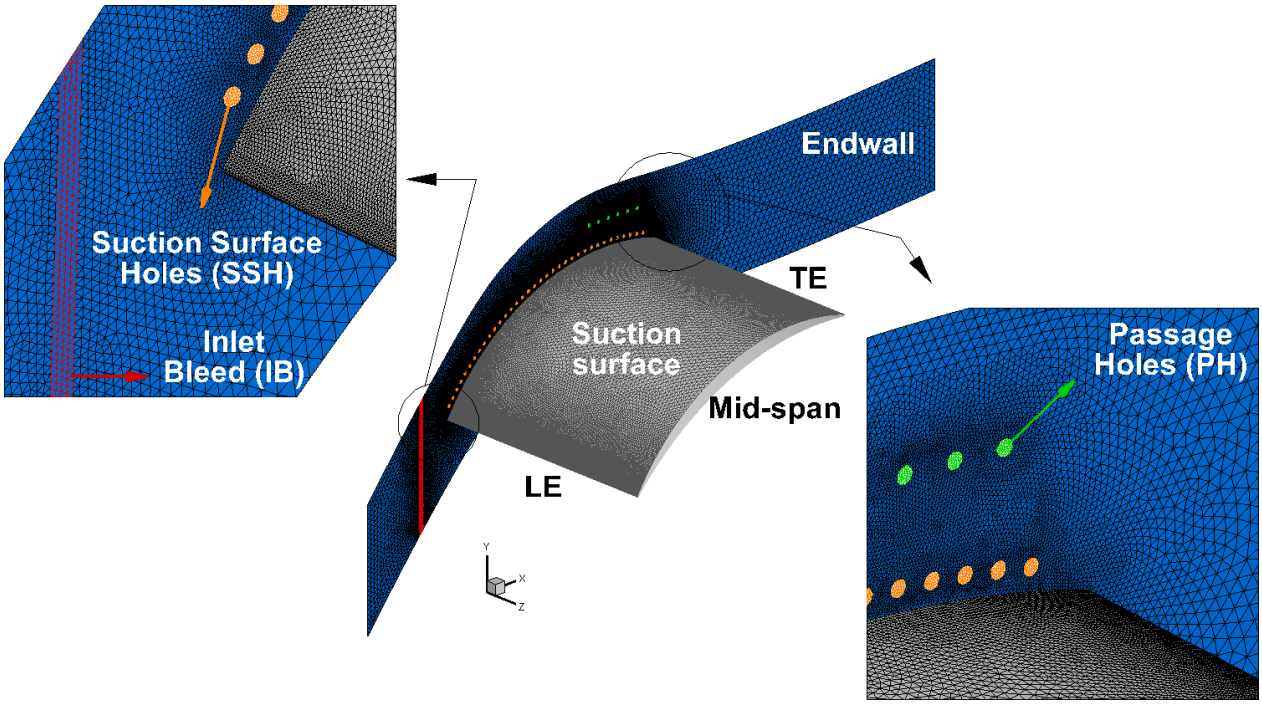

Figure A.7: Overview of the unstructured mesh

A.3 Net Plasma Actuator Force Calculation

The momentum balance in x and y directions was satisfied by carrying out a line integral around the rectangular control volume shown in Figure A.8. The viscous forces away from the solid wall were neglected together with the gravitational forces. The momentum balance in x and y directions were written as follows:

$$F_{act,x} = F_{inlet,x} + F_{outlet,x} + F_{SS,x} + F_{PS,x} \tag{A.11}$$

$$F_{act,y} = F_{lower,y} + F_{upper,y} + F_{SS,y} + F_{PS,y} \tag{A.12}$$

2-D flow simulations were performed at plasma actuation strengths of 50, 100, 150 and 200 mN/m using a plasma actuator located at 12.5%c_x. Figure A.9 shows the velocity vectors generated by the plasma actuation. As expected, the induced flow velocity and boundary layer thickness increases as plasma actuator strength increases. Figure A.10 illustrates the velocity profiles obtained at different axial locations on the blade suction surface. The induced flow velocity goes up to 15 m/s with the 200 mN/m plasma actuator strength. The velocity observed to decay significantly as the induced flow moves in the streamwise direction.

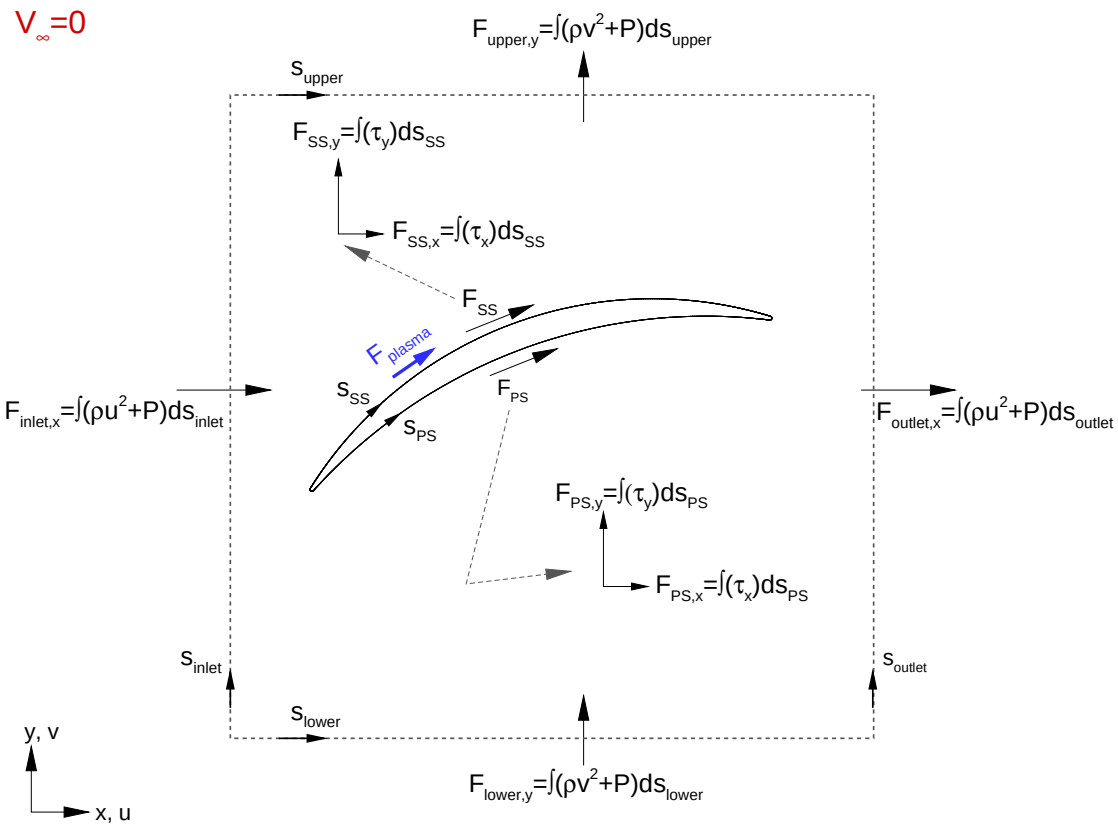

Figure A.8: Control volume and forces acting on boundaries

Table A.5 shows the plasma actuator forces are compared with the shear forces. This result shows that 22-25% of induced plasma actuator force has been used to overcome shear forces.

Table A.5: Plasma actuator and shear forces

F_{act} [mN/m]	$F_{shear,x}$ [mN/m]	$F_{shear,y}$ [mN/m]	$F_{plasma,x}$ [mN/m]	$F_{plasma,y}$ [mN/m]	F_{plasma} [mN/m]	F_{shear}/F_{plasma} [%]
50	10.3	5.8	48.8	7.2	49.3	23.96
100	21.3	12.3	98.8	15.3	100.0	24.60
150	29.1	16.2	150.5	20.5	151.9	21.93
200	38.4	21.6	198.1	27.4	200.0	22.03

In an effort to determine the variation of induced flow velocity with increasing plasma actuation strength, additional simulations were carried out at plasma actuation strengths of 300, 500, 1000, 2000 and 5000 mN/m using a plasma actuator located at 12.5%c_x. Figure A.11 shows the induced peak flow velocity versus plasma actuation strength at x/c_x=0.141 (right downstream of the plasma actuator). This figure clearly shows that the induced flow velocity exhibits a power law variation with applied actuation strength as $F_{act} = V^2_{induced}$. Indeed, this behavior is consistent with the

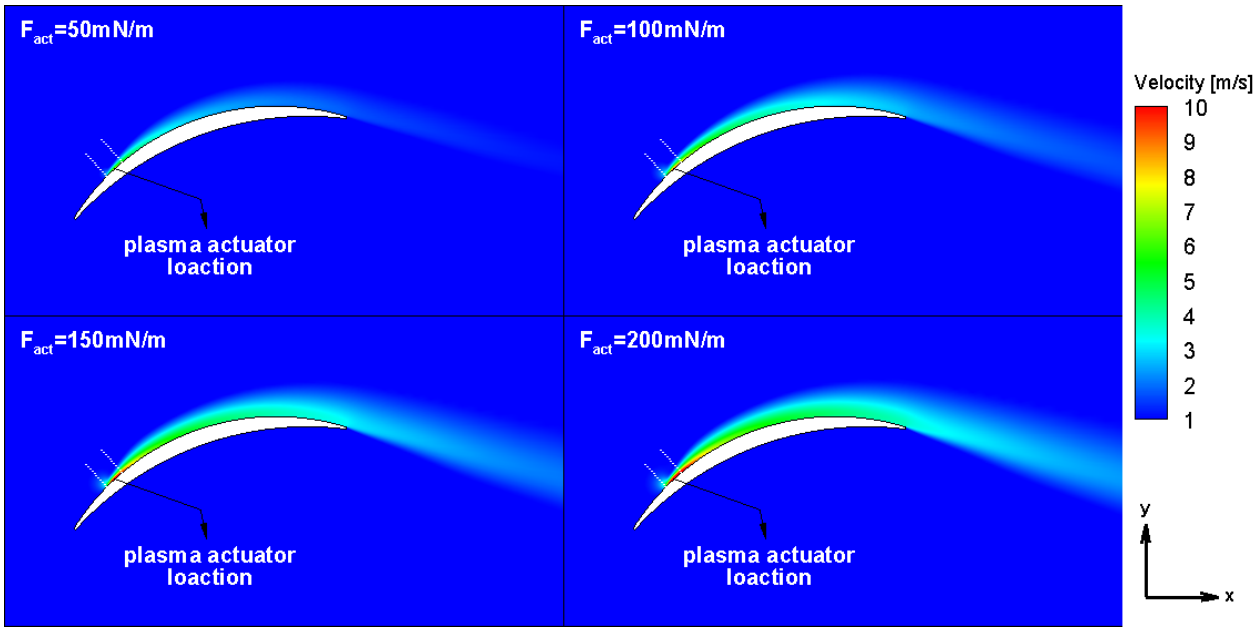

Figure A.9: Velocity contours (in quiescent air) for various plasma strengths

proportionality of force with the square of the velocity ($F = \dot{m}V = \rho V^2 A$).

A.4 Cases Studied in Parametric Studies

Table A.6 and Table A.7 show the cases studied for the parametric study of plasma actuation parameters for boundary layer separation control and wake/noise suppression concepts, respectively.

A.5 Rotor Equivalent Cascade Power Calculation

The rotor equivalent cascade power was predicted by assuming a rotor blade with an axial in coming velocity such that the cascade velocities are the relative velocities in the rotating frame and U is equal to the tangential component of the cascade inlet velocity. Figure A.12 shows cascade axial and tangential velocity components within the solid line boxes. The velocity triangles for an axial rotor row are shown in the same figure at the top within the dashed line boxes. The velocities shown by V and W, are in stationary and relative frames, respectively. The rotational speed is shown with U. The V_x is axial the velocity and V_θ is the tangential velocity. The subscripts 1 and 2 represent the inlet and outlet planes, respectively. In order to diffuse the flow, the blade exit area (A_2) is greater than the blade inlet area (A_1). The relative flow velocity decreases throughout the cascade passage due to diffusion of the air, $C_2 < C_1$.

Using the nomenclature presented above for cascade blade and rotor row, and also assuming

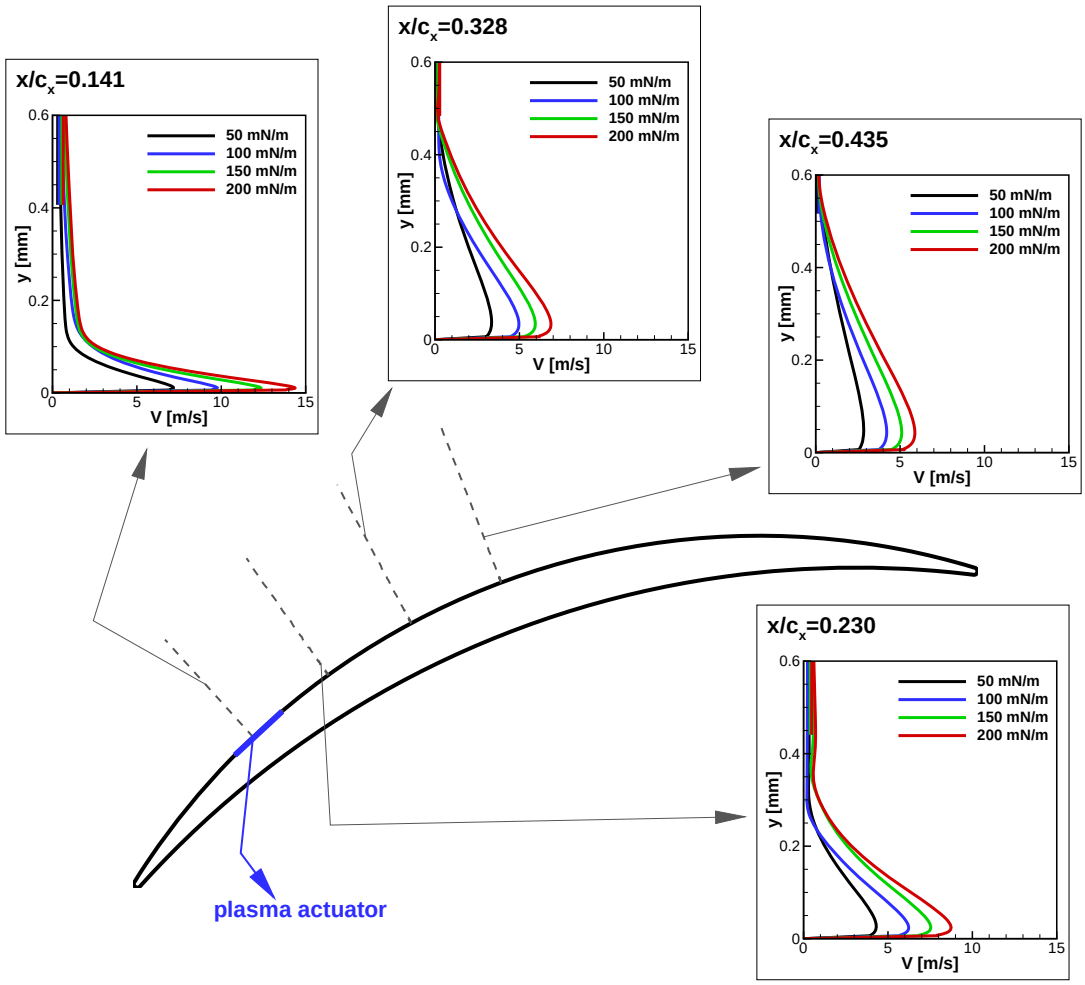

Figure A.10: Velocity profiles (in quiescent air) induced by the plasma actuator

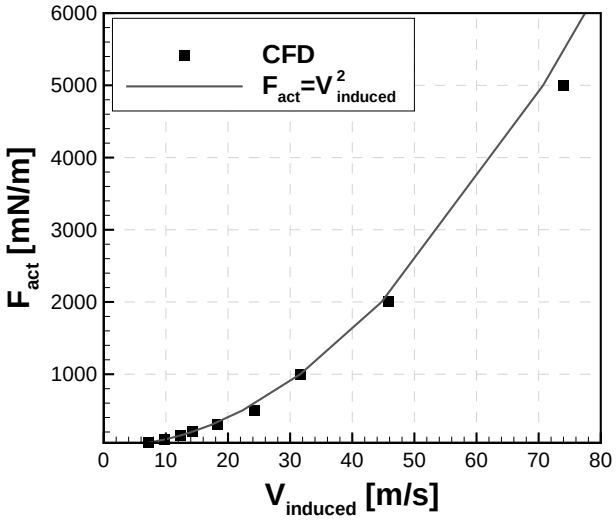

Figure A.11: Plasma induced peak flow velocity (in quiescent air) versus plasma actuation strength at x/c_x=0.141

Table A.6: Plasma actuation cases studied at blade boundary layer separation control

Case	x_{act} [chord]	F_{act} [mN/m]	f_{act} [Hz]	D
1	0.15	150	-	-
2	0.22	150	-	-
3	0.30	150	-	-
4	0.35	150	-	-
5	0.15	50	-	-
6	0.15	100	-	-
7	0.15	200	-	-
8	0.15	300	-	-
9	0.15	400	-	-
10	0.15	150	50	0.3
11	0.15	150	100	0.3
12	0.15	150	150	0.3
13	0.15	150	200	0.3
14	0.15	150	250	0.3
15	0.15	150	300	0.3
16	0.15	150	350	0.3
17	0.15	150	375	0.3
18	0.15	150	388	0.3
19	0.15	150	400	0.3
20	0.15	150	450	0.3
21	0.15	150	500	0.3
22	0.15	150	530	0.3
23	0.15	150	550	0.3
24	0.15	150	750	0.3
25	0.15	150	776	0.3
26	0.15	150	1000	0.3
27	0.15	150	530	0.1
28	0.15	150	530	0.5
29	0.15	150	530	0.7
30	0.15	150	530	0.9
31	0.15	150	530	0.9
32	0.15	45	-	-

Table A.7: Plasma actuation cases studied at blade wake control

Case	x_{act} [chord]	F_{act} [mN/m]	f_{act} [Hz]	D
1	0.65	150	-	-
2	0.70	150	-	-
3	0.75	150	-	-
4	0.80	150	-	-
5	0.85	150	-	-
6	0.80	50	-	-
7	0.80	100	-	-
8	0.80	200	-	-
9	0.80	150	50	0.5
10	0.80	150	150	0.5
11	0.80	150	225	0.5
12	0.80	150	275	0.5
13	0.80	150	304	0.5
14	0.80	150	325	0.5
15	0.80	150	375	0.5
16	0.80	150	450	0.5
17	0.80	150	650	0.5
18	0.80	150	50	0.5
19	0.80	150	304	0.1
20	0.80	150	304	0.3
21	0.80	150	304	0.7
22	0.80	150	304	0.9
23	0.80	77	-	-

air enters axially to the rotor row ($V_{\theta 1} = 0$); the equivalent velocity components for cascade were calculated as follows:

$$\overrightarrow{W}_1 = \overrightarrow{C}_1, \qquad \overrightarrow{U} = -\overrightarrow{C}_{\theta 1}, \qquad \overrightarrow{V}_{x1} = \overrightarrow{C}_{x1}, \qquad \overrightarrow{W}_{\theta 1} = \overrightarrow{C}_{\theta 1} \tag{A.13}$$

$$\overrightarrow{W}_2 = \overrightarrow{C}_2, \qquad \overrightarrow{V}_{x2} = \overrightarrow{C}_{x2}, \qquad \overrightarrow{W}_{\theta 2} = \overrightarrow{C}_{\theta 2}, \qquad \overrightarrow{V}_{\theta 2} = \overrightarrow{C}_{\theta 2} - \overrightarrow{C}_{\theta 1}$$

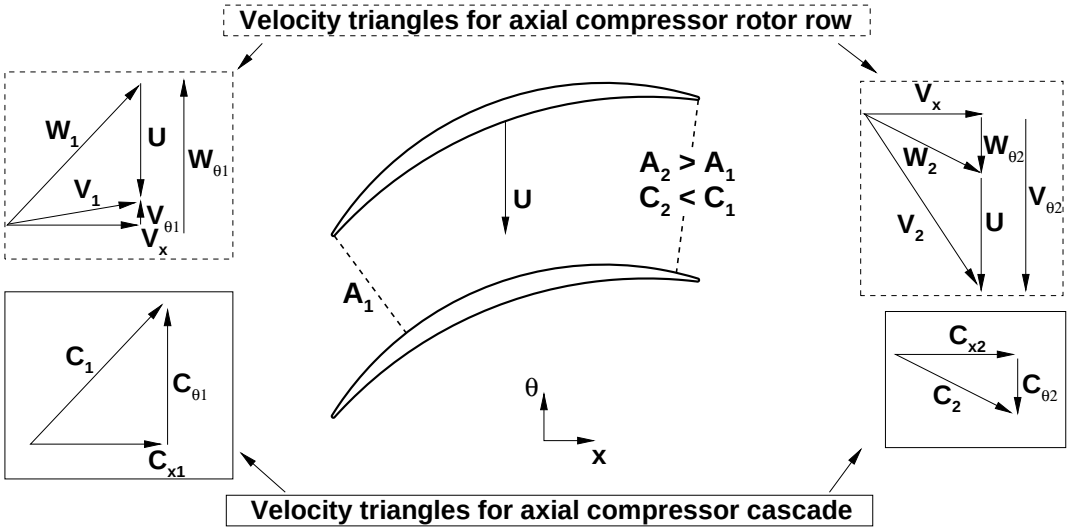

Figure A.12: Velocity diagrams for axial compressor cascade and axial compressor rotor row

The work done on flow is calculated using the Euler's equation for turbomachinery as follows:

$$\dot{W} = \dot{m}U(V_{\theta 2} - V_{\theta 1}) \tag{A.14}$$

where the subscripts 1 and 2 represent the inlet and outlet planes, respectively.
Therefore, the cascade power equivalent to an axial-inlet rotor is calculated as follows:

$$\dot{W}_{req} = \dot{m}C_{\theta 1}(C_{\theta 2} - C_{\theta 1}) \tag{A.15}$$

Appendix B

Details of Experimental Approach

B.1 Cascade Test Section

B.1.1 Test Section Modifications

The first modification to test the section arose from the addition of endwall boundary layer bleed slot to the test section. The current study aimed to control endwall flow through boundary layer bleed slots on the endwalls, just upstream of the cascade. In the original test section, the spacing between the upstream edge of the mounting plates and cascade leading edge was not enough to allow a boundary layer bleed slot on the mounting plate. Therefore, the cascade was moved downstream in axial direction by $24\%c_x$ as illustrated in Figure B.1. This modification caused difficulties in establishing flow uniformity.

The second modification to test the section arose from the problems encountered during inlet flow two-dimensionality and outlet flow periodicity establishment. By moving the location of the cascade on a mounting plate downstream, the flow control effectiveness was reduced especially at the top part of the cascade. As a result, inlet flow uniformity was not achieved satisfactorily by adjusting the control surfaces. Figure B.1 shows that the spacing between the top flaps and the top cascade airfoil was approximately 45% pitch larger than the blade pitch. Because of that larger spacing, the overall flow in the test section tended to move upwards, causing a negative flow angle throughout the test section. In order to correct the inlet flow angle, either the top side flap could be closed or the bottom side flap could be opened. Both alternatives observed to increase non-uniformity in inlet dynamic pressure.

The same problem was experienced by Mahallati (2003) in another low-speed cascade wind tunnel test section. To resolve that issue, a splitter plate was added to the upper surface/wall of the test section. Using the same approach, a 1.66mm thick, $20 \times 68.6cm$ metal plate was suspended from the test section top wall. The region above the splitter plate forms a cross sectional area of $20 \times 7.62cm$ where the mass flow through the additional channel was controlled by adjusting the top flap. The modified test section allowed establishing a more uniform inlet flow by forcing the flow to be more streamlined with the top wall.

These modifications made assessment of a uniform inlet flow and a periodic outlet flow possible through the use of control surfaces shown in Figure 2.12. The inlet flow uniformity was evaluated

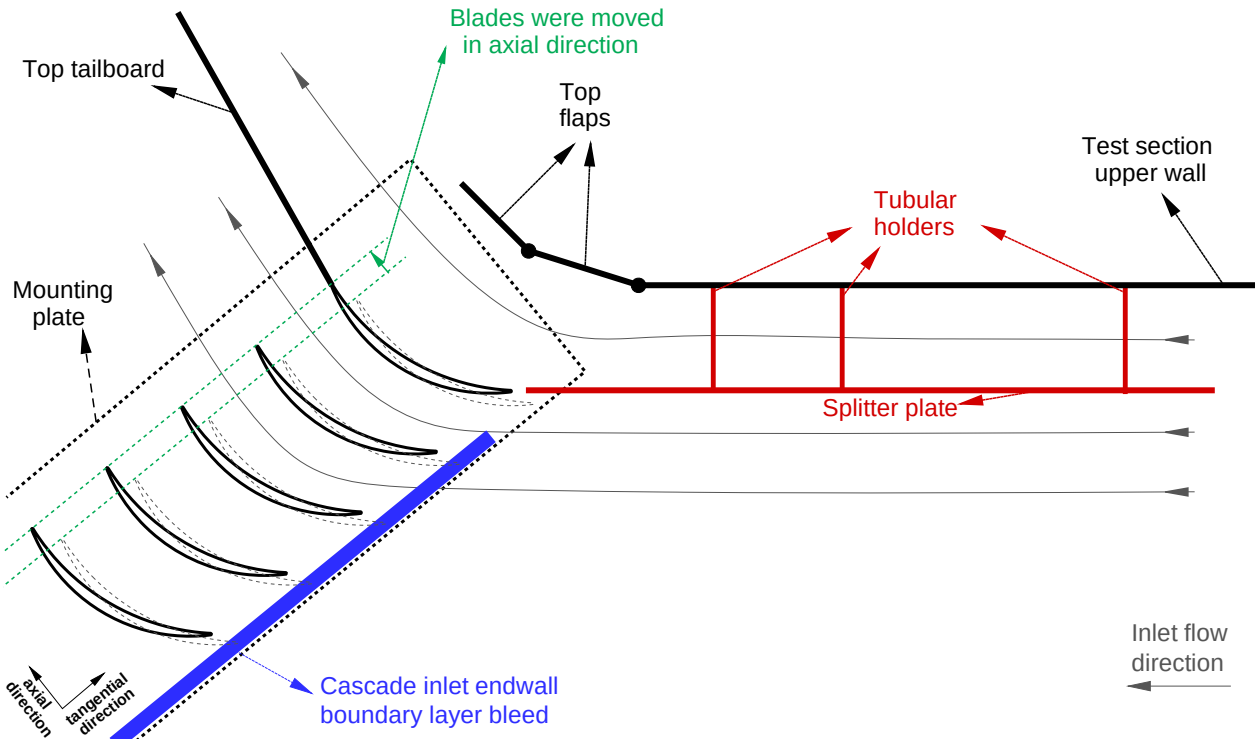

Figure B.1: Schematic representation of modifications made on test section

with three-hole pressure probe traverses at 1 c_x upstream of the blade pack leading edge. The outlet flow periodicity was evaluated with seven-hole probe traverses at 0.4 c_x downstream of the blade trailing edge.

B.1.2 Cascade Flow Quality Details

This section presents the results for the cascade inlet flow uniformity and outlet flow periodicity. The results for the endwall flow control cases are also presented in this section although the discussions for establishing a two-dimensional flow are left to Section 3.3.

The flow periodicity of the DCA-1 cascade was previously achieved by Zhang (2011) by means of adjusting angles of the tailboards and side flaps as well as using boundary layer bleed at the exit of the contraction section, referred as upstream boundary layer bleed in that study. However, the modifications mentioned previously in Appendix B.1.1 made re-establishing inlet flow uniformity and outlet flow periodicity compulsory for the current investigation. Three-hole pressure probe traverses at 1 c_x upstream of the blade pack leading edge were used to determine inlet flow uniformity. A seven-hole probe was traversed at 0.4 c_x downstream of the blade trailing edge to establish outlet flow periodicity. The pressure probe traverses were performed in pitchwise direction at the blade mid-span. For three-hole probe, a uniform spacing with 51 measurements points was used

for the traverses involving 5 center blades. For the seven hole probe, a non-uniform spacing was used to capture the large velocity and angle variations within the blade wake. As a result, 117 measurements points were used for the same blade passages.

By presuming that the equally spaced and identically oriented cascade blades will generate a periodic outlet flow as long as tailboard angles are not far from the exit flow angle, the inlet flow uniformity was achieved first. For that purpose, the control surfaces were initially moved in each direction to understand the resultant effect of control surface. Initial trials have shown that the control surfaces, namely, bottom side flap and top side flap, were ineffective in controlling the test section upper flow. Therefore, a splitter plate was added to the test section as mentioned previously in Appendix B.1.1. Then, the inlet flow uniformity was established by adjusting the bottom and top side flap angles until spanwise variations are sufficiently small. The addition of splitter plate was pivotal for inlet flow uniformity since the top side flap was ineffective in controlling the test section upper flow.

After establishing a uniform inlet flow, the outlet flow periodicity was established using tailboards. Since the inlet flow uniformity is not independent from the tailboard angles, the inlet flow uniformity was verified again and the control surface angles were adjusted. This process is repeated back and forth until the inlet flow uniformity and the outlet flow periodicity were achieved satisfactorily.

The inlet flow uniformity was determined based on the incidence angle, dynamic pressure coefficient and total pressure coefficient. For the outlet periodicity, the deviation angle was used instead of incidence angle. Inlet and outlet flow measurements, performed for baseline and endwall flow control cases, are presented in Figure 2.14. Considering the center blade and neighbouring two blades, a good inlet flow uniformity and outlet flow periodicity was established for all cases investigated in this study. The inlet flow angle was around -1° for the baseline case. Through the bottom of the test section, an increase in the inlet dynamic pressure has been observed especially for the 2-D flow case which could not be avoided during the tune up of control surfaces. Although the splitter plate added to control upper flow improved the inlet flow uniformity significantly, any further attempt to reduce dynamic pressure of the test section bottom part by closing the bottom side flap were observed to cause an increase in the inlet flow angle. The outlet flow periodicity was more satisfying. The deviation angle at the outlet plane was observed to be 12° and it shows a good periodicity at the central two passages. The variation in outlet dynamic pressure was observed to be less pronounced compared to the variation of inlet dynamic pressure.

B.1.3 Mass Flow Measurements for Endwall Bleed Arrangement

The mass flow through endwall bleed/suction openings was measured by calculating the mass flow passing through plastic tubes which are connected to a metal box mounted on the outside walls of the test section as shown in Figure B.2. The metal boxes were large enough ($27 \times 18 \times 8$ inch) to have a uniform static pressure inside. The air was prevented from leaking out of the box by applying silicon sealing to the edges of the box. The bleed/suction mass flow ingested from seven central passages through the endwall was collected inside each box. Each box was instrumented with 5 static pressure taps to monitor the static pressure. Since the static pressure inside the box increased above the ambient pressure, an Aeromech Model-LX vacuum pump was used to drive the air out of the box. The compressed shop air mass flow, with 90-100 psi pressure, was adjusted with a globe valve to control the mass flow rate through the vacuum pump. A regulator was connected to the shop air to avoid any fluctuation in the course of measurements. The vacuum pump and the box were connected through a plastic pipe with 1.6 inch inner diameter as schematically shown in Figure B.3.

A traverse mechanism mounted on the plastic tube as shown in Figure B.4. A gooseneck pitot-tube was traversed inside the tube from tube wall to the tube center to obtain the pipe velocity profile 12.5 L/D downstream of the box. Once the velocity profiles are obtained by carrying out pitot-tube measurements, the mass flow through the tube was calculated based on the centerline velocities measured by a pitot-static tube.

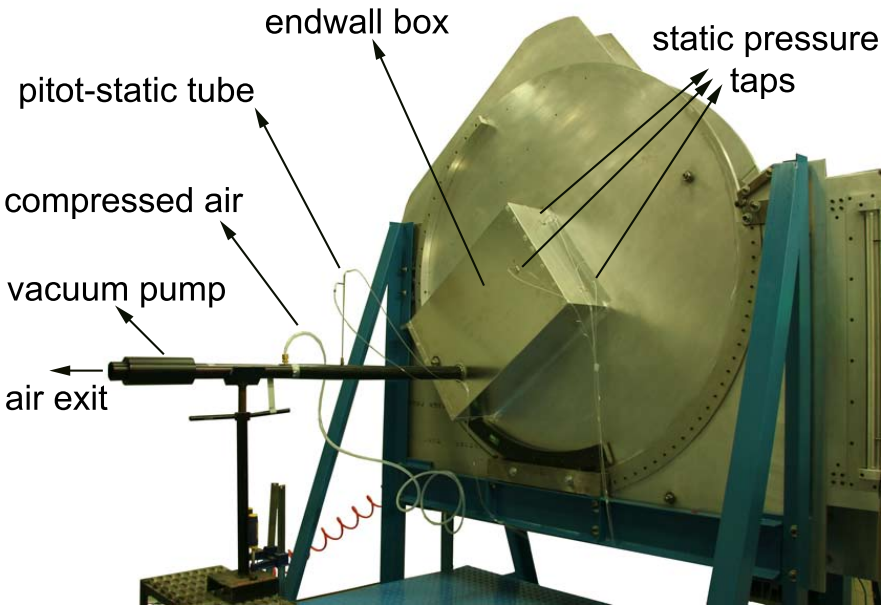

Figure B.2: Endwall bleed/suction mass flow measurement setup for moving endwall side

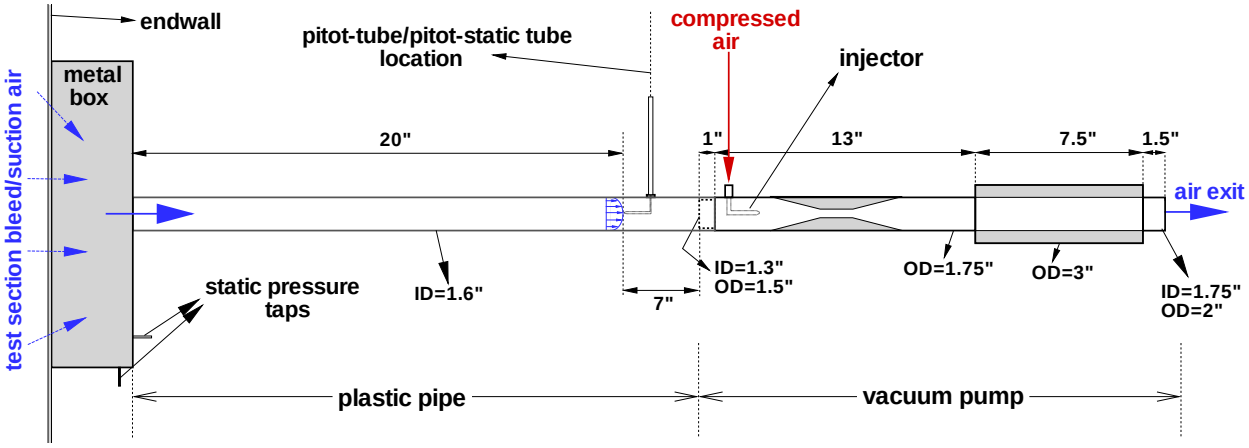

Figure B.3: Vacuum pump setup used to ingest air from the box

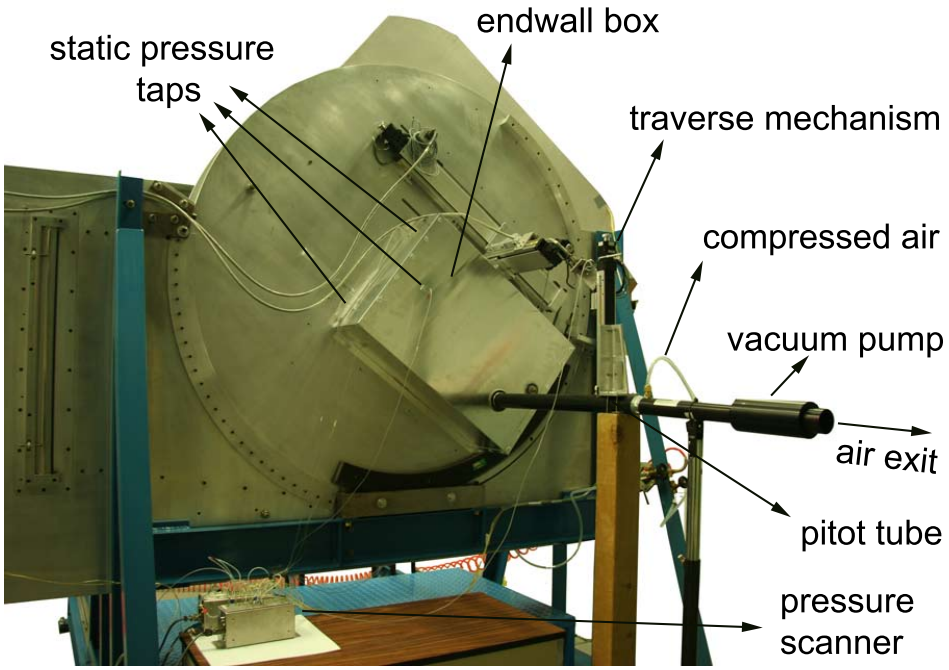

Figure B.4: Pipe B.L. profile measurement setup for fixed endwall side

B.2 Pressure Scanner Calibration

Sixteen channels of DSA3217 pressure scanner was calibrated using GE Druck DPI 615 pressure calibrator. As a sample, the calibration curve for channel 1 is shown in Figure B.5.

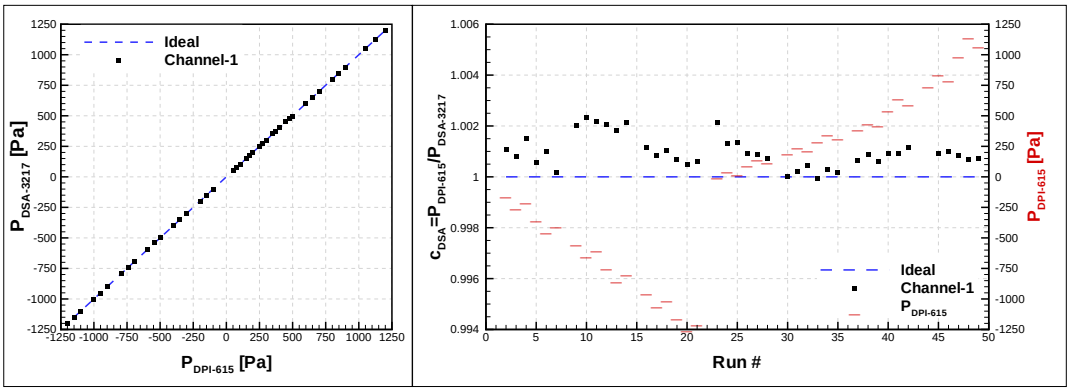

Figure B.5: DSA3217 pressure scanner calibration curve for channel 1

B.3 Probe Calibration Rig

The three-hole and seven-hole pressure probes were calibrated using an in-house probe calibration rig, shown in Figure B.6. The velocity at the calibration plane of rig can reach up to 45 m/s. A three-axis rotary traverse mechanism was used to traverse the probe.

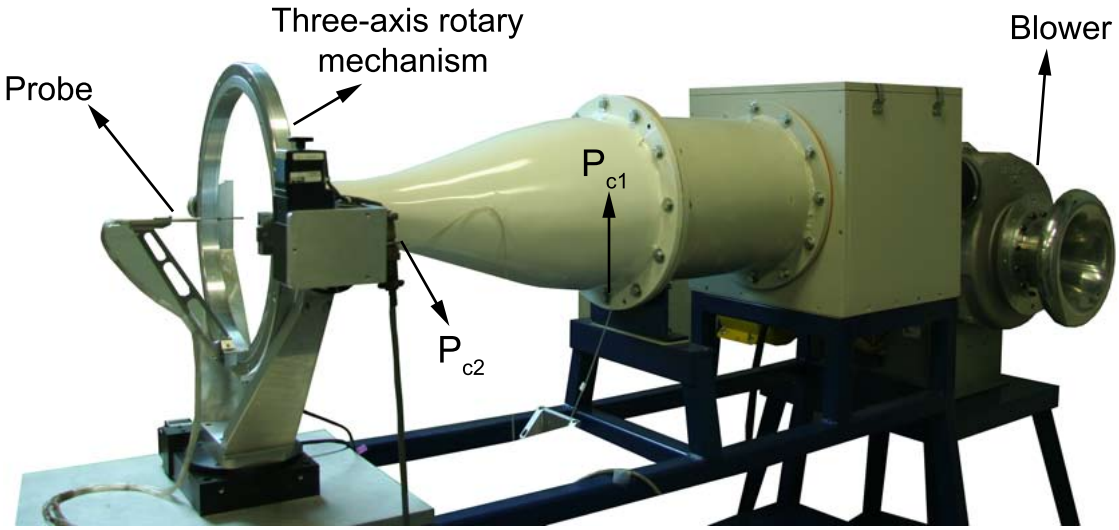

Figure B.6: Probe calibration rig

During the probe calibration process, the calibration rig operating pressure was measured using the nozzle total and static pressures, P_{c1} and P_{c2}. However, the nozzle dynamic pressure $(P_{c1} - P_{c2})$ was slightly larger than the dynamic pressure $(P_0 - P_s)$ at the measuring plane.

In order to correct the measured pressures (P_{c1} and P_{c2}) from the nozzle, a pitot-static tube was used. The pitot-static tube was first geometrically aligned with the nozzle centerline. Then, the probe was pitched and yawed by ±3° to find the correct orientation that gives the maximum total pressure. After aligning the probe aerodynamically, the calibration plane pressure coefficients for total pressure C_{p_0}, static pressure, C_{p_s}, and dynamic pressure, C_q, were calculated as follows:

$$C_{p_0} = \frac{P_0 - P_{c1}}{P_{c1} - P_{c2}} \tag{B.1}$$

$$C_{p_s} = \frac{P_s - P_{c2}}{P_{c1} - P_{c2}} \tag{B.2}$$

$$C_q = \frac{P_0 - P_s}{P_{c1} - P_{c2}} = 1 + C_{p_0} - C_{p_s} \tag{B.3}$$

Figure B.7 shows the calibration dynamic and static pressures coefficients as a function of Reynolds number, based on the pitot-static tube diameter. These calibration coefficients were used in the three-hole probe and seven-hole pressure probe calibrations. During calibration, the probe stem was first geometrically aligned with the nozzle centerline using a digital protractor. The calibration rig was set to a desired speed and the pressure coefficients were recorded at 0° roll angle over a range of ±2° pitch angle at 0.5° intervals. Then, the probe was rolled by 180° and the pressure coefficients were recorded for the same range of pitch angle. Using these two sets of measurements, the misalignment in the pitch direction was corrected. The same technique was applied to aerodynamically align the probe in yaw direction. For that purpose, a set of data was initially taken at 90° roll angle, then the probe was turned to 270° roll angle and a second set of data was recorded.

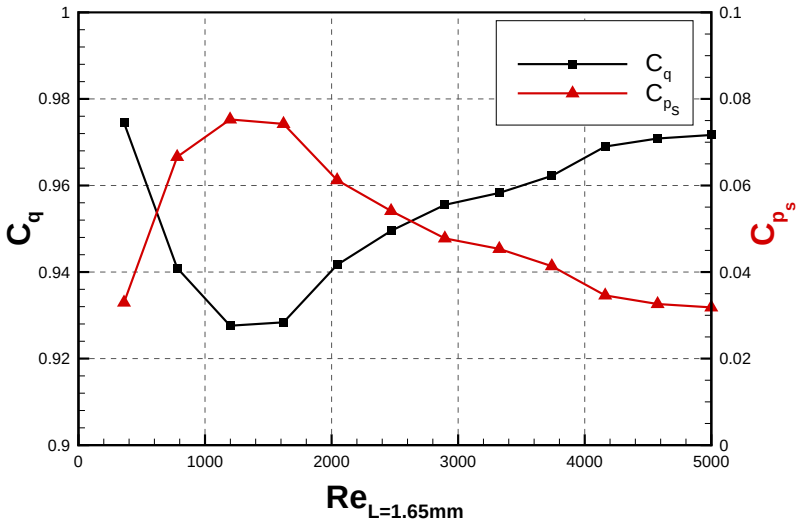

Figure B.7: Calibration rig dynamic and static pressure coefficients

B.4 Probe Calibration and Data Reduction

B.4.1 Three-Hole Pressure Probe

B.4.1.1 Probe Calibration

The probe was aerodynamically aligned with the calibration rig nozzle centerline. The gage pressures ($P_h - P_{C2}$ with h=1,2,3), measured through three separate channels, were normalized by the nozzle dynamic pressure (P_{C1}- P_{C2}), and corrected, such that:

$$C_{p_h} = \frac{P_h - P_s}{P_0 - P_s} = \frac{\frac{P_h - P_{c2}}{P_{c1} - P_{c2}} - C_{p_s}}{C_q} \tag{B.4}$$

where subscripts s and 0 refer to static and stagnation conditions, respectively. The calibration plane static and dynamic pressure coefficients, C_{p_s} and C_q, were calculated using Equations B.2 and B.3, respectively.

The pressure data measured from three holes were reduced according to the method of Lewis (1965) as follows:

$$\begin{aligned}
K_1 &= \frac{P_1 - P}{P_0 - P_s} = C_{p1} \\
K_{12} &= \frac{P_1 - P_2}{P_0 - P_s} = C_{p1} - C_{p2} \\
K_{13} &= \frac{P_1 - P_3}{P_0 - P_s} = C_{p1} - C_{p3} \\
K_{23} &= \frac{P_2 - P_3}{P_0 - P_s} = C_{p2} - C_{p3} \\
K_{\Phi 2} &= \frac{P_1 - P_2}{P_1 - P_3} = \frac{K_{12}}{K_{13}} \\
K_{\Phi 3} &= \frac{P_1 - P_3}{P_1 - P_2} = \frac{1}{K_{\Phi 2}}
\end{aligned} \tag{B.5}$$

where P_1, P_2 and P_3 represent the pressure measured from the three pressure holes, and P_s and P_0 refer to local static and total pressures at the measuring plane, respectively.

The probe calibration was performed in 0.5° steps over a pitch angle range of ±20°. The probe was used in non-nulling mode. Figure B.8 shows the calibration curves for a range of Re_w, where Re_w is based on the probe thickness, 2 mm.

In this study, the three-hole probe was used for the inlet flow measurements at the centerline where there was a minor variation in the flow velocity. Although the plane of measurement appears to be independent of Reynolds number variations, the data reduction routine includes Reynolds

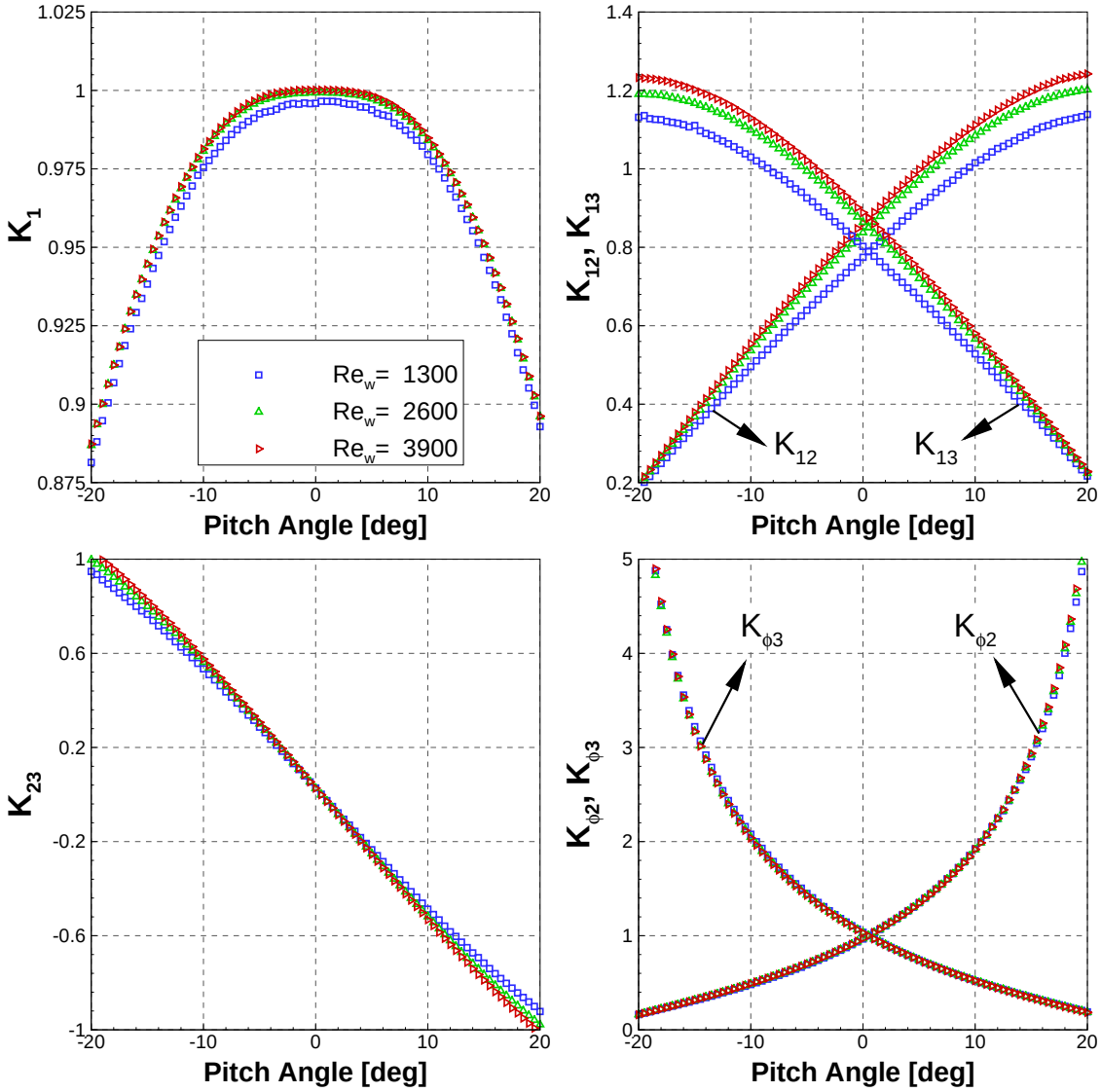

Figure B.8: Calibration curves for the three-hole pressure probe at various Reynolds numbers

number interpolation to increase the measurement accuracy by using calibration data for a range of Reynolds numbers.

B.4.1.2 Data Reduction

The pressure data measured from three ports of the probe were used to determine non-dimensional coefficients C_{ph}, h=1,2,3 using Equation B.4. These coefficients were substituted in Equation B.5 for the calculation of K_1, K_{12}, K_{13}, $K_{\Phi 2}$ and $K_{\Phi 3}$. Then, the flow angle was calculated using either $K_{\Phi 2}$ or $K_{\Phi 3}$ based on the following logic:

$$K_{\Phi 2} \leq K_{\Phi 3} \quad \Rightarrow \quad \Phi = interpolate(K_{\Phi 2}),$$

$$K_{\Phi 2} > K_{\Phi 3} \quad \Rightarrow \quad \Phi = interpolate(K_{\Phi 3}),$$

Once the flow angle was determined, the values of K_1, K_{12} and K_{13} were calculated using a linear interpolation between two flow angles. Then, the dynamic pressure coefficient, C_q, was obtained such that:

$$K_{\Phi 2} \leq K_{\Phi 3} \quad \Rightarrow \quad C_q = \frac{P_0 - P_s}{P_{0r} - P_{sr}} = (C_{p1} - C_{p2})/K_{12},$$

$$K_{\Phi 2} > K_{\Phi 3} \quad \Rightarrow \quad C_q = (C_{p1} - C_{p3})/K_{13}$$

Finally, static pressure and total pressure loss coefficients were calculated as follows:

$$C_{p_s} = \frac{P_s - P_{sr}}{P_{0r} - P_{sr}} = C_{p1} - K_1 C_q \tag{B.6}$$

$$C_{p_0} = \frac{P_0 - P_{0r}}{P_{0r} - P_{sr}} = 1 - C_q - C_{p_s} \tag{B.7}$$

B.4.2 Seven-Hole Pressure Probe

B.4.2.1 Probe Calibration

The method defined by Gerner *et al.* (1984) requires acquiring two sets of calibration data for low and high flow angles.

Low-Angle Coefficients The low-angles correspond to flow angles typically less than 30° where the flow is attached to the probe tip. The tangential reference system shown in Figure B.9 was adopted. The angle of attack, α_T, is the angle between the probe's x-axis and the projection of the

velocity vector in the vertical plane. The angle of sideslip, β_T, is the angle between the probe's x-axis and the projection of the velocity vector in the horizontal plane.

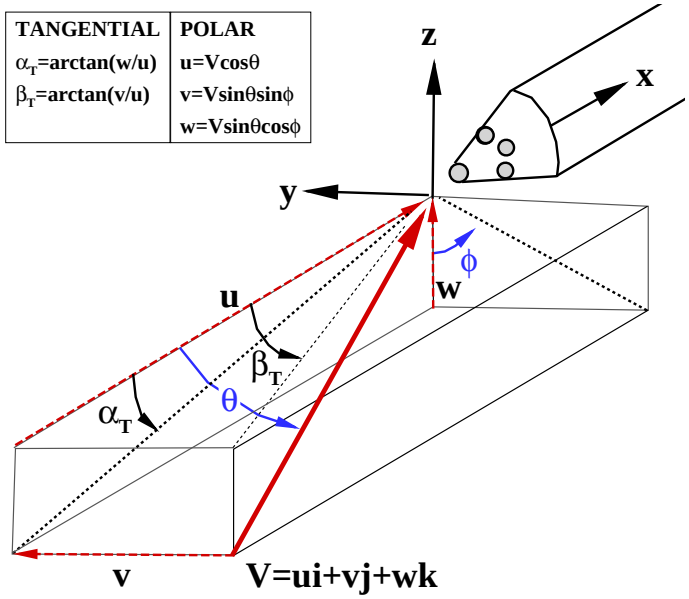

Figure B.9: Flow angle definitions, reproduced from Gerner *et al.* (1984)

Using measured pressure data from seven ports, the angular pressure coefficients for the angle of attack and side slip angles are defined as follows:

$$C_{\alpha_T} = \frac{1}{3}\left(2C_{\alpha_a} + C_{\alpha_b} - C_{\alpha_c}\right); \qquad C_{\beta_T} = \frac{1}{\sqrt{3}}\left(C_{\alpha_b} + C_{\alpha_c}\right) \tag{B.8}$$

where C_{α_a}, C_{α_b} and C_{α_c} are defined in the following form:

$$C_{\alpha_a} = \frac{P_4 - P_1}{P_7 - \overline{P}_{1-6}}; \qquad C_{\alpha_b} = \frac{P_3 - P_6}{P_7 - \overline{P}_{1-6}}; \qquad C_{\alpha_c} = \frac{P_2 - P_5}{P_7 - \overline{P}_{1-6}} \tag{B.9}$$

Then, the total and dynamic pressure coefficients were calculated from:

$$C_0 = \frac{P_7 - P_{0_L}}{P_7 - \overline{P}_{1-6}}; \qquad C_q = \frac{P_7 - \overline{P}_{1-6}}{P_{0_L} - P_{\infty_L}} \tag{B.10}$$

High-Angle Coefficients At high-angles, the flow separates at the probe tip and the ports in the separation region become insensitive to the changes in the flow angularity (Gerner *et al.*, 1984). Thus, only the ports in attached flow zone are used to obtain calibration coefficients. The port measuring the highest pressure is considered as the total pressure port and seven sets of coefficients, corresponding to each port, were calculated for each angular space. A polar reference system, shown in Figure B.9, was used. The pitch angle, θ, represents the absolute angle between the velocity vector and the probe's x-axis. The roll angle, ϕ, describes the azimuthal orientation of the

velocity vector in the y-z plane, measured positive counter clockwise from the negative z-axis as viewed from the front. For high-angles, the coefficients for the pitch and roll angle were calculated as follows:

$$C_{\theta_n} = \frac{P_n - P_7}{P_n - (P_{n^-} + P_{n^+})/2}; \qquad C_{\Phi_n} = \frac{P_{n^-} - P_{n^+}}{P_n - (P_{n^-} + P_{n^+})/2} \tag{B.11}$$

where n represents the pressure port with highest pressure reading. The convention for the selection of coefficients set is presented in Figure B.10.

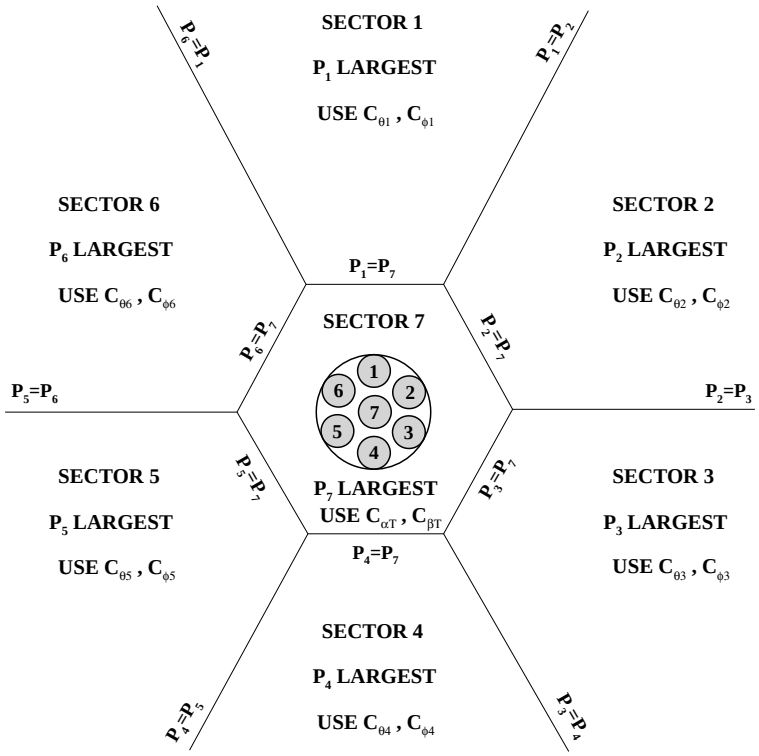

Figure B.10: Division of angular space, reproduced from Gerner *et al*. (1984)

For high-angles, the total and dynamic pressure coefficients are given by:

$$C_{0_n} = \frac{P_n - P_{0_L}}{P_n - (P_{n^-} + P_{n^+})/2}; \qquad C_{q_n} = \frac{P_n - (P_{n^-} + P_{n^+})/2}{P_{0_L} - P_{\infty_L}} \tag{B.12}$$

Using the method defined for the low and high angles, the coefficients were calculated for the calibration data. For low-angles, the probe calibration was performed in 2° steps over pitch and yaw angles at a range of ±26°. The calibration data for low-angles is shown in Figure B.11. A second set of calibration was performed for high-angles. The probe calibration was performed in 2° steps over pitch and yaw angles from 20° to 46°.

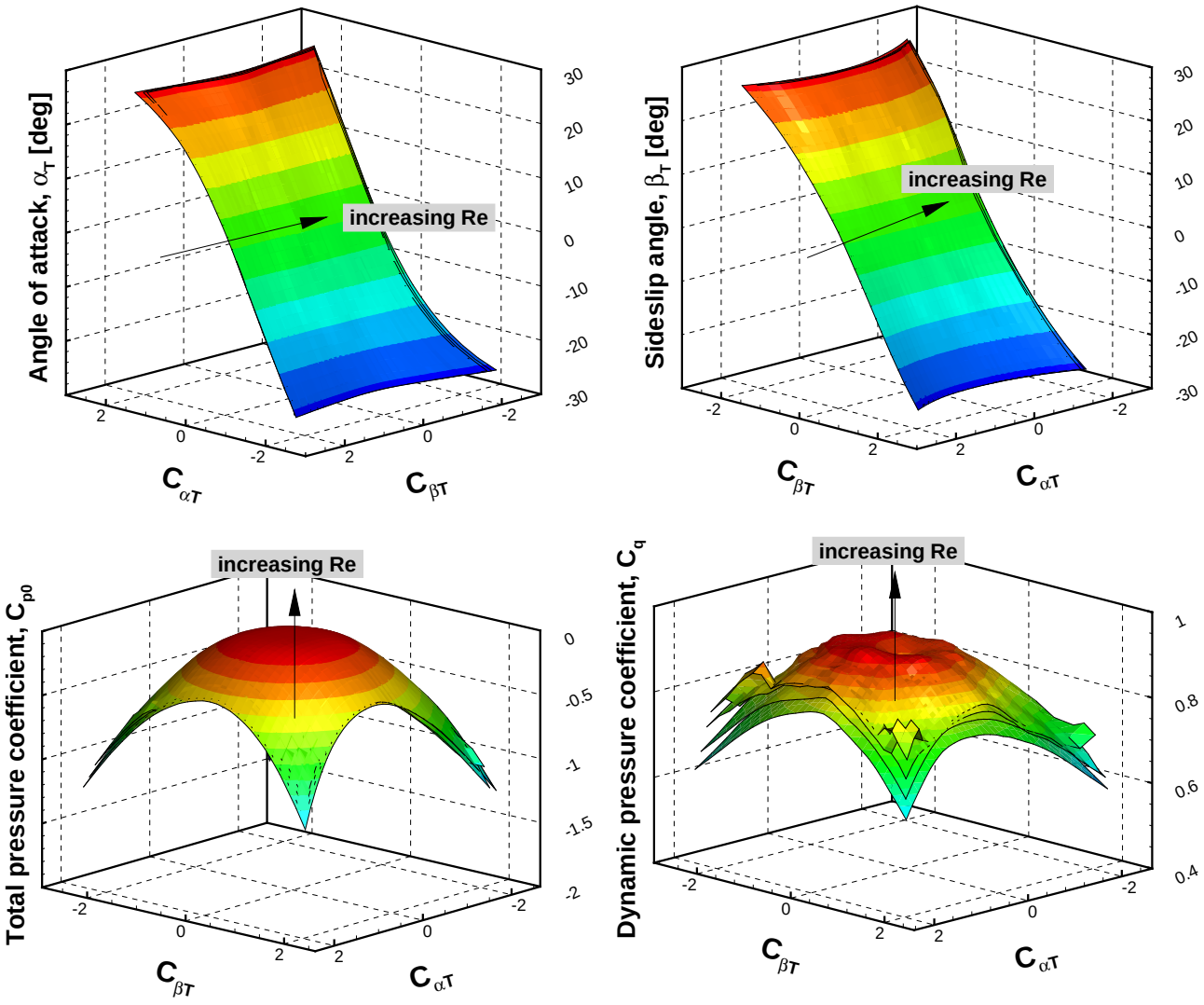

Figure B.11: Calibration curves for the seven-hole pressure probe at $Re_{w=2.4mm}$=1560, 3130, 4670 and 6720 (Corresponding to 10, 20, 30 and 43 m/s)

B.4.2.2 Data Reduction

Once the calibration coefficients were calculated for low and high angles, a fourth order polynomial expansion in the following form was used to determine flow variables:

$$\begin{aligned}[A_i] \;=\; & [K_1^A + K_2^A C_{\alpha T} + K_3^A C_{\beta T} + K_4^A C_{\alpha T}^2 + K_5^A C_{\alpha T} C_{\beta T} + \\ & K_6^A C_{\beta T}^2 + K_7^A C_{\alpha T}^3 + K_8^A C_{\alpha T}^2 C_{\beta T} + K_9^A C_{\alpha T} C_{\beta T}^2 + \\ & K_{10}^A C_{\beta T}^3 + K_{11}^A C_{\alpha T}^4 + K_{12}^A C_{\alpha T}^3 C_{\beta T} + K_{13}^A C_{\alpha T}^2 C_{\beta T}^2 + \\ & K_{14}^A C_{\alpha T} C_{\beta T}^3 + K_{15}^A C_{\beta T}^4]\end{aligned} \tag{B.13}$$

In matrix notation, the equation takes the following form:

$$[A] = [C]\,[K] \tag{B.14}$$

where $m \times 1$ $[A]$-matrix represents one of the four flow variables, C_{α_T}, C_{β_T}, C_0 and C_q for low angles and θ, ϕ, C_{0_n} and C_{q_n} for high angles with i representing the i_{th} data point. The 15×1 $[K]$-matrix represents the calibration constants. The $m \times 15$ $[C]$-matrix includes the terms calculated using the C_{α_T} and C_{β_T} for low flow angles and C_{θ_n} and C_{ϕ_n} for high flow angles. Therefore, the $[C]$-matrix and $[A]$-matrices were formed to calculate the $[K]$-matrix using the calibration data with the following equation:

$$[K] = \left[C^T C\right]^{-1} [C]^T\,[A] \tag{B.15}$$

The $[C]$-matrix was calculated using the measurement data. Finally, the flow variables for the unknown flow field were calculated using the Equation B.14. Details of data reduction procedure can be found in Gerner *et al*. (1984).

B.5 Pressure Tap Locations

Table B.1 shows the spanwise and chordwise locations of the pressure taps on the instrumented blades.

Table B.1: Static pressure taps' locations

Tap no	Chordwise locations (SS) x/c [%]	Chordwise locations (PS) x/c [%]	Spanwise locations z/s [%]
1	4.95	2.93	7.5
2	9.07	9.59	15
3	14.33	17.00	30
4	17.54	29.63	50
5	20.80	42.60	
6	26.29	57.40	
7	29.63	73.71	
8	32.99	82.46	
9	38.63	90.93	
10	42.60	95.05	
11	46.58		
12	50.00		
13	53.42		
14	57.40		
15	61.37		
16	67.01		
17	70.37		
18	73.71		
19	79.20		
20	83.00		
21	86.73		
22	90.41		
23	94.03		
24	97.07		

B.6 Plasma Actuator Force Measurements

The thrust induced by plasma actuator was measured in quiescent air. The setup used in plasma induced thrust measurement is shown schematically in Figure B.12(a). A support tool, made out of plexiglass to avoid discharge, was used to set the plasma instrumented airfoil to a certain angle and secure it in that orientation. The blade angle was adjusted such that the plasma induced thrust will act normal to the scale. The support tool, together with the blade, was placed on a high precision scale ($\pm 0.01g$). The plasma actuator was arranged such the induced flow acted upward and the induced thrust acted downward. The oil-film flow visualization presented in Figure B.12(c) demonstrates that the induced flow acts upward and the oil mixture moves up due to shear force. Figure B.12(d) shows a photograph taken during the oil flow visualization shows that the oil-powder mixture moves upward by the plasma actuator force. Figure B.13 shows a sample measurements data for the time variation of the current, voltage and power.

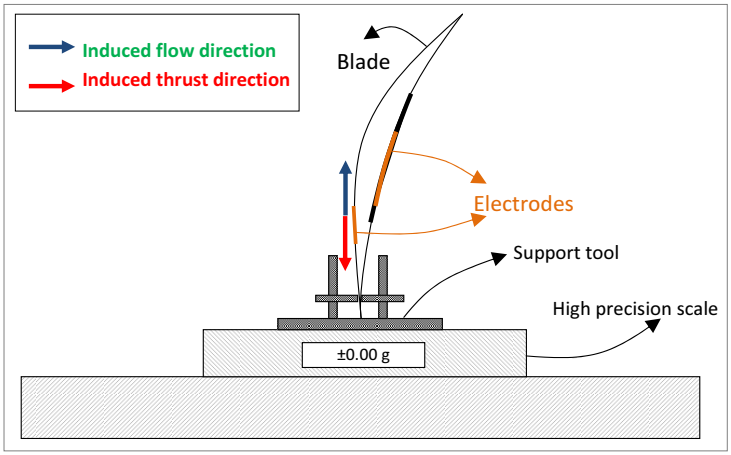

(a) The schematic representation

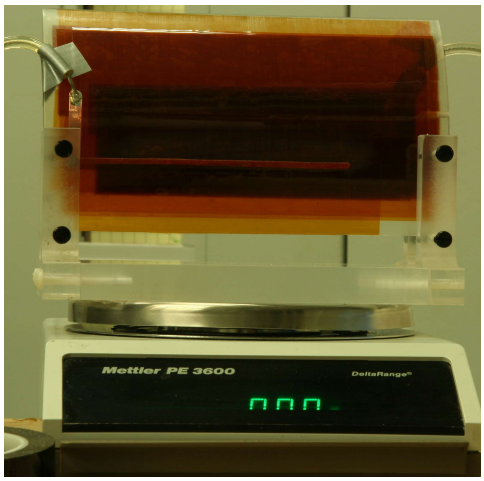

(b) Picture of the setup

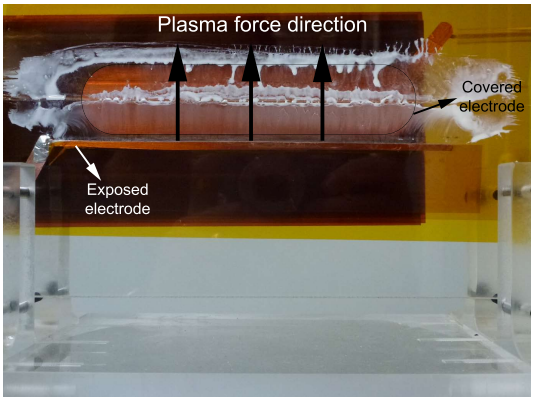

(c) Oil-film flow visualization for plasma actuation

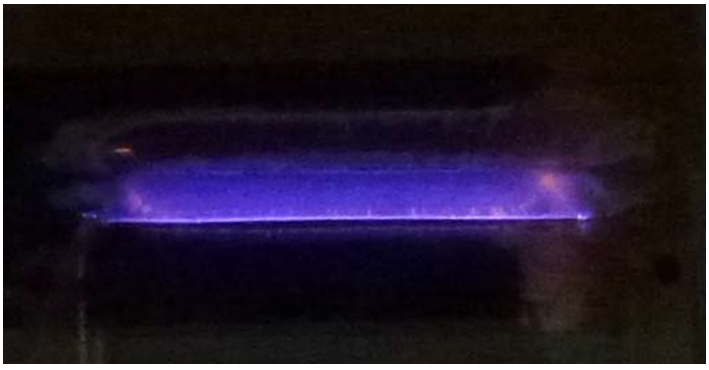

(d) Plasma formation

Figure B.12: Plasma actuator induced thrust measurement setup

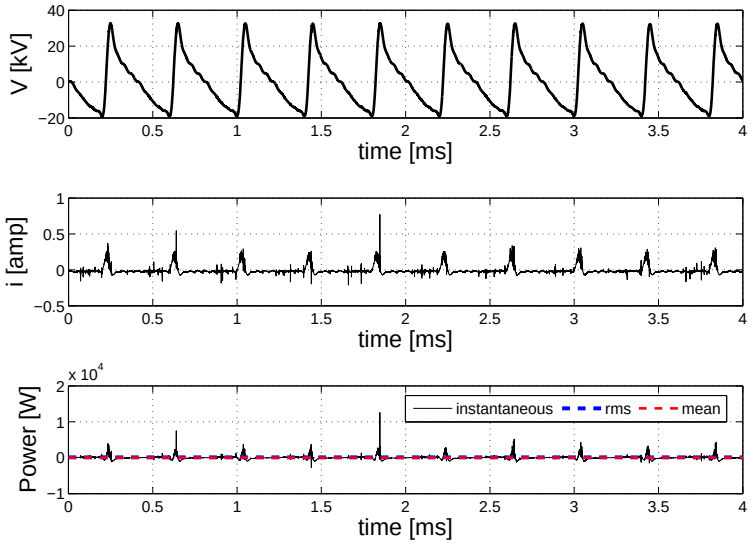

Figure B.13: Time histories of voltage, current and power for plasma actuation frequency 2.5 kHz

The plasma actuator force measurements for the SLA blade were initially performed using positive and negative sawtooth waveforms. Figure B.14(a) and Figure B.14(b) show the measurement results with negative and positive sawtooth waveforms for an AC voltage frequency of 2.5 kHz. The negative sawtooth wave generates more plasma actuation strength using a smaller power. Therefore, negative sawtooth waveform was used throughout the plasma actuation experiments. Then, the effect of AC voltage frequency was investigated at 1.5 kHz, 2.5 kHz and 3.5 kHz. Figure B.14(c) presents the actuator strength variations with AC voltage at various plasma actuation frequencies. The maximum achievable actuator strength was 77 mN/m at 52 kV_{pp} (14 kV_{rms}) AC voltage and at 2.5 kHz AC voltage frequency. Figure B.14(d) shows the corresponding power requirement to operate plasma actuator. For the maximum achievable actuation strength, the power consumed by the actuator was 22.9 W.

The plasma actuator force measurements performed for Teflon as the second dielectric material used in the plasma actuation experiments. Figure B.15 shows the results of the plasma force measurements for a 1/4 inch thick Teflon plate. The AC voltage frequency was set to 2.5kHz. Figure B.15(a) shows that the maximum actuation strength was 88.3 mN/m at 19.2 kV_{rms} (71.2 kV_{pp}) corresponding to a power consumption of 39.2 W.

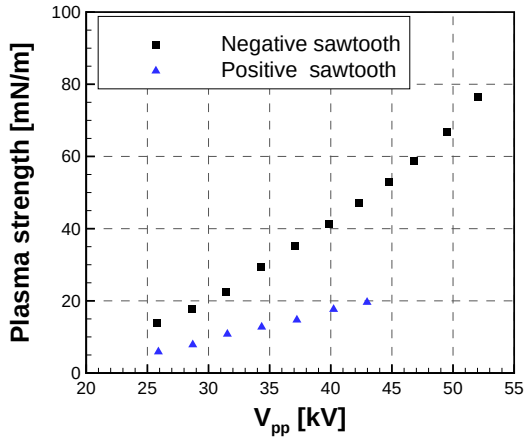

(a) AC signal form effect on the plasma actuation strength

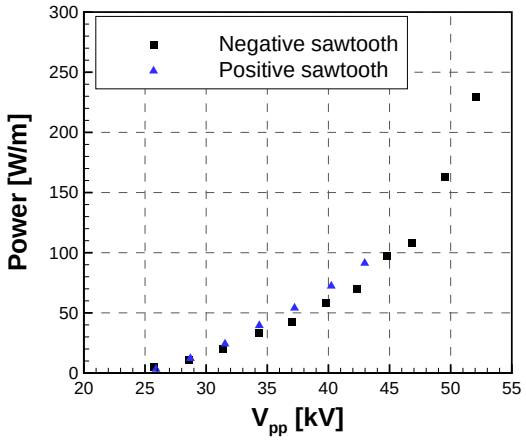

(b) AC signal form effect on the plasma power

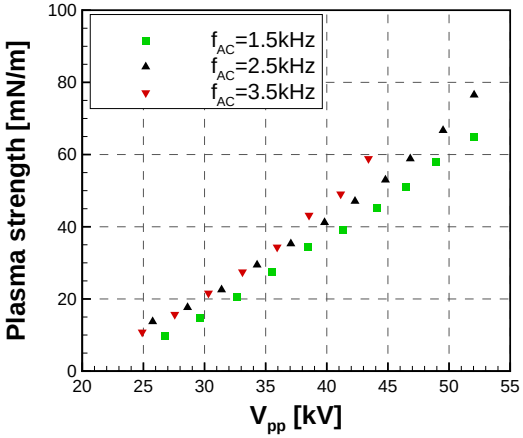

(c) AC voltage frequency effect on the plasma actuation strength

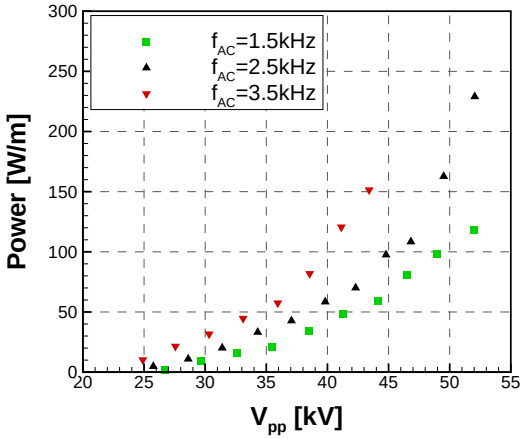

(d) AC voltage frequency effect on the plasma power

Figure B.14: Plasma actuator strength measurements for SLA blade

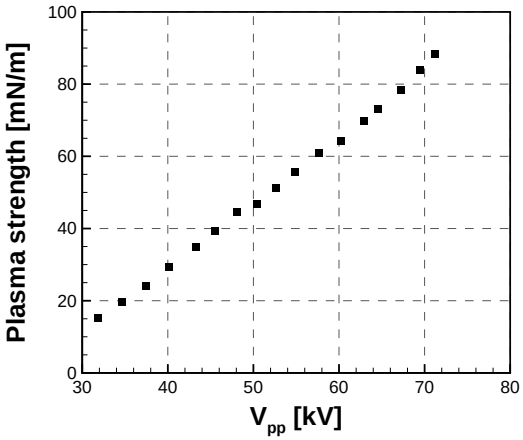

(a) Plasma actuator strength versus peak to peak voltage

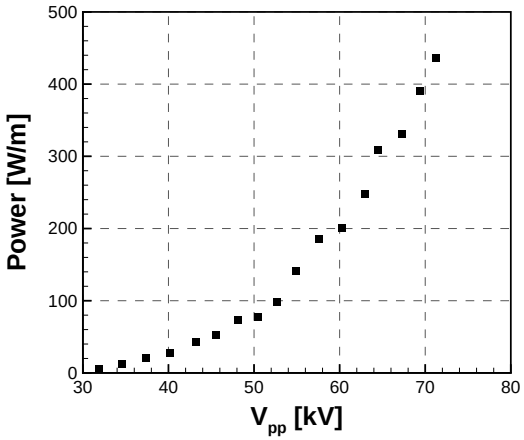

(b) Plasma power versus peak to peak voltage

Figure B.15: Plasma actuator strength measurements for Teflon

Appendix C

Details of Experimental and Computational Results

C.1 Endwall Bleed/Suction Mass Flow Measurements

As discussed in Section B, the mass flow through endwall suction surfaces was measured experimentally by calculating the mass flow passing through plastics tube connected to metal boxes mounted on the outside walls of the test section. The velocity measurements were performed at two Reynolds numbers, 2.6×10^4 and 3.7×10^4, based on the tube diameter. These Reynolds numbers correspond to bleed and suction cases, respectively. Based on these Reynolds numbers, the flow inside the tube was predicted as turbulent since the Reynolds numbers for both cases were larger than the critical Reynolds number for transition in pipe flows, where $\mathrm{Re}_{d,crit} \approx 2300$ (White, 1998). Figure C.1 shows the velocity profiles inside the tube which were normalized by the centerline velocity, V_{CL}. It can be seen that the velocity profiles are similar at each Reynolds number. The velocity profiles were used together with the centerline velocities measured by a pitot-static tube to determine the mass flow through the plastics tube.

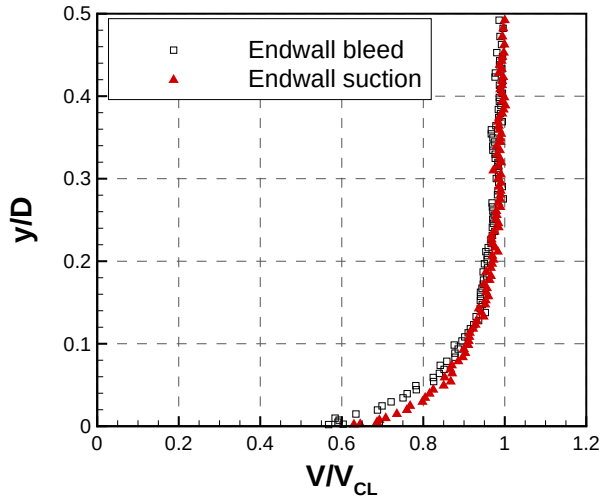

Figure C.1: Tube boundary layer profiles

C.2 Freestream Turbulence Intensity Effect

The inlet freestream turbulence intensity effect on the suction surface boundary layer is investigated by carrying out simulations at inlet turbulence intensity values of 0.3%, 0.5% and 1.0%. It can be seen from Figure C.2 that the laminar separation bubble becomes smaller as the inlet turbulence intensity increases. Moreover, the turbulent separation point moves closer to the blade trailing edge.

Figure C.3 shows turbulence intensity contour on symmetry plane. It can be seen that the turbulence intensity stays almost the same from inlet boundary to blade leading edge.

C.3 Surface Pressure Coefficient Distributions for Endwall Suction Mesh

Figure C.4 shows the experimental and computational (obtained with the unstructured endwall suction control mesh) surface pressure distributions at 50%, 30%, 15% and 7.5% spanwise locations. There is a good agreement between experimental and computational data at all spanwise locations.

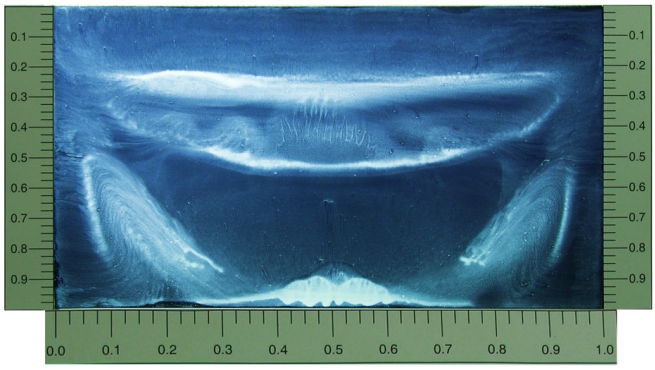

(a) Experiment

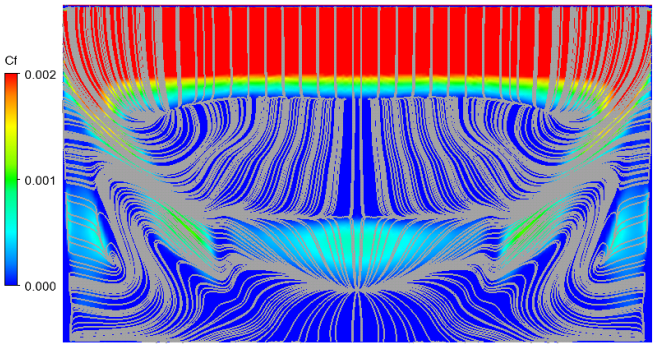

(b) CFD, Tu=0.3%

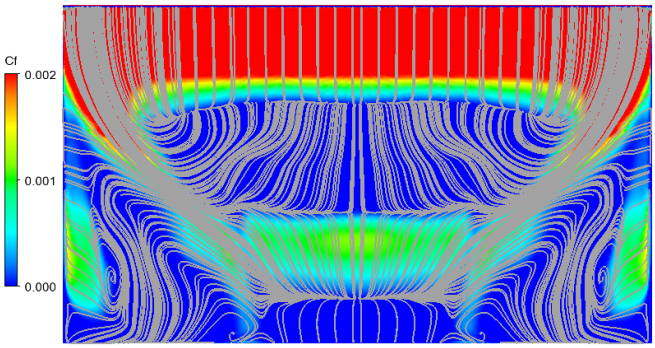

(c) CFD, Tu=0.5%

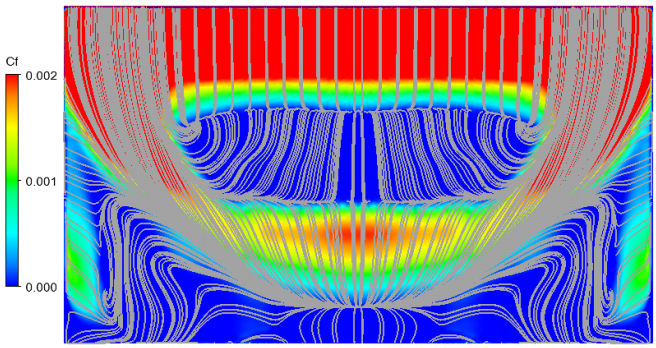

(d) CFD, Tu=1.0%

Figure C.2: Inlet turbulence intensity effect on predicted streamwise skin-friction coefficient plotted together with the limiting streamlines for velocity

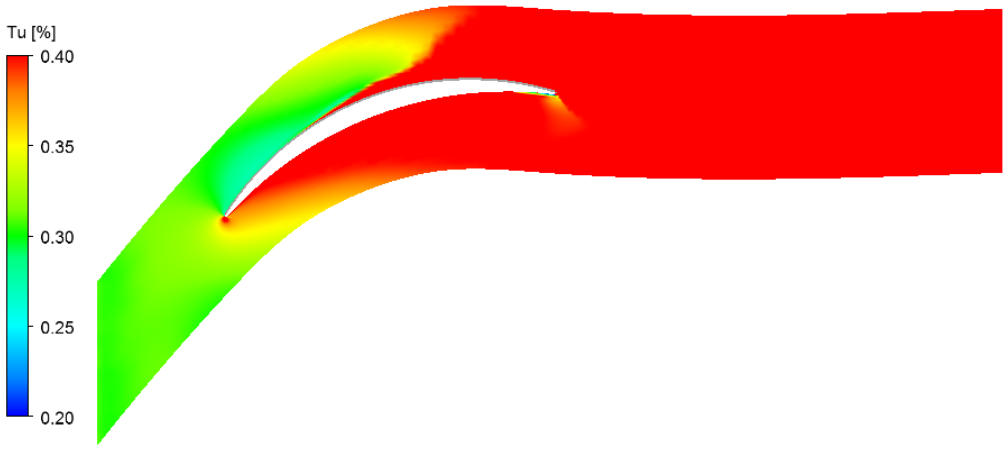

Figure C.3: Turbulence intensity contours on symmetry plane

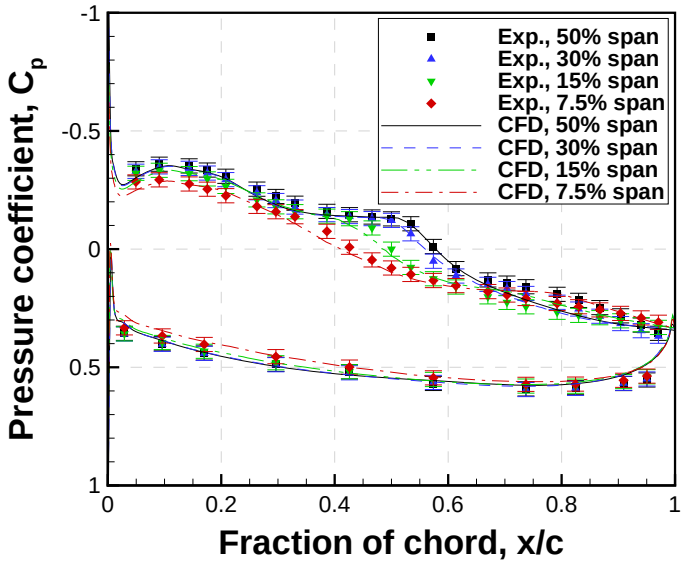

Figure C.4: Pressure coefficient distributions at various spanwise locations obtained with unstructured mesh for endwall suction flow control

C.4 Boundary Layer Tripping Effect of Plasma Actuator

Being one of the passive flow control techniques, the separation control using boundary layer trips is widely used in the literature. However, this study aims to control boundary layer flow separation by using plasma actuation. Therefore, the plasma actuator setup should not have a dominant effect on the boundary layer flow. To assess the effect of plasma actuator setup on the boundary layer flow, a parametric study was performed. An experimental study carried out by Zhang (2005) has shown that the surface trip should be located between the suction peak and separation point for the optimum control efficiency. The boundary layer trip becomes ineffective at the upstream of the suction peak since the acceleration of the flow suppresses the transition. Similarly, the boundary layer trip has no benefit after the separation point. Moreover, this study has shown that the optimum surface trip thickness corresponds to $t_{trip}/\delta^* = 0.6$.

The parametric study was carried out using rectangular surface trips on the suction surface of the instrumented blade with potential plasma actuator thicknesses at various chordwise locations. The surface trip effect was determined based on the surface pressure distribution measurements. The properties of surface trips used in the parametric study are presented in Table C.1. The relative thickness of the boundary layer trip, t_{trip}/δ^*, was calculated by normalizing the boundary layer trip thickness by the local displacement thickness.

Figure C.5(a) shows surface pressure coefficient variations when various surface thicknesses of surface trips are located at 0.1 chord. At this location, the boundary layer was very small such that the effect of surface trip was apparent even with the smallest thickness corresponding to 1.90 t_{trip}/δ^*. The surface trip changed leading edge surface pressure distribution significantly. The reattachment point moved upstream due to earlier boundary layer transition. Figure C.5(b) and Figure C.5(c) show that the surface static pressure becomes less sensitive to the surface trip as it moves downstream. At 0.3 chord with $t_{trip} = 0.0075inch$, corresponding to $t_{trip}/\delta^* = 0.63$, the surface trip has the minimum effect where the surface pressure almost stays the same and reattachment point moves upstream slightly.

C.5 Tollmien-Schlichting Wave Frequency Prediction

The point of instability, where the laminar boundary layer transition is triggered, was observed to have a Reynolds number momentum thickness ($Re_\theta = (\rho V\theta)/\mu$) of 200 for a flat plate (Schlichting and Gersten, 2000). This value becomes larger with favorable pressure gradients and becomes smaller with adverse pressure gradients. Howell *et al*. (2001) have investigated the performance of low-pressure turbines experimentally. Their measurements have shown that the wake-induced transition occurs around the laminar separation point. The deceleration of the boundary layer flow

Table C.1: Parameters used in the boundary layer sensitivity study

Case	x_{trip} [x/c]	t_{trip} [inch]	t_{trip}/δ^*
1	0.1	0.0075	1.90
2	0.2	0.0075	0.95
3	0.3	0.0075	0.63
4	0.1	0.0105	2.66
5	0.2	0.0105	1.33
6	0.3	0.0105	0.89
7	0.1	0.0135	3.42
8	0.2	0.0135	1.71
9	0.3	0.0135	1.14

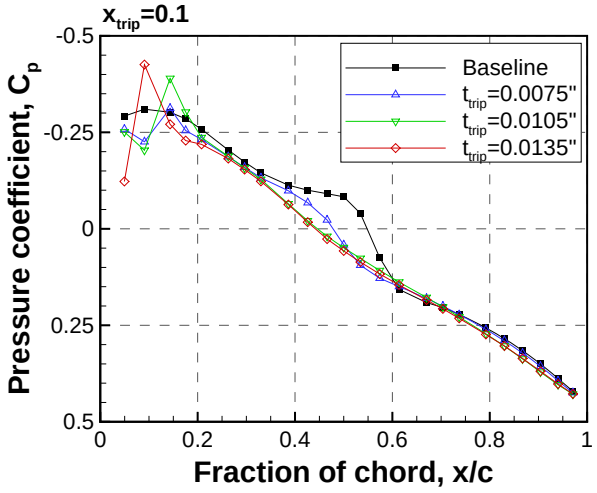

(a) Boundary layer trip at 0.1 chord

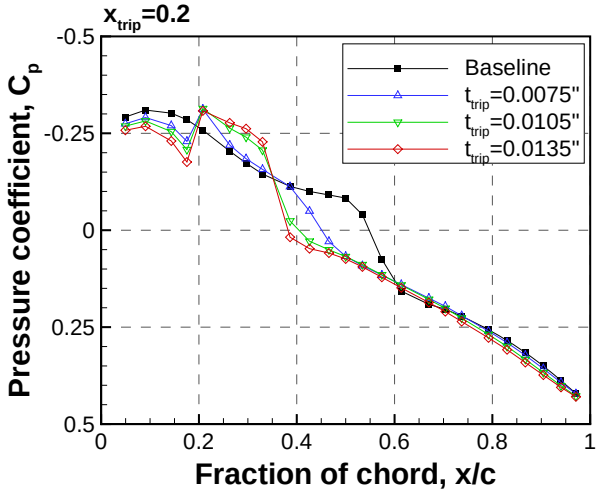

(b) Boundary layer trip at 0.2 chord

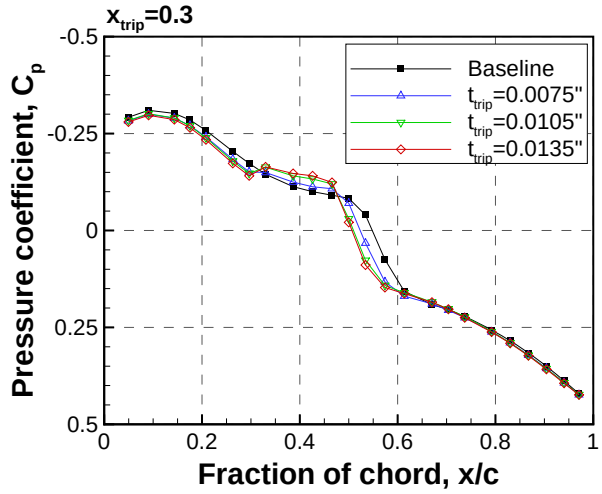

(c) Boundary layer trip at 0.3 chord

Figure C.5: Surface pressure coefficient variation with various boundary layer tripping thicknesses

velocity in the separation region increases receptivity of the boundary layer to disturbances. The disturbed boundary layer flow experiences an earlier transition and subsequently an earlier reattachment. Moreover, the value of Re_θ, measured by Howell *et al*. (2001) just before the separation point, was found to be approximately 250 for various profiles.

Based on this discussion, it may be inferred that critical Re_θ value for the compressor blades should be smaller than 200 due to presence of adverse pressure gradient where the flow becomes more unstable and therefore susceptible to disturbances. The Re_θ distribution, based on the CFD, is shown in Figure C.6(a) for the current airfoil. The Re_θ is observed to be smaller than 200 before 0.4 chord which suggests that the receptivity of the laminar boundary layer is very large. This location lies between the separation and reattachment points.

Walker (1989) states that the dominant disturbance breakdown frequency at the breakdown matches well with the T-S wave frequency having the maximum amplification ratio. This statement suggests that the boundary layer transition onset can be triggered earlier if T-S wave frequency is amplified externally. Using the T-S wave length approximation given by Walker (1989), the T-S wave frequency was calculated as follows:

$$f_{T-S} = \frac{\vartheta}{\lambda} = \frac{u_e^2}{2\upsilon Re_{\delta*}^{3/2}}$$

where ϑ is the phase velocity, λ is the wave length, υ is the kinematic viscosity, u_e is the boundary layer edge velocity and $Re_{\delta*}$ is the boundary layer displacement thickness Reynolds number. Figure C.6(b) presents the T-S wave frequency variation in the chordwise direction. The value of the T-S wave frequency corresponding to 0.4 chord is 300 Hz. This value was considered to be representing the T-S wave frequency.

In an effort to validate the computationally obtained T-S wave frequency in the present study, Huang *et al*. (2006) have made hot wire measurements to find out the spectra of the velocity fluctuations on a linear cascade of PakB turbine airfoils at $Re_c = 50000$. At the upstream of the reattachment point, the spectra has shown that the unsteadiness and the broad peak were centered around 300 Hz. This value was associated with the Kelvin-Helmholtz instability of the separated shear layer. The same frequency was measured at the downstream of the reattachment point. This result is consistent with the computationally obtained T-S wave frequency.

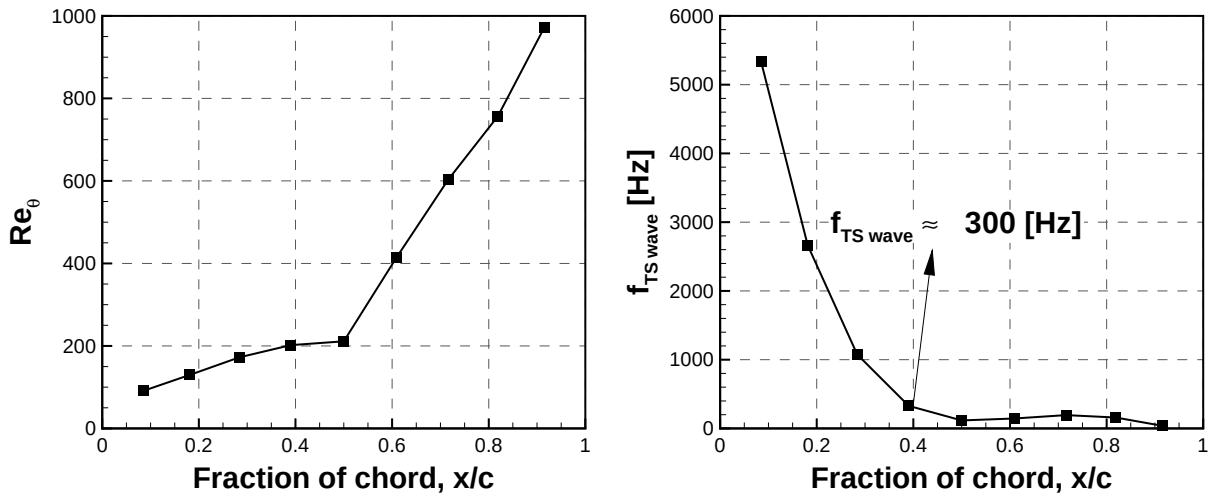

(a) Re_θ (b) T-S wave frequency

Figure C.6: Re_θ and T-S wave frequency distributions over the blade suction surface